Inhibition of Mdm2–p53 interaction as a therapeutic strategy for the treatment of p53 wild-type rhabdomyosarcoma

Guillem Pons Barcons

PhD thesis

Inhibition of Mdm2-p53 interaction as a therapeutic strategy for the treatment of p53 wild-type rhabdomyosarcoma

Presented by

Guillem Pons Barcons

Submitted to obtain the degree of Doctor of Philosophy in
Biochemistry, Molecular Biology, and Biomedicine

Performed at the Childhood Sarcoma Laboratory of the
Childhood Cancer and Blood Disorders research group at the
Vall d'Hebron Institute of Research (VHIR)

Candidate	Director	Director
Guillem Pons Barcons	**Josep Roma Castanyer**	**Lucas Moreno Martín-Retortillo**

Thesis affiliated with the PhD program in Biochemistry, Molecular Biology, and Biomedicine
Department of Biochemistry and Molecular Biology
Universitat Autònoma de Barcelona

Academic tutor: Dr. Jose Ramón Bayascas Ramírez

2024

To all those who helped turn childhood cancer into a mere comma for me,
enabling me to continue writing my story and pursue my dreams.

To my parents and those who love me.

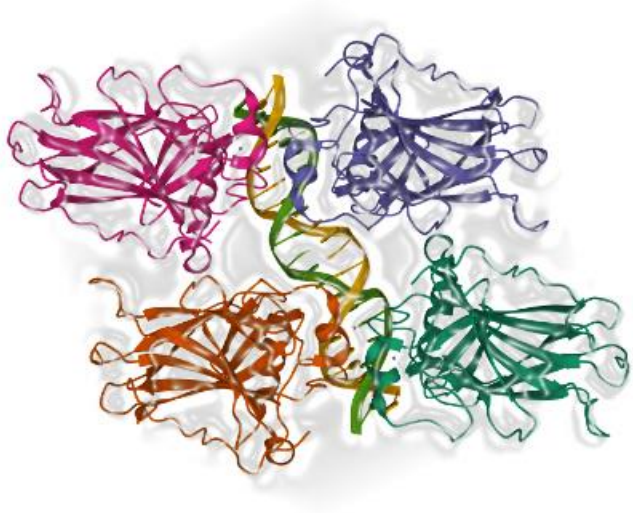

Cartoon adapted from the crystal structure of
the p53 core domain bound to a DNA full consensus site as
a self-assembled tetramer (Chen, Y. *et al.* Structure, 2010)

Acknowledgements

Embarking on this journey towards completing my doctoral thesis has been both a challenging and rewarding experience. The path has been marked by countless learning opportunities, and it would not have been possible without the invaluable support, guidance, and encouragement from a diverse group of individuals and institutions.

From the inception of this research project to its completion, I have been fortunate to collaborate with exceptional professionals and to be part of a supportive academic community. Their contributions, whether through direct involvement in the research or through moral and logistical support, have significantly enriched my academic journey.

First and foremost, I would like to express my deepest gratitude to my thesis director, Dr. Josep Roma, for his unwavering guidance, constant support, and patience throughout this process. From the very beginning, his trust in my abilities and his belief in the potential of this work have been fundamental in driving me forward and achieving this milestone.

I am also deeply thankful to my co-director Dr. Lucas Moreno, Head of the Childhood Cancer and Blood Disorders group, for his support and invaluable advice, which has contributed to the success of this project. I also wish to acknowledge the former heads of the group, Dr. Josep Sánchez de Toledo and Dr. Soledad Gallego, whose early encouragement and expertise were essential during the initial stages of my research career.

Special thanks go to my lab colleagues, Natalia and Patricia, who welcomed me warmly and provided me essential training in techniques and methodologies crucial for my research. Their mentorship, patience, and willingness to share their knowledge significantly shaped my development in the lab and laid the foundation for my work.

I am particularly grateful to Gabriel, whose support throughout my thesis journey has been invaluable. Our shared visions, in-depth discussions, and collaborative efforts have been fundamental to the progress and ultimate success of this research. His dedication and insightful contributions have been a cornerstone of this project.

I would also like to extend my heartfelt thanks to Lia and Júlia, the current PhD students, for their enthusiasm and collaboration, which enriched my experience and helped foster a positive working environment. I am equally grateful to Ainara, Paula, and Ana, the lab technicians during my thesis, whose daily technical support has been indispensable to the success of the research project.

Additionally, I would like to acknowledge my colleagues from the adjacent Paediatric Neural tumour's lab: Miguel, for his valuable advice and assistance; Carlos, Marc, Roby, Ariadna, for their companionship and suggestions; and Mari, Adrià, Marta, and Khloud for their support during the final years of my thesis. I would also want to extend my gratitude to the Paediatric Translational Medicine subgroup (Aroa, Andrea, Sergio, Carolina) and to the Master students involved in both laboratories for their contributions and collaboration.

The supportive environment at the research centre has played an essential role in my experience. I would like to thank the members of the Metabolism Lab, with whom I shared the cell cultures room, as well as colleagues from other labs, the technical support staff from VHIR-UAT, VHIR-Collserola lab coordinators, and the cafeteria staff for contributing to such a welcoming atmosphere.

I would like to express my gratitude to my research collaborators, particularly Dr. Jordi Puigvert from Uppsala University, for his invaluable contribution to this project. I would also like to thank my thesis committee members, Dr. Ibane Abasolo, Dr. Marta Crespo, and Dr. Cristian Moiola, for their annual evaluations of my work and their insightful suggestions, which greatly contributed to the development of this thesis. I also appreciate the AGAUR for awarding me the FI-AGAUR grant, which funded my salary throughout the project and enabled me to attend several international conferences to present my research findings.

Finally, I would like to extend my deepest thanks to my family, for their unconditional love, patience, and constant support, and to my friends for always being by my side during moments of stress and celebration. Without their understanding and encouragement, this achievement would not have been possible.

To all of you, my heartfelt thanks.

Abstract

Rhabdomyosarcoma is a high-risk paediatric cancer that results from errors in the myogenic differentiation process. Representing over 50% of paediatric soft tissue sarcomas and approximately 4% of all diagnosed paediatric tumours, RMS has an overall 5-year survival rate of 70%, which drops to below 30% in metastatic cases. RMS is categorized into two main types: fusion-positive (FP-RMS) and fusion-negative (FN-RMS). FP-RMS is characterized by translocations between the *PAX3* or *PAX7* genes and the *FOXO1* gene, leading to the formation of a fusion protein that acts as the main oncogenic driver of the disease. While FP-RMS is less common, it has a poorer prognosis compared to FN-RMS, with PAX3-FOXO1+ tumours exhibiting the worst outcomes. In contrast, FN-RMS shows significant survival rate variations based on distinct methylation patterns or mutations in genes such as *MYOD1*. These findings underscore the necessity of incorporating molecular features into high-risk protocols and to develop innovative therapeutic strategies to counteract resistance to standard treatments.

Unlike many adult cancers, loss-of-function *TP53* mutations are relatively rare in RMS, occurring in about 5–10% of cases at diagnosis. Instead, tumour cells often use alternative mechanisms to impede p53 activation, such as the overexpression or overactivation of MDM2, which promotes p53 degradation via ubiquitin-mediated pathways. Thus, disrupting the MDM2-p53 interaction is a promising strategy to release p53 from MDM2 control and restore its tumour suppressive functions in p53 wild-type tumours. Over the last decade, several compounds inhibiting the interaction between MDM2 and p53 have been synthesized, and their efficacy has been demonstrated at the preclinical level. However, results from early-phase clinical trials have shown limited efficacy of these compounds as a monotherapy, highlighting the need to study additional combinations with other drugs to enhance their antitumoral effect.

This thesis explores the single-drug efficacy of four promising MDM2 inhibitors (siremadlin, idasanutlin, navtemadlin, and MI-773) and provides the results from drug combination screening, highlighting the therapeutic potential of combining siremadlin with specific compounds, in particular with olaparib. Through a comprehensive study of the impact of this combination on RMS tumour growth *in vitro* and *in vivo*, as well as its integration with currently approved treatments, our study provides valuable insights into novel multidrug therapeutic strategies that could potentially be translated to the treatment of p53 wild-type RMS and other solid tumours.

List of publications

The following list includes all publications resulting from the research projects undertaken during my doctoral studies, encompassing abstracts, articles, and reviews.

1. **Pons G**, Gallo-Oller G, García-Gilabert L, Zarzosa P, Sansa-Girona J, Navarro N, et al. Combined inhibition of MDM2 and PARP lead to a synergistic anti-tumoral response in p53 wild-type rhabdomyosarcoma. Cancer Res. 2024;84(6_Supplement):5473.

2. Gallo-Oller G, **Pons G**, Sansa-Girona J, Navarro N, Zarzosa P, García-Gilabert L, et al. TRIB3 silencing promotes the downregulation of Akt pathway and PAX3-FOXO1 in high-risk rhabdomyosarcoma. Exp Hematol Oncol. 2024;13(1):38.

3. **Pons G**, Gallo-Oller G, Navarro N, Zarzosa P, Sansa-Girona J, García-Gilabert L, et al. Analysis of cancer genomic amplifications identifies druggable collateral dependencies within the amplicon. Cancers (Basel). 2023;15(6):1636.

4. Navarro N, Molist C, Sansa-Girona J, Zarzosa P, Gallo-Oller G, **Pons G**, et al. Integrin alpha9 emerges as a key therapeutic target to reduce metastasis in rhabdomyosarcoma and neuroblastoma. Cellular and Molecular Life Sciences. 2022;79(11):546.

5. Zarzosa P, Garcia-Gilabert L, Hladun R, Guillén G, Gallo-Oller G, **Pons G**, et al. Targeting the hedgehog pathway in rhabdomyosarcoma. Cancers (Basel). 2023;15(3):727.

6. Giralt I, Gallo-Oller G, Navarro N, Zarzosa P, **Pons G**, Magdaleno A, et al. Dickkopf proteins and their role in cancer: a family of Wnt antagonists with a dual role. Pharmaceuticals. 2021;14(8):810.

7. Giralt I, Gallo-Oller G, Navarro N, Zarzosa P, **Pons G**, Magdaleno A, et al. Dickkopf-1 inhibition reactivates Wnt/β-catenin signaling in rhabdomyosarcoma, induces myogenic markers in vitro and impairs tumour cell survival in vivo. Int J Mol Sci. 2021;22(23):12921.

8. Molist C, Navarro N, Giralt I, Zarzosa P, Gallo-Oller G, **Pons G**, et al. miRNA-7 and miRNA-324-5p regulate alpha9-Integrin expression and exert anti-oncogenic effects in rhabdomyosarcoma. Cancer Lett. 2020; 477:49–59.

Table of Contents

List of Figures

List of Tables

Abbreviations

Letter	*Abbreviation*	*Meaning*
#	β-cat	β-catenin
	λ_{EX}	Excitation fluorescence wavelength
	λ_{EM}	Emission fluorescence wavelength
	$\Delta logIC_{50}$	Difference in $logIC_{50}$ values
A	A	Actinomycin or adenine
	ac-	Acetyl-
	ACC	Adrenocortical carcinoma
	ACCTTIVE	Adriamycin, carboplatin, cyclophosphamide, topotecan, vincristine, etoposide
	ADC	Antibody drug conjugate
	AKT	AKT Serine/Threonine Kinase 1
	ALL	Acute lymphoid leukemia
	ALK	ALK Receptor Tyrosine Kinase
	AML	Acute myeloid leukemia
	ANOVA	Analysis of variance
	APC	Allophycocyanin
	APOBEC	Apolipoprotein B
	APS	Ammonium persulfate
	ARID1A	AT-Rich Interaction Domain 1A
	ARMS	Alveolar rhabdomyosarcoma
	ATM	Ataxia Telangiectasia Mutated
	AT-rich	Adenine and thymine rich zone
	ATRX	Alpha Thalassemia/Mental Retardation Syndrome X-Linked
B	B-ALL	B-Acute lymphoblastic leukemia
	BAX	BCL2 Associated X Protein
	BCL-2	BCL2 Apoptosis Regulator
	BCL-w	BCL2 Like 2
	BCL-xL	BCL2 Like 1
	BCOR	BCL6 Corepressor
	BCR-ABL1	BCR-ABL1 fusion
	BIM	BCL2 Like 11
	BP	Bladder/prostate
	BRAF	B-Raf Proto-Oncogene, Serine/Threonine Kinase
	BRCA1	Breast and Ovarian Cancer Susceptibility Protein 1
	BRCA2	Breast and Ovarian Cancer Susceptibility Protein 2
	BRD4	Bromodomain Containing 4
	BSA	Bovine serum albumin
	BUB1B	BUB1 Mitotic Checkpoint Serine/Threonine Kinase B

C	C	Cisplatin or contour and shape features or cytosine or cycle
	c-	Cleaved
	c-KIT	KIT Proto-Oncogene, Receptor Tyrosine Kinase
	CAR-T	Chimeric antigen receptor T-cell
	CBP	CREB Binding Protein
	CBFB-MYH11	CBFB-MYH11 fusion
	CCND1/2	Cyclin D1 or D2
	CDK2/4/6	Cyclin Dependent Kinase 2/4/6
	CDKN1A	Cyclin Dependent Kinase Inhibitor 2A
	CDKN2A	Cyclin Dependent Kinase Inhibitor 2A
	cDNA	Complementary deoxyribonucleic acid
	CDOX	Cell-derived orthotopic xenograft
	CDX	Cell-derived xenograft
	CEEA	Committee of ethics on animal experimentation
	CHD7/9	Chromodomain Helicase DNA Binding Protein 7/9
	CHEK2	Checkpoint Kinase 2
	ChIP-seq	Chromatin immunoprecipitation followed by sequencing
	CK2	Casein Kinase 2
	CNA	Copy number alteration
	CO_2	Carbon dioxide
	COG	Children's Oncology Group
	CR	Complete remission
	CRC	Core regulatory circuitry
	CRISPR	Clustered regularly interspaced short palindromic repeats
	CTCF	CCCTC-Binding Factor
	CTD	Carboxy-terminal domain
	ctDNA	Circulant tumour DNA
	CTNNB1	Catenin β1, gene
	CXCR4	C-X-C Motif Chemokine Receptor 4
	Cy	Cytoplasm
	Cytk	Cytoskeleton
D	D	Day or doxorubicin
	DAPI	4',6-diamidino-2-phenylindole
	dATP	Deoxyribose adenosine triphosphate
	DBD	DNA-binding domain
	DC	Detergent compatible
	DCEI	Doxorubicin, carboplatin, etoposide, ifosfamide
	dCTP	Deoxyribose cytosine triphosphate
	DDB2	Damage Specific DNA Binding Protein 2
	dGTP	Deoxyribose guanine triphosphate
	DICER	Dicer 1, Ribonuclease III

	DMSO	Dimethyl sulfoxide
	DNA	Deoxyribonucleic acid
	dNTP	Deoxynucleotide triphosphate
	DSB	Double-strand Break
	DSIF	DRB Sensitivity Inducing Factor
	DTT	Dithiothreitol
	dTTP	Deoxyribose thymidine triphosphate
E	E	Etoposide
	ECL	Enhanced chemiluminescence
	EDTA	Ethylenediaminetetraacetic acid
	EFS	Event-free survival
	EpSSG	European paediatric Soft-tissue sarcoma Study Group
	ER	Endoplasmic reticulum
	ERK	Extracellular Signal-Regulated Kinase 2
	ERMS	Embryonal rhabdomyosarcoma
	ETV6-RUNX1	ETV6-RUNX1 fusion
	EU	European Union
	EWS	Ewing's sarcoma
	EWSR1-FLI1	EWSR1-FLI1 fusion
	Ext	Extremity
F	FBS	Foetal bovine serum
	FBXW7	F-Box and WD Repeat Domain Containing 7
	FC	Fold-change
	FGF8	Fibroblast Growth Factor 8
	FGFR1/2/4	Fibroblast Growth Factor Receptor 1/2/4
	FISH	Fluorescence in situ hybridization
	FLT3	Fms Related Receptor Tyrosine Kinase 3
	FN-RMS	Fusion-negative rhabdomyosarcoma
	FOXO1	Forkhead Box O1
	FP-RMS	Fusion-positive rhabdomyosarcoma
G	G	Granularity or guanine
	GADD45A	Growth Arrest and DNA Damage Inducible Alpha
	GEMM	Genetically engineered mouse model
	GFs	Growth Factors
	GLI1	GLI Family Zinc Finger 1
	GPCR	G-Protein Coupled Receptor
	GSK3	Glycogen Synthase Kinase 3
	GU	Genitourinary
H	H&N	Head and neck
	H2AX	H2A Histone Family Member X
	H3K27	Tri-methylation on lysine 27 of histone H3

	HDAC	Histone Deacetylase
	HIPK2	Homeodomain Interacting Protein Kinase 2
	HO	Hoechst 33342
	HR	Homologous recombination or High-risk
	HRAS	HRas Proto-Oncogene, GTPase
	HRD	Homologous recombination Deficiency
	HRP	Horseradish peroxidase
	HSA	Highest single agent
	I	Irinotecan or intensity
	IC_{50}	Half maximal inhibitory concentration
	ID	Small insertions and deletions
	IGF1R	Insulin Like Growth Factor 1 Receptor
	IGF2	Insulin Like Growth Factor 2
	IgG	Immunoglobulin G
I	inh	Inhibitor
	IR	Ionizing radiation
	IRS	Intergroup Rhabdomyosarcoma Study Group
	IRS1	Insulin Receptor Substrate 1
	ITD	Internal tandem duplications
	IVA	Ifosfamide, vincristine, actinomycin D
	IVAD	Ifosfamide, vincristine, actinomycin D, doxorubicin
J	JAK	Janus Kinase
	K	Lysine
	KAT2B	Lysine Acetyltransferase 2B
K	KIAA1549-BRAF	KIAA1549-BRAF fusion
	KLF4	KLF Transcription Factor 4
	KRAS	Kirsten Rat Sarcoma Viral Oncogene Homolog
	L	Location and spatial distribution
	L-	Levogyre
	Leu	Leucine
L	LOH	Loss of heterozygosity
	LR	Low-risk
	LRP	LDL Receptor Related Protein 1
	Lys	Lysine
	M_0/M_1	No metastasis/metastasis
	MAP3K4	Mitogen-Activated Protein Kinase Kinase Kinase 4
	MAPK	Mitogen-Activated Protein
M	MB	Medulloblastoma
	MCL-1	Myeloid Cell Leukemia 1, BCL2 Family Member
	MDM2	Murine Double Minute 2 Proto-oncogene
	MDM2-p60	60 kDa MDM2 species

	MDMX	MDM2-Like P53-Binding Protein
	MEK	Mitogen-Activated Protein Kinase Kinase
	MEM	Minimum Essential Medium
	MET	MET Proto-Oncogene, Receptor Tyrosine Kinase
	MIC-1	Growth Differentiation Factor 15
	MIR17HG	MiR-17-92a-1 Cluster Host Gene
	MLL	Mixed-Lineage Leukemia
	M-MLV	Moloney murine leukemia virus
	MoA	Mechanism of action
	MRD	Minimal residual disease
	MRE11	MRE11 Homolog, Double Strand Break Repair Nuclease
	mRNA	Messenger ribonucleic acid
	MSH2/6	MutS Homolog 2/6
	MST1/2	Serine/Threonine Kinase 3/4
	mTOR	Mechanistic Target of Rapamycin Kinase
	MUT	Mutant or mutated
	MYC	V-Myc Avian Myelocytomatosis Viral Oncogene Homolog
	MYCN	MYC Neuroblastoma Derived
	MYOD1	Myogenic Differentiation 1
	MYOG	Myogenin
	MW	Molecular weight
N	n	Number of observations or data points
	N	Nuclear measurements
	$N_0/N_1/N_x$	Regional nodes not involved/involved/not known
	NaCl	Sodium Chloride
	NaOH	Sodium Hydroxide
	NB	Neuroblastoma
	NBS1	Nibrin
	NCCR	National Childhood Cancer Registry
	NELFB	Negative Elongation Factor Complex Member B
	NF1	Neurofibromin 1
	NICD	Notch intracellular domain
	NOXA1	NADPH Oxidase Activator 1
	NRAS	NRAS Proto-Oncogene, GTPase
	NTD	Amino-terminal domain
	NTRK1/2/3	Neurotrophic Receptor Tyrosine Kinase 1/2/3
	NuRD	Nucleosome Remodelling Deacetylase
O	O	Olaparib
	OD	Oligomerization domain
	OS	Osteosarcoma or Overall survival

P	P	Phosphoramide mustard
	p-	Phospho-
	P/CAF	Lysine Acetyltransferase 2B
	P/LP	Pathogenic/Likely Pathogenic
	$P14^{ARF}$	Alternate Reading Frame tumour suppressor, protein
	$P16^{INK4}$	Cyclin-Dependent Kinase 4 Inhibitor A
	P21	Cyclin Dependent Kinase Inhibitor 1A, protein
	P300	E1A Binding Protein P300
	P3F	PAX3-FOXO1
	p53	Tumour Protein P53, protein
	P7F	PAX7-FOXO1
	PARP	Poly (ADP-Ribose) Polymerase
	PAX3	Paired Box 3
	PAX3-FOXO1	PAX3-FOXO1 fusion
	PAX7	Paired Box 7
	PAX7-FOXO1	PAX7-FOXO1 fusion
	PBS	Phosphate-buffered saline
	PCR	Polymerase chain reaction
	PD-1	Programmed Cell Death 1
	PD-L1	Programmed Cell Death 1 Ligand 1
	PDGFRA	Platelet Derived Growth Factor Receptor Alpha
	PDX	Patient-derived xenograft
	PEG300	Polyethylene glycol 300
	Ph mustard	Phosphoramide mustard
	Phe	Phenylalanine
	PI	Propidium iodide
	PI3K	Phosphatidylinositol 3-kinase
	PIDD	P53-Induced Death Domain Protein 1
	PIK3CA	Phosphatidylinositol-4,5-Bisphosphate 3-Kinase Subunit Alpha
	PLAID	Plate Layouts using Artificial Intelligence
	PLK1	Polo Like Kinase 1
	PM	Parameningeal
	PMS2	PMS1 Homolog 2, Mismatch Repair System Component
	PPM1D	Protein Phosphatase, Mg2+/Mn2+ Dependent 1D
	pRb	Phosphorylated Retinoblastoma 1
	PRD	Proline-rich domain
	PRMS	Pleomorphic rhabdomyosarcoma
	PROTAC	Proteolysis targeting chimera
	PTCH1	Patched 1
	PTEN	Phosphatase and Tensin homolog
	PTPN11	Protein Tyrosine Phosphatase Non-Receptor Type 11

	PUMA	BCL2 Binding Component 3
	PVDF	Polyvinylidene difluoride
Q	qPCR	Quantitative PCR
R	R/R	Relapsed/Refractory
	RAF	Raf-1 Proto-Oncogene, Serine/Threonine Kinase
	RAD50	RAD50 Double Strand Break Repair Protein
	RAS	Ras Proto-Oncogene, GTPase
	Rb	Retinoblastoma 1, protein
	RB1	Retinoblastoma 1, gene
	RD	Radial distribution
	RICTOR	RPTOR Independent Companion Of MTOR Complex 2
	RIPA	Radioimmunoprecipitation assay buffer
	RMS	Rhabdomyosarcoma
	RNA	Ribonucleic acid
	RNA pol II	RNA polymerase II
	ROS	Reactive oxygen species
	rpm	Revolutions per minute
	RPTOR	Regulatory Associated Protein Of MTOR Complex 1
	RTK	Receptor tyrosine kinase
	RT-PCR	Real-time polymerase chain reaction
	RTx	Radiotherapy
	RUNX1-RUNXT1	RUNX1-RUNXT1 fusion
	RUNX2	RUNX Family Transcription Factor 2
S	S	Siremadlin
	S+O	Combination of siremadlin and olaparib
	SBS	Single base substitutions
	SC/SRMS	Spindle cell/Sclerosing rhabdomyosarcoma
	SCID	Severe combined immunodeficient
	SCRMS	Spindle-cell rhabdomyosarcoma
	SDS	Sodium dodecyl sulphate
	SDS-PAGE	Sodium dodecyl sulphate – polyacrylamide gel electrophoresis
	SEER	Surveillance Epidemiology and End Results
	SEM	Standard error of the mean
	Ser	Serine
	SHH	Sonic hedgehog
	SHH-MB	Sonic hedgehog medulloblastoma
	SMARCD2	SWI/SNF Related, Matrix Associated, Actin Dependent Regulator of Chromatin, Subfamily D, Member 2
	SMG	Significantly mutated genes
	SR	Standard-risk
	SRMS	Sclerosing rhabdomyosarcoma

	SSB	Single-strand breaks
	STAT	Signal Transducer And Activator Of Transcription
	STS	Soft-tissue sarcoma
	SWI/SNF	Switch/Sucrose Non-Fermentable
T	T	Temozolomide or thymine
	T_1/T_2	Primary tumour confined/with extension
	TAD	Transactivation domain
	TBP	TATA-Box Binding Protein
	TBS	Tris-buffered saline
	TBS-T	Tris-buffered saline – Tween20
	TCGA	The Cancer Genome Atlas program
	TECC	Topotecan, etoposide, carboplatin, cyclophosphamide
	TEMED	Tetramethylethylenediamine
	TF	Transcription factor
	TFAP2B	Transcription Factor AP-2 Beta
	TGF-β	Transforming Growth Factor Beta 1
	TIP60	Lysine Acetyltransferase 5
	TMZ	Temozolomide
	TOP1	DNA Topoisomerase I
	TOP2	DNA Topoisomerase II
	TP53	Tumour Protein P53, gene
	TRAIL	TNF Superfamily Member 10
	TRAIL-R1/2	TNF Receptor Superfamily Member 10a/b
	Tris	Tris(hydroxymethyl)aminomethane
	TRK	Tropomyosin receptor kinase
	Trp	Tryptophan
	t-SNE	t-distributed stochastic neighbour embedding
	TVD	Topotecan, vincristine, doxorubicin
	Tween20 or 80	Polysorbate 20 or 80
U	U.S.	United States
	UV	Ultraviolet light
V	V	Vincristine
	VA	Vincristine, actinomycin D
	VAC	Vincristine, actinomycin D, cyclophosphamide
	Val	Valine
	VCDE	Vincristine, cyclophosphamide, doxorubicin, etoposide
	VEGFR	Vascular Endothelial Growth Factor Receptor
	VHIR	Vall d'Hebron Institute of Research
	VHR	Very high risk
	VI	Vincristine, irinotecan
	VIT	Vincristine, irinotecan, temozolomide

W	WB	Western blot
	WHO	World Health Organization
	WIP1	Protein Phosphatase, Mg2+/Mn2+ Dependent 1D
	Wnt	Wingless-Type MMTV Integration Site Family
	WT	Wild-type
X	XIAP	X-Linked Inhibitor Of Apoptosis
	XPC	Xeroderma Pigmentosum, Complementation Group C
Y	YAP	Yes1 Associated Transcriptional Regulator
Z	ZIP	Zero interaction potency

1. Introduction

1.1. Childhood cancer

Childhood cancer is typically defined as a heterogeneous group of malignancies that affect individuals under 19 years old[1]. Approximately 400000 new cases of childhood cancer are diagnosed each year, with incidence rates slowly increasing over time for some tumour types[2] (Figure 1a). Nowadays, cancer ranks as the second leading cause of death among children aged 1–14 years in developed countries, and the fourth among adolescents aged 15–19 years[3]. Despite the scarcity of new drugs to treat childhood cancers over the past 30 years, cure rates for these diseases have steadily improved, with an overall cure rate of 80% in high-income countries[4]. This progress has been built on highly precise diagnostic procedures and the continuous enhancement of multimodal treatment strategies[5,6]. Unfortunately, survival does still lag for some cancer types, especially for central nervous system neoplasms, hepatoblastoma, soft-tissue sarcomas (STS), and bone tumours, which show 5-year survival rates of 70% (Figure 1b). Moreover, the use of cytotoxic chemotherapy and radiotherapies often results in significant side effects, potentially compromising survivors' life quality, underscoring the need to develop new and less toxic therapeutic approaches[7].

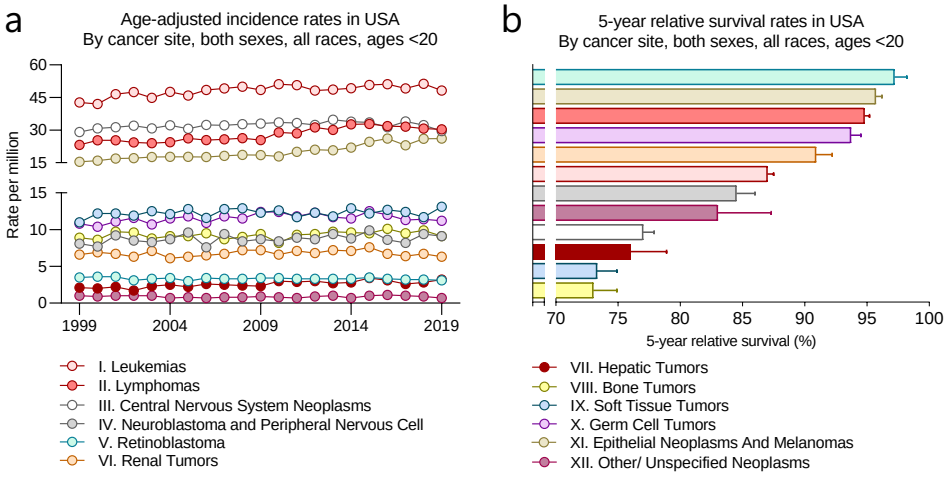

Figure 1. Incidence and survival rates of paediatric tumours in the United States (U.S.). (**a**) Trends in age-adjusted incidence rates (1998–2019) by cancer site for individuals under 20 years old, including both sexes and all races (**b**) Five-year relative survival rates (2013–2019) by cancer site for individuals under 20 years old, including both sexes and all races. Data were obtained from NCCR registries[8] and represents up to 70% of all U.S. children and adolescents (data available at: https://nccrexplorer.ccdi.cancer.gov). Cancer types are categorized according to the International Classification of Childhood Cancer[9].

1.1.1. Differences between childhood and adult cancer

Cancer types and mutations

Currently, there is a widespread belief that developing new, less toxic therapies for childhood cancers should focus on targeting the genetic alterations driving these diseases[10–12]. During the last years, several efforts have been made to elucidate the genetic alterations underlying childhood cancers and understand the pathobiology of these diseases to develop more effective and less toxic treatments[11]. In this regard, findings from global paediatric cancer projects have unveiled distinct molecular features in comparison to adult cancers, as well as a notable divergence in the spectrum of cancer types between the two populations[11–16]. For example, solid tumours commonly diagnosed in children, such as neuroblastoma (NB), medulloblastoma (MB), rhabdomyosarcoma (RMS), Ewing sarcoma (EWS), osteosarcoma (OS), and Wilms tumour, are exceedingly rare occurrences in adults[11–14] (Figure 2a). Similarly, the genetic subtypes of acute lymphoblastic leukemia (ALL), the most prevalent childhood malignancy, exhibit notable differences between paediatric and adult populations[11,17] (Figure 2b).

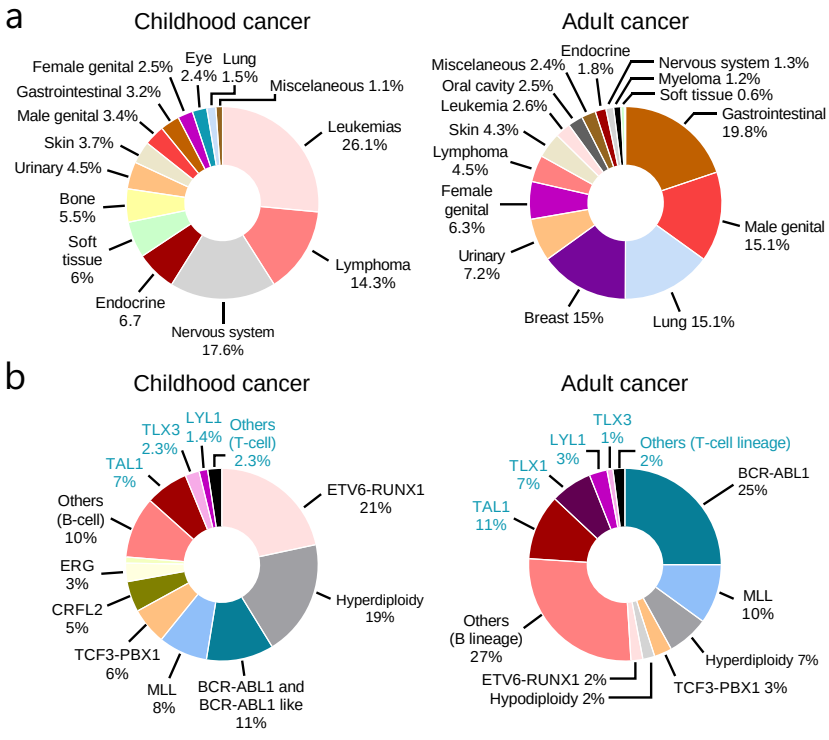

Figure 2. Tumour types and leukemia subtypes diagnosed in paediatric and adult populations. (a) The frequency of cancer types in children (left) and adults (right). Both charts are organized with cancers listed from the most common to the least common in a clockwise fashion. (b) The frequency of T-cell lineage (blue text) and B-cell lineage (black text) subtypes of ALL in children (left) and adults (right). Each chart is organized with ALL subtypes listed from the most common to the least common in a clockwise fashion. This figure was generated using data from the previously published manuscript by Downing et al.[11].

Additionally, coding mutation frequencies differ between paediatric and adult cancers, and the spectrum of mutations leading to malignant transformation also varies significantly[11–16] (Figure 3a). In childhood cancer, the most common group of significantly mutated genes (SMGs) includes genes linked to epigenetic modifications (25%) followed by transcriptional regulators (12%), and MAPK-associated genes (7%)[13]. By contrast, PI3K-associated SMGs are the most commonly altered genes in adult cancers (31%) (Figure 3b). Regarding the most common somatic mutations, *TP53* mutations are observed in 4% of childhood tumours, followed by *KRAS*, *ATRX*, *NF1*, and *RB1* mutations (Figure 3c). It is important to note that although *TP53* is the most commonly mutated gene in both cancer populations, *TP53* mutations are 10 times more frequent in adult cancers than in paediatric cancer[13]. Interestingly, only a small number of mutational signatures are found to be active in paediatric cancers compared to those previously identified in adult cancers[18]. Specifically, a significant proportion of single base substitutions (SBS) and small insertions and deletions (IDs) is attributed to clock-like signatures, including SBS1 (C>T transitions), SBS5 (T>C mutations), and indel signatures ID1 and ID2 (resulting from DNA damage induced by replication slippage)[18,19]. APOBEC signatures, such as SBS2 and SBS13, are particularly identified in bone sarcomas, ETV6–RUNX1 B-ALL, and adrenocortical carcinoma (ACC) while the ultraviolet light (UV) exposure signature SBS7 is observed in paediatric melanoma[18,19]. Additional frequent signatures in paediatric cancer included SBS8, SBS9, and SBS18, which are linked to DNA damage from homologous recombination deficiencies (HRD), polymerase η activity, and reactive oxygen species (ROS), respectively[18]. SBS31 and SBS35, associated with platinum treatment, are also identified in some tumours[18,19]. Given this unique mutational landscape, comprehensive cancer genomic profiling has become essential in the clinical management of children and adolescents with cancer[20,21]. This approach facilitates the diagnosis of cancer subtypes, the identification of targetable genetic alterations, and informed treatment decision-making, while enhancing the monitoring of treatment responses and the detection of minimal residual disease (MRD) or recurrence, ultimately leading to clinical benefits for some patients[21–23].

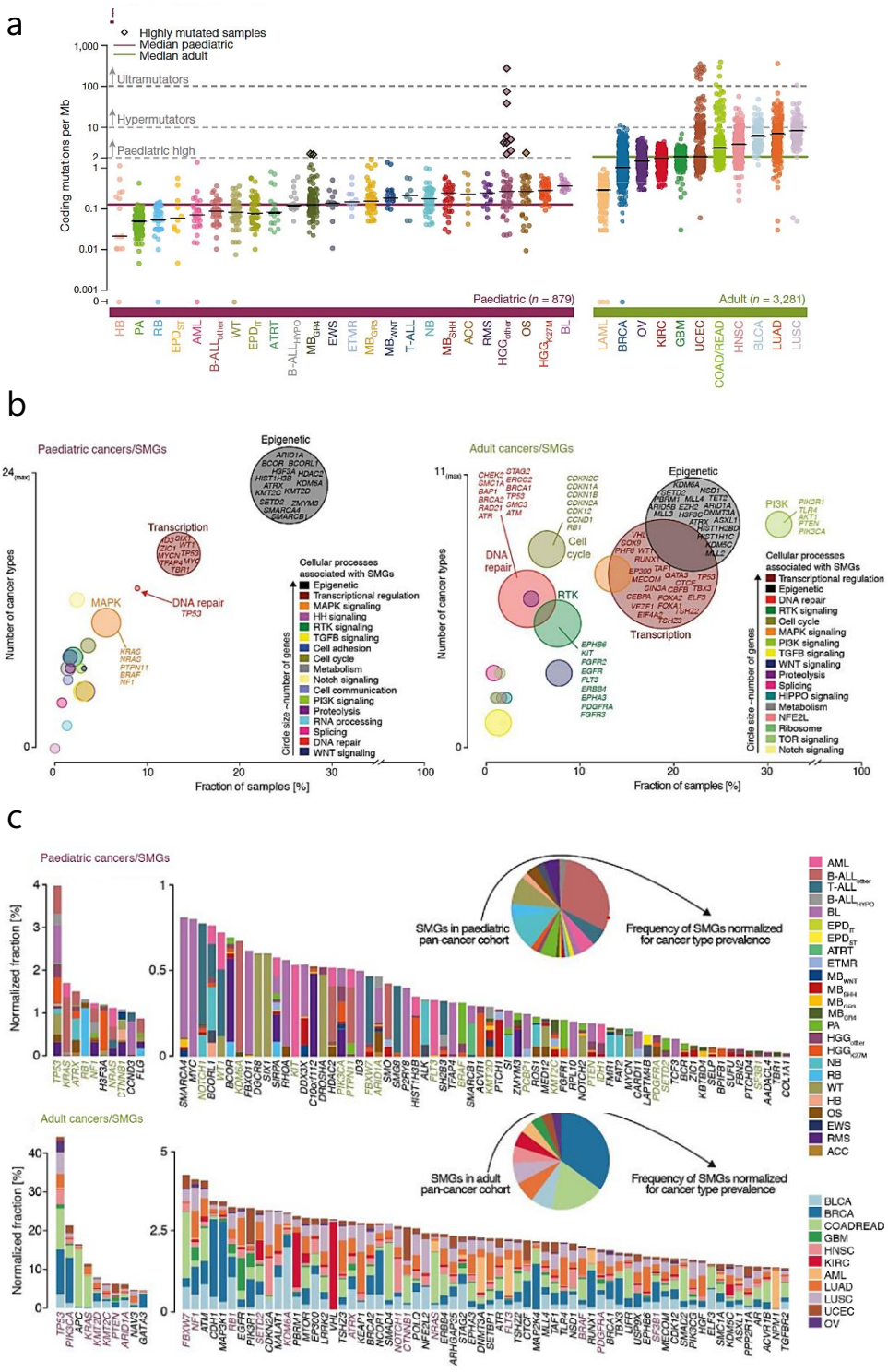
a
Highly mutated samples
Median paediatric
Median adult
Ultramutators
Hypermutators
Paediatric high
Coding mutations per Mb
Paediatric (n = 879)
Adult (n = 3,281)
HB
PA
RB
EPD_ST
AML
B-ALL_other
WT
EPD_IT
ATRT
B-ALL_HYPO
MB_GR4
EWS
ETMR
MB_GR3
MB_WNT
T-ALL
NB
MB_SHH
ACC
RMS
HGG_other
OS
HGG_K27M
BL
LAML
BRCA
OV
KIRC
GBM
UCEC
COAD/READ
HNSC
BLCA
LUAD
LUSC
b
Paediatric cancers/SMGs
Epigenetic
Transcription
MAPK
DNA repair
Number of cancer types
Fraction of samples [%]
Cellular processes associated with SMGs
Epigenetic
Transcriptional regulation
MAPK signaling
HH signaling
RTK signaling
TGFB signaling
Cell adhesion
Cell cycle
Metabolism
Notch signaling
Cell communication
PI3K signaling
Proteolysis
RNA processing
Splicing
DNA repair
WNT signaling
Circle size ~number of genes
Adult cancers/SMGs
Epigenetic
Cell cycle
DNA repair
RTK
Transcription
PI3K
Cellular processes associated with SMGs
Transcriptional regulation
Epigenetic
DNA repair
RTK signaling
Cell cycle
MAPK signaling
PI3K signaling
TGFB signaling
WNT signaling
Proteolysis
Splicing
HIPPO signaling
Metabolism
NFE2L
Ribosome
TOR signaling
Notch signaling
c
Paediatric cancers/SMGs
Normalized fraction [%]
SMGs in paediatric pan-cancer cohort
Frequency of SMGs normalized for cancer type prevalence
AML
B-ALL_other
T-ALL
B-ALL_HYPO
BL
EPD_IT
EPD_ST
ATRT
ETMR
MB_WNT
MB_SHH
MB_non
MB_GR4
PA
HGG_other
HGG_K27M
NB
RB
WT
HB
OS
EWS
RMS
ACC
Adult cancers/SMGs
Normalized fraction [%]
SMGs in adult pan-cancer cohort
Frequency of SMGs normalized for cancer type prevalence
BLCA
BRCA
COADREAD
GBM
HNSC
KIRC
AML
LUAD
LUSC
UCEC
OV

Figure 3. Somatic mutations in paediatric and adult cancer. (**a**) Somatic coding mutation frequencies in 24 paediatric (*n* = 879 primary tumours) and 11 adult (*n* = 3,281) cancer types from The Cancer Genome Atlas (TCGA). Hypermutated and highly mutated paediatric samples are highlighted with black squares. Median mutation loads are shown as solid lines (purple, all paediatric; green, all adult). (**b**) Cellular processes associated with paediatric (left) and adult (right) SMGs. (**c**) Projected mutation rates of SMGs based normalized by cancer type incidence. Data is presented for paediatric (top) and adult (bottom) cancers. This figure was adapted from the previously published manuscript by Gröbner et al[13].

Fusion genes and chromosomal rearrangements

Although tumour mutation burden is typically higher in adult cancers, oncogenic fusion genes are generally more prevalent in paediatric malignancies[24]. These fusion genes lead to aberrant activity of the encoded proteins and are hallmarks of many childhood cancers[25,26]. Recent genomic and transcriptomic analysis of paediatric samples have revealed that the number of fusion partners is greater than previously thought[26–28]. Nevertheless, despite these advances, most gene fusions identified in paediatric cancer are rare and have yet to be functionally validated[26,29]. Gene fusion events play a crucial role in the diagnosis and treatment of childhood cancers, serving as pathognomonic markers, prognostic indicators, and guides for the selection of optimal therapies[29]. For instance, in paediatric leukemia, *RUNX1-RUNXT1* and *CBFB-MYH11* are the most prevalent fusion genes, occurring in 10–15% of acute myeloid leukemia (AML) cases[26] (Figure 4a). These fusions disrupt the core binding factor complex, essential for the transcriptional regulation of normal haematopoiesis[26,30,31]. Similarly, in paediatric brain tumours, the *KIAA1549-BRAF* is the most frequently detected fusion, acting as a driver event in pilocytic astrocytoma and other gliomas[26,32,33] (Figure 4b). This fusion results in the loss of the N-terminal regulatory domain of BRAF, leading to its constitutive activation and subsequent activation of the downstream MAPK pathway[34]. As a result, tumours harbouring BRAF fusions are more likely to respond to MAPK pathway-targeted therapies, offering a promising treatment avenue for these patients[35]. In paediatric solid tumours, the *EWSR1-FLI1* fusion in EWS and the *PAX3-FOXO1* fusion in RMS are among the most commonly detected gene rearrangements (Figure 4c). Both fusions drive tumorigenesis by rewiring the transcriptome through core regulatory circuitries (CRCs) that are critical for the development of these tumours[36–39]. Indeed, the genetic vulnerabilities of EWS and RMS are intricately linked to the fusion genes and the transcription factors (TFs) that form the CRCs. Thus, targeting of these proteins and their interactions represents a promising strategy for developing effective therapeutic approaches for these paediatric malignancies[40].

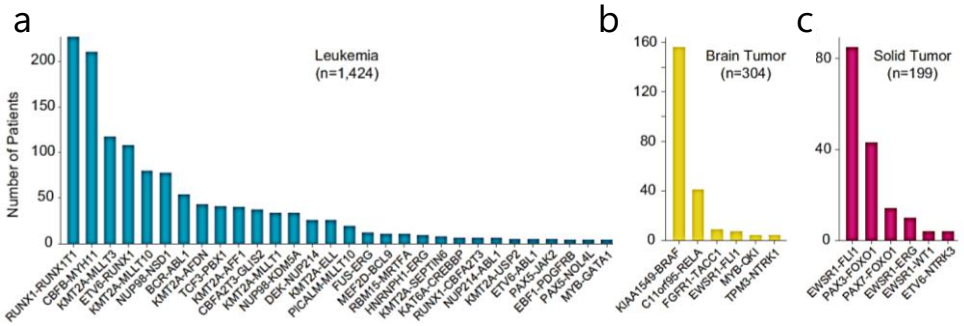

Figure 4. Fusion genes detected in paediatric cancer. In a cohort of 5190 childhood cancer patients, 2012 oncogenic fusion events involving 272 gene pairs were detected. Spectrum of canonical fusions in (**a**) leukemia (*n* = 1424, blue), (**b**) brain tumour (*n* = 304, yellow) and (**c**) solid tumours (*n* = 199, magenta). This figure was adapted from the previously published manuscript by Liu et al.[26]

Traditionally, TFs have been considered 'undruggable' due to their significant structural disorder and lack of defined small-molecule binding pockets[41]. However, this perspective has undergone a significant transformation in recent years, with numerous promising successes achieved. Significant progress has been made in ligand discovery and optimization, and novel approaches to targeted protein degradation, such as proteolysis targeting chimaeras (PROTACs), have emerged[41–43]. These advances hold great potential for generating new agents to target TFs and fusion proteins, which are likely to impact future paediatric cancer treatments. Despite the inherent difficulties directly targeting gene fusions involving TFs, some success has been achieved with other fusions. For instance, TRK inhibitors have demonstrated both safety and efficacy in treating TRK fusion-positive paediatric cancers[44–46]. Additionally, strategies to indirectly target fusion proteins by interfering with their regulatory pathways are being actively explored[47–50]. These developments highlight a transformative shift towards more targeted and personalized therapeutic approaches in paediatric oncology.

Origin, predisposition and environmental factors

Many paediatric cancers arise from tissues undergoing significant expansion during early stages of organ development, growth, and maturation[51]. As a result, paediatric tumours are mainly derived from mesodermal and ectodermal lineages rather than epithelial lineages. In contrast, adult cancers are predominantly epithelial and frequently associated with aging and exposure to environmental mutagens[52].

The observation that many tumour types are specific to childhood and seldom seen in adults suggests that the precursor cells for these paediatric cancers are absent in mature tissues[53]. Indeed, the timing of these tumours often aligns with specific developmental stages[54]. For instance, NTRK-fusion STS frequently occur in early neonatal periods, while ALL with *MLL* rearrangements primarily affects infants[55,56]. Other examples include Wilms tumour, which is commonly found in toddlers, and bone sarcomas, which are frequently linked to the pubertal growth spurt[57–59].

Morphological similarities between certain childhood tumours, such as hepatoblastoma, and embryonal tissues like the developing liver, also suggest that these tumours may originate from foetal developmental stages[59,60]. Additionally, analyses of transcription profiles, enhancer activities, and DNA methylation patterns support the notion that paediatric tumour cells often exhibit characteristics of blocked development[52]. Indeed, single-cell profiling studies have further correlated paediatric cancer cells with specific developmental cell types[61–64]. Interestingly, some paediatric tumours have demonstrated the ability to differentiate into benign tissue, either spontaneously or in response to treatment with cytotoxic chemotherapy or differentiation agents[65–67]. This phenomenon is currently being explored using single-cell multiomics to gain deeper insights and potentially leverage this capability for therapeutic purposes[67–69].

While environmental exposures are rarely implicated in childhood malignancies, growing evidence indicates that some inherited genetic factors play a significant role in their development[70]. Hereditary predisposition is particularly common in certain cancers, with ACC showing a 50% predisposition rate and hypodiploid B-ALL demonstrating a 28% rate. Other malignancies, including H3K27 high-grade gliomas, atypical teratoid rhabdoid tumours, SHH-MB, and retinoblastomas, exhibit predisposition rates between 15–25% (Figure 5a)[13]. Notably, most pathogenic or likely pathogenic (P/LP) germline variants are associated with DNA repair genes such as *TP53*, *BRCA2*, *MSH2/6*, *PMS2*, or *CHEK2*, which are more commonly linked to adult rather than paediatric cancers[13,71] (Figure 5b-c). Approximately 6–10% of childhood cancer patients may harbour germline variants indicative of hereditary predisposition[13,72–74] (Figure 5d). Consequently, identifying paediatric patients at increased risk for secondary malignancies through comprehensive clinical genetic testing, combined with the implementation of early personalized cancer surveillance and prevention strategies, is essential for significantly reducing mortality in this population[75].

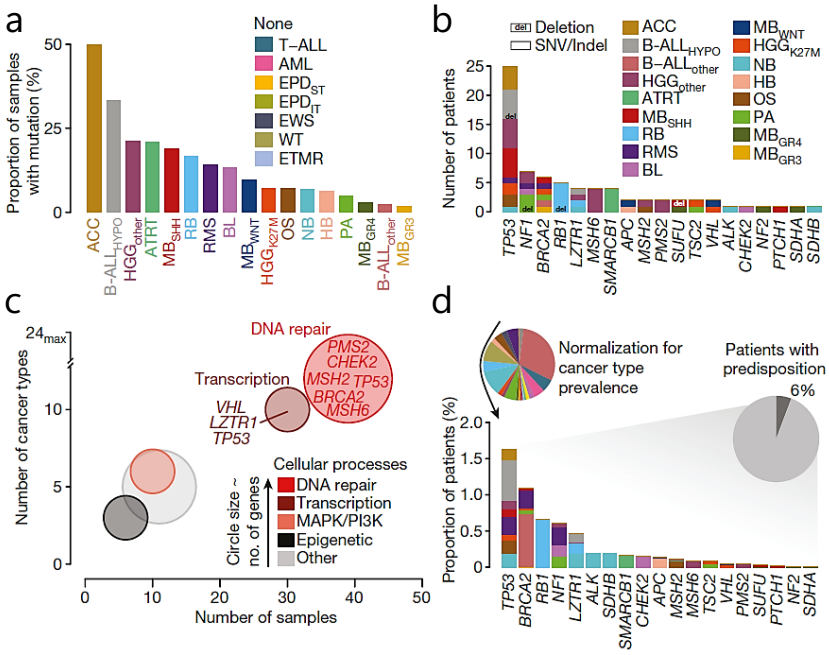

Figure 5. Germline mutations in cancer predisposition genes. (a) Frequency of patients with a pathogenic germline mutation by cancer type. (b) Mutated genes sorted by number of affected samples. (c) Cellular processes associated with cancer predisposition genes. (d) Frequency of germline mutations normalized for childhood cancer type prevalence. This figure was adapted from the previously published manuscript by Gröbner et al[13].

1.1.2. Challenges and perspectives in paediatric cancer research

Integrating multiomics profiling with targeted therapies

In recent years, paediatric cancer research has made remarkable progress, leading to ground-breaking discoveries that not only benefit childhood cancer patients but also have broader implications for various scientific fields[76]. The advent of comprehensive molecular profiling of paediatric tumours has become increasingly routine, paving the way for more personalized and effective treatment plans[77]. Techniques such as whole-genome sequencing and RNA sequencing now provide an in-depth view of the genetic and molecular landscape these tumours, allowing for the identification of actionable mutations, guiding the selection of targeted therapies, and ultimately improving patient outcomes[16,78,79].

Currently, combining different targeted therapies with traditional chemotherapies offers a promising strategy in paediatric oncology. This integrated approach aims to boost treatment efficacy while potentially minimizing toxicity[80,81]. By leveraging the combined strengths of different drugs, these treatments can produce additive or synergistic effects that enhance overall treatment outcomes[81]. Additionally, such combination therapies can target cancer cells through multiple mechanisms, which helps to reduce the likelihood of resistance thereby increasing the chances of successful treatment[82]. Importantly, using therapy combinations may allow for lower doses of each individual treatment, potentially reducing the severe side effects often associated with high-dose chemotherapy[81,83]. This is particularly important for paediatric patients, who are especially vulnerable to the long-term adverse effects of cancer treatments[84]. By achieving therapeutic efficacy with reduced toxicity, combination therapies can significantly improve the quality of life for young patients during and after treatment.

In the field of immunotherapy, clinical trials involving immune checkpoint inhibitors have yielded promising results, suggesting that selected subgroups of paediatric patients may benefit from these therapies[85,86]. Furthermore, chimeric antigen receptor T-cell (CAR-T) therapy has demonstrated significant efficacy in the treatment of certain types of paediatric leukemia[87]. This success has spurred further research to extend CAR-T cell therapy to other paediatric solid tumours, thereby broadening the potential impact of immunotherapy in the treatment of childhood tumours[88,89].

Emerging targets and cutting-edge therapies

Fusion proteins and the TFs that form the CRCs are pivotal in paediatric cancers, as they drive the expression of genes that promote tumour growth and survival[36,37,90–92]. Targeting these proteins offers a promising and attractive avenue for developing new therapies for paediatric cancers[40]. Currently, various approaches, including small molecules, peptides, PROTACs and other innovative strategies, are being explored to inhibit these key drivers of paediatric malignancies[41–43]. Concurrently, advances in understanding the epigenetic changes that underpin paediatric cancers have led to the development of drugs aimed at reversing these alterations[93,94]. Moreover, extensive research into key developmental pathways, including Notch, Wnt, TGF-β, YAP, Hippo, and Hedgehog, has facilitated the development of targeted inhibitors specifically designed to disrupt the aberrant signalling within these pathways in paediatric tumours[95–97].

Another class of targeted therapies that are likely to provide new therapeutic strategies for combating paediatric cancer are antibody–drug conjugates (ADCs). ADCs are innovative class of targeted therapies that combine the specificity of monoclonal antibodies with the powerful cell-killing capability of cytotoxic drugs[98]. By selectively delivering cytotoxic agents directly to cancer cells, ADCs can enhance the efficacy of treatment while minimizing damage to healthy tissues[99]. Several ADCs are currently being developed and tested for various paediatric cancer types, yielding promising outcomes in both preclinical and clinical settings[100–103].

Biomarkers and liquid biopsy

In conjunction with these advances, the identification and application of biomarkers have become crucial for optimizing paediatric cancer management[104]. Biomarkers of response, such as specific genetic mutations or alterations, play a key role in personalizing treatment plans[105,106]. By indicating which patients are more likely to benefit from targeted therapies, these biomarkers enable a more tailored approach, moving away from one-size-fits-all treatments and focusing resources on therapies with the highest likelihood of success[107]. Currently, circulating tumour DNA (ctDNA) is emerging as a powerful tool for non-invasive cancer detection and monitoring in paediatric patients[108]. ctDNA enables the early detection of paediatric cancers, potentially identifying them before clinical symptoms appear[109,110]. This early detection facilitates timely intervention, which can significantly improve patient outcomes[111]. ctDNA levels also provide valuable insights into treatment efficacy. A reduction in ctDNA often indicates a favourable response to therapy, whereas rising levels may signal disease progression or resistance[112]. Additionally, ctDNA is instrumental in detecting MRD post-treatment, offering crucial information about the likelihood of relapse[113]. Ongoing research and clinical trials are focused on refining ctDNA analysis techniques to improve their sensitivity and specificity[114]. These studies aim to validate the clinical utility of these biomarkers across various paediatric cancers. As these technologies advance, they are expected to integrate more seamlessly into routine clinical practice, providing powerful tools for early detection, personalized treatment, and ongoing monitoring[115,116]. By enabling precise patient stratification, offering predictive insights, and facilitating real-time monitoring of treatment responses, liquid-biopsy ctDNA analysis represent promising approaches for enhancing outcomes and personalizing treatment strategies for paediatric patients.

Preclinical xenograft models in paediatric cancer

To effectively study and develop new therapies in paediatric cancer, a range of preclinical models is essential. These models provide critical insights into tumour biology and therapeutic efficacy, serving as a bridge between basic research and clinical application[117]. Among these preclinical tools, cell-derived xenografts (CDXs) and patient-derived xenografts (PDXs) offer distinct advantages. CDXs involve the implantation of well-characterized cancer cell lines into immunocompromised mice. These models are highly valued for their consistency and reproducibility, making them particularly useful for high-throughput drug screening, mechanistic studies, and target validation[118]. However, their reliance on established cell lines can limit their ability to fully capture the genetic and phenotypic heterogeneity of primary tumours, as these cell lines may not always reflect the complexity of the original tumours due to genetic drift over time[119,120]. In contrast, PDXs are created by transplanting tumour tissues obtained directly from patients into immunocompromised mice[121]. PDX generally recapitulate patient tumours in histology, copy number, transcriptomic profiles, human leucocyte antigen characteristics and specific metabolic pathway signatures[122–124]. Despite their advantages, PDX models are not without limitations. Discrepancies in mutational profiles between patient tumours and PDX models have been observed in approximately 30% of cases, and clonal analysis has indicated that aggressive subclones from the primary tumour often dominate in PDXs[124]. This underscores the complex interplay between intratumoral heterogeneity and antitumor immunity, which can influence the fidelity of PDX models in representing the primary tumour. Additionally, genetically engineered mouse models (GEMMs) represent another critical tool in preclinical cancer research[125]. GEMMs involve the introduction of specific genetic alterations into the mouse genome, thereby recapitulating key aspects of human paediatric cancers. These models provide valuable insights into the genetic drivers of tumorigenesis and facilitate the evaluation of targeted therapies within a more physiologically relevant context[126]. GEMMs also enable researchers to study the interactions between genetic mutations and the tumour microenvironment, including the immune system's role in cancer progression[127,128]. These models collectively facilitate the development and testing of new treatments, elucidate mechanisms of drug resistance, and identify biomarkers for personalized therapy. By integrating insights from these preclinical approaches with findings from adult cancer research, the advancement of effective treatments can be accelerated, leading to improved survival rates and quality of life for paediatric cancer patients.

1.2. Rhabdomyosarcoma

1.2.1. Overview of rhabdomyosarcoma

RMS is the most prevalent STS in the paediatric population, accounting for approximately 50% of all paediatric STS and around 4% of all childhood cancers[129,130]. Histologically, RMS resembles developing muscle tissue and is thought to originate from myogenic progenitor cells that fail to complete the differentiation process[131]. Consequently, RMS cells can present with a range of differentiation states, from undifferentiated small round cells to more differentiated muscle-like cells, depending on the subtype and disease progression. Notably, RMS can also occur in anatomical regions without skeletal muscle, suggesting the potential involvement of alternative cells of origin[132].

Paediatric RMS is classified in two main subtypes: embryonal (ERMS) and alveolar RMS (ARMS), each characterized by distinct molecular mechanisms and clinical features[129] (Table 1). ERMS is the most prevalent subtype, and is generally associated with a favourable prognosis[133]. At the molecular level, ERMS tumours usually exhibit aneuploidies, copy number gains and losses, alterations in the RAS-MAPK, PI3K-AKT pathways, and occasionally, disruptions of the p53 pathway[134]. This subtype includes two variants: the embryonal and the botryoid variants[135]. The embryonal variant, characterized by a large, infiltrative mass of small round and spindle cells with differentiated rhabdomyoblasts, is typically located in the head and neck (H&N) or in the genitourinary (GU) tract[136]. Conversely, the botryoid variant, characterized by its distinctive "grape-like" appearance, is often detected on mucosal surfaces such as the vagina, bladder, biliary tract, or upper respiratory tract[133,135,137].

In contrast, ARMS has a more aggressive behaviour and is characterized by its distinctive alveolar pattern, where medium-sized round tumour cells are arranged in clusters separated by dense fibrous stroma[129]. This subtype is primarily associated with translocations involving *PAX3* or *PAX7* genes and *FOXO1* gene, resulting in *PAX3-FOXO1* (P3F) or *PAX7-FOXO1* (P7F) fusions that are key drivers of the disease[38,39,134]. However, some ARMS lack these fusion proteins and closely resemble ERMS both molecularly and clinically[138]. As a result, many experts categorize childhood RMS based on fusion status into fusion-positive (FP-RMS) and fusion-negative RMS (FN-RMS)[129].

Table 1. Main clinicopathologic features of RMS histologic subtypes

Subtype	*Age*	*Location*	*Morphology*	*Genetic alterations*	*Prognosis*
Embryonal (~60%)	Paediatric	H&N, GU tract	**Embryonal** Round and spindle cells with differentiated rhabdomyoblasts **Botryoid** Grape-like growth pattern	**Fusion negative** Aneuploidies, CNAs, RAS-MAPK, PI3K-AKT and P53 pathway alterations	Favourable
Alveolar (~25%)	Paediatric	Extremities	Clustered round cells separated by dense fibrous stroma, resembling the alveolar lung tissue	**Fusion positive** *PAX3/7-FOXO1* and alternative fusions (~85%)	Poor (P3F) or intermediate (P7F)
				Fusion negative (~15%)	Favourable
Pleomorphic (~10%)	Paediatric and adults	Extremities	Bizarre pleomorphic rhabdomyoblasts	*TP53*, *RB1* and/or *CDKN2A* alterations	Poor
Spindle cell/ Sclerosing (5-10%)	Paediatric and adults	H&N, GU tract, extremities	**SCRMS** Spindle cells in fascicles **SRMS** rhabdomyoblasts in a sclerosing "pseudovascular" pattern	**Congenital or infantile SC/SRMS** *VGLL2-CITED2/NCOA2* or *TEAD1/SRF-NCOA2* fusions	Very good
				Classic SC/SRMS *MYOD1* and/or *PIK3CA* mutations	Poor
				Intraosseous SC/SRMS *EWSR1/FUS-TFCP2* or *MEIS1-NCOA2* fusions	Poor

H&N: head and neck, GU: genitourinary; CNA: copy-number alteration; P3F: *PAX3-FOXO1* fusion; P7F: *PAX7-FOXO1* fusion; SCRMS: spindle-cell RMS; SRMS: sclerosing RMS.

In addition to ERMS and ARMS, the World Health Organization (WHO) recognizes two rarer RMS subtypes: pleomorphic and spindle cell/sclerosing RMS[139]. Pleomorphic RMS (PRMS) predominantly affects adults and is associated with a poorer prognosis compared to ERMS and ARMS[140–144]. Although PRMS is rare in the paediatric population, its occurrence may indicate an underlying genetic predisposition, such as Li-Fraumeni syndrome[145,146]. Histologically, PRMS is distinguished by a high degree of variability in cell size and shape, high mitotic activity, and areas of necrosis[140]. These tumours often arise in the extremities, but can also occur in the trunk or retroperitoneum[140,147]. Unlike other RMS subtypes, PRMS does not exhibit the gene fusions seen in ARMS, nor does it share the molecular features of ERMS[148]. Ongoing research aims to identify molecular targets and develop novel therapies to improve outcomes for this challenging and poorly understood subtype.

Another distinct subtype of RMS recognized for its unique histopathological and clinical features is spindle cell/sclerosing RMS (SC/SRMS). Unlike other RMS subtypes, SC/SRMS is characterized by elongated, spindle-shaped tumour cells and differentiated rhabdomyoblasts forming fascicles, often accompanied by a dense fibrous stroma with a pseudovascular pattern, particularly in the sclerosing variant[149]. This subtype can occur at various anatomical sites, with a predilection for the H&N, paratesticular region, and extremities[150–152]. Clinically, SC/SRMS is associated with a more favourable prognosis in children, but tends to follow a more aggressive course in adults[149,153,154]. Recent molecular studies have identified recurrent gene fusions and mutations SC/SRMS, distinguishing it from other RMS forms and underscoring the need for specific therapeutic strategies tailored to its unique biology[152,153,155–159]. Accordingly, the latest WHO classification further categorizes SC/SRMS into four subgroups: congenital SCRMS, classic SRMS, S/SCRMS without detectable genetic alterations, and intraosseous SRMS[139].

1.2.2. Epidemiology

Despite being a rare disease, the overall incidence rate of RMS in the U.S. is about 4.5 cases per million individuals under 20 years of age[8]. In Europe RMS incidence is modestly elevated with an overall incidence of about 5.4 cases per million in individuals under 15 years of age[160]. Notably, a lower incidence of RMS has been reported in several Asian countries, including Japan, India, and China, with approximately 2 cases per million individuals[161].

According to data from the Surveillance Epidemiology and End Results (SEER) Program, the incidence of RMS differs by both age and histology, and nearly two-thirds of cases are diagnosed in children younger than 10 years of age[162,163]. ERMS is diagnosed about 2.5 times more frequently than ARMS and is most commonly seen in early childhood, with some evidence indicating a second peak during early adolescence[162,164]. Conversely, the incidence of ARMS stays relatively stable throughout childhood and adolescence[165]. The incidence of RMS also differs by sex, with male children exhibiting a higher rate of ERMS than female children (male-to-female ratio of 1.51)[164]. In contrast, no significant differences in incidence have been observed across different ethnic groups[166,167]. Analysis of SEER data also reveals that the incidence of ERMS between 1975 and 2005 remained relatively stable, but the incidence of ARMS increased during the same period[164]. However, this rise might be influenced by evolving diagnostic criteria, such as the extent of specific features required for an ARMS diagnosis[129,168]. While a more objective classification of RMS, based on the presence of P3/7F could provide greater clarity, such information has not been consistently recorded by the SEER Program or other major cancer registries[129].

1.2.3. Clinical presentation and diagnosis

As previously noted, RMS can arise in almost any soft-tissue location, with the GU tract, H&N, extremities and parameningeal regions being the most common sites[169]. The presenting signs and symptoms of RMS can vary greatly influenced by the primary tumour site of origin, but also the age of the patient, and the presence or absence of metastatic disease[170]. In some cases, symptoms can also result from the pressure exerted by tumours on adjacent organs or tissue structures[129,171]. Notably, approximately 10–30% of children present radiographic or clinical signs of distant metastatic disease at diagnosis[172–174]. These metastases frequently spread through both lymphatic and hematogenous routes, and commonly involve the lungs, bones, and bone marrow[175].

The diagnosis of RMS requires the direct analysis of tumour tissue obtained through incisional, excisional, or core needle biopsy to identify malignant cells[129]. RMS cells typically exhibit characteristics indicative of skeletal muscle lineage, which can be observed using light microscopy after haematoxylin-eosin staining, or detected through immunohistochemistry and molecular assays[176,177]. Key indicators include the expression of muscle-specific actin, myosin, desmin, myoglobin, Z-band protein, and the TFs myogenin and MYOD1[178–182].

However, accurate diagnosis also requires careful consideration of cellular morphology and architecture, as myogenic proteins can be expressed in other childhood tumours[183,184]. Advances in molecular diagnostic tools have significantly improved the identification of RMS[136]. For instance, ARMS can be more accurately diagnosed as FP-RMS by detecting the PAX–FOXO1 fusions in tumour cells using techniques such as fluorescence in situ hybridization (FISH) or reverse transcription polymerase chain reaction (RT-PCR)[185,186]. Similarly, genetic testing is crucial for confirm the diagnosis and distinguish between distinct subgroups of FN-RMS, thereby providing better risk stratification and guiding therapeutic strategies[187]. Furthermore, artificial intelligence and deep learning technologies are increasingly advancing RMS diagnosis by analysing complex imaging and pathology data with high precision[188,189]. These tools can identify subtle differences that enhance the differentiation of RMS subtypes and support personalized treatment planning[190]. As artificial intelligence and deep learning continue to evolve, they hold the promise of further refining diagnostic accuracy and therapeutic approaches for RMS.

1.2.4. Risk factors and stratification

Given the absence of well-established prevention strategies for RMS, identifying associated risk factors is crucial[129]. Environmental exposures such as prenatal X-ray exposure, parental use of recreational drugs, vaginal bleeding during pregnancy, and a family history of ERMS have been linked to an increased risk of developing RMS[191–194]. Additionally, ~7% of RMS patients harbour P/LP variants in cancer susceptibility genes, many of which are associated with heritable syndromes like *TP53*, *NF1*, *HRAS*, *DICER*, or mismatch repair genes (e.g., *BRCA2*, MSH2/6, *ATM*, or *CHEK2*)[195,196] (Figure 6). Notably, these germline variants are more frequently observed in patients with ERMS or FN-RMS than in those with ARMS or FP-RMS[195,196]. Although patients with cancer predisposition variants tend to be younger at diagnosis, a great proportion of germline variants are identified in those older than 3 years of age, emphasizing the need to extend genetic testing to this age group[196]. Identifying these variants is essential not only for guiding targeted treatments and determining clinical trial eligibility but also for prompting genetic counselling and cascade testing, thereby allowing the identification of at-risk family members, and facilitating early intervention and preventive measures[195].

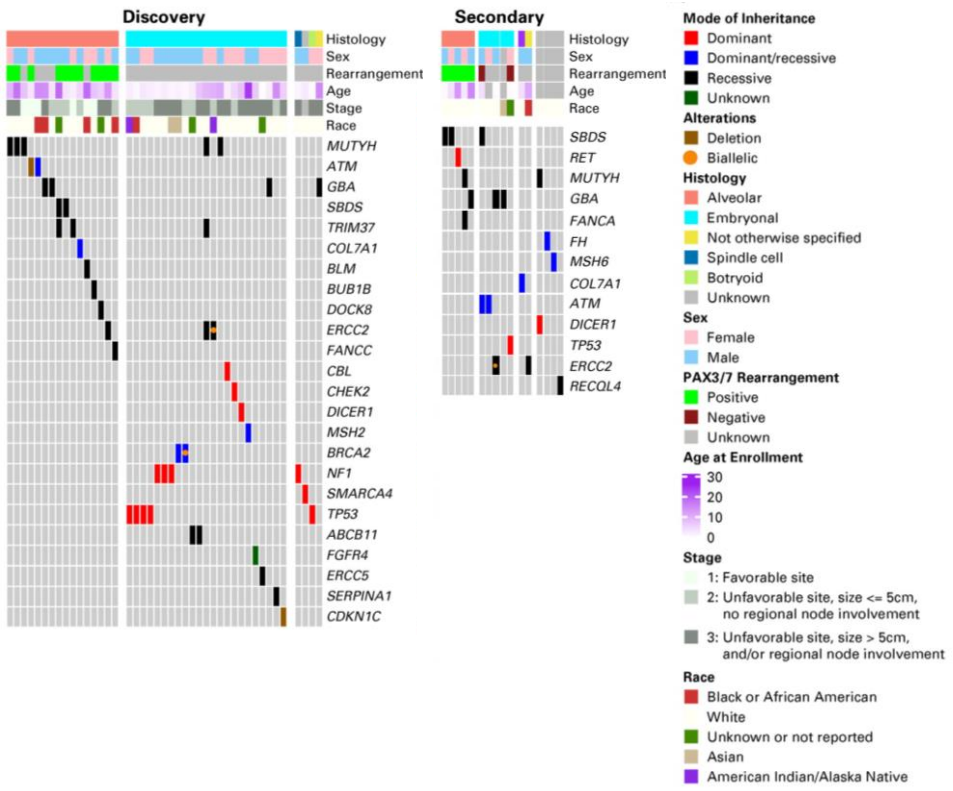

Figure 6. Oncoprint of pathogenic and likely pathogenic variants in cancer susceptibility genes. Results are shown for the discovery cohort (on the left) and the secondary cohort (on the right). This figure was adapted from the previously published manuscript by Kim et al.[195]

Over the past 30 years, the prognosis for RMS has markedly improved, with the 5-year overall survival (OS) now exceeding 70%[129,197–199]. This progress can be largely attributed to advancements in RMS management and treatment, as well as the effective implementation of risk stratification strategies[200]. The former Intergroup Rhabdomyosarcoma Study Group (IRS) played a pivotal role in developing these strategies by introducing a comprehensive approach to risk stratification, which includes both a pre-treatment staging system and a clinical classification[201,202]. The IRS staging system, which ranges from 1 to 4, classifies patients based on factors such as the location, size, and invasiveness of the primary tumour, lymph node involvement, and the presence of metastasis[202] (Table 2). In contrast, the IRS clinical grouping, determined after initial surgical intervention and before to the initiation of systemic therapy, categorizes patients according to the extent of tumour resection of localized and the presence or absence of distant metastasis[203] (Table 3).

Table 2. IRS staging classification for RMS patients

Stage	*Sites*	*Invasiveness*	*Size*	*Nodes*	*Metastasis*
1	Orbit, H&N (non-PM), GU (non-BP)	T_1 or T_2	A or B	N_0, N_1 or N_x	M_0
2	BP, Ext, PM, and other	T_1 or T_2	A	N_0 or N_x	M_0
3	BP, Ext, PM, and other	T_1 or T_2	A B	N_1 N_0, N_1 or N_x	M_0
4	Any	T_1 or T_2	A or B	N_0 or N_1	M_1

H&N: head and neck; PM: parameningeal; GU: genitourinary; BP: bladder/prostate; Ext: extremity; T_1: primary tumour confined to anatomical site of origin; T_2: primary tumour with extension and/or fixation to surrounding tissue; Size A: primary tumour ≤5 cm in diameter; Size B: primary tumour >5 cm in diameter; N_0: regional nodes not involved; N_1: regional nodes involved; N_x: status of regional nodes not known; M_0: no distant metastasis; M_1: metastasis

Table 3. IRS clinical grouping for RMS patients

Group	*Subgroup*	*Definition*
I	–	Localized disease, completely resected
II	–	Localized disease, positive margins and/or evidence for regional spread
	A	Gross resection with microscopic residual disease
	B	Total resection with no microscopic residual, involved regional lymph nodes
	C	Gross resection with microscopic residual, involved regional lymph nodes
III	–	Localized disease, incomplete resection with gross residual or biopsy only
IV	–	Distant metastatic disease

Both the IRS stage and clinical group have been demonstrated to strongly predict patient outcomes. In addition, prognostic factors such as age at diagnosis, the presence of P3/7F fusion, and the number of metastases have further refined RMS risk stratification[204–207]. However, while risk stratification guides treatment allocation, specific criteria for stratification differ between American Children's Oncology Group (COG) and the European Paediatric Soft-Tissue Sarcoma groups (EpSSG). For example, the EpSSG protocol (RMS 2005) stratifies RMS patients into low- (LR), standard- (SR), high- (HR), and very-high-risk (VHR) categories by considering fusion status, IRS clinical group, anatomical site, node involvement, tumour size, and age at diagnosis[208,209]. Conversely, the American COG protocol classifies patients into low-, intermediate- and high-risk categories focusing on IRS staging, IRS clinical group, age and fusion[207] (Table 4). These divergences in risk stratification criteria underscores both the challenge and the opportunity to develop a unified clinical practice with a standardized risk classification, thereby facilitating the creation of a global resource for the collection, storage and sharing of RMS clinical data[129].

Table 4. Risk stratification for RMS patients

European Paediatric Soft Tissue Sarcoma Group (EpSSG)

Risk group	*Subgroup*	*Fusion status*[1]	*IRS Group*	*Site*[2]	*Node stage*[3]	*Size or Age*[4]
Low	A	Negative	I	Any	N_0	Both favourable
Standard	B	Negative	I	Any	N_0	One or both unfavourable
	C	Negative	II, III	Favourable	N_0	Any
High	D	Negative	II, III	Unfavourable	N_0	Any
	E	Negative	II, III	Any	N_1	Any
	F	Positive	I, II, III	Any	N_0	Any
Very High	G	Positive	II, III	Any	N_1	Any
	H	Any	IV	Any	Any	Any

[1]*Fusion status*: It is recommended to stratify patients according to the fusion status, but if this would not available then histology (favourable vs unfavourable should be used: Favourable: ERMS (including botryoid RMS), SC/SRMS (non-*MYOD1* mutant) / Unfavourable: ARMS, SC/SRMS *MYOD1*-mutant.

[2]*Site*: favourable = orbit, genitourinary tract, head and neck non-parameningeal, biliary tract / unfavourable = `parameningeal, extremities and other sites.

[3]*Node stage*: N_0 = no clinical or pathological node involvement / N_1: clinical or pathological nodal involvement.

[4]*Size or Age*: Tumour size (maximum) ≤5 cm AND age <10 years / Unfavourable: all others (i.e. Size >5 cm OR age ≥10 years).

Children's Oncology Group

Risk group	*IRS Stage*	IRS Group	*Age*	*Fusion status*
Low	1	I, II, III (orbit only)	Any	Negative
	2	I, II	Any	Negative
Intermediate	1	III (non-orbit)	Any	Negative
	1,2,3	I, II, III	Any	Positive
	2,3	III	Any	Negative
	3	I, II	Any	Negative
	4	IV	<10 years	Negative
High	4	IV	≥10 years	Negative
	4	IV	Any	Positive

1.2.5. Current treatment modalities

RMS tumours exhibit significant sensitivity to chemotherapy, with response rates ranging from 80% to 85%[210–212]. Multimodal treatment protocols are tailored according to risk stratification and generally involve a combination of established cytotoxic drugs with local treatments like radiotherapy and surgery to maximize therapeutic efficacy[209] (Table 5).

First-line systemic treatments

Refinements in the intensity and combinations of chemotherapy drugs have led to significant treatment efficacy, particularly for LR and SR tumours, achieving 5-year OS rates of 96.7% and 90.6%, respectively[213]. LR and SR patients (Groups A–C) are treated with regimens that exclude alkylating agents, such as vincristine plus actinomycin (VA) or involve reduced doses of ifosfamide (IVA/VA), offering a more favourable toxicity profile while maintaining treatment efficacy[214]. However, significant treatment challenges remain for localized HR (Groups D–F) and VHR (Group G) tumours, with 5-year OS rates of 76.7% and 49.7%, respectively[213]. In Europe, ifosfamide, vincristine, and actinomycin D (IVA) has demonstrated the highest efficacy as an induction chemotherapy regimen for patients with HR RMS[211,215], whereas in North America, the combination of vincristine, actinomycin D, and cyclophosphamide (VAC) shows similar efficacy[198,199,216]. Notably, the introduction of doxorubicin (IVAD) in localized FP-RMS with nodal involvement (Group G) led to improved outcomes[217]. Following consolidation chemotherapy, maintenance therapy with daily oral cyclophosphamide and weekly vinorelbine for 6 months has been shown to improve disease-free survival and OS in HR patients[218]. In metastatic VHR RMS (Group H), the prognosis is significantly worse compared to other risk groups with a 5-year OS rate of 26%[219]. In these patients, the combination of systemic and local treatments may achieve complete remissions (CR); however, local and distant relapses remain frequent[208]. The standard systemic treatment for metastatic RMS typically involves IVA or VAC with the addition of doxorubicin during induction followed by IVA for consolidation[220]. If disease control is achieved following consolidation chemotherapy, maintenance therapy for 12 months with daily oral cyclophosphamide and weekly intravenous or oral vinorelbine is recommended[218].

Table 5. EpSSG systemic treatment protocol for RMS patients

Group Risk	*Subgroup*	*Chemotherapy*	*Local treatment*
Low	A	8xVA (28-day cycle)	Surgery
Standard	B	4xIVA + 5xVA (21-day cycle)	Surgery± RTx
	C	5xIVA + 4xVA[a] (21-day cycle)	
		9xIVA	RTx±Surgery[b]
High	D	9xIVA + 6xMaintenance	RTx±Surgery[b]
	E	9xIVA + 6xMaintenance	RTx±Surgery[b]
	F	9xIVA + 6xMaintenance	RTx±Surgery[b]
Very High	G	4xIVAD + 5xIVA + 12xMaintenance	RTx±Surgery[b]
	H	4xIVAD + 5xIVA + 12xMaintenance	RTx±Surgery[b]

Chemotherapy schedule

Treatment	*Chemotherapy*	*Schedule*	*Daily Dose*
First-line	**VA**	**21-day cycle/ 28-day cycle**	
	Vincristine	D1 / D1, D8, D15, D21	1.5 mg/m^2 (max 2 mg)
	Actinomycin D	D1/ D1, D21	1.5 mg/m^2 (max 2 mg)
	IVA / IVAD	**21-day cycle**	
	Ifosfamide	D1, D2	3 g/m^2
	Vincristine	D1, D8, D15 (C1-C2) / D1 (C3-C9)	1.5 mg/m^2 (max 2 mg)
	Actinomycin D	D1	1.5 mg/m^2 (max 2 mg)
	Doxorubicin	D1, D2 (C1-C4)	30 mg/m^2
	Maintenance	**28-day cycle**	
	Vinorelbine	D1, D8, D15	25 mg/m^2
	Cyclophosphamide	Daily	25 mg/m^2
Second-line	**VIT**	**21-day cycle**	
	Vincristine	D1, D8	1.5 mg/m^2 (max 2 mg)
	Irinotecan	D1-D5	50 mg/m^2
	Temozolamide	D1-D5	125 mg/m^2
	VCDE	**21-day cycle**	
	Vincristine	D1	1.5 mg/m^2 (max 2 mg)
	Cyclophosphamide	D1	1.5 g/m^2
	Doxorubicin	D1-D3	20 mg/m^2
	Etoposide	D1-D3	150 mg/m^2
	TVD	**21-day cycle**	
	Topotecan	D1-D5	1.5 mg/m^2
	Vincristine	D5-D6	1 mg/m^2 (max 1 mg)
	Doxorubicin	D5-D6	22,5 mg/m^2

[a] Patients will receive 9xIVA if a is achieved through secondary surgery, without the need for RTx. If RTx is included, 5xIVA + 4xVA. Bladder/prostate tumours will receive always 9xIVA.
[b] Unfavourable sites are usually treated with RTx alone.
RTx: Radiotherapy; D: day; C: cycle.

Second-line systemic treatments

Approximately 30% of patients with localized disease experienced an event within 5 years, while 66% of those with metastatic RMS had an event within 3 years[221]. Relapsed/Refractory (R/R) tumours are generally resistant to treatment, with a 5-year OS rate of less than 20%, highlighting the critical need for new therapeutic strategies[222]. In general, patients who received more intensive therapy at the time of initial diagnosis had worse outcomes following relapse than those who received less intensive therapy[129]. The treatment of R/R RMS varies depending on the timing of the relapse and prior treatments. Currently, the combination of vincristine, irinotecan, and temozolomide (VIT) is considered the EpSSG standard for treating R/R RMS, achieving an objective response rate of 44%[223]. If there is no response to VIT, it is recommended to either enroll the patient in a clinical trial or explore alternative combinations[208]. For patients who have not previously received anthracyclines, the VCDE (vincristine, cyclophosphamide, doxorubicin, etoposide) or TVD (topotecan, vincristine, doxorubicin) regimens may be considered[208,224,225].

Additional options include the DCEI (doxorubicin, carboplatin, etoposide, ifosfamide) or ACCTTIVE (adriamycin, carboplatin, cyclophosphamide, topotecan, vincristine, etoposide) regimens for LR and SR patients[226]. For HR or VHR R/R patients, the VI (vincristine, irinotecan) regimen combined with DCEI, or the TECC (topotecan, etoposide, carboplatin, cyclophosphamide) regimen, may be considered[221,226]. For patients who had not received maintenance chemotherapy, the combination of vinorelbine plus cyclophosphamide, with the possible addition of temsirolimus, has shown the best results[227,228].

Local treatments

If positive surgical margins are detected in localized tumours, patients may undergo additional surgical resection or receive radiation therapy[222]. The treatment approach is influenced by factors including the patient's age, histological subtype, tumour biology, anatomical location, tumour size, and response to chemotherapy[208]. However, the intensity of radiotherapy is ultimately determined by the risk stratification, ensuring that treatment is tailored to patient's specific needs (Table 6). Notably, advances such as intensity-modulated radiation therapy and proton beam therapy are increasingly being used to reduce tumour size while minimizing treatment side effects, particularly in young patients with RMS[229].

Table 6. EpSSG radiotherapy protocol for RMS patients

Radiotherapy dose prescription

Location	Group	Response to induction CTx	Doses and fractionation
Primary tumour	Resectable	NA	41.4 Gy in 23 fractions (4.5 weeks)
	Unresectable	Complete	41.4 Gy in 23 fractions (4.5 weeks)
		Incomplete	50.4 Gy in 28 fractions (5.5 weeks) – Phase I: 41.4 Gy in 23 fractions – Phase II: 9 Gy in 5 fractions
			55.8 Gy in 31 fractions (6 weeks) – Phase I: 41.4 Gy in 23 fractions – Phase II: 14.4 Gy in 8 fractions
Lymph nodes	NA	NA	50.4 Gy in 28 fractions (5.5 weeks) – Phase I: 41.4 Gy in 23 fractions – Phase II[a]: 9 Gy in 5 fractions
Metastatic sites[b]	Limited or oligometastatic	NA	Radical dose fractionation or stereotactic ablative RTx
	Lung[c]		15 Gy in 10 fractions
	Other		30 Gy in 10 fractions

[a] Only for bulky residual lymph nodes.
[b] Radiotherapy doses for metastatic sites is at discretion of the treating physician. The doses indicated are the most common doses used.
[c] Benefit of whole lung radiation is uncertain and still a matter of debate.

In the EpSSG study (RMS 2005), radiotherapy improved 3-year event-free survival (EFS) to 67% in HR RMS patients and 56% in VHR, significantly outperforming historical outcomes[215,230]. Additionally, re-excision of recurrent RMS can improve 5-year OS, increasing them from 8% to 37% compared to those who do not undergo aggressive re-excision[231]. For metastatic patients, global guidelines recommend systematic irradiation of all technically feasible sites where the risk-benefit analysis justifies its use[208]. However, the use of radiation therapy in metastatic RMS is variable, with limited evidence supporting its use[208,232]. Retrospective studies suggest that aggressive local management of metastatic disease, including surgery and radiotherapy when feasible, might positively influence EFS and OS rates[232,233]. However, conflicting results have been published regarding the benefit of whole-lung radiation[232–238]. Given the variability in patient circumstances and disease characteristics, universal recommendations for local treatment with radiotherapy cannot be established. Instead, each case must be evaluated individually to reach a consensus on the most appropriate treatment options.

1.2.6. Pathogenesis and molecular mechanisms

1.2.6.1. Fusion-positive rhabdomyosarcoma

Cytogenetic studies have identified recurrent chromosomal translocations in the majority of patients with ARMS, with the most notable being the t(2;13)(q35;q14) and t(1;13)(p36;q14) translocations[239,240]. These translocations result in the generation of chimeric TFs that combine the amino-terminal region of PAX3 or PAX7, which retains an intact DNA-binding domain (DBD), and the C-terminal region of FOXO1, which maintains an intact transcriptional activation domain[241,242] (Figure 7). In contrast to the PAX3 and PAX7 proteins, these fusion proteins exhibit significantly increased transcriptional activity[243]. This enhanced activity is due to a shared gain-of-function mechanism, where the FOXO1 transactivation domain becomes less sensitive to the inhibitory effects of the amino-terminal domains of PAX3 or PAX7[243,244]. In addition to their functional changes, P3F and P7F are overexpressed through different mechanisms. P3F transcription is upregulated by a mechanism that is independent of copy number changes, while the overexpression of P7F is driven by amplifications of the fusion gene[245].

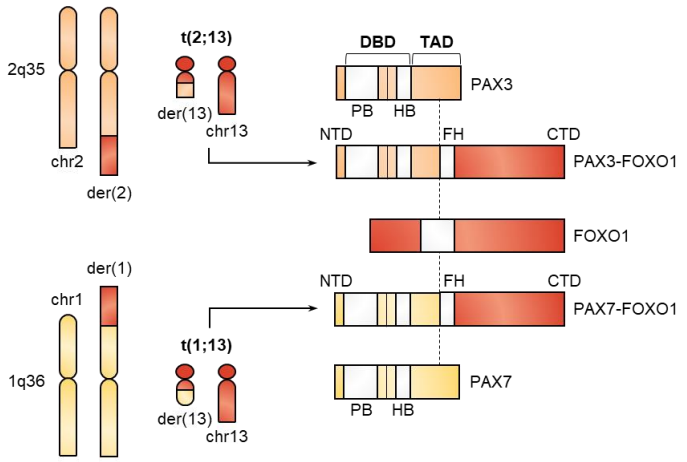

Figure 7. PAX3/7-FOXO1 fusions are key drivers of FP-RMS tumorigenesis. Balanced translocations between *PAX3* or *PAX7* and *FOXO1* result in the creation of PAX-FOXO1 fusions. These fusion proteins combine the amino-terminal domain (NTD) of PAX3/7 with the carboxy-terminal domain (CTD) of FOXO1. The NTD provides DNA-binding motifs from the respective PAX gene, while the CTD is believed to modify the trans-activation domain (TAD) of the oncogenic transcription factor. The other derivative chromosomes do not contribute to RMS pathogenesis. Chr: chromosome, der: derivative chromosome, DBD: DNA-binding domain, HB: homeobox domain, FH: forkhead domain; PB: paired box domain.

The function of the P3F fusion protein is also regulated by post-translational modifications, with key phosphorylation, acetylation, methylation, and O-linked β-N-acetylglucosamination sites within its carboxy-terminal FOXO1 region modulating its stability and function[47]. For instance, phosphorylation at S503 and S505 by PLK1, and acetylation at K426 and K429 mediated by P/CAF (KAT2B), stabilizes P3F[246,247]. Other kinases such as CK2, GSK3, CDK4 or AKT have also been shown to modulate PAX3-FOXO1 activity through phosphorylation[47]. Additionally, research utilizing the pharmacological kinase inhibitor PKC412 has highlighted the regulatory role of phosphorylation on the amino-terminal region of PAX3, affecting both DNA binding and the transcriptional activity of the fusion protein[248]. However, the precise proteins responsible for these phosphorylation events remain unidentified.

P3F and P7F function as potent oncoproteins by rewiring the transcriptome of FP-RMS cells through CRCs[38,39]. P3F promotes the expression of downstream target genes by binding to PAX3-binding sites near these genes, using its activation domain to recruit CBP/p300, and maintaining active RNA polymerase II (RNA pol II) clusters necessary for oncogenic transcription[249]. Chromatin immunoprecipitation followed by sequencing (ChIP-seq) has revealed that most P3F binding sites are positioned more than 2.5 kb away from the nearest transcription start site and are associated with active enhancer chromatin marks, such as acetylation of histone H3K27[39,250]. These regions often contain E-box DNA-binding motifs in addition to PAX3-binding sites. P3F co-binds these regions with E-box-specific transcription factor MYCN and myogenic basic helix-loop-helix TFs MYOD1 and MYOG[39,251]. Furthermore, P3F interacts with several chromatin-associated factors and complexes, including BRD4, cohesin-CTCF, SWI/SNF, NuRD, NELFB, DSIF and Mediator complexes. This interaction helps reprogram the chromatin landscape and establish super-enhancers, which then interact with target gene promoters through three-dimensional chromatin looping[39,92,252,253] (Figure 8). The oncogenic influence of these fusions extends to the regulation of growth, survival, differentiation, and other cellular processes by activating numerous downstream target genes, such as ALK, IGF2, IGF1R, FGF8, FGFR4, MET, MYCN, MYOD1, MYOG, TFAP2B, RUNX2, CXCR4, and KLF4[39,92,250,254,255]. In addition to fusion proteins, FP-RMS can involve other genetic alterations that cooperate in disease development, such as amplifications in *MYCN*, *CDK4*, and *MIR-17-92*, or deletions in *CDKN2A*. Additional candidate somatic driver mutations are rare in FP-RMS, reflecting the low somatic mutation rate observed in this disease[134].

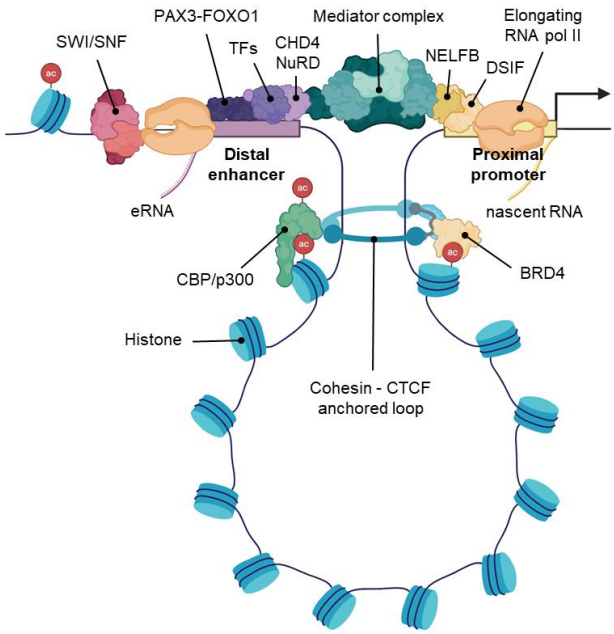

Figure 8. PAX3–FOXO1 rewires the transcriptome by inducing *de novo* super-enhancer. PAX3-FOXO1 uses super-enhancers to establish autoregulatory loops in collaboration with MYOG, MYOD, and MYCN. Moreover, PAX3-FOXO1 collaborates with various transcriptional complexes and chromatin-associated proteins to maintain an open chromatin structure, thereby facilitating the activation of its target genes.

1.2.6.2. Fusion-negative rhabdomyosarcoma

In contrast to FP-RMS, FN-RMS exhibit a higher degree of aneuploidies, CNAs, and mutational burden, primarily affecting a few key pathways[134] (Figure 9). Notably, some of these pathways are also disrupted in FP-RMS, either through the upregulation of downstream targets of the P3F and P7F fusion proteins or through genomic amplification, suggesting common molecular driving forces underlying both subtypes[129].

Alterations in receptor tyrosine kinases (RTKs) signalling

In FN-RMS, activating mutations in FGFR4, present in 7–12% of cases, lead to the activation of the RAS pathway, which plays a significant role in tumour growth[134,256,257]. In contrast, FP-RMS exhibits increased levels of FGFR4 and FGFR2, which are attributed to the upregulation induced by P3/7F fusions[39,250,258]. Similarly, fusion proteins upregulate IGF1R expression in FP-RMS, while in FN-RMS, increased expression of its ligand IGF2 results from either loss of heterozygosity (LOH) or imprinting at the 11p15.5 locus[134,250].

Notably, mutations in IGF1R have also been identified in both subtypes[259]. Increased IGF signalling in FN-RMS enhances the tyrosine phosphorylation of insulin receptor substrate 1 (IRS1), thereby activating downstream RAS–MAPK and PI3K–AKT signalling pathways[260]. Furthermore, increased MET signalling in FN-RMS supports invasive tumour growth, while in FP-RMS, PAX3–FOXO1-driven MET expression promotes cell motility via MAPK, thereby inhibiting myogenic differentiation[261–263]. Additionally, in FP-RMS, the fusion protein drives the expression of platelet-derived growth factor receptor-α (PDGFRA), which is occasionally mutated in FN-RMS[134,250,264]. PDGFRA activity is critical for regulating cancer cell stemness, differentiation, senescence, and apoptosis, highlighting the complex interplay of signalling pathways in RMS pathology[265]. Less frequently mutated RTKs, such as FGFR1 and ALK, also contribute to the diverse molecular landscape that underpins RMS[259].

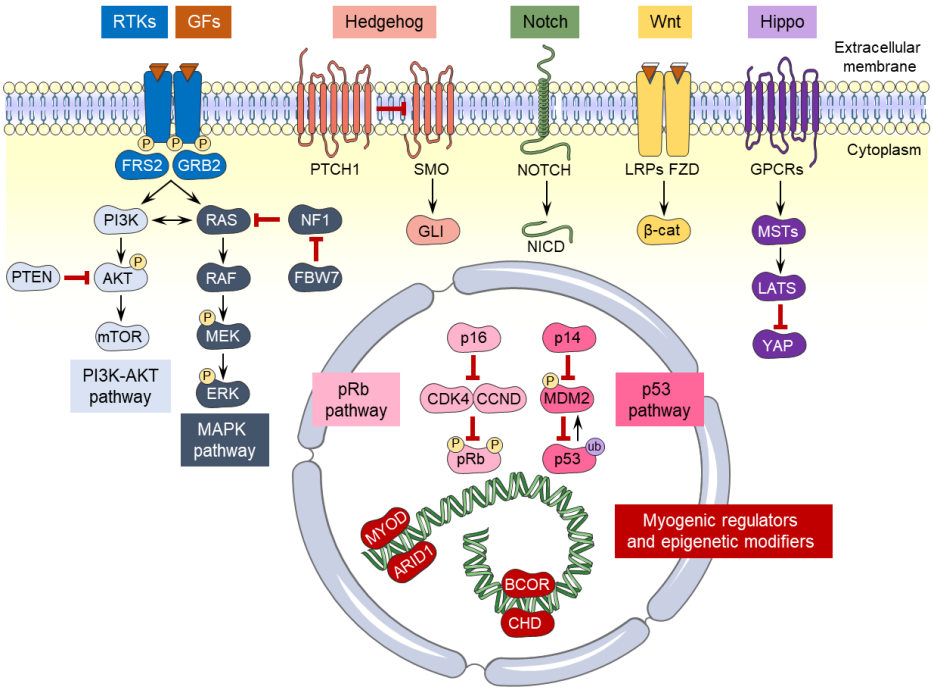

Figure 9. Pathways significantly altered in FN-RMS. Alterations in receptor tyrosine kinases (RTKs), as well as the PI3K-AKT and MAPK pathways, are observed in most FN-RMS cases. Dysregulation of cell cycle-related pathways, including the p53 and Rb pathways, is also prevalent. Mutations in key myogenic regulatory factors like MYOD1, along with epigenetic modifiers, such as BCOR, ARID1A, and CHD7, have also been identified. Furthermore, defects in developmental pathways including Hedgehog, Notch, Wnt, and Hippo, further contribute to the disease pathogenesis. GFs: growth factors; GPCR: G protein-coupled receptor; NICD: Notch intracellular domain; β-cat: β-catenin; LRPs: LRP5/6; MSTs: MST1/2.

Alterations in RAS-MAPK and PI3K-AKT pathways

In addition to alterations in RTKs, >50% of FN-RMS tumours harbour mutations that affect RAS–RAF–MAPK and/or PI3K–AKT–mTOR pathways[134,257,266]. Approximately one-third of these patients exhibit activating mutations in critical RAS pathway components, such as *NRAS*, *KRAS*, and *HRAS*[134,257,266]. Moreover, additional mutations have been identified in genes associated with RAS pathway signalling, including *PTPN11*, *NF1*, *MAP3K4* and *BRAF*[134,257,259,266]. In the PI3K–AKT–mTOR pathway, mutations are predominantly found in the *PIK3CA*, with additional mutations in *PTEN*, *MTOR*, *RICTOR*, and *RPTOR*[134,257,259,266]. Additionally, *PTEN* promoter hypermethylation is frequently observed in FN-RMS, and PTEN copy number loss occurs in approximately 25% of cases, leading to its inactivation, thus contributing to increased PI3K signalling activity[257,267]. Interestingly, PTEN-deleted tumours exhibit increased expression of PAX7, and PAX7 deletion completely rescues the effects of PTEN loss, suggesting a close connection between PTEN loss and PAX7 expression to maintain FN-RMS identity[267]. These genetic alterations collectively underscore the complex and overlapping signalling disruptions driving RMS pathology.

Alterations in cell-cycle genes

Unlike most adult tumours, loss-of-function *TP53* mutations are relatively rare in RMS, occurring in 5–20% of FN-RMS and 0–5% of FP–RMS at diagnosis[134,257,259]. Additionally, LOH at 17p13.1, which includes *TP53*, is observed in 12–17% of all RMS tumours[134,257]. However, p53 function can also be compromised by the overexpression and/or overactivation of MDM2 (Murine Double Minute 2 proto-oncogene), the main E3 ubiquitin ligase of p53, with gene amplifications detected in ~10% of RMS cases[134,257]. Furthermore, frequent alterations in the tumour suppressor *CDKN2A* are observed in both FP- and FN-RMS, including mutations, homozygous deletions (3–25%), and LOH at 9p21.3 (10–20%)[134,257,268]. Loss of *CDKN2A* directly affects Rb and p53 pathways, both involved in cell-cycle regulation [269,270]. Specifically, *CDKN2A* encodes $p16^{INK4A}$, which regulates CDK4/6 activity and Rb phosphorylation, and $p14^{ARF}$, which inhibits MDM2 and stabilizes p53. Interestingly, mutations in *FBXW7*, a p53 downstream target, have also been detected in 2.4–7% of FN-RMS[134,257]. Other alterations observed in cell cycle genes, include *CDK4* amplifications in 9% of RMS cases (primarily FP-RMS), and *BUB1B*, *CCND1*, and *CCND2* mutations in approximately 1–1.4% of FN-RMS cases[134].

Involvement of developmental pathways

As a paediatric cancer, RMS exhibits a low mutational burden, suggesting that deregulation of pathways involved in embryonal development could play a significant role in its pathogenesis[52]. Studies of primary tumours, cell lines, and mouse models have revealed the involvement of developmental pathways in RMS tumorigenesis and progression, including Wnt[271–273], Notch[274–276], Hedgehog[277–279], and Hippo-YAP[280,281] signalling pathways. Specifically, some mutations in the β-catenin (*CTNNB1*) and *NOTCH* genes are observed in RMS, and components of these pathways are frequently hyperactivated[134,259,272,282]. Similarly, dysregulation of Sonic Hedgehog (SHH) signalling is common in FN-RMS, with some tumours harbouring *GLI1* amplifications and/or *PTCH1* loss[278]. Additionally, YAP1 is highly expressed in both FP- and FN-RMS, driving tumour growth and survival when the upstream Hippo tumour suppressor pathway is silenced[283]. The crosstalk between these developmental pathways and other oncogenic pathways altered in RMS creates an integrated network that supports the development of the disease[97].

Alterations in myogenic regulators and epigenetic modifiers

In addition to alterations in developmental pathways, mutations in genes involved in myogenesis, such as *MYOD1*, have been identified in FN-RMS patients[134,152,259,284]. These *MYOD1* mutations frequently co-occur with mutations in genes of the PI3K–AKT–MTOR pathway, defining a particularly aggressive FN-RMS subtype (classic SC/SRMS)[152,284]. Such mutations occur in the conserved DBD of *MYOD1* and lead to transactivation and MYC-like functions[285]. Furthermore, global and specific changes in DNA methylation and histone modifications that might affect myogenesis processes have been observed in RMS[39,257,259,286]. Notably, mutations predominantly found in FN-RMS affect genes associated with the polycomb repressive complex 1 (e.g., *BCOR*), the SWI/SNF chromatin remodelling complex (e.g., *ARID1A*, *SMARCD2*), as well as chromodomain-helicase-DNA-binding proteins such as *CHD7* and *CHD9*[134,257,259]. Indeed SWI/SNF complex has been recently demonstrated to drive proliferation and block myogenic differentiation in FP-RMS and mutations in CHDs are known to cause multiple developmental disorders[253,287,288]. The interplay between myogenic regulators and epigenetic modifiers highlights the multifaceted nature of FN-RMS, emphasizing the need to identify novel vulnerabilities associated to certain pathways to develop new targeted therapies.

1.2.7. The MDM2-p53 axis: an intersection of multiple pathways altered in FP- and FN-RMS

Despite the distinct genetic and molecular profiles that define FP-RMS and FN-RMS, a critical intersection in their pathogenesis lies in the MDM2-p53 axis, which emerges as a central node in RMS biology (Figure 10). Understanding the mechanisms driving the dysregulation of this axis is crucial, as it reveals potential therapeutic vulnerabilities applicable across both RMS subtypes. In FP-RMS, P3F and P7F act as the main drivers of the disease by rewiring the transcriptome of FP-RMS cells through CRCs[38,39]. These fusions facilitate the expression of downstream target genes by binding to PAX3/7-binding sites and maintaining active RNA pol II clusters, which are essential for sustaining oncogenic transcription[249]. As a result, P3F and P7F promote the transcription of several RTKs and growth factors, leading to the hyperactivation of the PI3K-AKT and RAS-MAPK signaling pathways[39,250,258,261,264]. These pathways are also frequently altered in most FN-RMS cases, primarily due to genetic alterations in RTKs and components of both PI3K-AKT and RAS-MAPK pathways[134,257,266]. A key downstream effect of PI3K-AKT and RAS-MAPK pathway activation is the phosphorylation and subsequent overactivation of MDM2[289–296]. Specifically, AKT and ERK phosphorylate MDM2 at Ser166, 183, 186 or 188, resulting in an increased MDM2 stability, activity and its translocation to the nucleus[289–296].

In FP-RMS, the oncogenic influence of the P3F on MDM2-p53 axis extends further by significantly increasing the transcription of MYCN which directly upregulates MDM2 transcription, adding another layer of MDM2 overactivation and p53 suppression[297,298]. As an E3 ubiquitin ligase, MDM2 binds to p53, ubiquitinates it, and mediates its transport from the nucleus to the cytoplasm, promoting its degradation in the proteasome[299–302]. Consequently, the overactivation of MDM2 inhibits the tumour-suppressive functions of p53, representing a key mechanism by which RMS cells evade p53-mediated cell cycle arrest and apoptosis[300,303,304]. Furthermore, MDM2 overactivation has been implicated in therapeutic resistance, as the suppression of p53 may reduce the efficacy of conventional treatments such as chemotherapy and radiation, which often rely on intact p53 pathways to induce tumour cell death[305,306]. Irrespective of p53-mediated ubiquitination, MDM2 amplification and overexpression has also been shown to inhibit MYOD1-mediated myogenesis, suggesting its contribution to the blocked myogenesis observed in RMS[307].

Beyond these indirect mechanisms, direct genetic alterations further consolidate the central role of MDM2 in RMS. As aforementioned, MDM2 amplifications identified mainly in FN-RMS cases provide an additional mechanism for p53 inhibition[134,257]. Moreover, loss of CDKN2A observed in some RMS removes another critical checkpoint on MDM2 activity, leading to unrestrained MDM2-mediated p53 degradation[134,257,268].

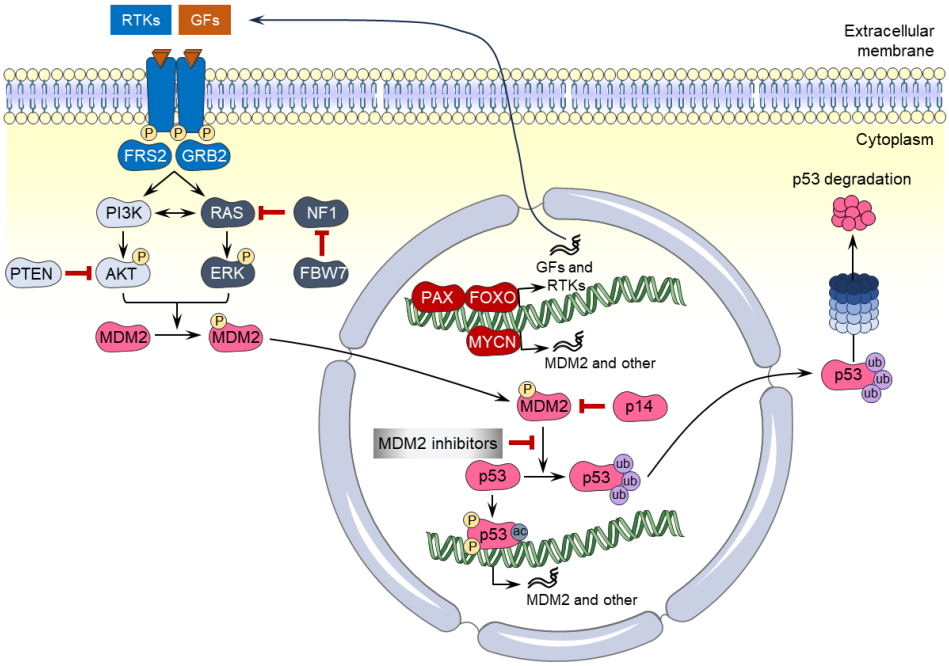

Figure 10. The MDM2-p53 axis as a central node of multiple pathways altered in RMS. In fusion-negative RMS (FN-RMS), genetic alterations in receptor tyrosine kinases (RTKs) and disruptions in the RAS-MAPK and PI3K-Akt signaling pathways often lead to overactivation of AKT and ERK. In contrast, fusion-positive RMS (FP-RMS) features PAX-FOXO1 fusions, which enhance RTK and growth factor expression, driving excessive activation of the RAS-MAPK and PI3K-Akt pathways. The resultant activation of AKT and ERK promotes the phosphorylation of MDM2 at critical residues within its nuclear localization signal, enhancing its stability, activity, and nuclear localization. Additionally, in FP-RMS, MYCN—either overexpressed through PAX3-FOXO1 fusions or amplified in some cases—further upregulates MDM2 transcription. Loss of CDKN2A, which encodes p14ARF, is also observed in some RMS cases, exacerbating MDM2 overactivation. Elevated MDM2 levels lead to increased ubiquitination and proteasomal degradation of p53. Thus, MDM2 inhibitors, which disrupt the MDM2-p53 interaction and restore p53 activity, present a promising therapeutic approach for targeting p53 WT tumours, potentially improving treatment outcomes for this aggressive paediatric cancer.

Despite the molecular complexity and heterogeneity of RMS, it is notable that the disease typically presents with a low mutation burden at diagnosis[134,308]. Importantly, although the mutational burden at relapse is higher than at diagnosis, the majority of R/R RMS retain p53 wild-type (p53 WT)[309]. The persistence of p53 WT status in R/R RMS, together with the critical role of the MDM2-p53 axis in the pathogenesis of both FP- and FN-RMS, underscores the potential of MDM2 inhibitors. These inhibitors could disrupt the interaction between MDM2 and p53 across both RMS subtypes, offering a novel approach to develop more targeted and effective treatments for patients with this highly aggressive paediatric cancer.

1.3. Targeting the MDM2-p53 pathway in RMS

The protein p53, encoded by the *TP53* gene, is a critical regulator of cellular fate, coordinating responses such as cell cycle arrest, DNA repair, senescence, or apoptosis in response to various stress signals[310,311]. Under normal conditions, p53 levels are tightly controlled through rapid proteasomal degradation to prevent excessive accumulation, which can impair normal cell proliferation and development[311]. However, in response to certain cellular stresses, p53 becomes activated and stabilized, underscoring its essential role as a tumour suppressor[312]. One of the key functions of p53 is to protect against early cancerous changes by initiating repair mechanisms in response to DNA mutations and by promoting the elimination of severely damaged cells[311,313,314].

In cancer, p53 function is often compromised not only by mutations in the *TP53* gene, but also by mechanisms such as overexpression and/or overactivation of MDM2, which collectively diminish its tumour-suppressive capabilities[315–318]. To address these challenges, significant efforts in medicinal chemistry have been directed towards developing therapies designed to restore p53 function in cancer cells, especially for tumours that retain p53 WT[318]. Over the past two decades, researchers have developed several small molecules aimed at inhibiting the interaction between p53 and its primary repressor, MDM2[304,319,320]. These inhibitors effectively disrupt the MDM2-p53 complexes in p53 WT cells, thereby reducing p53 ubiquitination and degradation[320,321]. This disruption leads to the accumulation and activation of p53, which in turn induces the expression of a broad range of p53-regulated genes, eliciting diverse cellular responses that vary depending on the specific context and extent of the damage[311,322].

1.3.1. MDM2 inhibitors: disrupting the interaction between p53 and MDM2

Since the discovery of potent small-molecule inhibitors that target MDM2-p53 interactions, a broad range of chemical scaffolds has been developed and assessed[304]. Crystallographic studies of the p53–MDM2 complex identified three specific subpockets within the hydrophobic cleft of MDM2 that interact with the Leu26, Trp23, and Phe19 side chains of p53[323]. This structural information provided a basis for developing a range of structurally unique small-molecule inhibitors targeting this interaction.

In the early 2000s, Hoffman-La Roche developed a series of cis-imidazoline derivatives known as nutlins (including nutlin-1, -2, and -3), which were the first selective inhibitors of MDM2[324,325]. Building on this foundation, researchers also developed RG7112, a more potent *cis*-imidazoline derivative with improved efficacy in disrupting the MDM2-p53 interaction[326]. Notably, Hoffman-La Roche further advanced the field with the introduction of idasanutlin (RG7388), a second-generation antagonist featuring a pyrrolidine core[327]. Idasanutlin not only offered enhanced potency and selectivity compared to RG7112 but also demonstrated better bioavailability, leading to its evaluation in several clinical trials[327]. Similarly, Amgen developed navtemadlin (AMG-232) by refining an initial lead structure based on a piperidinone scaffold[328]. In this compound, the isopropyl group specifically fits into the Leu26 pocket, while two trans-oriented chlorophenyl groups bind to the Trp23 and Phe19 pockets[329,330].

Another notable class of MDM2 antagonists are the spiro-oxindole-pyrrolidines, initially identified at the University of Michigan[331]. This discovery led to the development of early compounds such as MI-63, as well as other related molecules, MI-219 and MI-319[332,333]. Subsequent optimization produced advanced second-generation compounds, including MI-773[334]. Structural analysis of the co-crystal complex of MI-773 with MDM2 revealed a binding mode that not only mirrored the interactions of earlier spiro-oxindole-pyrrolidines but also introduced novel interactions[335]. Notably, MI-773 induced the refolding of the N-terminal region of MDM2, which enhanced its binding affinity and potentially increased its therapeutic efficacy[334,335]. More recent developments include a new generation of spiro-oxindoles with a dispiropyrrolidine core. Noteworthy examples of these novel compounds are alrizomadlin (APG-115), developed by Ascentage Pharma Group, and milademetan (DS-3032b), created by Daiichi-Sankyo[336,337].

Novartis has also developed two additional classes of MDM2 antagonists that are currently undergoing clinical trials. These compounds were designed around the 'central valine' concept, positioning a planar aromatic ring near the Val93 residue[338]. The initial design, which used a dihydroisoquinolinone core, resulted in the highly potent compound CGM097[339]. Further optimization of the dihydroisoquinoline scaffold resulted in a new class of inhibitors with a pyrazolo-pyrrolidinone core, among which siremadlin (HDM-201) stands out due to its enhanced properties[340]. Concurrently, Boehringer Ingelheim developed brigimadlin (BI-907828), an MDM2 inhibitor characterized by its multicyclic core structure[341–343]. This compound demonstrated favourable pharmacokinetic and pharmacodynamic properties in several preclinical models and is currently being evaluated in clinical trials[341–343]. In addition to small-molecule inhibitors, peptide-mimetic compounds targeting the MDM2 protein have been developed. A notable example is ALRN-6924, created by Aileron Therapeutics, which is currently being evaluated in multiple clinical trials[344,345].

Limitations of MDM2 inhibitors as monotherapy: the necessity for combination therapies

Despite their potential to disrupt the interaction between MDM2 and p53, the use of MDM2 inhibitors as monotherapy has encountered significant limitations, highlighting the need for a more sophisticated approach to their clinical application[320,346]. Initially, MDM2 inhibitors were anticipated to activate the p53 pathway in p53 WT cells, thereby inducing robust apoptosis. However, accumulating evidence has revealed that the apoptotic response triggered by these inhibitors is often constrained by the complex and context-dependent nature of p53 activity[319,347,348]. Moreover, cancer cells frequently develop resistance mechanisms that undermine the effectiveness of MDM2 inhibitors, leading to a diminished apoptotic response[346,349,350]. This reduction in effectiveness is often due to the tumour's specific molecular context and the presence of compensatory mechanisms that mitigate the intended therapeutic effects of MDM2 inhibition[351–353]. Furthermore, the integration of MDM2 inhibitors into cancer therapy has faced significant challenges, particularly in early-phase clinical trials, where monotherapy with these agents has demonstrated limited efficacy[320,354,355]. Although MDM2 inhibitors are generally well-tolerated, with relatively mild adverse effects, they are not without their own set of issues. Hematologic toxicities, gastrointestinal problems, and other systemic side effects may limit the feasibility of their long-term use, presenting an additional challenge for their effectiveness as standalone treatments[304,349,350].

Given these limitations, there is increasing interest in exploring combination therapies to enhance the therapeutic efficacy of MDM2 inhibitors and overcome resistance mechanisms[346]. Combining MDM2 inhibitors with other modalities, such as chemotherapy, radiation, or targeted therapies, presents a promising strategy to improve treatment outcomes[304,319]. Both clinical trials and preclinical studies are now increasingly focused on identifying synergistic combinations that could enhance the overall efficacy of MDM2 inhibitors, especially in the context of certain adult cancers. (Figure 11).

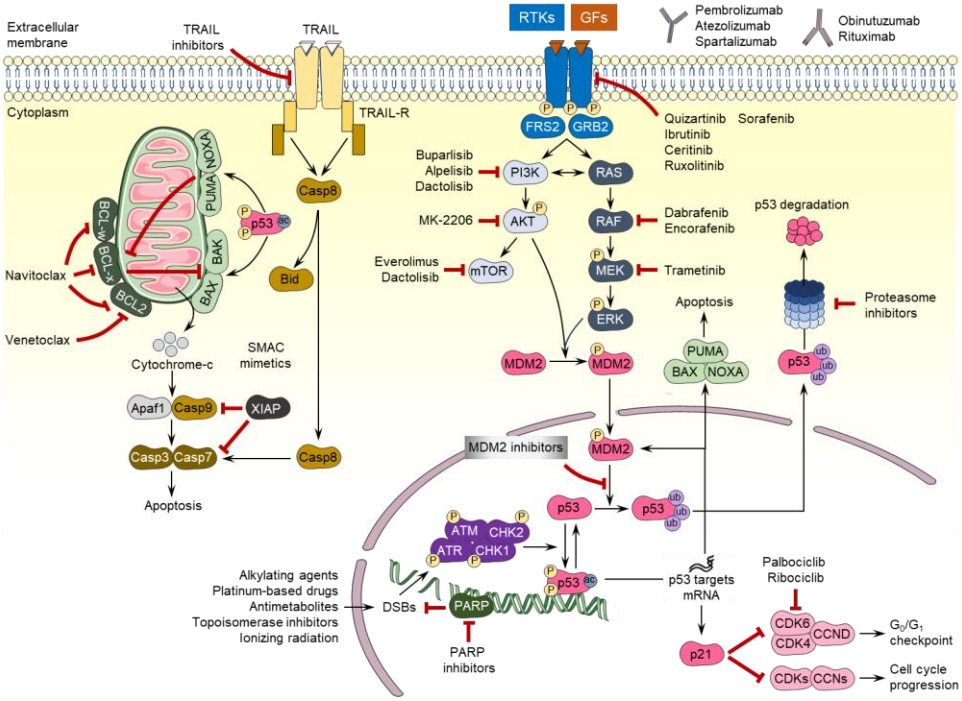

Figure 11. Combination strategies enhancing the efficacy of MDM2-p53 inhibitors. Combining MDM2 inhibitors with DNA-damaging agents, such as chemotherapeutics and ionizing radiation, enhances p53 activation through post-translational modifications, thereby amplifying its tumour-suppressive effects. To further enhance the pro-apoptotic potential of MDM2-p53 inhibitors, strategies such as targeting anti-apoptotic proteins (e.g., BCL-2, BCL-xL, BCL-w, and XIAP) or inducing apoptotic signaling with TRAIL agonists can be employed. Integrating MDM2 antagonists with inhibitors of RTK, RAS-MAPK, and PI3K-AKT-mTOR pathways can also reduce MDM2 activation and suppress pro-survival signaling pathways often dysregulated in cancer. Moreover, cell cycle dysregulation can be addressed by combining MDM2 inhibitors with CDK inhibitors to reduce tumour cell proliferation through cell cycle arrest induction. Exploring combinations with immunotherapies, such as anti-PD-1/PD-L1 agents, or proteasome inhibitors provides new opportunities to enhance the therapeutic efficacy of MDM2 inhibitors.

In RMS, the strategy of combining MDM2 inhibitors with other treatments has shown initial promise in preclinical studies. For example, combinations of nutlin-3a, a first-generation MDM2 inhibitor, with vincristine or actinomycin D have demonstrated encouraging results in p53 WT RMS cells *in vitro*[356]. Similarly, idasanutlin has been found to enhance the efficacy of ionizing radiation in MDM2-amplified RH18 cells and their xenografts *in vivo*[357]. Despite these promising findings, existing studies often focus on specific combinations and may not fully explore the potential synergistic interactions with newly developed or currently tested compounds. Additionally, there is a notable absence of systematic research comparing the potency and selectivity of different MDM2 inhibitors. This lack of comparative studies impedes a comprehensive assessment of which inhibitors might offer superior efficacy and specificity, thereby constraining the optimization of therapeutic strategies. Expanding research to include a broader array of combination therapies and conducting systematic comparisons of MDM2 inhibitors could reveal more effective strategies for managing R/R cancers, potentially leading to improved treatment outcomes and more effective management of challenging malignancies.

1.3.2. Combinations of MDM2 inhibitors with other therapies: the experience from other tumours

The limitations of MDM2 inhibitors as monotherapy have prompted extensive research into combination therapies to enhance their antitumor efficacy. This section will explore the current knowledge and experiences of combining MDM2 inhibitors with other therapies across various tumour types, providing insights into the strategies that may inform future therapeutic approaches in RMS and other cancers.

1.3.2.1. DNA damage inducers

DNA is a crucial target in cancer therapy, particularly in chemotherapy and radiotherapy, due to the increased proliferation rates of cancer cells and their frequent deficiencies in DNA repair mechanisms[358]. Genotoxic agents, including chemotherapeutic drugs and ionizing radiation, induce significant and often irreversible genomic damage, which disproportionately affects cancer cells compared to normal cells[359]. This genomic stress triggers a complex cellular DNA damage response, leading to a progressive activation of p53 through a series of post-translational modifications[312,360] (Figure 12a).

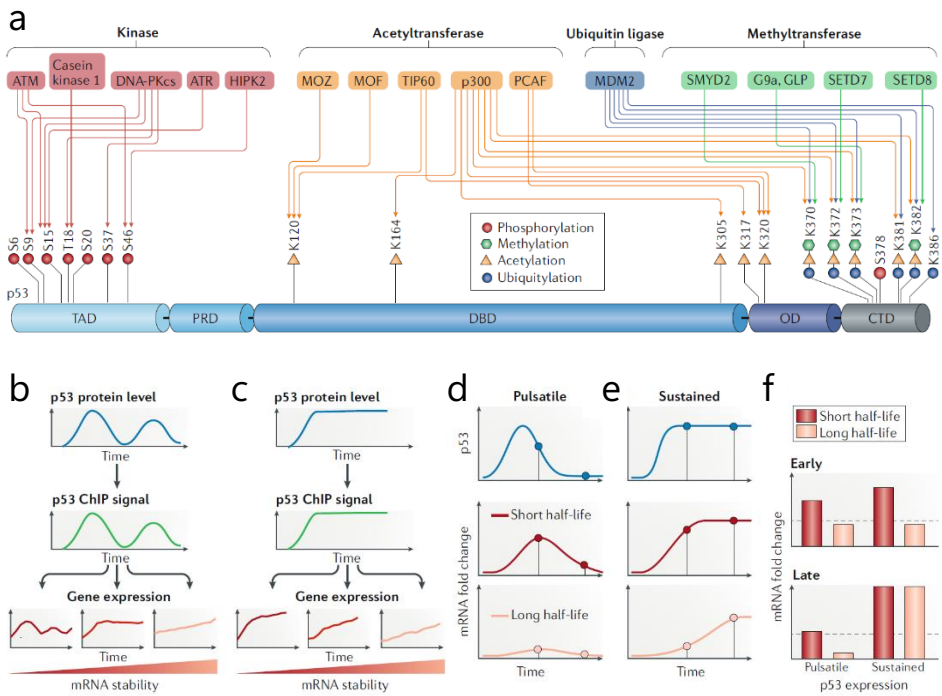

Figure 12. Regulation of p53 dynamics by post-translational modifications. (**a**) Key post-translational modifications of p53 and their corresponding enzymes. Multiple enzymes can modify a single residue, creating antagonism between different modifications. (**b**) Pulsatile p53 protein levels lead to fluctuating p53 DNA binding and result in varied gene expression dynamics that depend on the stability of the target mRNAs. (**c**) Sustained p53 expression produces more consistent mRNA expression (**d**) The expression levels of short-lived target mRNAs mirror the p53 pulses, while stable mRNAs may not rise significantly above baseline during brief periods of p53 activity. (**e**) Conversely, under sustained p53 activity, unstable mRNAs increase rapidly above their basal levels, while stable mRNAs take longer to accumulate significantly. (**f**) This panel exemplifies how the timing of measurement, p53 dynamics, and mRNA half-life influence gene expression classification post-p53 activation. Early measurements may fail to detect significant induction of stable mRNAs, while later measurements capture both unstable and stable mRNAs during sustained p53 activity, but may underestimate stable mRNA induction after p53 pulses. ChIP: chromatin immunoprecipitation; TAD: trans-activation domain, DBD: DNA-binding domain; OD: oligomerization domain; PRD: proline-rich domain. This figure was adapted from the previously published manuscript by Hafner et al.[312].

Phosphorylation at these sites facilitate the binding of lysine acetyltransferases such as p300/CBP, P/CAF, TIP60, leading to the acetylation of p53 at particular residues such as Lys320[361–365]. These modifications are crucial for stabilizing p53 by decreasing its interaction with MDM2, allowing p53 to accumulate in the nucleus and induce the transcription of cell cycle arrest (e.g. *CDKN1A*, *GADD45A*) and DNA damage repair genes (e.g. *XPC*, *DDB2*)[312].

Despite these activating modifications, p53 also induces the expression of its negative feedback regulators, MDM2 and PPM1D (also known as WIP1), which are responsible for attenuating the p53 response, thereby creating a dynamic pulsatile pattern of p53 activation[312,360]. In cases of severe or irreparable DNA damage, p53 undergoes additional phosphorylation at Ser46, a process primarily mediated by HIPK2 and ATM[366–369]. Notably, MDM2-mediated degradation of HIPK2 inhibits p53 phosphorylation at Ser46, thereby regulating the balance between cell survival and apoptosis and ensuring that pro-apoptotic signals are restrained unless a complete apoptotic response is required[370]. Phosphorylation at Ser46 enhances subsequent acetylation at multiple residues (e.g. Lys120, Lys373, and Lys382) leading to increased p53 concentration and amplified activation of apoptosis-related genes (e.g., *BAX*, *NOXA1*, *PUMA*)[312,371–373]. The different dynamics of p53 activation – whether it is transient (pulsatile) or sustained – are therefore crucial determinants of cell fate[312,374] (Figure 12b). Pulsatile and sustained p53 activity led to the induction of cell cycle arrest and DNA damage, but only sustained activation led to apoptosis and senescence[375].

Targeting the MDM2-p53 axis, particularly through the use of MDM2 inhibitors, represents a highly promising strategy for enhancing the efficacy of conventional cancer therapies[304,319,320]. MDM2 inhibitors work by stabilizing and activating p53 WT, effectively preventing its degradation and thereby amplifying its tumour-suppressive functions without introducing additional genotoxic stress[304]. The combination of MDM2 inhibitors with DNA-damaging agents can promote a more robust and sustained activation of p53 by disrupting the MDM2-mediated negative feedback loop that normally limits p53 activity[312]. This disruption can convert the naturally pulsatile activation of p53 into a sustained response, thereby enhancing the transcriptional activation of genes involved in apoptosis and potentially reducing the likelihood of resistance associated with single-agent therapies[304,319].

Alkylating agents

Alkylating agents, such as cyclophosphamide, ifosfamide, and temozolomide (TMZ), constitute a class of reactive chemicals that covalently attach alkyl groups to DNA, leading to the formation of DNA strand cross-links[376]. These cross-links impede critical cellular processes such as DNA replication and transcription, ultimately leading to cell death[377]. However, the therapeutic efficacy of these agents can be compromised by the tumour cells' ability to repair DNA damage, which limits their overall effectiveness[376,378].

Despite the wide range of alkylating agents available, research involving MDM2 inhibitors has largely focused on enhancing the efficacy of TMZ in neural tumours. For example, the combination MDM2 inhibitors such as brigimadlin and nutlin-3a with TMZ has been shown to improve survival in orthotopic glioblastoma xenograft models[379,380]. Similarly, the therapeutic efficacy of TMZ has been further enhanced when combined with idasanutlin in p53 WT NB models[381]. The combination of TMZ with idasanutlin not only enhanced tumour suppression but also promoted the activation of apoptosis-related genes, underscoring the potential of this strategy to overcome resistance mechanisms and improve therapeutic outcomes in neural tumours.

Platinum based drugs

Platinum-based chemotherapeutics, such as cisplatin, carboplatin, and oxaliplatin act by forming covalent bonds between DNA nucleobases, creating inter-strand, intra-strand, and DNA-protein cross-links[382,383]. These cross-links, mediated by platinum-containing moieties, result in DNA bending and disrupt essential processes such as DNA replication and transcription[384–386]. However, the effectiveness of platinum-based agents can be limited by the tumour cells' ability to repair these DNA lesions and evade apoptosis, contributing to the development of resistance[387]. Recent studies have explored the combination of platinum-based drugs with MDM2 inhibitors to overcome resistance mechanisms[319]. For instance, the combination of cisplatin with nutlin-3a has shown synergistic effects in p53 WT sarcoma cell lines, preserving antitumor efficacy while reducing genotoxic side effects[388]. Similarly, this combination has also enhanced cisplatin-induced cytotoxicity in nasopharyngeal carcinoma cells[389]. In p53 WT NB cells, the combination of cisplatin with idasanutlin significantly increased apoptosis, while in ovarian cancer cells, this combination increased p53 activation, further promoted apoptosis, and induced cell cycle arrest[390,391]. Additionally, the combination of navtemadlin with cisplatin and carboplatin has significantly enhanced antitumor efficacy in several cancer cell lines and *in vivo* mouse models while MI-219 has demonstrated improved growth inhibition in p53 WT cancer cell lines in combination with oxaliplatin[392,393]. Notably, alrizomadlin is currently in clinical trials in combination with carboplatin for salivary gland carcinoma (NCT03781986)[394]. This ongoing trial underscores the promise of combining MDM2 inhibitors with platinum-based therapies as a strategy to address the challenge of treatment resistance and optimize treatment regimens.

Antimetabolites

Antimetabolites are synthetic analogues of naturally occurring molecules that interfere with key biochemical pathways necessary for cell division and survival[395]. Many of the antimetabolites used in cancer treatment resemble nucleotides, enabling them to block nucleotide synthesis or become integrated into DNA strands[396]. This disrupts DNA replication and repair processes, causing errors and hindering the proliferation of cancer cells[396,397]. Antimetabolites are widely utilized in cancer treatment and are also being investigated in combination with MDM2 inhibitors in preclinical and clinical studies.

For example, fludarabine, a pyrimidine nucleoside analogue, has shown synergistic effects with nutlin-3a, enhancing p53 activation and promoting apoptosis in p53 WT chronic lymphocytic leukemia cells[398]. Additional studies have explored other pyrimidine analogues in combination with MDM2 inhibitors, including 5-fluorouracil plus CGM097[399], and gemcitabine plus MI-63[399]. In the clinical setting, a phase I trial (NCT01635296) evaluated the combination of RG7112 with cytarabine for AML patients[400]. This regimen yielded promising results, including CRs in elderly and heavily pretreated patients who had been refractory to prior cytarabine-based regimens. Pharmacodynamic analyses revealed activation of the p53 pathway, as evidenced by increased expression of *MIC-1* and *MDM2*[400]. More recently, the combination of cytarabine with idasanutlin has been evaluated in a phase III trial (NCT02545283) for R/R AML patients. However, despite an improvement in overall response rate compared to cytarabine alone, the addition of idasanutlin did not enhance OS or CR rates[401]. Furthermore, an ongoing phase I trial (NCT03041688) is assessing the combination of decitabine with navtemadlin for AML patients.

Topoisomerase inhibitors

Topoisomerases, classified into type I (TOP1) and type II (TOP2), are enzymes that regulate DNA topology during essential cellular processes, including replication, transcription, recombination, and chromosome segregation[402,403]. As DNA undergoes supercoiling during these processes, topoisomerases alleviate the torsional stress, allowing replication and transcription machinery to proceed efficiently[404,405]. Given their central role in DNA metabolism, TOP1 and TOP2 have become important therapeutic targets in cancer treatment[402,406]. Inhibiting these enzymes disrupts their function, leading to the accumulation of DNA damage, particularly in rapidly dividing cancer cells, where replication stress is already elevated[407,408].

Topoisomerase inhibitors are categorized based on their specificity for either TOP1 or TOP2, each with a distinct mechanism of action[409–411]. TOP1 inhibitors, such as topotecan and irinotecan, prevent the religation of DNA after TOP1 introduces transient single-strand breaks (SSBs) to alleviate supercoiling. These SSBs can then be converted into double-strand breaks (DSBs) during replication, ultimately leading to apoptosis[410]. In contrast, TOP2 inhibitors, such as etoposide and doxorubicin, interfere with the DNA breakage and re-ligation process performed by TOP2[411]. These inhibitors stabilize the TOP2-DNA complex after the enzyme has introduced DSBs but before the re-ligation step can occur[411]. This stabilization prevents the re-ligation of the breaks, leading to the accumulation of persistent DSBs. The unresolved DSBs ultimately result in increased DNA damage and cytotoxicity, promoting cell death[411,412].

Tumour cells that overexpress MDM2 often exhibit reduced DNA DSBs in response to TOP2 inhibitors and resistance to treatment[413]. MDM2 inhibitors can counteract this protective effect by disrupting the interaction between MDM2 and NBS1, a crucial component of the MRE11-RAD50-NBS1 DNA repair complex[414]. This disruption delays the repair of TOP2-induced DSBs, leading to the accumulation of unrepaired DNA damage. Consequently, MDM2 inhibitors have been shown to synergize with TOP2 inhibitors, enhancing their cytotoxic effects and promoting more effective cancer cell death[414]. For instance, the combination of etoposide with nutlin-3a has resulted in increased activation of effector caspases, thereby promoting apoptosis in pancreatic cancer cells[414]. Additionally, doxorubicin has been tested in combination with both navtemadlin and nutlin-3a in several tumours, further highlighting the therapeutic potential of combining TOP2 inhibitors with MDM2 antagonists for more effective cancer treatments[392,414,415].

Preclinical studies have also supported the effectiveness of combining MDM2 inhibitors with TOP1 inhibitors. topotecan, for example, has been shown to synergize with idasanutlin in p53 WT NB cells[390], while irinotecan combined with navtemadlin has demonstrated improved therapeutic efficacy compared to monotherapy in colorectal adenocarcinoma[392]. However, despite promising preclinical results that demonstrate the synergistic potential of combining TOP1 or TOP2 inhibitors with MDM2 inhibitors, there are currently no clinical trials investigating this combination therapy.

Ionizing radiation

Ionizing radiation (IR) is a common treatment modality in cancer therapy, frequently administered alone or in combination with chemotherapy drugs[416]. IR affects DNA through direct damage, such as causing DNA SSBs and DSBs, or indirectly by generating ROS[417,418]. These ROS, in turn, can lead to various DNA alterations, including abasic sites, DNA adducts, SSBs, DSBs, DNA-protein crosslinks, base oxidation, and base deamination[419,420].

Research has demonstrated that IR can upregulate MDM2 expression in a p53-dependent manner, prompting studies into combining IR with MDM2 inhibitors to enhance p53 activity[421,422]. For example, nutlin-3a has been shown to induce senescence and increase radiosensitivity in p53 WT laryngeal carcinoma cells[423]. Similarly, nutlin-3a sensitizes p53 WT lung cancer cells to radiation, leading to cell cycle arrest and apoptosis[424]. This approach has also shown promise in glioblastoma, where it increased apoptosis and senescence while improving the radiation response *in vitro*[425]. Moreover, alrizomadlin has been shown to sensitize p53 WT gastric cancer cells to radiation[426], while the combination of navtemadlin and IR resulted in significant tumour growth inhibition in p53 WT adenoid cystic carcinoma PDXs[427]. Currently, navtemadlin is being evaluated in clinical trials in combination with IR for STS patients (NCT03217266). Preliminary results indicate that neoadjuvant navtemadlin, administered concurrently with standard-dose preoperative radiation therapy, is well tolerated in patients with p53 WT STS[428]. A daily oral dose of 120 mg of navtemadlin, administered five days per week, has been recommended for future trials involving radiation therapy for extremity STS[428].

DNA damage response agents

PARP enzymes play a critical role in the repair of SSBs in DNA by facilitating the recruitment of DNA repair proteins to sites of damage[429–431]. Upon recognizing DNA damage, PARP enzymes bind to the site and catalyse the addition of poly-ADP ribose chains to target proteins, which subsequently attracts additional repair factors to mediate the repair process[432,433]. PARP inhibitors, by blocking the activity of these enzymes, prevent the effective repair of SSBs, resulting in the persistence of damage[430,433]. If left unrepaired, these SSBs progress to more deleterious DSBs, which are typically repaired via homologous recombination (HR), a mechanism dependent on BRCA1 and BRCA2 proteins[434–436].

In normal cells, even with PARP inhibition, DSBs can be efficiently repaired through HR, allowing cell survival. However, in cancer cells harbouring BRCA1 or BRCA2 mutations, the HR repair pathway is defective, and the accumulation of unrepaired DSBs becomes lethal to the cell[437,438]. Additionally, other tumours, including EWS, certain types of prostate cancer, and small cell lung cancer, exhibit increased sensitivity to PARP inhibitors despite having an apparently intact HR pathway[439,440]. In these HR-intact tumours, the efficacy of PARP inhibitors may involve alternative mechanisms, potentially related to high levels of replication stress[439]. Interestingly, some preclinical studies have recently uncovered new targets that can induce a "chemical HRD" phenotype, thereby overcoming PARP inhibitor resistance[439,441–444].

Up to now, only one preclinical study has explored the combination of MDM2 and PARP inhibitors. This study demonstrated that the combination of idasanutlin with rucaparib was particularly effective in p53 WT ovarian cancer cell lines, inducing both apoptosis and cell cycle arrest[445]. Importantly, the observed synergistic effects were evident in both PARP-sensitive and PARP-resistant cell lines, suggesting that MDM2-p53 inhibition may potentially resensitize cells to PARP inhibition *in vitro*[445]. These findings highlight the need for further investigation into the potential of MDM2/PARP inhibitor combinations as a strategy to enhance therapeutic responses across various cancer types.

1.3.2.2. Apoptosis inducers

The activation of p53 initiates apoptosis by disrupting the balance between pro-apoptotic and anti-apoptotic proteins, either through direct interactions or by inducing mitochondrial membrane permeabilization[446–448]. Effective apoptosis requires sustained p53 activity, which enhances the transcription of pro-apoptotic factors such as BAX, NOXA, and PUMA[312,360,374,449]. In addition, p53 directly engages with multidomain members of the BCL-2 family to induce mitochondrial outer membrane permeabilization, thus contributing to the intrinsic apoptosis pathway[450]. However, MDM2 inhibitors typically induce a pulsatile p53 activity, leading to cell cycle arrest rather than optimal apoptosis[319]. Moreover, the overexpression of anti-apoptotic proteins from the BCL-2 family, such as BCL-2, BCL-xL, and MCL-1, can undermine the pro-apoptotic effects of p53[451–453]. Consequently, effective strategies to enhance the pro-apoptotic potential of MDM2 antagonists may include the down-regulation of these anti-apoptotic proteins or the augmentation of pro-apoptotic signaling pathways.

Research on MDM2 inhibitors in combination with anti-apoptotic agents has predominantly focused on their synergy with BH3 mimetics, particularly venetoclax, a selective BCL-2 inhibitor. Preclinical studies have demonstrated that dual targeting of MDM2 and BCL-2 provides superior efficacy compared to monotherapy across various malignancies, including p53 WT AML[454,455], NB[456], breast cancer[457], and ovarian and endometrioid carcinomas[458]. These promising preclinical outcomes have prompted their investigation in clinical trials. For example, a phase Ib study (NCT02670044) evaluating the combination of venetoclax with idasanutlin in patients with R/R AML reported manageable safety profiles and encouraging preliminary efficacy, supporting further exploration of this therapeutic approach[459]. This combination has recently been assessed in conjunction with chemotherapy in a phase I/II study (NCT04029688) involving paediatric and young adult patients with R/R acute leukemia or solid tumours. Additionally, another phase I/II trial (NCT03135262) examined the combination of idasanutlin, venetoclax, and obinutuzumab (anti-CD20) in patients with R/R non-Hodgkin lymphoma[460]. However, despite initial feasibility and promise, this combination was ultimately discontinued due to the emergence of alternative therapeutic strategies. Similarly, siremadlin has demonstrated promising preliminary antileukemic activity in combination with venetoclax in a phase Ib trial (NCT03940352) involving patients with R/R AML[461]. Furthermore, a clinical study (NCT05155709) is currently investigating the triple combination of siremadlin, venetoclax, and azacytidine, with results anticipated in the near future[462]. Beyond the combination of MDM2 inhibitors with venetoclax, other therapeutic strategies involving BH3 mimetics, such as navitoclax[463,464], as well as combinations with XIAP inhibitors[465–467] or TRAIL agonists[468,469], are also under investigation.

1.3.2.3. Targeted therapies of pro-survival signalling pathways

Tyrosine kinase inhibitors

Tyrosine kinase receptors are critical for the initiation, transmission, and regulation of numerous cellular pathways related to cell proliferation and survival, including the JAK-STAT, PI3K-AKT-mTOR, and RAS-MAPK pathways[470,471]. Currently, numerous tyrosine kinase inhibitors are being evaluated in clinical trials, sometimes in combination with MDM2 antagonists. For instance, the combination of siremadlin with pazopanib, a multi- kinase inhibitor that targets VEGFR, PDGFR, and c-KIT, is being evaluated in clinical trials for patients with p53 WT advanced or metastatic STS (NCT05180695).

Two additional clinical studies, a phase Ib/2 (NCT04485260) and a phase III (NCT06479135), are evaluating the combination of navtemadlin with ruxolitinib, a JAK inhibitor, in patients with myelofibrosis who have exhibited a suboptimal response to ruxolitinib monotherapy[472]. In the preclinical setting, combined ALK and MDM2 inhibition has shown synergistic antitumor activity in ALK-aberrant NB cell lines and PDX models[473,474]. The combination of MDM2 and FGFR inhibitors has also demonstrated a highly synergistic effect on both cell viability and apoptosis across liposarcoma cell lines[475]. The combination of milademetan with the FLT3 tyrosine kinase inhibitor quizartinib demonstrated synergistic antileukemic activity in preclinical models of FLT3-ITD-mutant AML[476]. However, the phase I study (NCT03552029) evaluating this combination was ultimately terminated due to a business decision by the sponsor. Other RTK inhibitors tested preclinically in combination with nutlin-3a include ibrutinib in leukemia[477,478], and sorafenib in AML and renal cell carcinoma[479,480].

MAPK and PI3K-AKT pathway inhibitors

The crosstalk between the p53 pathway and the PI3K/mTOR/AKT and MEK/ERK signaling pathways is crucial for regulating cell fate, particularly in determining whether a cell undergoes apoptosis or survives[481–483]. Given that alterations in p53 and these signaling pathways are common in human cancers, targeting these pathways simultaneously represents a promising therapeutic strategy[484,485].

Preclinical studies in AML models have demonstrated that combining MDM2 and MEK inhibitors produces synergistic effects by activating pro-apoptotic proteins PUMA and Bim, regulating p53 localization, and upregulating target genes to promote apoptosis over proliferation[486,487]. Similarly, dual inhibition of MDM2 and MEK has shown synergy in KRAS mutant non-small cell lung cancer and colorectal cancers, leading to increased expression of PUMA and BIM, apoptosis *in vitro*, and tumour regression *in vivo*[488]. This combination has also proven effective in PDXs of p53 WT MDM2-amplified lung adenocarcinoma[489]. Furthermore, combining MDM2 inhibitors with BRAF and/or MEK inhibitors has shown efficacy in PDXs of BRAF mutant, p53 WT metastatic melanoma[490]. Notably, the addition of MEK inhibitors to continued idasanutlin treatment effectively overcame acquired resistance to MDM2 inhibition in glioblastoma, both *in vitro* and *in vivo*[491]. These encouraging results have led to several clinical trials exploring the therapeutic potential of combining MDM2 with MEK and/or BRAF inhibitors across various cancer types.

In a phase Ib study (NCT02016729) involving patients with R/R AML, the combination of navtemadlin and the MEK inhibitor trametinib exhibited a safety profile similar to that of the individual agents and showed early evidence of antileukemic activity[492]. Another phase I clinical trial (NCT02110355) evaluated navtemadlin with trametinib and dabrafenib for metastatic melanoma. Although the triple combination had a favourable pharmacokinetic profile and resulted in objective responses, it did not provide additional clinical benefit compared to trametinib plus dabrafenib alone[493]. Recently, siremadlin has also been evaluated in combination with trametinib for treating advanced or metastatic RAS/RAF mutant and p53 WT colorectal carcinomas (NCT03714958), but results from this study have not yet been reported.

In addition to RAF and MEK inhibitors, combinations involving PI3K-AKT-mTOR pathway inhibitors have yielded promising preclinical results. Specifically, the combination navtemadlin and CGM-097 with PI3K inhibitors such as buparlisib, pictilisib, and alpelisib demonstrated a moderate to strong synergistic effect in AML cell lines[494]. Furthermore, the combination of idasanutlin with dactolisib (BEZ235), a dual PI3K and mTOR inhibitor, produced a robust therapeutic response in liposarcoma[495]. Additionally, in another preclinical study involving various p53 WT cell lines, navtemadlin exhibited broad synergy with dactolisib, as well as with other PI3K inhibitors like GDC-0941, the AKT inhibitor MK-2206, and the mTOR inhibitor AZD8055[496].

Cyclin-dependent kinase inhibitors

Alterations in cell cycle control are common in various human cancers, making cyclin-dependent kinase (CDK) inhibitors a crucial class of anticancer drugs. In cancer cells, persistent activation of CDK regulatory pathways often bypasses essential cell cycle checkpoints, leading to uncontrolled growth and proliferation. In preclinical studies, the combination of idasanutlin with palbociclib significantly enhanced apoptosis *in vitro* and improved tumour volume regression in dedifferentiated liposarcoma *in vivo*[497]. In a phase Ib/II clinical study (NCT02343172) of locally advanced or metastatic liposarcoma, the combination of siremadlin with the CDK4/6 inhibitor ribociclib exhibited a manageable safety profile and preliminary evidence of antitumor activity[498]. Additional studies are currently ongoing (NCT04116541) to investigate the combination of MDM2 and ribociclib in patients with advanced/metastatic p53 WT solid tumours who meet specific criteria, including amplification of CDK6 and/or CDK4, homozygous deletion of CDKN2A, amplification of CCND1 and/or CCND3, and no more than a single copy loss of RB1.

1.3.2.4. Immunotherapies and other anti-cancer agents

Immunotherapies

Patients with MDM2-amplified tumours often exhibit poor clinical outcomes and hyperprogressive disease when treated with single-agent PD-1/PD-L1 immune checkpoint inhibitors[499]. This reduced efficacy is partially attributed to the role of MDM2 and p53 in regulating essential immune processes, such as antigen presentation, interferon responses, IL-15 production, and TRAIL receptor expression in cancer cells[500] (Figure 13). As a result, there is growing interest in evaluating the potential benefits of combining MDM2 inhibitors with various immunotherapies to overcome these limitations and improve patient outcomes.

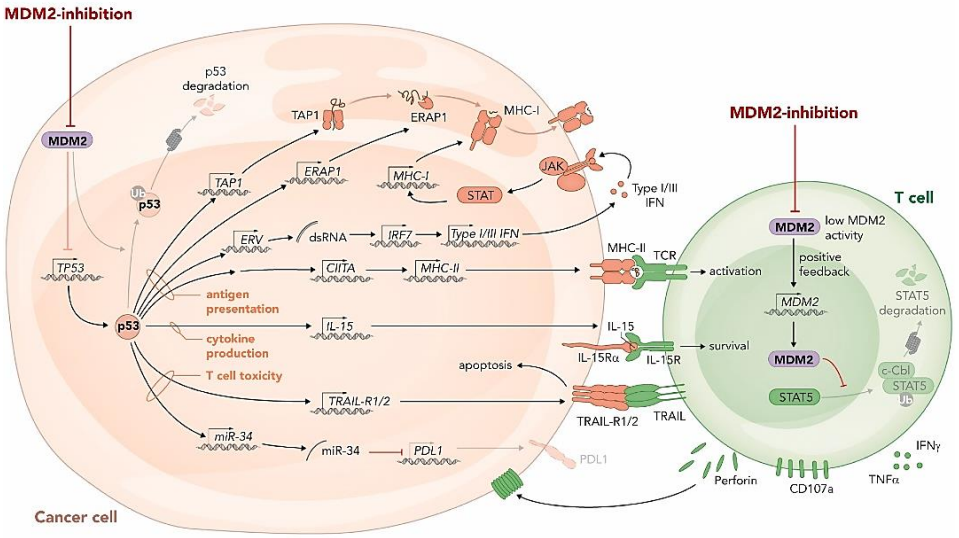

Figure 13. Proposed mechanisms by which MDM2-p53 axis influences antitumor immunity. Inhibition of MDM2 and the resulting elevation of p53 levels enhance the expression of MHC class I and II molecules, and trigger the release of double-stranded RNA, which stimulates type 1 and 3 interferon responses. This process also increases IL-15 production and TRAIL-R1/2 transcription in malignant cells. Additionally, MDM2 inhibition or deletion in effector T cells leads to increased production of perforin and other cytotoxic molecules.

Currently, siremadlin is being evaluated in a phase Ib/II (NCT05447663), both as a monotherapy and in combination with donor lymphocyte infusions, for patients with high-risk AML following allogeneic hematopoietic cell transplantation. Additionally, siremadlin is being tested in a phase Ib study (NCT03940352) in combination with an anti-TIM3 antibody for patients with AML or myelodysplastic syndrome (NCT03940352).

MDM2 inhibition is also being investigated in combination with various immunotherapies across different solid tumours. For instance, a phase I dose-escalation study (NCT03611868) of alrizomadlin with pembrolizumab (anti-PD1) in metastatic melanoma and advanced solid tumours demonstrated objective clinical responses in a subset of patients without dose-limiting toxicities[501]. Likewise, a phase Ib/II trial (NCT04785196) is exploring the same combination in patients with liposarcoma and other advanced solid tumours. Moreover, the combination of spartalizumab (anti-PD1) with siremadlin is being evaluated in a phase I study (NCT02890069) across multiple solid tumour types, including colorectal, non-small cell lung, breast, and renal cell carcinomas. Additionally, a phase II trial (NCT03964233) is assessing brigimadlin in combination with ezabenlimab (anti-PD-1), with or without BI-754111 (anti-LAG-3), in solid tumours, with early data suggesting manageable safety profiles and initial signs of anti-tumour activity[502,503]. These investigations highlight a broader trend in oncology, where MDM2 inhibitors are being increasingly explored in combination with various immunotherapeutic strategies across diverse cancer types. This trend reflects a growing interest in addressing the limitations of single-agent treatments and improving patient outcomes across a range of tumour types.

Other anti-cancer agents

Given that p53 degradation is mediated through the proteasome, there is significant interest in exploring the combined use of MDM2 inhibitors and proteasome inhibitors to potentially enhance p53 WT levels[504,505]. In this regard, the clinical potential of this strategy is being investigated through trials examining the combination of idasanutlin with ixazomib in the treatment of R/R multiple myeloma (NCT02633059).

Furthermore, the combination of protein kinase C (PKC) and MDM2 inhibition has shown synergistic antiproliferative effects and tumour regression in xenograft models of uveal melanoma, a malignancy marked by hyperactivation of the PKC/MAPK pathways[506]. To further explore this promising therapeutic approach, a clinical trial was initiated to evaluate the efficacy of this dual inhibition strategy in patients with metastatic uveal melanoma (NCT02601378). However, the results for the combination arm have not yet been reported.

Beyond these examples, other less frequently studied combinations with MDM2 inhibitors have also demonstrated the versatility and potential of these agents in overcoming resistance mechanisms and enhancing antitumor efficacy[319]. As research progresses, the integration of MDM2 inhibitors into combination therapies, may offer new avenues for treating a wide range of malignancies. This approach could address the limitations of single-agent therapies and potentially improve patient outcomes, particularly in paediatric sarcomas, where the application of targeted therapies has been less extensively studied compared to adult cancers.

2. Hypothesis and Objectives

Background and rationale

RMS is a highly aggressive STS, primarily diagnosed during childhood and adolescence, resulting from genetic alterations during the myogenic differentiation process[129]. In contrast to many adult tumours, p53 loss-of-function mutations in RMS are uncommon and detected in only ~5% of cases[134]. However, tumour cells may employ alternative mechanisms to disrupt normal p53 function, such as the overexpression and/or overactivation of MDM2, thereby ensuring their survival and proliferation[311]. MDM2 acts as an E3 ubiquitin ligase of p53, playing a crucial role in its negative regulation through ubiquitin-mediated proteasomal degradation[299,302,507]. Under normal circumstances, MDM2 ubiquitinates and targets p53 for proteasomal degradation[303]. However, in response to stimuli such as excessive proliferation or DNA damage, MDM2-mediated ubiquitination of p53 is suppressed, allowing p53 to activate a plethora of genes and proteins aimed at cell cycle arrest, DNA repair, and/or apoptosis induction[300,321,322].

Thus, the disruption of MDM2-p53 interaction using small-molecules represents a promising strategy for treating p53 WT tumours due to its ability to block p53 degradation, increase p53 levels and potentially activate its tumour suppressor activities[304,319,508]. In the past decade, multiple compounds inhibiting the MDM2-p53 interaction have been synthesized, demonstrating efficacy in preclinical studies involving p53 WT tumours[320,350]. However, early-phase clinical trials have revealed limited effectiveness of these compounds when used alone, underscoring the necessity to explore combinations with other drugs to enhance their antitumoral effects[320,355]. On this matter, various combination strategies involving MDM2 inhibitors and chemotherapies or other targeted therapies are being explored in both preclinical studies and clinical trials to overcome the mild-to-moderate therapeutic effects that many of these drugs have shown when administered as monotherapy[304,319].

Hypothesis

We hypothesize that disrupting the MDM2-p53 interaction will restore p53 tumour-suppressive functions, leading to reduced cell proliferation and increased cell death in p53 WT RMS. Additionally, we also hypothesize that the combination of MDM2 inhibitors with selected therapeutic agents will enhance their antitumor efficacy in p53 WT RMS cells through putative additive/synergistic mechanisms.

Objectives

1. Investigate the differential drug responses of p53 wild-type (WT) vs. p53-mutant (MUT) RMS cells to MDM2 inhibitors
   - Conduct a comprehensive drug screening to evaluate the sensitivity of p53 WT and p53 MUT RMS cells to various MDM2 inhibitors *in vitro*.
   - Analyse the expression of p53 pathway genes that may serve as biomarkers of response and efficacy of MDM2 inhibitors in RMS models.
2. Evaluate the synergistic efficacy of combining MDM2 inhibitors with other therapeutic agents in p53 WT RMS cells *in vitro* and *in vivo*
   - Perform a comprehensive drug combination screening to identify synergistic interactions between MDM2 inhibitors and other therapeutic agents.
3. Validate the most promising drug combinations and investigate the molecular mechanisms driving the potential additive or synergistic effects.

3. Materials and Methods

3.1. Cell line culture

Seven different RMS cell lines were used in this study: RH18, RH36, CW9019, RD, RH4, and RH28. All RMS cell lines were cultured in adhesion in Minimum Essential Medium with Earle's Salts (MEM, Biowest) supplemented with 10% foetal bovine serum (FBS, Biowest), 2 mM L-glutamine (Biowest), 1 mM sodium pyruvate (Biowest), 1X MEM non-essential aminoacids (Biowest), 100 U/mL penicillin, and 100 µg/mL streptomycin (Biowest). Cultures were maintained at 37 °C in a 5% CO_2 atmosphere and were regularly tested for mycoplasma contamination. Molecular features of each RMS cell line are detailed in Table 7.

Table 7. RMS cell line molecular features

Cell lines	*RRID*	*Fusion*	*TP53 status*	*Other molecular features*
RH18	CVCL_1659	Negative	Wild-type	MDM2 amplification
RH36	CVCL_M599	Negative	Wild-type	$HRAS^{Q61K}$, $TP53BP1^{P1565fs}$
CW9019	CVCL_N820	PAX7-FOXO1	Wild-type	CDKN2A loss, $ATRX^{N104S}$
RH28	CVCL_8752	PAX3-FOXO1	$TP53^{G187C}$	$CDKN2A^{R29*}$
RH4	CVCL_5916	PAX3-FOXO1	$TP53^{P152fs}$	$ARID1A^{S1001del}$
RD	CVCL_1649	Negative	$TP53^{R248W}$	$NRAS^{Q61H}$, $NF1^{E977*}$

Before reaching confluence, cells were washed with phosphate-buffered saline (PBS, Cytiva), detached using trypsin-EDTA (Thermo Fisher Scientific), collected in fresh medium, and centrifuged at 1500 rpm for 3 minutes. The pelleted cells were then resuspended and seeded into new culture dishes or flasks with fresh medium. This procedure was also used for cell counting. For counting, pelleted cells were resuspended in an appropriate volume, and 10 µl of the cell suspension were mixed with 10 µl of 0.4% trypan blue (GE Healthcare). Subsequently, 10 µl of the cell suspension was loaded onto Cell Counting slides (NanoEnTek), and total and viable cell counts were determined using the Cell Counter EVE (NanoEnTek). For cryopreservation, pelleted cells were resuspended in FBS containing 5% dimethyl sulfoxide (DMSO, Sigma-Aldrich) and slowly frozen using an isopropanol freezing container (Thermo Fisher Scientific) at -80 ºC, prior to storage in liquid nitrogen. For resuscitation, frozen cells were thawed by a fast warming in a 37 ºC water bath, diluted into pre-warmed growth medium, and centrifuged. The thawed cells were then resuspended and plated at high density to optimize recovery. Details of all reagents and resources used for cell culture are provided in Table 8.

Table 8. Reagents and resources used for cell culture

Cell culture

Reagent or Resources	*Reference*	*Source*
MEM	#L0440	Biowest
FBS	#S1810	Biowest
L-glutamine 100X, 200mM	#X0550	Biowest
Sodium pyruvate 100X, 100mM	#L0642	Biowest
MEM non-Essential AA 100X	#X0557	Biowest
Penicillin/Streptomycin 100X	#L0022	Biowest
PBS, 10X	#SH30258.02	Cytiva
Trypsin-EDTA	#25200072	Thermo Fisher Scientific
Trypan blue	#SV30084.01	GE Healthcare
EVE™ Cell counting slides	#EVS-050	NanoEnTek
EVE™ Automated cell counter	#E1000	NanoEnTek
DMSO	#D8418	Sigma-Aldrich, Merck
Isopropanol	#I9516	Sigma-Aldrich, Merck
Mr. Frosty™ freezing container	#5100-0001	Thermo Fisher Scientific

Headquarters: Biowest (Nuaillé, France), Cytiva (Marlborough, MA, USA), Thermo Fisher Scientific (Waltham, MA, USA), GE Healthcare (Chicago, IL, USA), NanoEntek (Seoul, South Korea), Sigma-Aldrich (St. Louis, MO, USA).

3.2. Cell proliferation analysis and drug screenings

Cell proliferation assays were performed by seeding RH18, RH36, CW9019, RH28, RH4, or RD in p96-well plates (Thermo Fisher Scientific). The number of cells was previously optimized to ensure an exponential growth at a constant rate during the assays (Table 9). After 24 hours, compounds were diluted in medium before being added to the cells at specified concentrations (Table 10).

3.2.1. Crystal violet staining

Cell proliferation was assessed by crystal violet staining. Briefly, medium was removed from 96-well plates after the treatments, and cells were washed with PBS (Cytiva). Cells were then stained with 50 µl of a 0.5% crystal violet solution (Sigma-Aldrich) in 20% ethanol (VWR) for 10 minutes at room temperature. Crystal violet excess was removed by rinsing with PBS, and the stained cells were allowed to air-dry overnight. Finally, the resulting crystals were dissolved in 50 µl of 15% acetic acid (Roth), and absorbance was measured at 590 nm in an Epoch® microplate spectrophotometer (Agilent Technologies).

Cell survival percentages were determined by normalizing the absorbance values of each condition to their respective controls within each experiment. IC_{50} values and drug combination effects were assessed at 72 hours post-treatment, while cell proliferation over time was assessed from 24 to 168 hours post-treatment.

3.2.2. Dose-response curves and synergy scoring

Dose-response curves and IC_{50} values were determined using non-linear regression analysis implemented in GraphPad Prism 6.0 (GraphPad Software). Drug combination effects were measured using the Bliss independence model[509], either implemented in Synergy Finder 2.0[510] or calculated manually. This model measures from the expected additive effect (Bliss score = 0), based on the assumption of multiplicative effects when both drugs act independently. Details of all reagents, resources, and drugs used for cell proliferation assays and drug screenings are provided on Table 11.

Table 9. Number of cells seeded per well or dish

	96-well plates		*24-well plates*	*60 mm dish*	*100 mm dish*
Cell lines	*72 h*	*Time course*	*Assays*	*Assays*	*Assays*
RH18	4×10^3	2×10^3	2.5×10^4	5×10^6	1×10^6
RH36	3×10^3	1×10^3	2×10^4	4×10^6	8×10^5
CW9019	4×10^3	2×10^3	2.5×10^4	5×10^6	1×10^6
RH28	1×10^4	-	-	1×10^6	2×10^6
RH4	2×10^3	-	-	2.5×10^5	5×10^5
RD	1.5×10^3	-	-	2×10^5	2×10^5

Table 10. Drugs and doses used

IC50			
Name	*Target*	*Doses in p53 WT*	*Doses in p53 MUT*
Siremadlin	MDM2	10 µM to 1.05 nM	65 µM to 1.05 nM
Idasanutlin	MDM2	10 µM to 1.05 nM	65 µM to 1.05 nM
Navtemadlin	MDM2	10 µM to 1.05 nM	65 µM to 1.05 nM
MI-773	MDM2	10 µM to 1.05 nM	65 µM to 1.05 nM
ME-240	MDM2/X (exp)	10 µM to 1.05 nM	
ME-242	MDM2/X (exp)	10 µM to 1.05 nM	
ME-62	MDM2/X (exp)	10 µM to 1.05 nM	
ME-258	MDM2/X (exp)	10 µM to 1.05 nM	
Olaparib	PARP	10 µM to 19.53 nM	
Actinomycin	Chemotherapy	10 nM to 0.0195 nM	
Vincristine	Chemotherapy	100 nM to 0.195 nM	

Ph. mustard	Chemotherapy	10 µM to 19.53 nM
Irinotecan	Chemotherapy	10 µM to 19.53 nM
TMZ	Chemotherapy	10 µM to 19.53 nM
Cisplatin	Chemotherapy	10 µM to 19.53 nM
Doxorubicin	Chemotherapy	10 µM to 19.53 nM
Etoposide	Chemotherapy	10 µM to 19.53 nM

Drug screenings		*Monotherapy*			*Combination*
Name	*Target*	*Dose 100X*	*Dose 10X*	*Dose 1X*	*Dose 1X*
Siremadlin	MDM2	1 µM	0.1 µM	0.01 µM	0.1 µM
Idasanutlin	MDM2	1 µM	0.1 µM	0.01 µM	-
Navtemadlin	MDM2	1 µM	0.1 µM	0.01 µM	-
MI-773	MDM2	1 µM	0.1 µM	0.01 µM	-
Linsitinib	IGF1R	10 µM	1 µM	0.1 µM	0.1 µM
Omipalisib	PI3K	1 µM	0.1 µM	0.01 µM	0.01 µM
Buparlisib	PI3K	10 µM	1 µM	0.1 µM	1 µM
Everolimus	mTOR	10 nM	1 nM	0.1 nM	1 nM
MK-2206	AKT	10 µM	1 µM	0.1 µM	1 µM
Trametinib	MEK	1 µM	0.1 µM	0.01 µM	0.1 µM
Selumetinib	MEK	1 µM	0.1 µM	0.01 µM	0.1 µM
Venetoclax	BCL2	100 nM	10 nM	1 nM	1 µM
Palbociclib	CDK4/6	10 µM	1 µM	0.1 µM	10 µM
Bortezomib	Proteasome	100 nM	10 nM	1 nM	5 nM
Vorinostat	HDAC	1 µM	0.1 µM	0.01 µM	1 µM
Olaparib	PARP	10 µM	1 µM	0.1 µM	10 µM
PTC-028	BMI1	1 µM	0.1 µM	0.01 µM	0.1 µM
Adavosertib	WEE1	1 µM	0.1 µM	0.01 µM	0.1 µM
Actinomycin	Chemotherapy	1 nM	0.1 nM	0.01 nM	0.1 nM
Vincristine	Chemotherapy	100 nM	10 nM	1 nM	10 nM
Ph. mustard	Chemotherapy	10 µM	1 µM	0.1 µM	10 µM
Cisplatin	Chemotherapy	10 µM	1 µM	0.1 µM	10 µM
Irinotecan	Chemotherapy	10 µM	1 µM	0.1 µM	1 µM
TMZ	Chemotherapy	10 µM	1 µM	0.1 µM	10 µM
Doxorubicin	Chemotherapy	10 µM	1 µM	0.1 µM	0.1 µM
Etoposide	Chemotherapy	10 µM	1 µM	0.1 µM	1 µM

Combination 5x5 matrix

Name	*Target*	*Doses*
Siremadlin	MDM2	0, 20, 40, 80, 160 nM
Olaparib	PARP	0, 1, 2, 4, 8 µM

Table 11. Reagents, resources and drugs used for cell proliferation assays and screenings

Reagent or Resource	*Reference*	*Source*
96-well plates	#130188	Thermo Fisher Scientific
PBS, 10X	#SH30258.02	Cytiva
Crystal violet	#CO775	Sigma-Aldrich, Merck
Ethanol	#20821.330	VWR
Acetic acid	#3738.2	Carl Roth
BioTek® Epoch™ Microplate Spectrophotometer	-	Agilent Technologies
Synergy Finder 2.0	-	https://synergyfinder.fimm.fi
Drugs	*Reference*	*Source*
Siremadlin	#HY-18658	MedChemExpress
Idasanutlin	#HY-15676	MedChemExpress
Navtemadlin	#HY-12296	MedChemExpress
MI-773	#HY-17493	MedChemExpress
Linsitinib	#HY-10191	MedChemExpress
Omipalisib	#HY-10297	MedChemExpress
Buparlisib	#HY-70063	MedChemExpress
Everolimus	#HY-10218	MedChemExpress
MK-2206	#HY-108232	MedChemExpress
Trametinib	#HY-10999	MedChemExpress
Selumetinib	#HY-50706	MedChemExpress
Venetoclax	#HY-15531	MedChemExpress
Palbociclib	#HY-50767A	MedChemExpress
Bortezomib	#HY-10227	MedChemExpress
Vorinostat	#ab144480	Abcam
Olaparib	#HY-10162	MedChemExpress
PTC-028	#HY-103696	MedChemExpress
Adavosertib	#HY-10993	MedChemExpress
Actinomycin D	#A13239	Adooq Bioscience
Vincristine	#HY-N0488	MedChemExpress
Ph. mustard	#HY-137316	MedChemExpress
Cisplatin	#HY-17394	MedChemExpress
Irinotecan	#HY-16562	MedChemExpress
Temozolamide	#Y0001960	Sigma-Aldrich, Merck
Doxorubicin	#D9891	Sigma-Aldrich, Merck
Etoposide	#HY-13629	MedChemExpress

Headquarters: Thermo Fisher Scientific (Waltham, MA, USA), Cytiva (Marlborough, MA, USA), Sigma-Aldrich (St. Louis, MO, USA), VWR (Radnor, PA, USA), Carl Roth (Karlsruhe, Germany), Agilent Technologies (Santa Clara, CA, USA), GraphPad Software (La Jolla, CA, USA), MedChemExpress (Monmouth Junction, NJ, USA), Abcam (Cambridge, UK), Adooq Bioscience (Irvine, CA, USA).

3.3. Cell death assay

3.3.1. Double staining with Hoechst 33342 and PI

Nuclear condensation and cell membrane permeability are key indicators for distinguishing healthy cells from apoptotic or dead cells. The Hoechst 33342 (HO) and propidium iodide (PI) double staining assay leverages the distinct biochemical properties of these dyes to differentiate cell states. HO is a cell-permeable nuclear counterstain that emits blue fluorescence upon binding to DNA, particularly AT-rich double-stranded DNA. In contrast, PI is a DNA intercalating agent that emits red fluorescence when bound to nucleic acids. Due to its membrane impermeability, PI is excluded from the nuclei of viable cells and is used to distinguish dead, necrotic, or late apoptotic cells from viable ones. In the experimental procedure, RMS cells were plated in 24-well plates and treated under specified conditions. Following treatment, cells were stained with a solution containing 5 µg/mL Hoechst 33342 (Sigma-Aldrich) and 3 µg/mL propidium iodide (PI, Sigma-Aldrich) in PBS (Cytiva). The stained cells were incubated for 15 minutes at 37 °C, and the stained nuclei were visualized and photographed using an epifluorescence microscope (Nikon). Cell counts were subsequently performed using ImageJ[511]. All reagents and resources used for HO/PI staining assays are listed on Table 12.

Table 12. Reagents and resources used for cell death assay

Cell death assays		
Reagent or Resource	*Reference*	*Source*
24-well plates	#930186	Thermo Fisher Scientific
Hoechst 33342 (HO)	#14533	Sigma-Aldrich, Merck
Propidium iodide (PI)	#537059	Sigma-Aldrich, Merck
PBS, 10X	#SH30258.02	Cytiva
Epifluorescence microscope	#2CE-MPKH-9	Nikon
Image J	-	https://imagej.net/

Headquarters: Thermo Fisher Scientific (Waltham, MA, USA), Sigma-Aldrich (St. Louis, MO, USA), Cytiva (Marlborough, MA, USA), Nikon (Tokyo, Japan).

3.4. High-content image-based assays

Cell painting is a high-content, image-based assay for morphological profiling[512]. In this approach, cells seeded in multiwell plates are treated with various compounds, subsequently fixed and imaged using a high-throughput microscope.

Approximately 2000 morphological features, including size, shape, texture, and intensity of cellular compartments and organelles, are then quantified in single cells using automated image analysis software. These morphological profiles enable the detection of subtle phenotypic changes, facilitating comparisons across different treatments, determining phenotypic effects of chemical perturbations, and identifying treatment-specific signatures. Cell painting assays were performed in collaboration with the Pharmaceutical Bioinformatics Research Group at the University of Uppsala (co-led by Dr. Jordi Carreras-Puigvert). The following materials and methods section is based on the protocol of the research group. For any further details, please see the full protocol described by Rietdijk et al.[513].

3.4.1. Cell seeding and compound treatment

Briefly, RH36 (1300 cells/well) were seeded in 24 µl volumes in 384 multiwell plates (Corning) using a Biotek Multiflo FX microplate dispenser (Agilent Technologies). The plates were incubated overnight at 37 °C in a 5% CO_2 atmosphere to allow cell attachment. Morphological changes induced by olaparib and siremadlin were assessed in both single-drug and combination experiments (Table 13). Additionally, four reference compounds were included: tetrandrine, metoclopramide, fenbendazole, and etoposide. D-Sorbitol was used as negative control and DMSO as the vehicle (all from Sigma-Aldrich). A 5X source plate containing the compounds diluted in MEM was prepared using an automated OT-2 liquid handler (Opentrons Labworks). From this source plate, 6 µl of the solution was transferred to assay plates using a Viaflo 384 electronic pipette (Integra Biosciences), with compounds achieving a final 1X concentration. Cells were then incubated for 48 h at 37 °C under 5% CO_2. Each condition was tested in three technical replicates and two biological replicates. Plate layouts were optimized with PLAID[514] to ensure even distribution of conditions.

Table 13. Drugs and doses used in high-content imaged-based assays

Single-drug		
Name	*Target*	*Doses*
Siremadlin	MDM2	0.02 µM to 1.6 µM
Olaparib	PARP	0.05 µM to 10 µM
Tetrandrine	Calcium channels	1 µM, 3 µM, and 10 µM
Metoclopramide	D2, 5HT3, 5HT4	10 µM, 30 µM, 100 µM
Fenbendazole	B-tubulin	0.3 µM, 1 µM, and 3 µM
Etoposide	DNA topoisomerase II	0.3 µM, 1 µM, and 3 µM
D-Sorbitol	-	1 µM, 10 µM, and 30 µM

Combined

Compound (steady)	*Doses*	*Compound (increasing)*	*Doses*
Siremadlin	0.04 and 0.08 µM	Olaparib	0.05 µM to 10 µM
Olaparib	3, 4 and 8 µM	Siremadlin	0.02 µM to 1.6 µM

3.4.2. Cell painting

Cell painting experiments were conducted according to the protocol described by Bray et al.[512] with minor modifications. After 48 hours of chemical exposure, cells were washed three times with 80 µl PBS (Thermo Fisher Scientific) using a Biotek 405 LS microplate washer (Agilent Technologies), leaving 10 µl in the wells to minimize cell disturbance. Subsequently, 35 µl of MitoTracker (Thermo Fisher Scientific) was added to a final concentration of 900 nM, and the cells were incubated for 30 min at 37 °C in a humidified atmosphere with 5% CO_2. After removing the MitoTracker solution, cells were washed again three times with 80 µl PBS and fixed with 50 µl of 4% paraformaldehyde (Histolab) for 20 minutes. Following fixation, cells were washed three times, and permeabilized with 50 µl of 0.1% Triton X-100 (Cytiva) for 20 min. After removing Triton X-100, cells were washed three additional times. Subsequently, a staining mixture (20 µl per well) was added, achieving final well-concentrations of 1 µg/ml Hoechst 33342, 15 µg/ml Wheat Germ Agglutinin, 10 µl/ml Phalloidin, 4 µM SYTO 14, and 80 µg/ml Concanavalin A (all from Thermo Fisher Scientific), and the cells were incubated for 20 minutes. Finally, plates were washed three times, sealed, and stored at 4 °C, protected from light until image acquisition.

3.4.3. Image acquisition and processing

Fluorescence microscopy was performed using a high throughput ImageXpress Micro XLS (Molecular Devices) microscope equipped with a 20X objective and laser-based autofocus. Specific offsets were established and maintained throughout the experiment. For each well, six sites were imaged using five fluorescence channels to capture various cellular compartments: DNA (Hoechst), mitochondria (MitoTracker), Golgi apparatus and plasma membrane (Wheat Germ Agglutinin), F-actin (Phalloidin), nucleoli and cytoplasmic RNA (SYTO 14), and the endoplasmic reticulum (Concanavalin A). The excitation wavelengths (λ_{EX}) were set as follows: 377/50 nm for Hoechst, 628/40 nm for MitoTracker, 562/40 nm for Phalloidin and Wheat Germ Agglutinin, 531/40 nm for SYTO 14, and 482/35 nm for Concanavalin A.

The emission wavelengths (λ_{EM}) were set to detect signals at 447/60 nm for Hoechst, 692/40 nm for MitoTracker, 624/40 nm for Wheat Germ Agglutinin and Phalloidin, 593/40 nm for SYTO 14 and 536/35 for Concanavalin A. Image processing and analysis was performed using CellProfiler[515] and CellPose[516]. Analysis was divided into three steps: quality control, illumination correction, and segmentation and feature extraction. A total of 2330 features were extracted from each cell, and exported for multivariate analysis using Python 3. All reagents and resources used for high-content image-based assays are listed on Table 14.

Table 14. Reagents and resources used for high-content image-based assays

High-content image-based assays		
Reagent or Resource	*Reference*	*Source*
Biotek® Multiflo™ FX microplate dispenser	-	Agilent Technologies
Falcon® 384-well Optilux Flat Bottom plates	353962	Corning
Siremadlin	#HY-18658	MedChemExpress
Olaparib	#HY-10162	MedChemExpress
Tetrandrine	#SML3048	Sigma-Aldrich, Merck
Metoclopramide	#M0763	Sigma-Aldrich, Merck
Fenbendazole	#F5396	Sigma-Aldrich, Merck
Etoposide	#E1383	Sigma-Aldrich, Merck
D-Sorbitol	#S1876	Sigma-Aldrich, Merck
DMSO	#D2438	Sigma-Aldrich, Merck
OT-2 Liquid Handler	-	Opentrons Labworks
Viaflo 384 electronic pipette	#6030	INTEGRA Biosciences
PBS	#11510546	Thermo Fisher Scientific
Biotek® 405™ LS washer	-	Agilent Technologies
MitoTracker™ Dye	#M22426	Thermo Fisher Scientific
Formaldehyde 4.0%	#02176	Histolab
Triton X-100	#17-1315-01	Cytiva
Hoechst 33342	#H3570	Thermo Fisher Scientific
SYTO 14 green	#S7576	Thermo Fisher Scientific
Concanavalin A (conj. with A488)	#C11252	Thermo Fisher Scientific
Wheat Germ Agglutinin (conj. with A555)	#W32464	Thermo Fisher Scientific
Phalloidin (conj. with A568)	#A12380	Thermo Fisher Scientific
ImageXpress Micro XLS Widefield High-Content Analysis System	-	Molecular Devices, Danaher
PLAID	https://github.com/pharmbio/plaid	
CellProfiler™ cell image analysis software	https://cellprofiler.org/	
CellPose	https://www.cellpose.org/	
Python™ 3	https://www.python.org/downloads/	

Headquarters: Agilent Technologies (Santa Clara, CA, USA), Corning (Corning, NY, USA), MedChemExpress (Monmouth Junction, NJ, USA), Sigma-Aldrich (St. Louis, MO, USA), Opentrons Labworks (Queens, NY, USA), INTEGRA Biosciences (Zizers, Switzerland), Thermo Fisher Scientific (Waltham, MA, USA), Histolab (Gothenburg, Sweden), Cytiva (Marlborough, MA, USA), Molecular Devices (San José, CA, USA).

3.5. DNA damage assay

3.5.1. Quantification of γH2AX foci by ICC/IF

Phosphorylation of the Ser139 residue of the histone protein H2AX (γH2AX) is an early cellular response to the induction of DNA DSBs. Quantification of γH2AX serves as a specific and sensitive marker for monitoring the initiation and resolution of DNA damage, especially in the context of ionizing radiation, as well as other genotoxic stresses such as ultraviolet radiation, oxidative stress, and various genotoxic drugs.

In the experimental procedure, RMS cells plated in 96-well plates and treated under specified experimental conditions were washed with PBS (Cytiva) and fixed with a 4% formaldehyde solution (Labbox Labware) for 10 minutes at room temperature. After fixation, cells were permeabilized and blocked with a solution of 5% bovine serum albumin (BSA, Sigma-Aldrich) and 0.5% Triton X-100 (Cytiva) in PBS for 30 minutes at room temperature. Following permeabilization and blocking, cells were incubated overnight at 4 °C with a mouse anti-phospho-Histone H2AX (S139) antibody (1:1000 dilution, Millipore). Cells were then washed twice with 0.05% Tween20 (Sigma-Aldrich) in PBS and incubated with the secondary antibody Alexa Fluor 568-tagged goat anti-mouse IgG (1:500 dilution, Thermo Fisher Scientific) for 2 hours at room temperature. After the secondary antibody incubation, cells were gently washed with the washing buffer (0.05% Tween20 in PBS) and stained with 10 ug/mL 4'-6-diamidino-2-fenilindol (DAPI, Thermo Fisher Scientific) in PBS for 10 minutes. Following staining, cells underwent two additional washes for 5 minutes each, with gentle rocking. Finally, 100 μL PBS was added to each well, and stained nucleus were observed and photographed using an epifluorescence microscope (Nikon). The percentage of γH2AX-positive nuclei was determined by counting the number of γH2AX-positive nuclei divided by the number of DAPI-stained nuclei using ImageJ[511]. All reagents and resources used for the quantification of γH2AX foci by ICC/IF are listed on Table 15.

Table 15. Reagents and resources used for the quantification of γH2AX foci by ICC/IF

DNA damage assay

Reagent or Resource	*Reference*	*Source*
96-well plates	#130188	Thermo Fisher Scientific
PBS, 10X	#SH30258.02	Cytiva
Formaldehyde 4.0%	#FORM-D0P-10K	Labbox Labware
BSA	#A7030	Sigma-Aldrich, Merck
Triton X-100	#17-1315-01	Cytiva
Mouse anti-γH2AX (Ser139) Antibody, clone JBW301	#05-636	Merck Millipore
Tween20	#P1379	Sigma-Aldrich, Merck
Goat anti-Mouse IgG Secondary Antibody, Alexa Fluor™ 568	#A11004	Thermo Fisher Scientific
DAPI	#D1306	Thermo Fisher Scientific
Epifluorescence microscope Eclipse Ts2R-FL	#2CE-MPKH-9	Nikon
Image J	-	https://imagej.net/

Headquarters: Thermo Fisher Scientific (Waltham, MA, USA), Cytiva (Marlborough, MA, USA), Labbox Labware (Premià de Dalt, Spain), Sigma-Aldrich (St. Louis, MO, USA), Merck Millipore (Burlington, MA, USA), Thermo Fisher Scientific (Waltham, MA, USA), Nikon (Tokyo, Japan).

3.6. Gene expression analysis by qPCR

Quantitative PCR (qPCR) was used to measure mRNA gene expression levels in both cultured cell lines and tumours derived from *in vivo* mouse models. For *in vitro* experiments, cells were collected from culture dishes or plates, centrifuged for 3 minutes at 1500 rpm, rinsed twice with 1 mL of PBS (Cytiva), and pelleted. Pellets were either stored at -80 ºC or used immediately for RNA extraction. For tumours from *in vivo* experiments, ~5 mm diameter sections were processed for RNA extraction immediately after thawing.

3.6.1. RNA extraction and reverse transcription

Total RNA was extracted from samples using the RNeasy® Mini Kit (Qiagen) according to the manufacturer's instructions. The extracted RNA was quantified using Nanodrop™ 2000 Spectrophotometer (Thermo Fisher Scientific) and stored at -80 ºC prior to reverse transcription. To generate complementary DNA (cDNA) from the extracted mRNA, reverse transcription was performed.

Briefly, 1 µg of RNA was mixed with 1 µg of random primers in nuclease-free water (Thermo Fisher Scientific) in a sterile RNase-free microcentrifuge tube to a final volume of 15 µL, and heated at 70 ºC for 5 minutes. Then, 5 µL of 5X Maloney Murine Leukemia Virus Reverse Transcriptase (M-MLV) reaction buffer (Promega), 5 µL of a mixture of 10 mM of four deoxynucleoside triphosphate (dNTPs (dATP, dCTP, dGTP, dTTP), Promega) and 200 U of M-MLV retrotranscriptase (Promega) were added to the mixture. The reaction was incubated at 37 ºC for 60 minutes.

3.6.2. Quantitative PCR (qPCR)

The PCR reaction was performed by mixing 0,5 µL of cDNA with 5 µL of 2X TaqMan™ Universal Master Mix (Thermo Fisher Scientific), 0,5 µL of TaqMan™ probes (Thermo Fisher Scientific, Table 16), and 4 µL of nuclease-free water (Thermo Fisher Scientific) in PCR tubes (Thermo Fisher Scientific). Then, 10 µL of each reaction mixture was transferred a MicroAmp™ 384-well plates (Thermo Fisher Scientific) and sealed with a MicroAmp™ Optical adhesive film (Thermo Fisher Scientific). The plates were briefly centrifuged to spin down the contents and remove any air bubbles and loaded into an ABI PRISM™ 7900HT real-time PCR system (Thermo Fisher Scientific) to run the amplification program. The following thermal cycling parameters were set: polymerase activation at 95 ºC for 10 minutes, followed by 40 cycles of PCR with denaturation at 95 ºC for 15 seconds and annealing/extension at 60 ºC for 1 minute. TATA-binding protein (*TBP*) gene expression was used as an endogenous control to relatively quantify the gene expression differences between samples using the $2^{(-\Delta\Delta CT)}$ method[517]. All reagents and resources used for RT-qPCR are listed on Table 16.

Table 16. Reagents and resources used for RT-qPCR

RT-qPCR *Reagent or Resource*	*Reference*	*Source*
PBS, 10X	#SH30258.02	Cytiva
RNeasy® Mini Kit	#74104	QIAGEN
Nanodrop™ 2000	#ND-2000	Thermo Fisher Scientific
Invitrogen™ Random primers	#48190011	Thermo Fisher Scientific
Ambion® DEPC-treated water	#AM9906	Thermo Fisher Scientific
M-MLV RT 5X buffer	#M531A	Promega
dATP	#U120B	Promega
dGTP	#U121B	Promega
dCTP	#U122B	Promega

dTTP	#U123B	Promega
M-MLV RT	#M170B	Promega
Applied Biosystems™ Thermal cycler	#12313653	Thermo Fisher Scientific
TaqMan™ Universal Master Mix	#4304437	Thermo Fisher Scientific
Fisherbrand™ PCR tubes	#12134102	Thermo Fisher Scientific
MicroAmp™ 384-well plates	#4343370	Thermo Fisher Scientific
MicroAmp™ Optical adhesive film	#4311971	Thermo Fisher Scientific
ABI PRISM™ 7900HT	#4329002	Thermo Fisher Scientific

TaqMan™ probes

Gene	*Reference*	*Source*
MDM2	#Hs01066930_m1	Thermo Fisher Scientific
CDKN1A	#Hs00355782_m1	Thermo Fisher Scientific
FBXW7	#Hs00217794_m1	Thermo Fisher Scientific
MDMX	#Hs00159092_m1	Thermo Fisher Scientific
TBP	#Hs00172424_m1	Thermo Fisher Scientific

Headquarters: Cytiva (Marlborough, MA, USA), QIAGEN (Venlo, Netherlands), Thermo Fisher Scientific (Waltham, MA, USA), Promega (Madison, WI, USA)

3.7. Western blot

Western blot (WB) was used to quantify protein levels in cultured cell lines and tumours derived from *in vivo* mouse models. For *in vitro* experiments, cells were collected from culture dishes or plates under the specified experimental conditions, centrifuged for 3 minutes at 1500 rpm, rinsed twice with 1 mL of PBS (Cytiva), and pelleted. Pellets were either stored at -80 ºC or used immediately for protein extraction. In the case of tumours from *in vivo* experiments, ~5 mm diameter sections were used for protein extraction immediately after thawing.

3.7.1. Protein extraction, quantification and sample preparation

Pelleted cells were lysed by resuspension in RIPA lysis buffer (Thermo Fisher Scientific) supplemented with Halt™ Protease and Phosphatase Inhibitor Single-Use Cocktail (Thermo Fisher Scientific). For frozen tissues, ~5 mm diameter sections were homogenized in 200-400 µl of RIPA buffer using a Bead Ruptor 12 (Omni International) in one agitation cycle (20 seconds, 5 m/s). In both cases, the lysates were incubated on ice for 20 minutes to ensure efficient cell lysis, and then centrifuged for 15 minutes at 13,300 rpm and 4 ºC to remove cell debris. The resulting supernatant fraction was transferred to a new collection tube, and total protein concentration was measured with the DC Protein Assay Kit (Bio-Rad), using a standard curve of 0.125 - 2 µg/µL BSA (Sigma-Aldrich).

3.7.2. Electrophoresis and transfer

For electrophoresis, 30 µg of each protein sample were mixed with Laemmli loading buffer and adjusted to a final volume of 20 µl using RIPA buffer. Samples were then heated at 70 ºC for 10 minutes before loading onto 8-12% sodium dodecyl sulphate-polyacrylamide gels (SDS-PAGE), located in a mini-PROTEAN® Tetra electrophoresis cell (Bio-Rad) filled with running buffer. SDS-PAGE gels were manually prepared by mixing the appropriate volumes of ultrapure water, 30% Acrylamide/Bis Solution, 37.5:1 (Bio-Rad), 10% w/v SDS, and either 0.5 M Tris (pH 6.8) for the stacking gel or 1.5 M Tris (pH 8.8) for the resolving gel. Polymerization reaction was initiated by adding 10% ammonium persulfate (APS; Sigma-Aldrich) and tetramethylethylenediamine (TEMED; Sigma-Aldrich) to the gel mixture. Precision Plus Protein™ Dual Colour Standards (Bio-Rad) were used as molecular weight marker. Proteins were separated under an electric field at 35 mA per gel. Following electrophoresis, proteins were transferred onto polyvinylidene difluoride (PVDF) membranes (Cytiva) activated with methanol (Thermo Fisher Scientific). PVDF membranes and polyacrylamide gels were sandwiched between two Whatman filter papers (Cytiva) and one sponge on each side. Transfer was performed in a Mini Trans-Blot® Cell (Bio-Rad) at a constant 200 mA and 4 ºC for 2.5 hours in cold transfer buffer. The composition of all buffers used in Western Blot is listed on Table 17.

Table 17. Composition of buffers used in Western Blot

Buffer	*Composition*
Laemmli (1X)	50 mM Tris base, 2% SDS, 10% glycerol, 0.01% blue bromophenol, and 100 mM dithiothreitol (DTT)
Running (1X)	25 mM Tris base, 192 mM glycine (pH 8.3), and 0.1% SDS
Transfer (1X)	25 mM Tris base, 192 mM glycine (pH 8.3), and 20% methanol
TBS-T	20 mM Tris base, 150 mM NaCl (pH 7.6), and 0.1% Tween20
High-salt washing	20 mM Tris base, 500 mM NaCl, 0.2% SDS, and 0.1% Tween20

3.7.3. Protein detection

After transferring the proteins onto membranes, each membrane was blocked for 1 hour in 5% non-fat dried milk diluted in TBS-T to prevent non-specific antibody binding. Membranes were then incubated overnight at 4 ºC with primary antibodies diluted in the same blocking solution. The following day, membranes were washed three times for 10 minutes each with TBS-T and incubated for 1 hour with horseradish peroxidase (HRP)-conjugated secondary antibodies diluted in 5% milk/TBS-T solution.

After three additional 10-minute washes with TBS-T, membranes were incubated for 2 minutes in Amersham ECL WB Detection Reagent (Cytiva), a luminol-based HRP substrate, before exposure to SuperRX Fuji Medical X-ray films (Fujifilm). The exposed films were marked and scanned for digitalization. Densitometric quantification of protein bands was performed using Image J[518,519]. To enable reprobing with alternative antibodies, both primary and secondary antibodies were stripped using Re-blot Plus Strong Antibody Stripping Solution (Sigma-Aldrich) or NaOH 0.5 M (Sigma-Aldrich). If persistent high background was observed after ECL incubation, membranes were washed with a high salt washing buffer (Table 17). All antibodies, reagents, and resources used for Western Blot are listed on Table 18.

Table 18. Reagents, resources, and antibodies used for Western Blot

Western Blot		
Reagent or Resource	*Reference*	*Source*
PBS, 10X	#SH30258.02	Cytiva
Pierce RIPA Buffer	#89900	Thermo Fisher Scientific
Halt™ Protease and Phosphatase Inhibitor Single-Use Cocktail	#78429	Thermo Fisher Scientific
Bead Ruptor 12	#SKU19-050A	Omni International
DC™ Protein Assay Kit	#5000112	Bio-Rad
BSA	#A7030	Sigma-Aldrich, Merck
Tris base	#173182	Thermo Fisher Scientific
30% Acrylamide/Bis Solution	#1610158	Bio-Rad
APS	#A3678	Sigma-Aldrich, Merck
TEMED	#T9281	Sigma-Aldrich, Merck
SDS	#L3771	Sigma-Aldrich, Merck
Glycerol	#24.388.295	VWR
Blue bromophenol	#B0026	Sigma-Aldrich, Merck
DTT	#D632	Sigma-Aldrich, Merck
Glycine	#J64365.A1	Thermo Fisher Scientific
Methanol	#M/4000/21	Thermo Fisher Scientific
NaCl	#12314	Thermo Fisher Scientific
Tween20	#P1379	Sigma-Aldrich, Merck
Mini-PROTEAN® Tetra Cell	#1658000	Bio-Rad
Precision Plus Protein™ Standards	#1610374	Bio-Rad
Mini Trans-Blot® Transfer Cell	#1703930	Bio-Rad
Amersham HyBond™ P 0.45 PVDF Blotting membrane	#10600023	Cytiva

Whatman filter paper	#10331687	Cytiva
Non-fat dried milk	#A0830	VWR
Amersham ECL WB Detection Reagent	#RPN2134	Cytiva
SuperRX Fuji Medical X-ray film	#47410	Fujifilm
Reblot Plus Strong Stripping Solution	#2504	Sigma-Aldrich, Merck
NaOH	#S8045	Sigma-Aldrich, Merck

Antibodies used for Western Blot

Primary Ab

Target	*MW*	*Origin*	*Dilution*	*Reference*	*Company*
PARP (total)	115	Rabbit	1:1000	#9542	Cell Signaling Technology
p-Rb (S807/11)	110	Rabbit	1:1000	#9308	Cell Signaling Technology
cl-PARP	90	Rabbit	1:1000	#9542	Cell Signaling Technology
MDM2	90	Mouse	1:1000	#sc965	Santa Cruz Biotechnology
cl-MDM2	60	Mouse	1:1000	#sc965	Santa Cruz Biotechnology
Cyclin B1	58	Mouse	1:1000	#05-373	Merck Millipore
p53	53	Mouse	1:2000	#sc126	Santa Cruz Biotechnology
ac-p53 (K382)	53	Rabbit	1:1000	#2525	Cell Signaling Technology
Actin	43	Mouse	1:8000	#sc47778	Santa Cruz Biotechnology
BAX	17	Rabbit	1:2000	#ABC11	Merck Millipore
p21	19	Rabbit	1:2000	#2947	Cell Signaling Technology

Secondary Ab

Target	*MW*	*Origin*	*Dilution*	*Reference*	*Company*
Rabbit IgG	–	Goat	1:5000	#A0545	Sigma-Aldrich, Merck
Mouse IgG	–	Rabbit	1:2000	#P0260	Agilent Technologies

Headquarters: Cytiva (Marlborough, MA, USA), Thermo Fisher Scientific (Waltham, MA, USA), Omni International (Kennesaw, GA, USA), Bio-Rad (Hercules, CA, USA), Sigma-Aldrich (St. Louis, MO, USA), VWR (Radnor, PA, USA), Fujifilm (Tokyo, Japan), Cell Signaling Technology (Danvers, MA, USA), Santa Cruz Biotechnology (Dallas, TX, USA), Merck Millipore (Burlington, MA, USA), Agilent Technologies (Santa Clara, CA, USA).

3.8. Flow cytometry

3.8.1. Cell cycle assay

Cell cycle assays were performed by quantifying the DNA content of DAPI-stained cell suspensions via flow cytometry. DAPI fluorescence, emitted upon binding to DNA in permeabilized and fixed cell populations, allowed the determination of cell proportions in G1, S, and G2/M phases based on fluorescence signal intensity.

In the experimental procedure, cells harvested from cell culture dishes under specified conditions were resuspended in 300 µl PBS and fixed at a density of 1 x 10^6 cells/mL in 700 µl of 100% ice-cold ethanol (VWR) overnight at -20 °C. After 24 hours, fixed cells were centrifuged at 5000 rpm for 5 minutes and washed twice with PBS to remove the ethanol. Subsequently, cells were incubated in a staining solution composed of 0.1% Triton X-100 (Cytiva) and 10 µg/mL DAPI (Thermo Fisher Scientific) in PBS, to a final volume of 1 mL. The staining process was conducted at room temperature (~25°C) for 30 minutes prior to measuring DAPI fluorescence intensity on individual cells using a BD FACSCalibur™ flow cytometer (BD Biosciences). Flow cytometry data were analysed using the Watson cell cycle univariate model[520] implemented in FlowJo™ v10.8 Software (BD Biosciences) to interpret the results and determine cell cycle distributions accurately. Cells in the G2/M phase exhibited approximately twice the fluorescence intensity of those in the G1 phase, while cells in the S phase displayed intermediate fluorescence, indicating ongoing DNA replication.

3.8.2. Apoptosis assay

Apoptosis was evaluated using allophycocyanin (APC) conjugated Annexin V (BD Biosciences), which specifically binds to phosphatidylserines translocated to the outer leaflet of the cell membrane during apoptosis. Additionally, Sytox™ Blue Dead Cell Stain (Thermo Fisher Scientific) was used to identify and quantify dead cell by staining nucleic acids in cells with compromised plasma membranes.

In the experimental procedure, cells harvested from cell culture dishes under specified conditions were resuspended at a density of 10^6 cells/mL in 100 µl of Annexin V Binding buffer (BD Biosciences). Next, 100 µl of APC Annexin V was added to the cell suspension, and the samples were incubated for 15 minutes at room temperature (~25°C). Subsequently, 400 µl of Annexin V Binding buffer and 0.5 µl of Sytox™ Blue Dead Cell Stain were added to the samples, which were then incubated for an additional 30 minutes at room temperature. After incubation, fluorescence intensities of APC Annexin V and Sytox™ Blue Dead Cell Stain were measured on single cells using a BD FACSCalibur™ flow cytometer (BD Biosciences). Unstained cells and cells stained with either APC Annexin V or Sytox™ Blue Dead Cell Stain were used to establish gates for apoptotic and dead cell populations. Cells treated with 1 nM actinomycin (MedChemExpress) for 72 hours served as a positive control of apoptosis. Flow cytometry data was analysed using FlowJo™ v10.8 Software (BD Biosciences).

Single cells were gated based on forward and side scatters, while Annexin V-positive cells and Sytox™ Blue-positive cells were identified using C-red (λ_{EM} = 640 nm) and F-Violet (λ_{EM} = 405 nm) detectors, respectively. Cells negative for both markers were classified as viable, Annexin V-positive cells as early apoptotic, Sytox™ Blue-positive cells as dead, and cells positive for both markers as late apoptotic. Details of all reagents and resources used for cell cycle and apoptosis assays can be found in Table 19.

Table 19. Reagents, resources, and antibodies used for flow cytometry

Cell cycle assays

Reagent or Resource	*Reference*	*Source*
PBS, 10X	#SH30258.02	Cytiva
Ethanol	#20821.330	VWR
Triton X-100	#17-1315-01	Cytiva
DAPI	#D1306	Thermo Fisher Scientific
BD FACSCalibur™ flow cytometer	#342973	BD Biosciences
FlowJo™ v10.8 Software	–	BD Biosciences

Apoptosis assays

Reagent or Resource	*Reference*	*Source*
PBS, 10X	#SH30258.02	Cytiva
APC Annexin V	#550474	BD Biosciences
Sytox™ Blue Dead Cell Stain	#S34857	Thermo Fisher Scientific
Annexin V Binding Buffer, 10X	#556454	BD Biosciences
BD FACSCalibur™ flow cytometer	#342973	BD Biosciences
FlowJo™ v10.8 Software	–	BD Biosciences
Actinomycin D	#A13239	Adooq Bioscience

Headquarters: Cytiva (Marlborough, MA, USA), VWR (Radnor, PA, USA), Thermo Fisher Scientific (Waltham, MA, USA), BD Biosciences (Franklin Lakes, NJ, USA), Adooq Bioscience (Irvine, CA, USA).

3.9. Cell-derived orthotopic xenografts

RMS cell-derived orthotopic xenografts (CDOX) were established by injecting 2 x 10^6 RH36 cells into the gastrocnemius muscle of 5-week-old severe combined immunodeficient (SCID) mice (Charles River Laboratories). Tumour growth was monitored by measuring limb dimensions with a calliper, and tumour volume was calculated using the formula: Tumour volume = $4\pi/3((\text{length} + \text{width})/4)^3$. Mice were randomized into treatment groups once tumours reached tumours reached ~25 mm^3.

Pilot study

In the pilot study, mice were randomized into six groups (n = 2 per group) and received the following treatments orally twice a week: control (vehicle), siremadlin at 50 mg/kg, olaparib at 100 mg/kg, a combination of siremadlin (50 mg/kg) plus olaparib (100 mg/kg), a combination of siremadlin (25 mg/kg) plus olaparib (50 mg/kg), or a combination of siremadlin (12.5 mg/kg) plus olaparib (25 mg/kg). Both siremadlin and olaparib were dissolved in a vehicle composed of 5% DMSO (Sigma-Aldrich), 40% PEG300 (Sigma-Aldrich), 5% Tween-80 (Sigma-Aldrich), and 50% PBS (Cytiva), added sequentially.

Experimental studies

In the experimental study, mice were randomized into four treatment groups (n = 6 per group) and received the following treatments orally twice a week: control (vehicle), siremadlin at 50 mg/kg, olaparib at 100 mg/kg, and a combination of siremadlin (25 mg/kg) plus olaparib (50 mg/kg). Tumour volume was measured regularly, and animals were euthanized when tumours reached 1500 mm^3. Ethical endpoint criteria, including acute weight loss (>10% of total body weight) or poor general appearance, were monitored throughout the study.

Simultaneously, an additional experiment was conducted to assess the molecular effects of the treatments following three dosage regimens (1, 3, and 5 doses). Mice were randomized into the same treatment groups as in the experimental study, with additional stratification based on the number of doses administered, resulting in 12 experimental conditions (n = 2 per group). In order to obtain enough tumour sample size for subsequent studies, treatment was initiated when tumours reached ~250 mm^3, and tumour samples were collected 24 hours after the last dose. The specimens were divided in two portions: one was preserved at -80 °C, while the other was fixed in 4% formaldehyde (Labbox Labware).

All CDOX experimental procedures were conducted at the Rodent Platform of the Laboratory Animal Service of the Vall d'Hebron Institute of Research, under pathogen-free conditions. These procedures had received prior approval from the regional Institutional Animal Care and Ethics Committee of Animal Experimentation of the Vall d'Hebron Research Institute (CEEA 70/19) and complied with EU directive 2010/63/EU. All reagents and resources used for *in vivo* experiments are listed on Table 20.

Table 20. Reagents and resources used for *in vivo* experiments

Cell-derived orthotopic xenografts

Reagent or Resource	*Reference*	*Source*
Fox Chase SCID® mouse CB17/Icr-*Prkdc*^{scid}/IcrIcoCrl mouse	#236	Charles River Laboratories
Sterican® hypodermic needles	#46557705	B. Braun
Digital electronic calliper	#30087-00	Fine Science Tools
Single-use feeding needles	#18061-20	Fine Science Tools
Siremadlin	#HY-18658	MedChemExpress
Olaparib	#HY-10162	MedChemExpress
DMSO	#D8418	Sigma-Aldrich, Merck
PEG300	#202371	Sigma-Aldrich, Merck
Tween® 80	#P4780	Sigma-Aldrich, Merck
PBS, 10X	#SH30258.02	Cytiva
Formaldehyde 4.0%	#FORM-D0P-10K	Labbox Labware

Headquarters: Charles River Laboratories (Wilmington, MA, USA), B. Braun (Melsungen, Germany), Fine Science Tools (Foster City, CA, USA), MedChemExpress (Monmouth Junction, NJ, USA), Sigma-Aldrich (St. Louis, MO, USA), Cytiva (Marlborough, MA, USA), Labbox Labware (Premià de Dalt, Spain), Inotiv (West Lafayette, IN, USA).

3.10. Statistical analysis

Statistical analysis was performed using GraphPad Prism 6.0 (GraphPad Software). Parametric or non-parametric test were chosen after assessing the normality and homoscedasticity of the data. Statistical significance between two groups were conducted using Student's *t*-test or the Mann-Whitney *U* test. Statistical significance between three or more groups was determined by using one- or two-way analysis of variance (ANOVA) followed by Dunnett's or Tukey's post-hoc test for multiple comparisons. Each *p*-value was adjusted to account for multiple comparisons. The level of significance was denoted using asterisks (*) or hashes (#) as follows: $p < 0.05$ (* or #), $p < 0.01$ (** or ##), and $p < 0.001$ (*** or ###). Plots representing the data indicate the mean ± standard error of the mean (s.e.m.) of three independent replicates, unless otherwise stated. Additional details regarding statistical analysis can be found on each section.

4. RESULTS

4.1. p53 WT RMS cells were especially vulnerable to MDM2 inhibitors

Initially, a comprehensive drug screening was conducted to evaluate the differential responses of p53 WT and p53 MUT RMS cells to a range of pharmaceutical agents. This screening involved 26 distinct drugs, tested at three different concentrations across six RMS cell lines: three p53 WT cells (RH18, RH36, CW9019) and three p53 MUT cells (RH28, RH4, RD) (Figure 14a). The drug panel included both targeted therapies–some of which are approved for clinical use or are in clinical trials for cancer treatment–and standard chemotherapeutic agents commonly used in paediatric oncology.

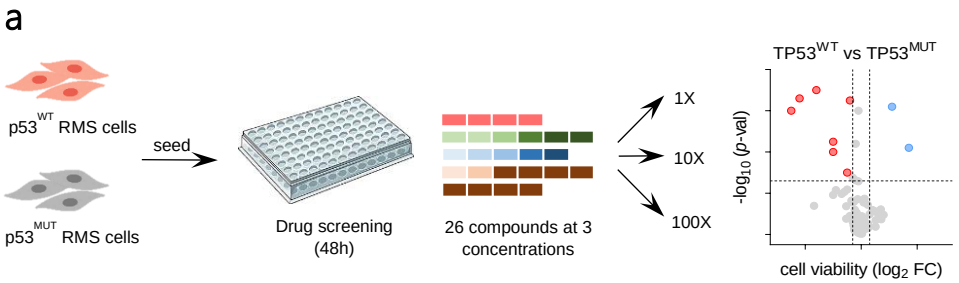

Figure 14. Schematic representation of the initial drug screening workflow conducted on both p53 WT and p53 MUT RMS cells. (a) RMS cells were cultured in 96-well plates and exposed to 26 compounds at three distinct concentrations (refer to section 3.2 for details) for 72h. Differences in cell viability, measured as log_2 fold-change (log_2FC), between p53 WT and p53 MUT were assessed for each compound and dose.

Cell survival analysis revealed an increased vulnerability of p53 WT RMS cells to the tested MDM2 inhibitors (siremadlin, idasanutlin, navtemadlin, and MI-773) while no significant differences were observed in response to the remaining drugs (Figures 15a-b). To accurately assess the sensitivity and specificity of these MDM2 inhibitors, IC_{50} values were subsequently determined for each compound. Siremadlin and idasanutlin exhibited lower IC_{50} values in p53 WT cells compared to navtemadlin and MI-773, indicating greater potency of these compounds in inhibiting MDM2-p53 interaction (Figure 15c). Furthermore, the difference in $logIC_{50}$ values ($\Delta logIC_{50}$) between p53 WT and p53 MUT cells was significantly greater for siremadlin, suggesting a superior specificity and selectivity of siremadlin in disrupting the MDM2-p53 interaction compared to other MDM2 inhibitors tested (Figure 15c).

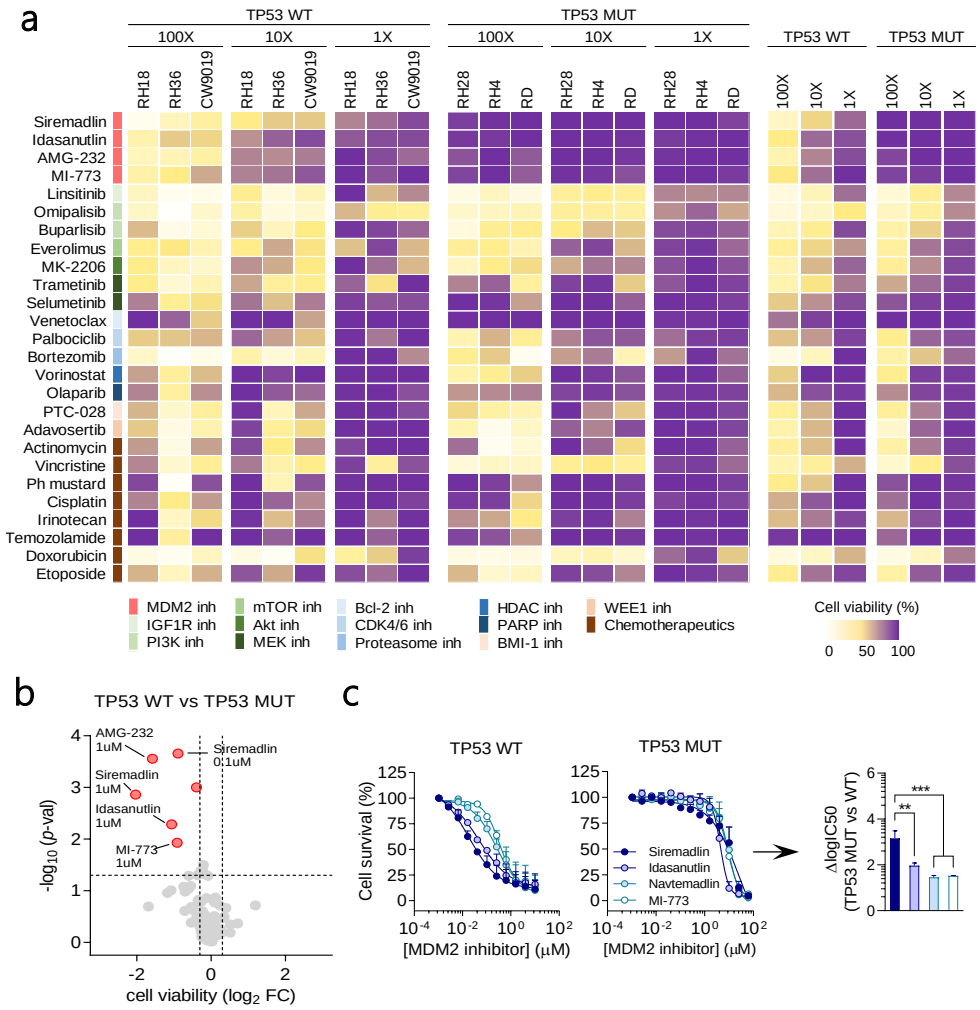

Figure 15. MDM2 inhibitors were able to reduce cell survival and modulate p53 activity in p53 WT RMS cells. (**a**) Heatmap summarizing cell viability results (in %) for 26 drugs tested at three concentrations (100X, 10X and 1X) in six RMS cell lines: three p53 WT (RH18, RH36, CW9019) and three p53 MUT (RH28, RH4, RD) cell lines, after 48 hours (n=3). (**b**) Volcano plot showing the differential response of p53 WT and p53 MUT cell lines to the 26 drugs tested. The x-axis represents the difference in cell viability, expressed as $\log_2$ fold-change ($\log_2$FC), between p53 WT and p53 MUT cell lines for each drug and concentration, while the y-axis shows the associated significance level, expressed as -$\log_{10}$ p-value. Statistical significance was determined using Student's t-test. Results were considered significant according to the following cut-off levels: p-value < 0.05, and abs($\log_2$FC) > 0.25. (**c**) Dose-response curves of MDM2 inhibitors (siremadlin, idasanutlin, navtemadlin, and MI-733) are shown for p53 WT (left) or p53 MUT (middle) cell lines (n=3). IC_{50} values were calculated using a non-linear regression approach (least squares regression without weighting). The right panel displays the difference in IC_{50} values between p53 WT and p53 MUT cells, expressed as the mean ± SEM. Statistical significance was assessed using one-way ANOVA followed by Tukey's post-hoc test.

To assess how the MDM2 and p53 expression levels influence the sensitivity of RMS cells to MDM2 inhibitors, the expression levels of these proteins were quantified. In addition, the expression of p21, a well-established target of p53, was measured. The results showed no significant differences in the expression levels of p53, MDM2, and p21 between p53 WT and p53 MUT cells (Figures 16a-b). Similarly, gene expression analysis revealed no significant differences in *MDM2* and *CDKN1A* (which encodes p21), likely due to the substantial variability in the expression of these genes among p53 WT cells (Figure 16c). Despite this variability, significant correlations were observed between the expression levels of MDM2 and p21, both at the gene and protein levels, and the IC_{50} values of MDM2 inhibitors (Figure 16d). However, the strongest correlation was found between *TP53* status and IC_{50} values, indicating that *TP53* status was a more reliable predictor of response to MDM2 inhibitors compared to the individual expression levels of its downstream targets, MDM2 and p21.

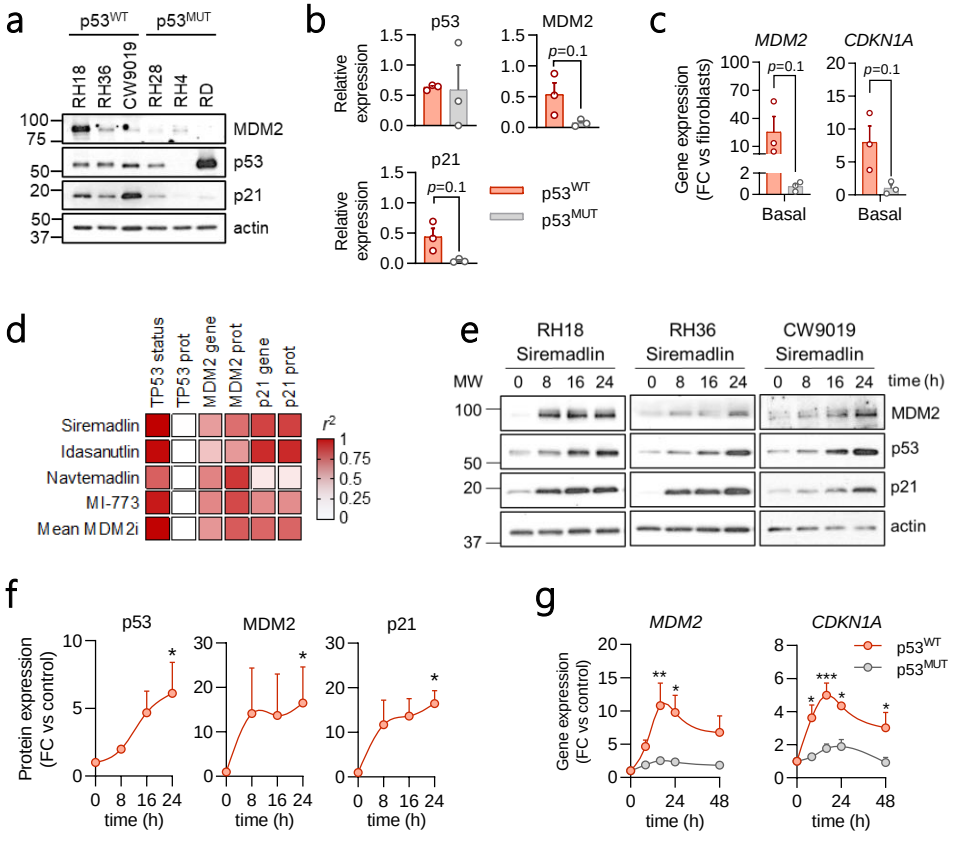

Figure 16. Comprehensive assessment of siremadlin in p53 WT and p53 MUT RMS cells. (**a**) Western blot showing the basal expression of MDM2, p53 and p21 in six RMS cells. (**b**) Bar plots showing the protein quantification normalized to β-actin of results presented in panel (a). Data represent the mean ± SEM from three p53 WT and three p53 MUT RMS cells (*n*=3). Statistical significance was assessed using Mann Whitney's test. (**c**) Bar plots showing the basal gene expression of *MDM2* and *CDKN1A* in p53 WT RMS and p53 MUT RMS cells (*n*=3). Gene expression fold-change (mean FC ± SEM) is relative to the basal expression of fibroblasts. Statistical significance was assessed using Mann Whitney's test. (**d**) Heatmap showing the correlation between $\log IC_{50}$ values for each MDM2 inhibitor and *TP53* status, p53 protein expression, and MDM2 and p21 protein and gene expression. (**e**) Western blot showing the expression of MDM2, p53 and p21 in p53 WT cells treated with 0.08 µM siremadlin for 0, 8, 16, and 24 hours. (**f**) Bar plots showing the protein quantification normalized to β-actin of results presented in panel (e). Data represent the mean ± SEM from three p53 WT RMS cells (n=3). Statistical significance was assessed using one-way ANOVA followed by Kruskal-Wallis post-hoc test. (**g**) Dot plots showing the expression of *MDM2* (left) and *CDKN1A* (right) in p53 WT (orange) and p53 MUT (grey) cell lines treated with 0.08 µM siremadlin for 8, 16, 24, and 48 hours (*n*=3). Gene expression fold-change (mean FC ± SEM) is relative to untreated cells. Statistical significance was assessed using two-way ANOVA followed by Sidak's post-hoc test.

Subsequently, temporal changes in p53, MDM2, and p21 levels were analysed to assess the impact of siremadlin on p53 activity. Western blot analysis revealed a progressive accumulation of p53 (6-fold), as well as an increased expression of its downstream targets, MDM2 (18-fold) and p21 (18-fold), in p53 WT cells at 24-hours post-treatment (Figure 16e-f). These results indicated a time-dependent activation of the p53 pathway by siremadlin in p53 WT RMS cells. Consistently, gene expression analysis showed increased levels of *MDM2* (10-fold) and *CDKN1A* (6-fold) at 16- and 24-hours post-treatment in p53 WT cell lines (Figure 16g). In contrast, the expression levels of MDM2 and p21 remained largely unchanged in p53 MUT cells following siremadlin treatment, suggesting that siremadlin selectively activates p53 transcriptional activity in p53 WT RMS cells. The enhanced sensitivity of p53 WT cells to siremadlin, along with the increased p53 transcriptional activity as evidenced by the accumulation of MDM2 and p21, underscores the effective modulation of p53 activity by siremadlin in p53 WT RMS *in vitro*.

4.1.1. Cell survival analysis revealed limited specificity of novel experimental MDM2/X inhibitors

Building on the promising results of existing MDM2 inhibitors, particularly siremadlin, a collaboration was established with the Medicinal Organic Chemistry group of the University of Lisbon (PI: Dr. Maria M. M. Santos). This collaboration aimed to test new experimental compounds designed to inhibit both MDM2 and MDMX, a homologous protein of MDM2 that can partially compensate for its function.

Hence, p53 WT and p53 MUT cells were treated with these experimental compounds (designated ME240, ME242, ME258, and ME62) for 72 hours to generate dose-response curves. However, these compounds exhibited limited efficacy, with high IC_{50} values and no significant specificity, as indicated by the absence of differential activity between p53 WT and p53 MUT cells (Figure 17a). Consequently, these compounds were deemed non-viable, and the project refocused on siremadlin.

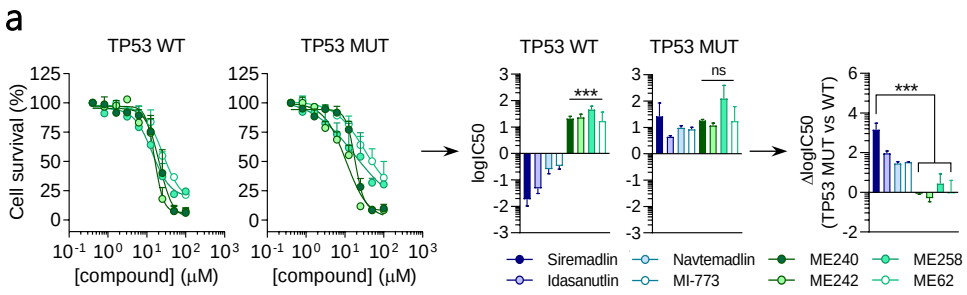

Figure 17. Cell survival analysis revealed limited specificity of novel experimental MDM2/X inhibitors. (a) On the left, dose-response curves are shown for the experimental compounds (ME240, ME242, ME258, and ME62) in p53 WT and p53 MUT cells (n=3). In the middle, bar plots comparing $logIC_{50}$ values of MDM2 inhibitors with those of the experimental compounds in both p53 WT and p53 MUT cells. On the right, bar plots displaying the differences in $logIC_{50}$ (mean ± SEM) between p53 WT and p53 MUT cells for both MDM2 inhibitors and experimental compounds. Statistical significance in the differences between siremadlin and the experimental compounds was assessed using one-way ANOVA followed by Tukey's post-hoc test.

4.2. A comprehensive drug combination screening revealed the synergistic efficacy of combining siremadlin with olaparib in p53 WT RMS cells

In recent years, results from early-phase clinical trials have demonstrated the limited efficacy of MDM2 inhibitors as monotherapy, emphasizing the necessity of exploring additional combinations with other agents to enhance their antitumor effects. Furthermore, the initial assumption that MDM2 inhibitors would induce strong apoptosis in p53 WT cells has been challenged by emerging evidence suggesting limited apoptosis response, potentially due to distinct patterns of p53 activation. In view of these findings, this study aimed to evaluate the synergistic efficacy of siremadlin combined with 22 other drugs in p53 WT RMS cells to identify therapeutic combinations that may improve clinical outcomes (Figure 18a).

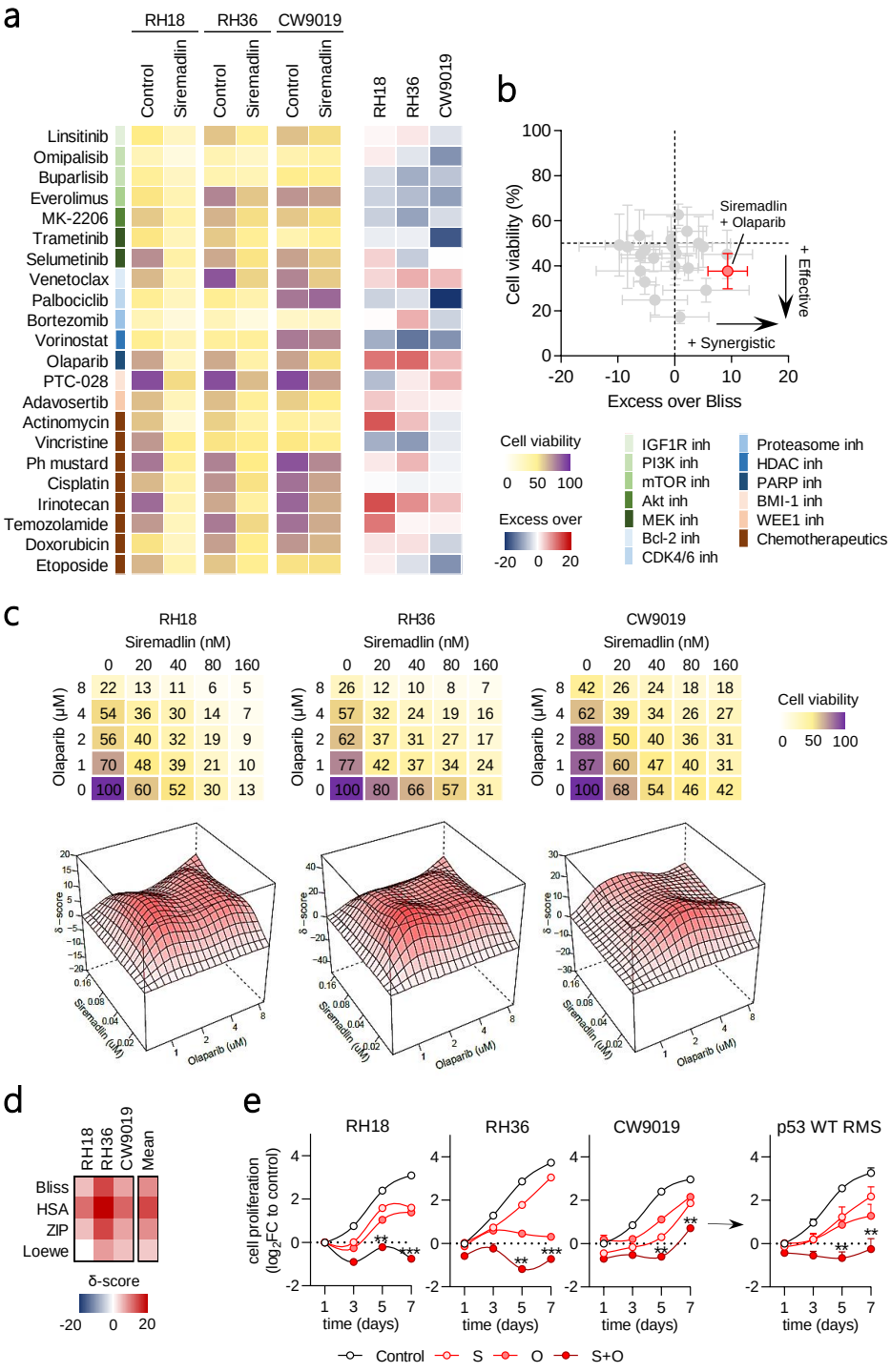
a
RH18
RH36
CW9019
Control
Siremadlin
Linsitinib
Omipalisib
Buparlisib
Everolimus
MK-2206
Trametinib
Selumetinib
Venetoclax
Palbociclib
Bortezomib
Vorinostat
Olaparib
PTC-028
Adavosertib
Actinomycin
Vincristine
Ph mustard
Cisplatin
Irinotecan
Temozolamide
Doxorubicin
Etoposide
b
Cell viability (%)
Excess over Bliss
Siremadlin + Olaparib
+ Effective
+ Synergistic
Cell viability
Excess over
IGF1R inh
PI3K inh
mTOR inh
Akt inh
MEK inh
Bcl-2 inh
CDK4/6 inh
Proteasome inh
HDAC inh
PARP inh
BMI-1 inh
WEE1 inh
Chemotherapeutics
c
RH18
RH36
CW9019
Siremadlin (nM)
Olaparib (μM)
Cell viability
δ-score
Siremadlin (uM)
Olaparib (uM)
d
Bliss
HSA
ZIP
Loewe
Mean
δ-score
e
cell proliferation (log2FC to control)
time (days)
Control
S
O
S+O
p53 WT RMS

Figure 18. Synergistic antitumoral effects of combining siremadlin with olaparib in p53 WT RMS cells. (**a**) On the left, heatmap summarizing the effects on cell viability (in %) of p53 WT RMS cells treated siremadlin in combination with 22 different drugs for 48 hours. On the right, heatmap showing the degree of synergism (Bliss > 10), additivity (Bliss ≈ 0), or antagonism (Bliss < -10) between the drug combinations, based on the Bliss independence model. (**b**) Dot plot summarizing the results from panel (a). The excess over Bliss is displayed on *x*-axis, while the cell viability (in %) is displayed on *y*-axis. The lower-right quadrant highlights the most synergistic combinations with the greatest reduction in cell viability. Each dot represents the mean ± SEM from three p53 WT RMS cell lines (*n*=3). (**c**) On the upper section, cell viability (in %) of p53 WT RMS cells treated with increasing concentrations of siremadlin (0–160 nM) and olaparib (0–8 µM) for 72 hours. Data represent the mean viability from three replicates (*n*=3). On the lower section, SynergyFinder δ-score (Bliss score) plots generated from 5x5 dose-response matrices, indicating additive to synergistic effects between siremadlin and olaparib at the tested doses across each p53 WT RMS cell line. (**d**) Heatmap showing the mean synergy δ-scores for each cell line using four reference models: Bliss, Highest Single Agent (HSA), Loewe and Zero Interaction Potency (ZIP). The mean δ-scores across all three p53 WT RMS cell lines are summarized on the right. (**e**) Quantitative analysis of cell proliferation in p53 WT RMS cells treated with 80 nM siremadlin and 4 µM olaparib over 1, 3, 5, or 7 days. Cell proliferation is expressed as log_2 fold-change (log_2FC) relative to vehicle-treated control cells. Dots represent the mean ± SEM of three replicates (*n*=3). Statistical significance was assessed using two-way ANOVA followed by Dunnett's post-hoc test.

Cell viability and excess over Bliss score were used to assess the efficacy and nature of drug-drug interactions (synergism, additivity, or antagonism) at specific doses. Notably, the combination of siremadlin and olaparib demonstrated the highest excess over Bliss score, significantly reducing cell viability and emerging as the most promising therapeutic strategy tested (Figure 18a-b). To confirm these results, p53 WT RMS cells were treated with increasing doses of siremadlin and olaparib, either as single agents or in combination, using a 5x5 dose-response matrix. Synergy Finder δ-score plots showed additive to synergistic effects between the two compounds at the tested doses (Figure 18c). These effects were consistent across multiple synergy models (Bliss, HSA, ZIP, and Loewe) at 72 hours post-treatment, suggesting an enhanced therapeutic efficacy of the combination beyond that of the individual agents (Figure 18d). Additionally, a time-course analysis of cell proliferation revealed a significant reduction in cell proliferation at 3, 5, and 7 days post-treatment, with the combination treatment outperforming either drug alone (Figure 18e). These findings underscored the potential of combining siremadlin with olaparib to synergistically enhance their individual therapeutic effects, particularly in reducing cell viability and inhibiting proliferation. Moreover, additional promising combinations, such as siremadlin with irinotecan and siremadlin with venetoclax, were identified in the initial screening, warranting further investigation as potential therapeutic strategies for p53 WT RMS.

4.3. Cell painting analysis was able to capture the phenotypic changes triggered by the combination of siremadlin with olaparib

Building on the observed synergistic effects of combining siremadlin and olaparib on cell viability and proliferation, this study aimed to elucidate the underlying mechanisms driving these effects, particularly heir impacts on cellular morphology and function. To achieve this, cell painting, a high-content image-based assay for morphological profiling, was conducted in collaboration with the Pharmaceutical Bioinformatics Research Group at the University of Uppsala (co-led by Dr. Jordi Carreras-Puigvert).

In this technique, cells are seeded in multiwell plates, treated with compounds, fixed, and then imaged using a high-throughput microscope. Approximately 2000 morphological features–including size, shape, texture, and intensity of cellular compartments and organelles–are quantified in single cells using automated image analysis software. The resulting morphological profiling allows for the detection of subtle phenotypic changes and identification of treatment-specific signatures, facilitating comparisons across different treatments. Thus, cell painting provided a comprehensive evaluation of the impacts of siremadlin and olaparib, both individually and in combination, on cellular morphology and function, offering a detailed understanding of their potential synergistic effects.

4.3.1. Phenotype profiling revealed dose-dependent morphologic changes induced by siremadlin and olaparib

The phenotypic effects of siremadlin and olaparib on cellular and organelle morphology were initially assessed by comparing them with those induced by compounds with known mechanism of action (MoA). For this purpose, RH36 cells were treated with siremadlin and olaparib, and their effects were compared with those triggered by four reference compounds: tetrandrine, metoclopramide, fenbendazole, and etoposide. Cells treated with D-sorbitol (negative control) and DMSO (vehicle) served as the baseline phenotypic state. To visualize the effects of these treatments, a two-dimensional plot derived from t-distributed stochastic neighbour embedding (t-SNE) was generated. This method reduces high-dimensional data into a two-dimensional space, revealing distinct clustering patterns for different treatments (Figure 19a).

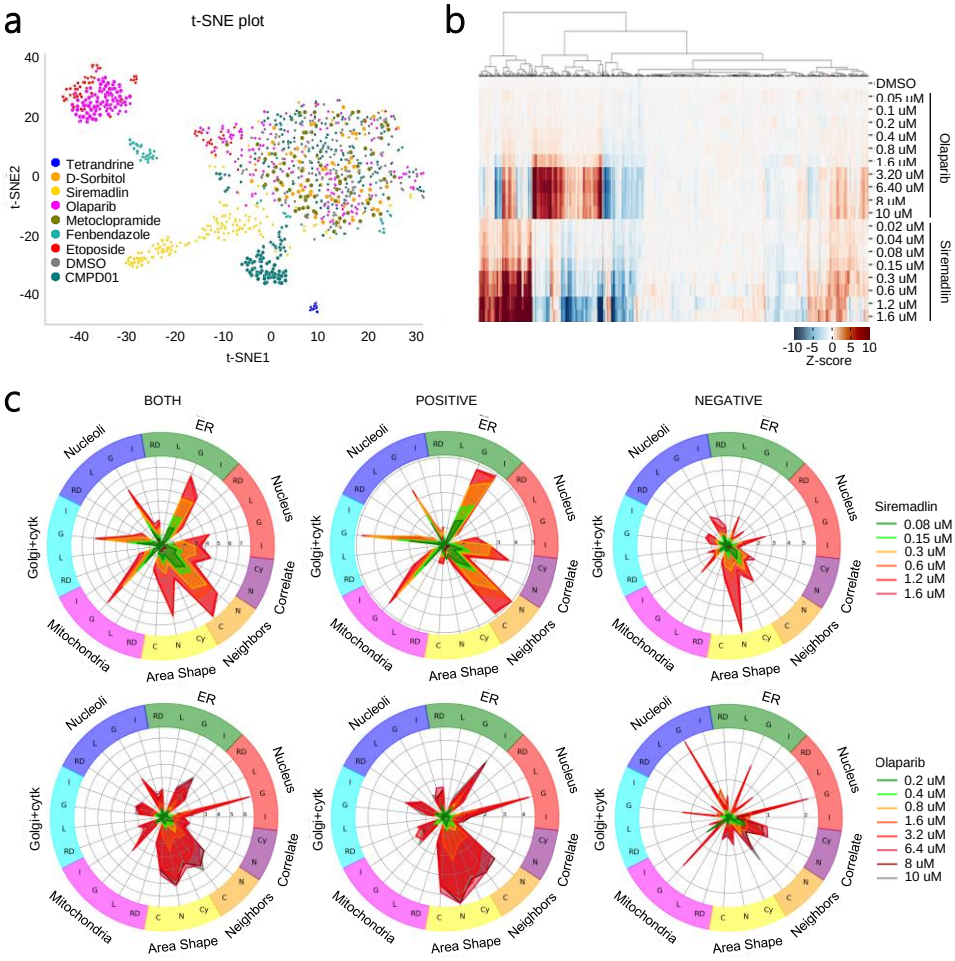

Figure 19. Phenotype profiling revealed dose-dependent morphologic changes induced by siremadlin and olaparib in RH36 cells. (**a**) Two-dimensional plot, derived from t-SNE analysis, representing the morphological changes triggered by siremadlin and olaparib in comparison to other compounds in RH36 cells. Dot colours represent different treatments, and dot sizes indicate the doses of the compound tested, with larger dots corresponding to higher doses. (**b**) Heatmap showing the hierarchical clustering of ~2000 morphologic features analysed by cell painting after treating RH36 cells with increasing doses of siremadlin and olaparib. The colour in the heatmap (Z-score) represents the deviation of each morphological feature from the mean value of the DMSO-treated control cells. (**c**) On the left, radial plots show both positive and negative differences, while on the right results are categorized in positive and negative differences. Concentric marks indicate Z-scores. All morphological features analysed are grouped into eight main groups: endoplasmic reticulum (ER), nucleus, nucleoli, Golgi + cytoskeleton, mitochondria, cellular area and shape, characteristics of the neighbour cells, and correlates between nucleus and cytoplasm regions. At the same time, these features are further categorized into the following subgroups: RD (radial distribution), L (location and spatial distribution), G (granularity), I (integrated intensity), C (cell measurements), N (nuclear measurements), and Cy (cytoplasm measurements).

Notably, olaparib and etoposide formed closely related clusters, suggesting similar phenotypic changes and indicating a convergence in their effects on RH36 cells. In fact, both compounds are known to target DNA damage pathways—olaparib as a PARP inhibitor and etoposide as a topoisomerase II inhibitor—leading to DNA damage accumulation and subsequent cellular responses. In contrast, siremadlin exhibited a distinct cluster profile, underscoring its unique phenotypic effects compared to the other compounds. Subsequently, hierarchical clustering of approximately 2000 morphological features was used to assess the dose-dependent effects of olaparib and siremadlin. This analysis resulted in the generation of a heatmap, which illustrated the clustering of molecular profiles at increasing doses of both drugs (Figure 19b). The hierarchical cluster analysis revealed both distinct and overlapping phenotypic alterations induced by siremadlin and olaparib. Furthermore, the differences in phenotypic features increased with dose levels, indicating that the morphological changes induced by siremadlin and olaparib are dose-dependent. These results were then visualized in radial plots to illustrate both positive and negative phenotypic effects of increasing doses of siremadlin and olaparib on specific cellular components (Figure 19c).

Radial plots showed changes in morphological features associated with various cellular structures, including the endoplasmic reticulum (ER), nucleus, nucleoli, Golgi, cytoskeleton, and mitochondria, as well as features related to cell shape, cell area, neighbouring cells, and comparisons between cytoplasmic and nuclear regions. Concentric marks on the plots represented the average deviation of morphological features from the mean value of the control (DMSO-treated cells), facilitating the observation of dose-dependent changes in cellular morphology, function, and interactions across multiple cellular components following treatment exposure. The morphologic profiles revealed a marked dose-dependent increase in granularity of organelles such as the ER, Golgi, nucleoli, and mitochondria, following siremadlin treatment. This increase may reflect disruptions in organelle function, potentially affecting processes like protein synthesis, trafficking, and metabolic activity. Additionally, changes in nuclear and cytoplasmatic area and shape were observed. For olaparib, the increased ER intensity and nucleus granularity, along with changes in nuclear and cytoplasmic area and shape, suggested significant alterations in cellular morphology and function, including impacts on protein synthesis, cell cycle regulation, and DNA repair processes.

4.3.2. The combination of siremadlin and olaparib synergistically induced morphological changes in the ER, Golgi, cytoskeleton, and nucleus

After analysing the individual effects of siremadlin and olaparib on cellular morphology, the study investigated the combined impact of these drugs on RH36 cells. For this purpose, the phenotypic effects induced by the combination of siremadlin and olaparib were compared to those observed with each drug alone. t-SNE analysis of the morphological profiles revealed a distinct cluster of cells treated with the combination of 0.04 and 0.08 μM siremadlin and 3.2 μM olaparib (Figure 20a). The formation of this separate cluster indicated that the combination treatment induced a unique morphological phenotype, supporting a synergistic interaction between the two drugs.

Hierarchical clustering of morphological profiles showed that the changes induced by the combination treatment were more similar to those caused by siremadlin alone than to those caused by olaparib alone (Figure 20b). Indeed, olaparib appeared to synergistically potentiate a substantial proportion of the mild phenotypic changes triggered by siremadlin. Radial plots demonstrated a marked increase in morphological features associated with ER and nuclear intensity, as well as granularity in the Golgi apparatus and cytoskeleton, indicating significant morphological changes that reflect alterations in cellular function (Figure 20c). Additionally, changes were observed in the nucleus and cytoplasm regions of neighbouring cells.

The increased intensity of the ER suggested not only changes in its morphology but also alterations in its function, such as modifications in protein synthesis rates, and potential ER stress. Similarly, the elevated granularity observed in the Golgi apparatus and cytoskeleton indicated significant changes in their composition or organization, potentially disrupting essential processes such as protein trafficking and cellular structure maintenance. The increased nuclear intensity suggested increased nuclear activity, potentially reflecting enhanced transcriptional activity, DNA replication, or DNA repair processes. These changes indicated a strong cellular response to the combination treatment that could impact overall cell function.

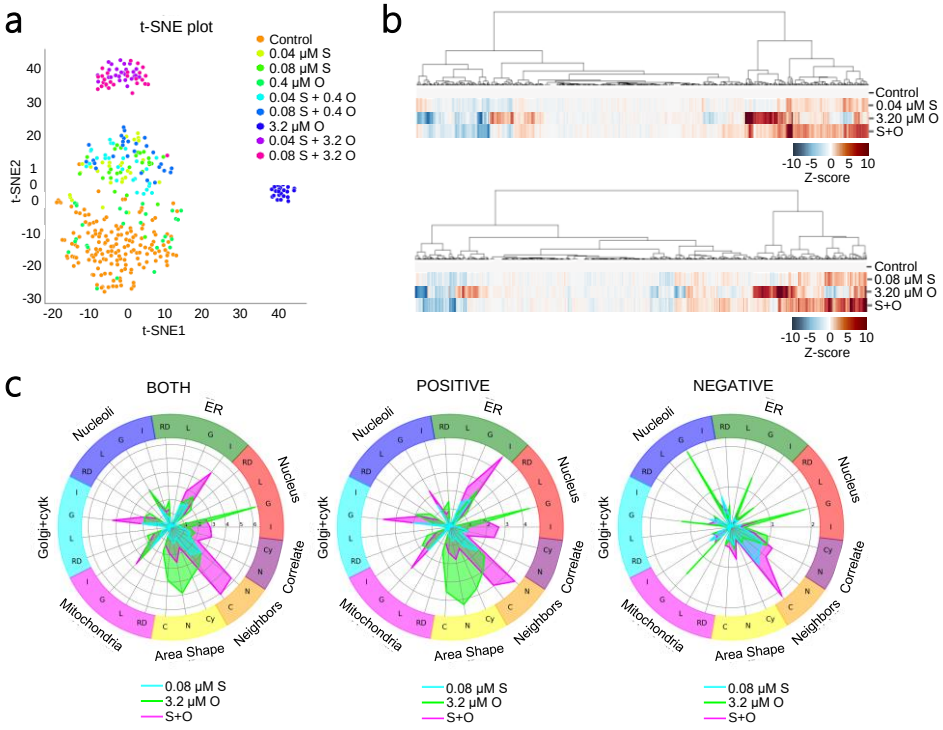

Figure 20. Combination of siremadlin and olaparib synergistically induced morphological changes in the ER, Golgi, cytoskeleton and nucleus. (a) Two-dimensional plot, derived from t-SNE analysis, showing the distinct morphological cluster formed by the combination of siremadlin (S) and olaparib (O) compared to individual treatments and control in RH36 cells. Scores on both axes represent the relative distance between clusters. (b) Heatmaps displaying the hierarchical clustering of ~2000 morphological features analysed by cell painting after treating RH36 cells with 0.04 or 0.08 µM siremadlin (S), 3.2 µM olaparib (O), and their combination (S+O). The colour in the heatmap (Z-score) represents the deviation of each morphological feature from the mean value of the DMSO-treated control cells. (c) Radial plots showing the findings from panel (b) for RH36 cells treated with 0.08 µM siremadlin (S), 3.2 µM olaparib (O), and their combination (S+O). On the left, radial plots show both positive and negative differences, while on the right results are categorized in positive and negative differences. Concentric marks represent Z-scores. All morphological features analysed are grouped into eight main groups: endoplasmic reticulum (ER), nucleus, nucleoli, Golgi + cytoskeleton, mitochondria, cellular area and shape, characteristics of the neighbour cells, and correlates between nucleus and cytoplasm regions. At the same time, these features are further categorized into the following subgroups: RD (radial distribution), L (location and spatial distribution), G (granularity), I (integrated intensity), C (cell measurements), N (nuclear measurements), and Cy (cytoplasm measurements).

4.4. Olaparib induced DNA damage in p53 WT RMS cells *in vitro*

PARP inhibitors (PARPi), such as olaparib, have emerged as a promising strategy for tumours with defects in HR genes, including those harbouring mutations in *BRCA1* and/or *BRCA2*. Beyond their established efficacy in HR-deficient cells, PARPi are being investigated in combination with other therapeutic agents to enhance their efficacy through synergistic interactions and to potentially sensitize tumours that are inherently resistant to PARPi. In RMS, where HR deficiencies are relatively uncommon, PARPi have been evaluated as radiosensitizers and in combination with agents targeting alternative DNA damage repair pathways, such as the newly developed ATR inhibitors. However, while the ability of PARP inhibitors to induce DNA DSBs has been demonstrated in p53 MUT RMS cells, their effects on p53 WT RMS cell lines have been less explored.

4.4.1. Olaparib elicited a dose-dependent accumulation of γH2AX in p53 WT RMS nuclei *in vitro*

To assess the induction of DSBs by olaparib in p53 WT RMS cells, cells were treated with increasing doses of olaparib (1, 2, 4, and 8 μM) for 24, 48, and 72 hours, and the number of nuclei positive for γH2AX foci was quantified using fluorescence microscopy. Etoposide (2.5 μM) was used as a positive control due to its established ability to bind TOP2, inhibit the religation of DNA breaks, and induce DSBs.

Microscopy analysis revealed a dose-dependent increase in γH2AX foci in p53 WT RMS cells treated with olaparib for 24, 48, and 72 hours (Figure 21a-b). Notably, in CW9019 cells, DNA damage induced by olaparib was detectable only at concentrations of 4 μM or greater, indicating that these cells require higher doses of olaparib to achieve similar levels of DNA damage compared to other cell lines. Moreover, the number of γH2AX-positive nuclei was lower in olaparib-treated cells compared to etoposide-treated cells, suggesting that while olaparib is effective in inducing DNA damage, it is less potent compared to etoposide at the tested doses. These findings demonstrated the ability of olaparib to induce DSBs in p53 WT RMS cells, albeit with lower efficiency compared to etoposide. Furthermore, the results suggested potential differences in cellular sensitivity and resistance to olaparib-induced DNA damage among different RMS cell lines.

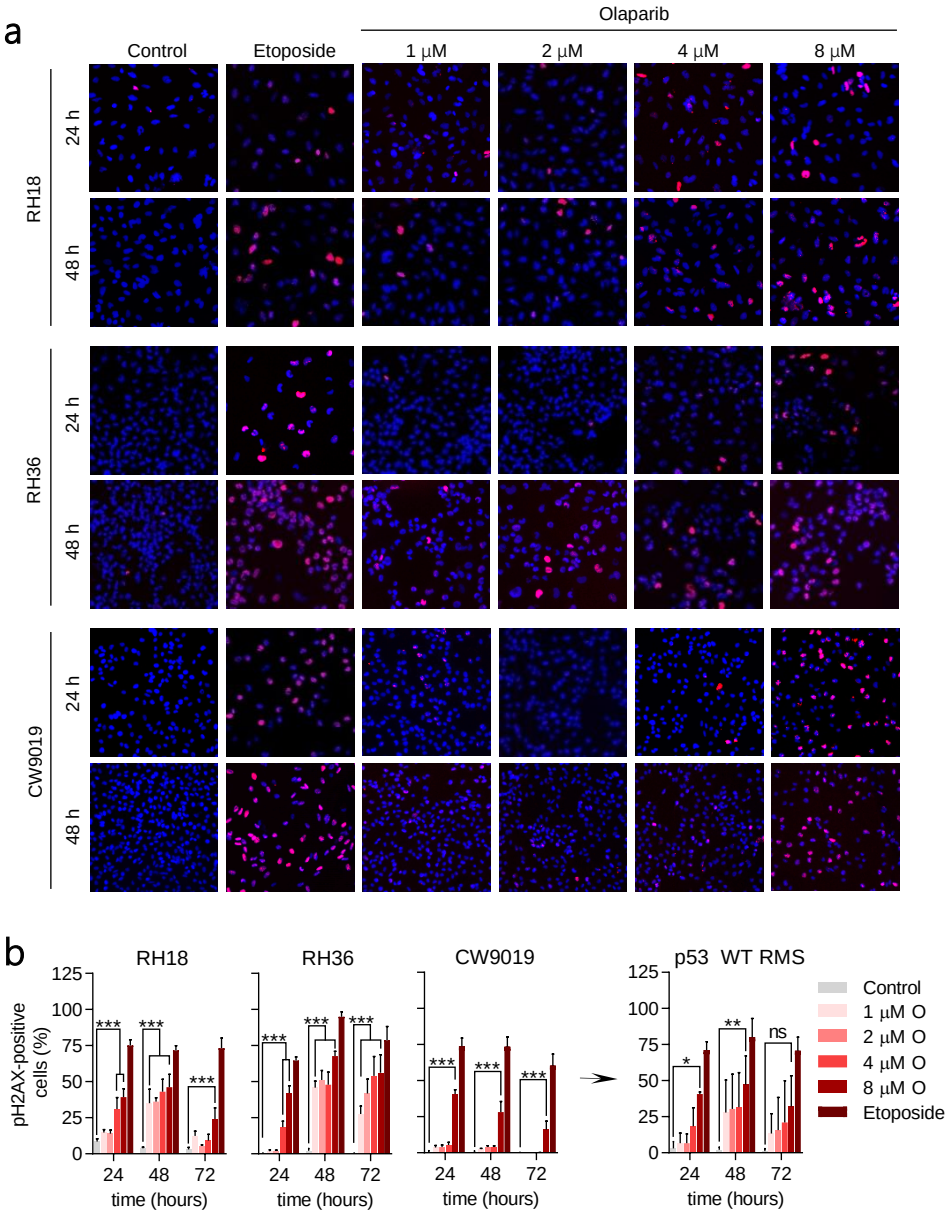

Figure 21. Olaparib elicited a dose-dependent accumulation of γH2AX in p53 WT RMS cell nuclei *in vitro*. (a) Microscope fluorescence images showing pH2AX / DAPI double staining of p53 WT RMS cells treated with vehicle (control), 2.5 μM etoposide (positive-control) and 1, 2, 4, and 8 μM olaparib at 24 and 48 hours post treatment. Pink-doted nuclei indicate the presence of pH2AX foci in the nucleus. (b) Bar plots representing the % of pH2AX-positive nuclei in cells treated with vehicle (control), 2.5 μM etoposide, 1, 2, 4, and 8 μM olaparib for 24, 48, and 72 hours. Bars represent the mean ± SEM of three replicates for each condition (n=3). Statistical significance was assessed using two-way ANOVA followed by Dunnett's post-hoc test.

4.4.2. The combination of siremadlin and olaparib did not enhance DNA damage beyond olaparib alone in p53 WT RMS cells

Given the previously observed synergistic effects of combining siremadlin and olaparib on cell survival and proliferation, the next objective was to determine whether this combination also led to a greater accumulation of DNA DSBs compared to the individual treatments. To address this, p53 WT RMS cells were treated with 0.08 μM siremadlin and 8 μM olaparib for 24, 48, and 72 hours. Subsequently, the number of γH2AX-positive nuclei was quantified and compared with those from the individual treatments and control (Figure 22a). The results indicated that the combination of siremadlin and olaparib did not result in a significantly higher accumulation of γH2AX foci compared to olaparib alone at any of the time points examined (24, 48, or 72 hours).

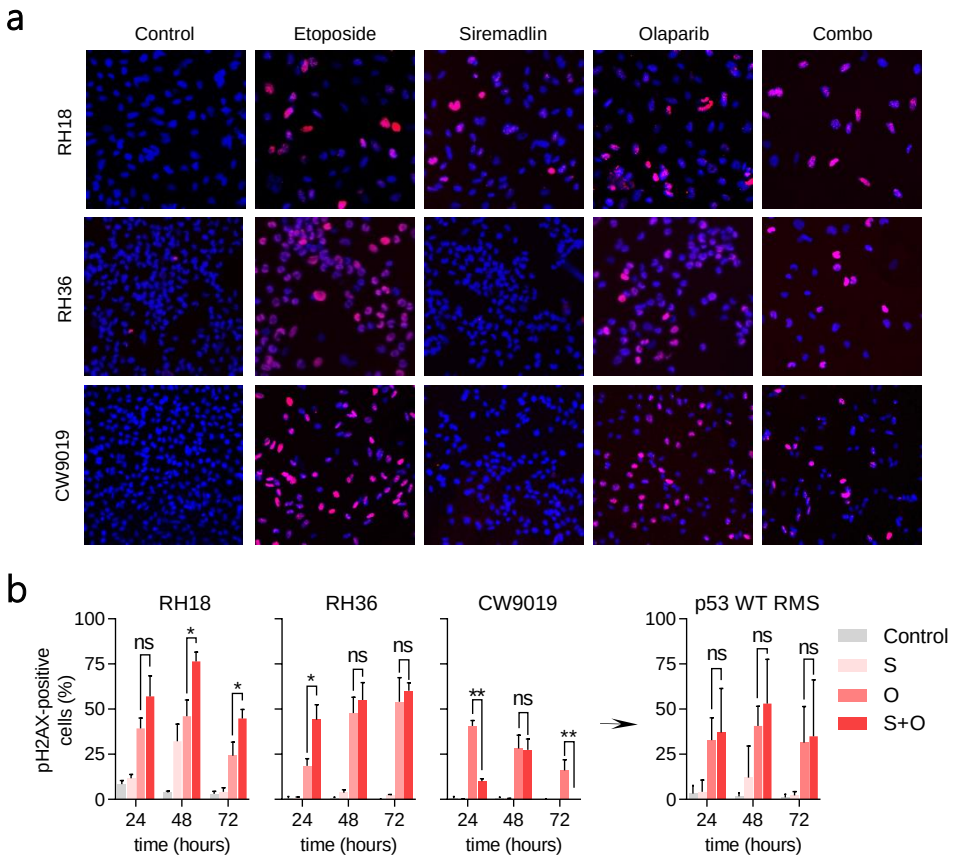

Figure 22. Evaluation of DNA damage in p53 WT RMS cells treated with siremadlin, olaparib, and their combination. (a) Fluorescence microscope images showing pH2AX / DAPI double staining in p53 WT RMS cells treated with vehicle (control), 2.5 μM etoposide (positive-control), 0.08 μM siremadlin, 8 μM olaparib, and their combination (combo) for 48 hours. Pink-stained nuclei indicate the presence of pH2AX foci, which are markers of DNA DSBs. (b) Bar plots showing the % of pH2AX positive nuclei in cells treated with vehicle (control), 2.5 μM etoposide (positive-control), 0.08 μM siremadlin (S), 8 μM olaparib (O), and their combination (S+O) for 24, 48, and 72 hours. Data are presented as the mean ± SEM of three replicates (n=3) for each condition. Statistical significance was assessed using two-way ANOVA followed by Dunnett's post-hoc test.

The variability in the response observed among the different RMS cell lines suggested that the effectiveness of the combination treatment may be influenced by both the duration of the treatment and intrinsic molecular features of each cell line. Overall, these findings indicated that combining siremadlin with olaparib did not consistently increase DNA damage levels compared to olaparib alone, suggesting that the observed synergistic effects on cell survival and proliferation were not due to an increased induction of DNA damage and may instead be related to other mechanisms or pathways.

4.5. The combination of siremadlin and olaparib synergistically enhanced the induction of apoptosis *in vitro*

Effective cancer therapies often involve the combination of agents that synergistically enhance cytotoxicity. In this study, the combination of siremadlin and olaparib demonstrated a synergistic reduction in p53 WT RMS cell survival and proliferation. However, the mechanisms driving these enhanced cytotoxic effects were not fully understood. To address this, we comprehensively examined the combined effects of siremadlin and olaparib on cell death, apoptosis, and cell cycle progression using a set of complementary techniques.

Hoechst/PI double staining, which differentiates between viable and dead or dying cells (e.g. apoptotic and necrotic cells), was initially used to assess cell death. The results revealed a significant increase in cell death rates in all p53 WT RMS cell lines treated with the combination for 72 hours, confirming enhanced cytotoxicity compared to individual treatments (Figure 23a). This enhanced cell death was further corroborated by apoptosis analysis using Annexin V/Sytox staining followed by flow cytometry, which demonstrated a marked increase in apoptotic cells following treatment with the combination (Figure 23b). These results suggested that the combination of siremadlin and olaparib enhanced apoptotic cell death in p53 WT RMS, potentially through the activation of p53-mediated apoptotic pathways.

Moreover, asynchronous cell cycle analysis using DAPI staining and flow cytometry revealed impaired cell cycle progression in p53 WT RMS cells treated with either olaparib alone or the combination of siremadlin and olaparib (Figure 23c). To further elucidate the molecular mechanisms underlying these effects, WB was used to quantify the expression levels of phosphorylated retinoblastoma protein (pRb, Ser807/811) and Cyclin B1, key regulators of G1/S and G2/M cell cycle transitions. Notably, a substantial reduction in both pRb and Cyclin B1 levels was observed in p53 WT RMS cells treated with the combination for 72 hours (Figure 23d). The reduction of these markers suggested that the combination therapy interfered with both G1/S and G2/M checkpoints, thereby contributing to the previously observed antiproliferative effects. These findings highlighted the pharmacological effects of siremadlin and olaparib in combination therapy, demonstrating strong antiproliferative effects, increased apoptosis, and disrupted cell cycle progression in p53 WT RMS cells.

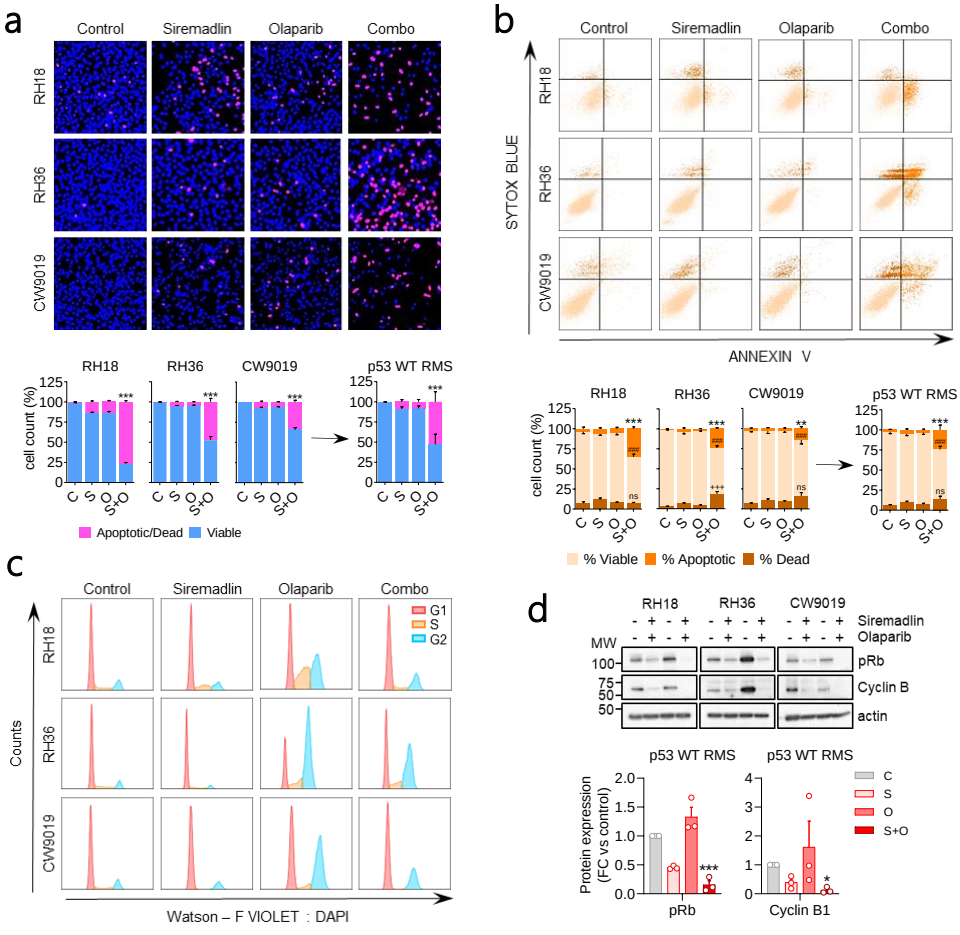

Figure 23. The combination of siremadlin and olaparib synergistically induced apoptosis and cell death in p53 WT RMS cells. (**a**) On the upper section, images of Hoechst / PI double staining showing the effects on cell death/apoptosis induction in p53 WT RMS cells treated with 80 nM siremadlin (S), 4 μM olaparib (O), or their combination (S+O) for 72 hours. Viable cells are stained in blue while dead/apoptotic cells are stained in pink. On the lower section, bar plots representing the % of viable or dead/apoptotic cells for each cell line and treatment. Data are expressed as the mean ± SEM of three replicates (*n*=3). (**b**) On the upper section, flow cytometry plots of Annexin V / Sytox double staining revealing the effects on apoptosis in p53 WT RMS cells treated with 80 nM siremadlin (S), 4 μM olaparib (O), or their combination (S+O) for 72 hours. On the lower section, bar plots representing the % of viable (Annexin V - / Sytox -), apoptotic (Annexin V +), or dead cells (Annexin V - / Sytox +) for each cell line and treatment condition. Bars represent the mean ± SEM of three replicates (*n*=3). (**c**) Representative plots of DNA content from flow cytometry analysis of p53 WT RMS cells treated with 80 nM siremadlin (S), 4 μM olaparib (O), or their combination (S+O) for 72 hours. The area under each peak represents the number of cells in G1 (red), S (orange), or G2/M (blue) phases according to the intensity of DAPI staining. (**d**) On the upper section, WB showing the expression of p-Rb or Cyclin B in p53 WT RMS cells treated with 80 nM siremadlin (S), 4 μM olaparib (O), or their combination (S+O) for 72 hours. Molecular weight (MW) markers are indicated by dashes on the left side of the membrane. On the lower section, bar plots showing the quantification of p-Rb (left) or Cyclin B (right). Protein expression was normalized to β-actin and is expressed as fold-change (FC) relative to vehicle-treated cells. Data are presented as the mean ± SEM of three p53 WT RMS cells (*n*=3). Statistical significance was assessed using two-way ANOVA followed by Dunnett's post-hoc test for all experiments.

4.6. Combination of siremadlin and olaparib led to an increased MDM2 cleavage and p53 transcriptional activity in p53 WT RMS

To explore the molecular effects of simultaneous treatment with siremadlin and olaparib, the expression levels of their respective target proteins, MDM2 and PARP, were quantified. Additionally, the impact on p53 was examined by assessing both total p53 expression and acetylated p53 (ac-p53, K382). Measuring acetylated p53 was of particular importance due to its critical role in modulating transcriptional activity, stability, and interactions with key regulatory proteins. Moreover, the expression of two p53 transcriptional targets, p21 and BAX, was evaluated alongside the aforementioned MDM2 to provide a comprehensive understanding of the molecular changes induced by the combination therapy.

In RH18 cells, treatment with siremadlin alone or in combination with olaparib led to a reduction in PARP expression, while olaparib alone led to a slight increase in both cleaved and total PARP at 72 hours (Figure 24a). Conversely, no significant differences were observed in PARP expression or its cleaved form in RH36 and CW9019 cells (Figures 24b-c).

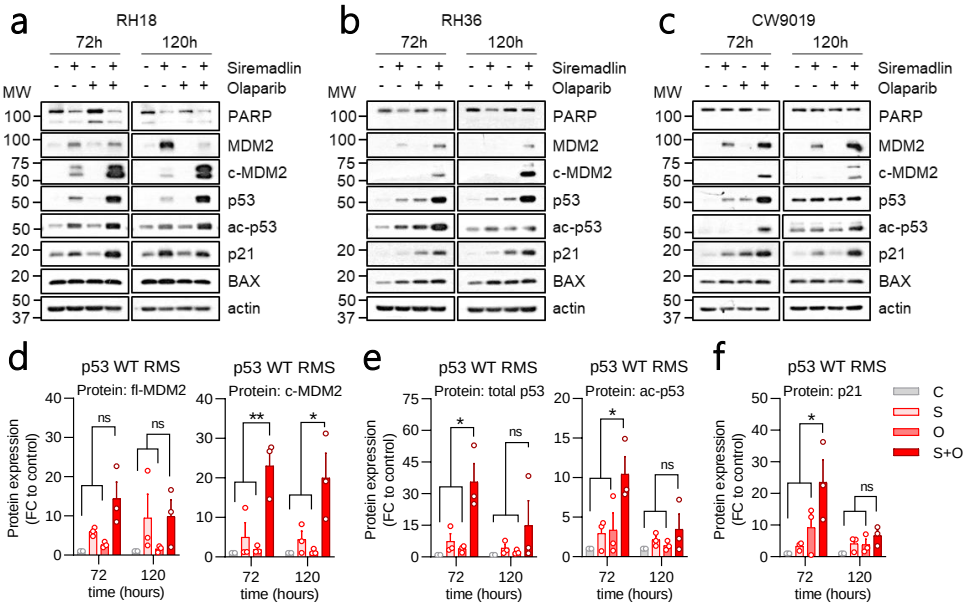

Figure 24. Combination of siremadlin and olaparib induces MDM2 cleavage and p53 accumulation surpassing the effects of both drugs individually. (**a - c**) Western blot showing the expression of PARP, full length MDM2 (MDM2), cleaved MDM2 (c-MDM2), total p53, acetylated p53 on K382 (ac-p53), p21 and BAX in p53 WT RMS cells treated with 80 nM siremadlin (S), 4 µM olaparib (O), or their combination (S+O) for 72 and 120 h. Molecular weight (MW) markers are indicated by dashes on the left side of the membrane. (**d-f**) Bar plot showing the quantification of (**d**) full length and cleaved MDM2 (c-MDM2), (**e**) total and acetylated p53, and (**f**) p21 in p53 WT RMS cells treated with 80 nM siremadlin (S), 4 µM olaparib (O), or their combination (S+O) for 72 and 120 h. Protein expression was normalized to β-actin and is expressed in fold-change (FC) relative to vehicle-treated cells (C). Data values are expressed as the mean ± SEM of three p53 WT RMS cells (*n*=3). Statistical significance was assessed using two-way ANOVA with Dunnett's post-hoc test.

Remarkably, the combination of siremadlin and olaparib led to a significant increase in MDM2 cleavage across all cell lines, indicating increased caspase activity towards MDM2 (Figures 24a; 24d). Simultaneously, the combination of both drugs also elicited the accumulation of p53 in all p53 WT RMS cells at 72 hours (Figures 24a-c; 24e). The observed correlation between MDM2 cleavage and p53 accumulation suggested that MDM2 cleavage may contribute to p53 stabilization and accumulation. Moreover, increased levels of acetylated p53 were also detected, indicating an enhanced transcriptional activity of p53 (Figures 24a-c; 24e). Notably, p53 levels returned to baseline after 120 hours of treatment with the combination in CW9019 cells, whereas p53 levels remained elevated in RH18 and RH36 cells, suggesting sustained p53 activity in these cell lines.

Regarding p53 targets, an increase in p21 expression was observed in all cell lines treated with the combination for 72 hours, supporting the obtained cell cycle results (Figures 24a-c; 24f). However, no significant differences were observed in BAX expression, suggesting that other proapoptotic proteins or molecular processes, such as the transcription-independent activation of BAX by p53, may contribute to the apoptotic process triggered by the combination of siremadlin and olaparib (Figures 24a-c).

To further assess the enhanced p53 transcriptional activity prompted by the combination, gene expression of established p53 target genes (*MDM2*, *CDKN1A*, *FBXW7*, *MDMX*) was quantified in p53 WT RMS cells using RT-qPCR at 24-, 48-, and 72-hours post-treatment. A strong increase in *MDM2* expression was observed in p53 WT RMS cells treated with the combination compared to control (12- to 30-fold), siremadlin (4- to 5-fold), and olaparib alone (8- to 25-fold), with levels peaking at 48 hours (Figure 25a). Similar increases were observed for other downstream p53 targets, including *CDKN1A*, *FBXW7*, and *MDMX*, following the treatment with the combination (Figures 25b-d). These results demonstrated the synergistic effect of combining siremadlin and olaparib in activating p53-mediated pathways, evidenced by the cleavage of MDM2, accumulation of p53, and the increased expression of its transcriptional targets, particularly MDM2 and p21, at bot h protein and gene level.

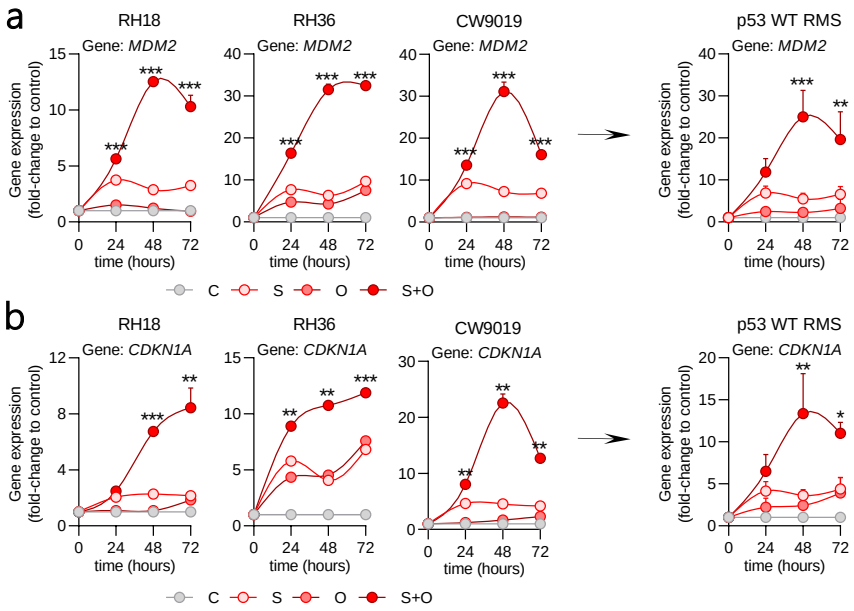

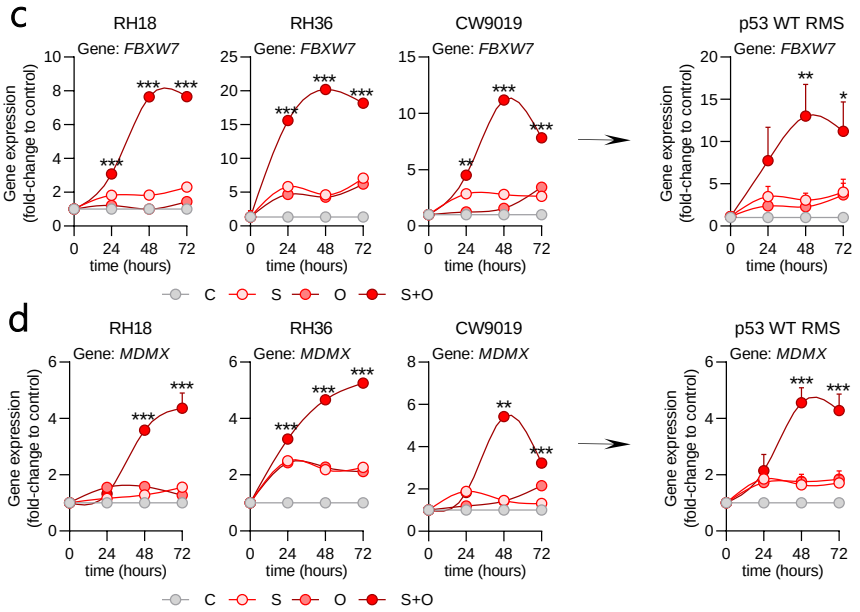

Figure 25. Combination of siremadlin and olaparib induces the expression of p53 transcriptional targets. Dot plots showing the gene expression of (a) *MDM2*, (b) *CDKN1A*, (c) *FBXW7*, and (d) *MDMX* in p53 WT RMS cell lines treated with 80 nM siremadlin (S), 4 µM olaparib (O), or their combination (S+O) for 24, 48, or 72 h. The housekeeping gene *TBP* was used as an endogenous control. Gene expression fold-change (FC) is relative to the expression of each gene in vehicle-treated cells (C). Data values represent the mean ± SEM of three p53 WT RMS cells (n=3). Statistical significance was assessed using two-way ANOVA followed by Dunnett's post-hoc test.

4.7. Combination of siremadlin and olaparib impaired tumour growth and extended mice overall survival *in vivo*

To evaluate the *in vivo* efficacy of combining siremadlin and olaparib, CDOX were established by injecting RH36 cells into the gastrocnemius muscle of SCID mice. Initially, a pilot study was conducted to identify effective dosing regimens that would reduce tumour growth while minimizing toxicity. Thus, RH36 CDOX were treated with 50 mg/kg siremadlin, 100 mg/kg olaparib, and their combination at different concentrations (1X, 0.5X, and 0.25X) twice weekly via oral gavage. Results demonstrated that all combination regimens reduced tumour growth compared to single-drug treatments and control, suggesting a potential synergistic effect *in vivo* (Figure 26a). Among these regimens, the combination of 50 mg/kg siremadlin and 100 mg/kg olaparib achieved the most favourable tumour reduction outcomes. However, the use of 50 mg/kg siremadlin resulted in a notable reduction in body weight after 30 days of treatment, indicating potential systemic toxicity associated with this dosing regimen (Figure 26b).

In a subsequent *in vivo* study, RH36 CDOX were treated with 25 mg/kg siremadlin and/or 50 mg/kg olaparib, with the sample size increased to six mice per group. Consistently, a significant reduction in tumour growth and extended overall survival was observed in mice treated with the combination (Figure 26c-d). Notably, no reduction in mice weight was observed throughout the treatments (Figure 26e). These results underscored the enhanced therapeutic efficacy of the combination regimen without causing apparent side effects at the tested doses.

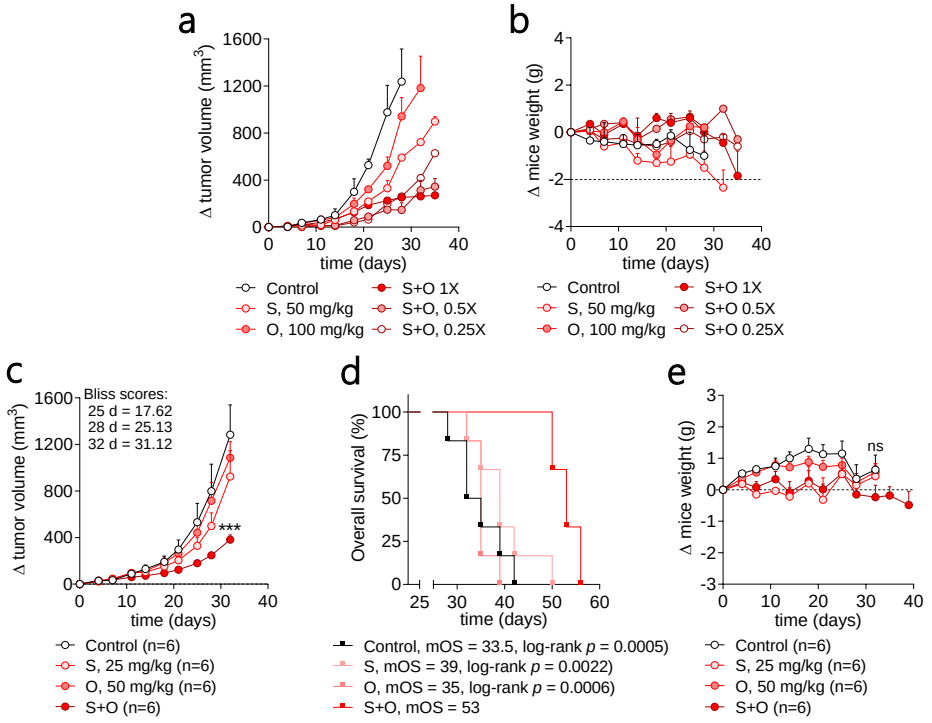

Figure 26. Combination of siremadlin and olaparib reduced tumour growth and extended mice overall survival. (**a**) Dot plot showing tumour volume increase over time for RH36-derived tumours treated with 50 mg/kg siremadlin (S), 100 mg/kg olaparib (O), or their combination at various doses: full (S+O 1X), half (S+O 0.5X), and quarter (S+O 0.25X). Each dot represents the mean ± SEM of two replicates (*n*=2). (**b**) Dot plot displaying the changes in mice weight over time for the same treatments as in panel (a). Each dot represents the mean ± SEM of two replicates (*n*=2). (**c**) Dot plot showing the increase in tumour volume over time of RH36-derived tumours treated with 25 mg/kg siremadlin (S), 50 mg/kg olaparib (O) or their combination (S+O). Each dot represents the mean ± SEM of six tumours (*n*=6). Two-way ANOVA with Dunnett's post-hoc test was used to determine statistical significance. (**d**) Kaplan-Meier curves showing overall survival (in %) of mice treated with 25 mg/kg siremadlin (S), 50 mg/kg olaparib (O) or their combination (S+O). Statistical significance was assessed using log-rank test (*n*=6). (**e**) Dot plot showing changes in mice weight over time for the same treatments as in panels (c) and (d). Statistical significance was determined using two-way ANOVA followed by Dunnett's post-hoc test.

Simultaneously, to evaluate the molecular effects of various cumulative doses, a separate cohort of RH36 CDOX received 1, 3, and 5 doses of 25 mg/kg siremadlin and/or 50 mg/kg olaparib. Tumour samples were collected 24 hours after the last administration. Protein expression analysis revealed increased levels of total and acetylated p53, as well as elevated expression of its downstream targets, p21 and MDM2, in RH36-derived tumours treated with 3 and 5 doses of the combination (Figure 27a). These results suggested that the combination of siremadlin and olaparib significantly enhanced p53 activity after 3 and 5 doses. Additionally, gene expression analysis by RT-qPCR revealed increased mRNA levels of *MDM2* and *CDKN1A* following 3 and 5 doses of the combination (Figure 27b). However, by the study endpoint, *MDM2* and *CDKN1A* mRNA levels had reverted to baseline levels similar to those in control and single-drug treatments, indicating an adaptive response of RH36 cells to the treatment likely occurring between the administration of 5 doses and the endpoint of the study. Altogether, these results demonstrate the *in vivo* efficacy of combining siremadlin and olaparib, highlighting its effectiveness in reducing tumour growth and extending overall survival while enhancing p53 activity. Molecular findings further suggest that an adaptive response developed over time, underscoring the need for further investigation into the mechanisms driving this adaptation.

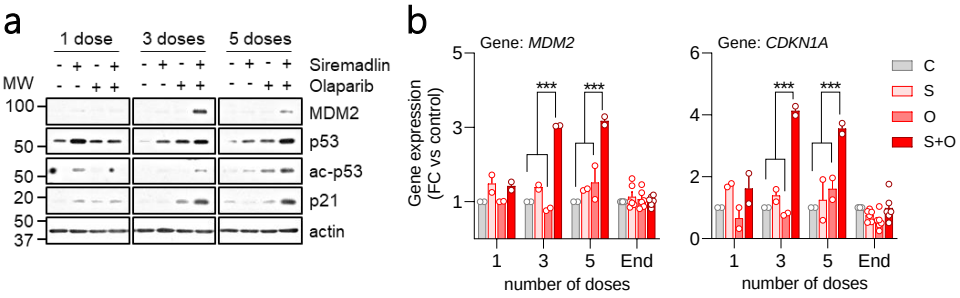

Figure 27. Protein and gene expression analysis of RH36 xenografts treated with the combination of siremadlin and olaparib. (**a**) Western blot showing the expression levels of MDM2, total p53, acetylated p53 on K382 (ac-p53), and p21 in RH36-derived tumours treated with 1, 3, or 5 doses of 25 mg/kg siremadlin (S), 50 mg/kg olaparib (O), or their combination (S+O). β-actin was used as loading control. Molecular weight (MW) markers are indicated by dashes on the left side of the membrane. (**b**) Bar plots showing the gene expression levels of *MDM2* (left) and *CDKN1A* (right) in RH36-derived tumours. Tumours were treated with 25 mg/kg siremadlin (S), 50 mg/kg olaparib (O) or their combination (S+O) for 1, 3, 5 doses, or until the study endpoint. The housekeeping gene *TBP* was used as an endogenous control. Gene expression fold-change (mean FC ± SEM) is relative to the basal expression of each gene in vehicle-treated tumours. Statistical significance was determined using restricted maximum likelihood followed by Dunnett's post-hoc test, accounting for the differing number of replicates across groups (n=2 for tumours treated with 1, 3, or 5 doses, and n=6 for tumours treated until the endpoint).

4.8. Combining siremadlin and olaparib with selected chemotherapies further enhanced their therapeutic effects

While the combination of siremadlin and olaparib showed potential in reducing tumour growth, it did not achieve complete tumour eradication as a standalone treatment. Thus, integrating siremadlin and olaparib with currently approved chemotherapy regimens for RMS was explored as a strategy to optimize clinical efficacy, minimize toxicity, and overcome treatment resistance. To assess the efficacy of combining these agents with conventional chemotherapy regimens, two distinct experimental approaches were followed (Figure 28a).

In the first approach, p53 WT RMS cells were pre-treated with actinomycin, vincristine, or phosphoramide mustard (an active metabolite of cyclophosphamide) for 2 days (48 hours). Subsequently, siremadlin and olaparib were added to the pre-treated cells for an additional 3 days. The results demonstrated that the addition of siremadlin and olaparib, both individually and in combination, led to enhanced suppression of cell survival compared to chemotherapy alone, indicating that both drugs retained their antitumoral efficacy when administered after conventional chemotherapies (Figure 28b). In the second approach, p53 WT RMS cells were treated simultaneously with siremadlin and/or olaparib along with first-line chemotherapeutics over a period of 7 days. Similar to the first approach, the triple combination significantly inhibited cell survival at 3 days. However, the synergistic effect diminished over time, and no statistically significant differences were observed at 5 and 7 days (Figure 28c).

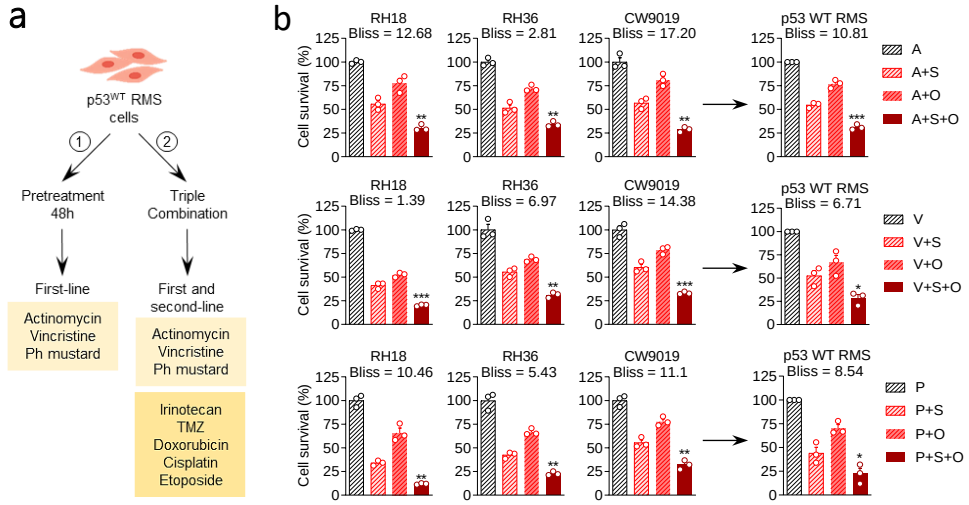

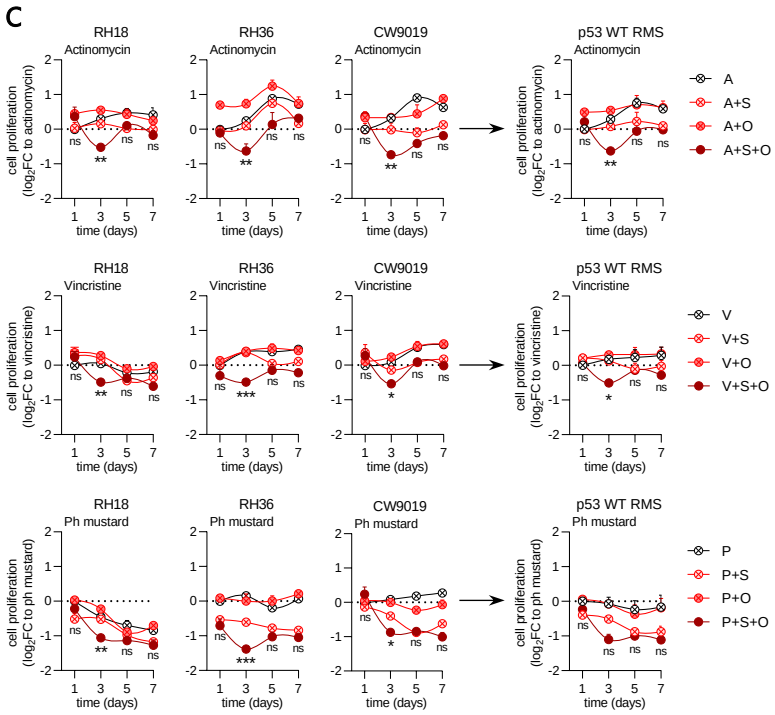

Figure 28. The combination of siremadlin and olaparib retained their antitumoral efficacy following conventional chemotherapy treatments (**a**) Schematic representation of the two distinct approaches used to evaluate the efficacy of incorporating both siremadlin and olaparib into conventional chemotherapy regimens. (**b**) Bar plots showing the effects siremadlin (S) and olaparib (O) on cell survival of p53 WT RMS cells previously treated with actinomycin-D (A), vincristine (V), or phosphoramide mustard (P) for 2 days (48 hours). Cell survival (in %) is relative to the pre-treated cells. Data represent the mean ± SEM from three replicates (*n*=3). Statistical significance was assessed using one-way ANOVA followed by Dunnett's post-hoc test. (**c**) Dot plots showing the effect on cell proliferation of combining siremadlin (S) and olaparib (O) with first-line chemotherapeutics. Cell proliferation is expressed as log_2 fold-change (log_2FC) relative to cells treated with chemotherapy alone. Dots represent the mean ± SEM from three replicates (*n*=3). Statistical significance was determined using two-way ANOVA followed by Dunnett's post-hoc test.

Given the variable efficacy observed with the combination of siremadlin and olaparib with first-line chemotherapies, their combination with second-line chemotherapies was also explored. This investigation was prompted by the need to develop alternative therapeutic strategies for patients who either do not respond to first-line treatments or experience disease progression following initial therapy. By integrating siremadlin and olaparib with second-line chemotherapeutics, we aimed to enhance treatment outcomes and provide additional therapeutic options for RMS patients.

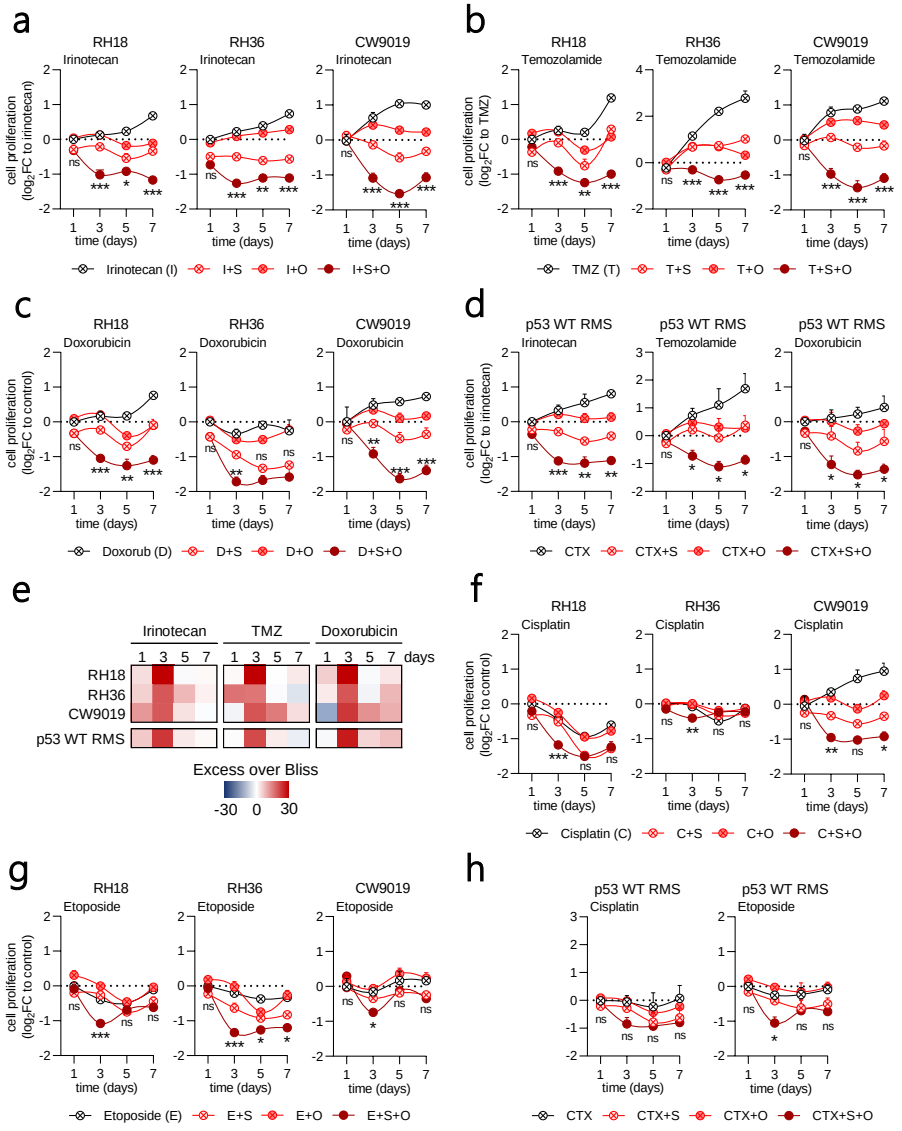

Figure 29. The combination of siremadlin and olaparib showed synergistic effects with irinotecan, TMZ, and doxorubicin. (**a-d**) Dot plots showing the effects on cell proliferation in p53 WT RMS cells treated simultaneously with siremadlin (S) and olaparib (O) in combination with (**a**) irinotecan, (**b**) TMZ, or (**c**) doxorubicin. Panel (**d**) shows the mean results for these combinations across all p53 WT RMS cells. (**e**) Heatmap displaying the mean synergy Bliss-scores for the combination shown in panels (a-d). (**f-h**) Dot plots showing the effects on cell proliferation in p53 WT RMS cells treated simultaneously with siremadlin (S) and olaparib (O) in combination with (**f**) cisplatin or (**g**) etoposide. Panel (**h**) presents the mean results for these combinations across all p53 WT RMS cell lines. In all cases, cell proliferation is expressed as log2 fold-change (log_2FC) relative to cells treated with chemotherapy alone. Data represent the mean ± SEM from three replicates (n=3). Statistical significance was assessed using two-way ANOVA followed by Dunnett's post-hoc test.

To evaluate this approach, p53 WT RMS cells were treated with siremadlin and/or olaparib in combination with second-line chemotherapeutic agents, including irinotecan, TMZ, doxorubicin, cisplatin, and etoposide. Notably, the combination of siremadlin and olaparib consistently demonstrated synergistic effects with irinotecan, TMZ, and doxorubicin across all p53 WT RMS cell lines (Figures 29a-c). Although the synergistic effects observed at 3 days tended to become additive at 5 and 7 days (Figure 29d), these combinations continued to exert potent cytotoxic effects, significantly reducing cell proliferation compared to chemotherapy alone or dual combinations. In contrast, as observed with actinomycin, vincristine, and phosphoramide mustard, the combination of siremadlin and olaparib with cisplatin or etoposide yielded inconsistent results (Figure 29f-h). This variability suggests that while the initial synergistic responses to the triple combinations of siremadlin, olaparib, and first-line chemotherapeutics or etoposide were promising, these effects were not consistently sustained over the long term.

Conversely, the consistent and robust results obtained with the combination of siremadlin and olaparib with irinotecan, TMZ, and doxorubicin underscored their potential for sustained therapeutic benefit. Integrating siremadlin and olaparib with these specific second-line chemotherapeutics may offer more durable responses compared to its combination with first-line treatments. Future research should focus on optimizing these combination strategies and elucidating the underlying mechanisms that sustain their synergistic effects. The encouraging results from combining siremadlin and olaparib with irinotecan, TMZ, and doxorubicin present an exciting opportunity for advancing treatment protocols and improving patient care in RMS. Continued exploration in preclinical and clinical settings is warranted to validate these results and develop new, more effective therapeutic approaches.

5. Discussion

RMS is the most common soft-tissue sarcoma in children and adolescents, characterized by aggressive neoplasms containing tumour cells that resemble skeletal myoblasts[129]. Unlike many adult tumours, p53 loss-of-function mutations are rare in RMS, occurring in only about 5-10% of cases[134]. However, the tumour suppressive functions of p53 can still be compromised in RMS through alternative genetic alterations, such as those affecting the RAS-MAPK or PI3K-AKT-mTOR pathways, MDM2 amplifications, or CDK2NA deletions, leading to persistent MDM2 activation[521–524]. Several studies have reported MDM2 overexpression in RMS, linking high MDM2 levels to multidrug resistance, particularly in response to chemotherapy, in both RMS and other malignancies[525–529]. As a result, MDM2 inhibition has emerged as a potential therapeutic vulnerability in p53 WT RMS, particularly when combined with standard chemotherapies.

Preclinical studies have supported this strategy, showing promising results when MDM2 inhibitors are combined with specific treatments for p53 WT RMS. For instance, nutlin-3a, a first-generation MDM2 inhibitor, enhanced the antitumor activity of vincristine and actinomycin D in p53 WT RMS cells[356]. Similarly, idasanutlin enhanced the efficacy of ionizing radiation in MDM2-amplified RH18 cells and xenografts[357]. However, these studies primarily focused on specific combinations, potentially overlooking other synergistic interactions with newly developed or currently tested compounds for R/R RMS.

In this study, we evaluated the efficacy of four promising MDM2 inhibitors (siremadlin, idasanutlin, navtemadlin, and MI-773), along with four experimental MDM2/X inhibitors, as single agents. Additionally, we conducted a drug combination screening, pairing siremadlin with selected targeted therapies and standard chemotherapies commonly used in paediatric cancer treatment. Our findings underscore the therapeutic potential of combining siremadlin with specific compounds, notably olaparib, for the treatment of p53 WT RMS. Through comprehensive investigations of the impact of this combination both *in vitro* and *in vivo*, and its integration with currently approved treatments, our study provides valuable insights into novel multidrug therapeutic strategies. These findings hold promise for advancing effective therapies not only for p53 WT RMS but also for other solid tumours exhibiting similar molecular features.

5.1. Exploiting the MDM2-p53 axis: the therapeutic vulnerability of p53 WT cells to MDM2 inhibitors

Targeting the MDM2-p53 interaction with small-molecule inhibitors represents a promising therapeutic strategy for treating p53 WT tumours. MDM2 inhibitors have shown efficacy in inhibiting the proliferation of p53 WT cells both *in vitro* and *in vivo* by preventing p53 degradation, and potentially restoring its tumour-suppressive activities[304,319,508]. Currently, several MDM2 inhibitors with distinct chemical scaffolds, including idasanutlin (RG7388), siremadlin (HDM201), navtemadlin (AMG-232), MI-773, CGM097, alrizomadlin (APG-115), and brigimadlin (BI-907828), are being evaluated in clinical trials[320,354]. However, despite their potential, their efficacy, specificity, and antitumoral effects in RMS remain poorly understood. Thus, the primary aim of this thesis was to evaluate the differential effects of these MDM2 inhibitors on p53 WT versus p53 MUT RMS cells. By assessing how these inhibitors impacted cells with distinct p53 statuses, this study aimed to identify the most effective and selective compounds for further investigation. In addition to influencing sensitivity to MDM2 inhibitors, extensive research has highlighted the pivotal role of p53 status in modulating responses to a variety of therapeutic agents across different cancers[530–533]. Interestingly, while mutations in p53 are often linked to increased resistance to therapies, the presence of functional p53 WT can, paradoxically, reduce therapeutic efficacy in certain tumors[534–537]. Despite these findings, there is a significant gap in the literature regarding how p53 status influences drug sensitivity specifically in RMS. This thesis aims to address this gap by systematically evaluating the differential responses of p53 WT and p53 MUT RMS cells to a variety of targeted therapies and standard chemotherapeutics.

5.1.1. Enhanced sensitivity of p53 WT RMS cells to siremadlin

To address these questions, RMS cells classified by p53 status were treated with four MDM2 inhibitors (siremadlin, idasanutlin, navtemadlin, and MI-773) along with twenty-two additional drugs, including standard chemotherapeutics and targeted therapies commonly used in paediatric oncology. Cell survival analysis demonstrated that p53 WT RMS cells were significantly more sensitive to several MDM2 inhibitors compared to p53 MUT RMS cells, highlighting the potential of these compounds for selectively targeting p53 WT RMS cells (Figure 15a-b). This finding is consistent with previous research indicating that first- and second-generation MDM2 inhibitors are particularly effective against p53 WT tumours by preventing MDM2-mediated degradation of p53[356,538,539].

Conversely, no significant differences were observed in the sensitivity of p53 WT or p53 MUT RMS cells to chemotherapeutics and other targeted therapies, suggesting that p53 status may not substantially influence the response to these drugs (Figure 15a-b). To further elucidate this aspect, future investigations employing p53 knockout models could provide valuable insights by comparing drug responses in isogenic cell lines. Additionally, conducting time-course and dose-response experiments could help uncover subtle differences in drug sensitivity related to p53 status, thereby refining our understanding of how p53 status impacts therapeutic efficacy in RMS.

Regarding MDM2 inhibitors, the comparative analysis of its dose-responses indicated lower IC_{50} values for siremadlin and idasanutlin in p53 WT RMS cells, suggesting a higher potency of these compounds in activating the p53 pathway compared to navtemadlin and MI-773 (Figure 15c). Remarkably, siremadlin exhibited a greater difference in $logIC_{50}$ values between p53 WT and p53 MUT cells compared to other inhibitors, indicating its superior specificity and selectivity in targeting MDM2-p53 interaction (Figure 15c). Based on these findings, siremadlin was selected for further studies to explore and validate its efficacy and therapeutic potential alone and in combination with other drugs.

5.1.2. Expression levels of p53, p21, and MDM2 as predictive biomarkers of response to MDM2 inhibitors in RMS cell lines

The tumour suppressor p53, together with its downstream effectors p21 and MDM2, play pivotal functions in cell cycle regulation, apoptosis, and genomic stability[310,311]. Increased transcriptional activity of p53 typically results in increased expression of its target genes, reflecting the functional activity of either p53 WT or p53 mutant MUT cells. While p53 WT cells are generally more responsive to MDM2 inhibitors, incorporating the expression levels of specific p53 targets can enhance predictive models. This approach can identify p53 MUT cells that retain partial p53 activity and might respond to MDM2 inhibitors, as well as p53 WT cells that have lost p53 activity and are less likely to benefit from the treatment[540,541].

Prior to this work, the potential predictive value of p53 and its downstream targets for MDM2 inhibitors in RMS had not been thoroughly investigated. Therefore, we first evaluated the expression levels of p53, p21, and MDM2 in six RMS cell lines and correlated these levels with the IC_{50} values of MDM2 inhibitors in these cells (Figures 16a-d).

Our analysis revealed that the expression levels of p53, p21, and MDM2 did not significantly differ between p53 WT and p53 MUT cells, likely due to substantial variability among p53 WT cells (Figure 16a-c). This variability may be attributed to molecular heterogeneity, such as MDM2 amplification in RH18 cells and CDKN2A loss in CW9019 cells [40,525,542], which may influence the basal expression levels of these p53 targets.

Despite this variability, gene and protein expression levels of MDM2 and p21 correlated with the IC_{50} values of MDM2 inhibitors (Figure 16d). Notably, the strongest correlation was observed between p53 status and IC_{50} values, suggesting that p53 status serves as a more robust predictor of response to MDM2 inhibitors than the expression levels of individual p53 targets. Furthermore, the strong correlation between gene and protein expression levels for MDM2 and p21 supports the interchangeability of these measurements in predictive models. Overall, these findings highlight the potential of p53 status as a key factor in predicting therapeutic response and underscore the importance of considering molecular heterogeneity in future studies. Expanding the study to include additional RMS cell lines could further elucidate the diversity in responses to MDM2 inhibitors and enhance the development of more accurate predictive models.

5.1.3. Time-dependent activation of the p53 pathway by siremadlin

To investigate the molecular effects of siremadlin on p53 activity, the temporal changes in gene and protein expression levels of p53 and its downstream targets, MDM2 and p21, were analysed in RMS cells. Treatment with siremadlin resulted in a progressive accumulation of p53 and its downstream targets, MDM2 and p21, in p53 WT RMS cells at 8,16, and 24 hours post-treatment (Figures 16e-f). Gene expression analyses further supported these observations, revealing increased levels of *MDM2* and *CDKN1A* in p53 WT RMS cells treated with siremadlin, indicating effective activation of p53 transcriptional activity (Figure 16g). These results are consistent with previous studies demonstrating a p53 accumulation followed by elevated p21 expression in p53 WT RMS cells treated with other MDM2 inhibitors[356,538]. In addition, the induction of p21 had also been observed in MDM2-amplified OS cells treated with siremadlin[543]. Collectively, these findings underscore the potential of siremadlin to effectively activate the p53 pathway in p53 WT RMS cells and emphasize the importance of quantifying MDM2 and p21 expression to evaluate p53 pathway activation.

5.2. Evaluating the efficacy and specificity of novel dual MDM2/X inhibitors

The rationale for developing MDM2/X dual inhibitors stems from the intricate regulatory roles that MDM2 and MDMX (also known as MDM4) play in the p53 pathway. MDMX is a paralog of MDM2 that also acts as critical negative regulator of p53 through both redundant and complementary roles[544]. Unlike MDM2, MDMX does not directly promote p53 ubiquitination and degradation nor its transport from the nucleus to the cytoplasm, as it lacks E3 ubiquitin ligase activity[545]. However, similar to MDM2, MDMX binds to p53 the TAD1 and TAD2 regions, thereby inhibiting its transactivation activity. By binding to p53, both MDM2 and MDMX can interfere with p300/CBP-mediated acetylation of p53, thereby reducing its transcriptional activity[546,547]. Moreover, MDMX is often amplified and highly expressed in p53 WT human cancers[548–550]. The redundant and complementary roles of MDM2 and MDMX suggest that inhibiting only MDM2 may not be sufficient to fully reactivate p53, as MDMX can compensate for MDM2 inhibition, resulting in incomplete p53 activation[320,551,552]. Additionally, tumours can develop resistance to MDM2 inhibitors potentially through upregulation or stabilization of MDMX, suggesting that dual inhibition could be beneficial in addressing potential resistance mechanisms[320,346,551–553]. By targeting both MDM2 and MDMX, these dual inhibitors could be effective across a wider range of cancer types and genetic backgrounds, while also addressing tumour heterogeneity by affecting all tumour cells, regardless of their MDM2/X expression levels.

The collaborative research with the Medicinal Organic Chemistry group at the University of Lisbon aimed to evaluate the efficacy of new experimental compounds as dual inhibitors of MDM2/X. This study included compounds from two different chemical classes: spiropyrazoline oxindole derivatives (ME240, ME242, ME258) and a tryptophanol-derived oxazoloisoindolinone derivative (ME62). Previous studies had indicated that these compounds had limited selectivity for targeting p53 WT ($p53^{+/+}$) compared to p53 MUT ($p53^{-/-}$) HCT166 colorectal carcinoma cells[554,555]. However, co-immunoprecipitation experiments had demonstrated that ME-62 effectively binds to and inhibits both MDM2-p53 and p53-MDMX interactions. Furthermore, ME-62 had shown enhanced selectivity *in vivo* in p53 WT HCT166 xenografts compared to its p53 MUT counterparts, highlighting ME-62 as a promising anticancer drug candidate[554].

In this study, p53 WT and p53 MUT RMS cells were treated with escalating doses of ME240, ME242, ME258, and ME62 (also known as DIMP53-1) for a 72 hours to establish dose-response curves. The experimental compounds exhibited significantly higher IC_{50} values in p53 WT RMS compared to established MDM2 inhibitors (siremadlin, idasanutlin, navtemadlin, and MI-773), indicating lower potency (Figure 17a). Additionally, unlike the results observed with MDM2 inhibitors, $logIC_{50}$ values did not differ between p53 WT and p53 MUT RMS cells, indicating a lack of selectivity for p53 WT RMS cells.

Given that p53 status is a major determinant of the response to MDM2/X inhibitors[325,346,398,556], and based on the results obtained with established MDM2 inhibitors in RMS cells, these findings suggested that the experimental compounds lacked specificity in targeting MDM2/X-p53 interactions. Consequently, these compounds were excluded from further consideration in the project, and the focus shifted to continuing the project with the MDM2 inhibitor siremadlin. However, it is important to note that subsequent studies with these compounds have proposed ME-62 derivatives (SLM53-1/2) as a p53-activating agents rather than MDM2/X inhibitors, with the ability to interact with and activate both p53 wild-type and multiple hotspot p53 mutants[557,558]. Similarly, a new set of spiropyrazoline oxindole derivatives has been developed with the aim of inhibiting both MDM2-p53/X protein-protein interactions[559].

5.3. Enhancing siremadlin efficacy with olaparib in p53 WT RMS: morphological changes, DNA damage induction, cell cycle arrest and apoptosis

The initial rationale for using MDM2 inhibitors stemmed from their ability to activate the p53 pathway in p53 WT cells, theoretically inducing strong apoptotic responses. However, accumulating evidence indicates that the apoptotic response elicited by p53 activation in response to MDM2 inhibitors is often limited due to the complex and context-dependent patterns of p53 activity[319,347,348]. Furthermore, incorporating MDM2 inhibitors into cancer therapy has faced significant hurdles, particularly in early-phase clinical trials where monotherapy with these agents has demonstrated limited efficacy[320,354,355]. These observations have prompted the exploration of combination therapies to enhance their antitumoral effects.

Given that MDM2 inhibitors activate p53 WT without inducing significant genotoxic effects, these compounds are considered promising candidates for improving the efficacy of chemotherapy and radiotherapy, while also minimizing the likelihood of resistance associated with single-agent treatments[304,319]. Furthermore, combining MDM2 inhibitors with other targeted therapies has emerged as a promising strategy to enhance the often-modest therapeutic effects observed with these drugs alone. For example, co-treatment of p53 WT cells with MDM2 inhibitors and apoptotic inducers, such as venetoclax (a BCL-2 inhibitor), has demonstrated efficacy in preclinical studies, and this combination is currently under investigation in clinical trials[560–563]. Additionally, MDM2 inhibitors are being tested in combination with tyrosine kinase inhibitors, as well as inhibitors targeting the RAS-MAPK and PI3K-AKT-mTOR pathways, due to the interconnected nature of these frequently dysregulated pathways in cancer[494,564–569]. Ongoing clinical trials are also investigating various combinations of MDM2 antagonists with monoclonal antibodies targeting the PD-1/PD-L1 interaction or B-lymphocyte antigen CD20, while alternative combination regimens involving CDK4/6 or proteasome inhibitors are being explored to further enhance the antiproliferative effects of p53 activation[570–576]. Overall, the exploration of diverse combination regimens involving MDM2 inhibitors represents a dynamic and promising approach in cancer treatment. However, while advancements are being made in understanding and implementing combination strategies in adult cancers, the need for parallel research in paediatric oncology remains a critical frontier[350].

5.3.1. A comprehensive drug combination screening identifies the synergistic effect of combining siremadlin with olaparib in reducing survival of p53 WT RMS cells

To address the limitations observed with MDM2 inhibitors as monotherapies, our study employed a comprehensive drug combination screening approach to identify synergistic combinations that could enhance therapeutic efficacy in p53 WT RMS. This screening involved the combination of siremadlin with selected targeted therapies and standard chemotherapies commonly used in paediatric cancer treatment (Figure 30). Notably, among the tested combinations, the pairing of siremadlin with olaparib emerged as the most promising, demonstrating the highest excess over Bliss score and a notable reduction in cellular viability compared to either drug alone (Figures 18a-b).

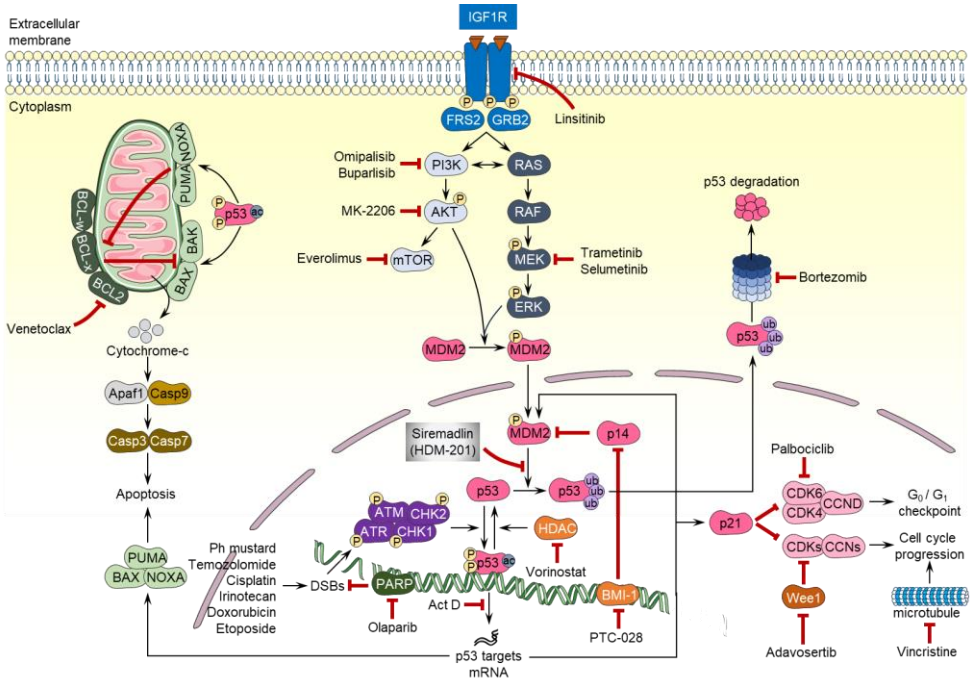

Figure 30. Combination strategies tested for enhancing the efficacy of MDM2-p53 inhibitors in p53 WT RMS. A comprehensive drug combination screening was employed to identify synergistic combinations that could enhance therapeutic efficacy in p53 WT RMS. This screening evaluated siremadlin (HDM-201) in combination with various targeted therapies such as linsitinib (IGF1R inhibitor), omipalisib and buparlisib (PI3K inhibitors), MK-2206 (AKT inhibitor), everolimus (mTOR inhibitor), trametinib and selumetinib (MEK inhibitors), venetoclax (BCL-2 inhibitor), bortezomib (proteasome inhibitor), palbociclib (CDK4/6 inhibitor), vorinostat (HDAC inhibitor), PTC-028 (BMI-1 inhibitor), adavosertib (Wee1 inhibitor), and olaparib (PARP inhibitor). Additionally, siremadlin was tested in combination with standard chemotherapies commonly used in paediatric cancer treatment, including DNA-damaging agents such as phosphoramide mustard, temozolomide, cisplatin, irinotecan, doxorubicin, and etoposide, as well as microtubule inhibitors like Vincristine and the transcription inhibitor actinomycin D (Act D).

These results were further validated through a 5 × 5 dose-matrix approach, which confirmed the synergistic effects of siremadlin and olaparib across multiple synergy scoring models (Figure 18c-d). Additionally, the combination of these compounds resulted in sustained inhibition of cell proliferation over a 7-day period, exceeding the effects observed with either drug administered individually (Figure 18e). These findings are consistent with a previous study that demonstrated synergistic effects when combining idasanutlin with rucaparib (a PARP inhibitor) in both PARP-sensitive and PARP-resistant ovarian cancer cell lines, suggesting that MDM2-p53 inhibition may resensitize cells to PARP inhibition[445].

In addition to the promising combination of siremadlin and olaparib, our screening identified other potentially effective therapeutic combinations, such as siremadlin with irinotecan (TOP1 inhibitor) or venetoclax (BCL-2 inhibitor), which warrant further investigation (Figures 18a-b). While previous studies have demonstrated synergistic effects when combining MDM2 inhibitors with either topoisomerase I/II (TOP1/2) or BCL-2 inhibitors across various tumours[415,577–581], this is the first study to reveal such synergistic interactions specifically in RMS.

Interestingly, both irinotecan and olaparib, which demonstrated the highest synergy scores in our screening, target DNA damage pathways. Irinotecan inhibits TOP1, thereby preventing the religation of SSBs during DNA replication, which results in the formation of DSBs[582]. Similarly, olaparib inhibits PARP enzymes, leading to the accumulation of SSBs that are eventually converted into DSBs during DNA replication, particularly in HRD tumours[437,438]. Additionally, both TOP1 and PARP inhibitors are known TOP1 and PARP inhibitors are known to impede DNA replication and induce replication stress, thereby amplifying their cytotoxic effects[583]. Our findings underscore the potential of combining MDM2 inhibitors with certain drugs, particularly with agents that induce DNA damage and replication stress, such as olaparib and irinotecan, to significantly inhibit cell proliferation and reduce cellular viability in p53 WT RMS.

5.3.2. Individual effects of olaparib and siremadlin: morphological changes, DNA damage, and cell cycle arrest

Olaparib and other PARP inhibitors have been extensively studied in HRD tumours, particularly those with BRCA1/2 mutations[429–431]. These tumours are unable to repair SSBs via HR, resulting in the accumulation of DSBs upon PARP inhibition, leading to genomic instability and ultimately cell death[434–436]. However, tumours such as EWS, and certain types of prostate and small cell lung cancer, show increased sensitivity to PARP inhibitors despite having an ostensibly intact HR pathway (HR-intact)[439,440]. In these HR-intact tumours, the efficacy of PARP inhibitors may be attributed to alternative mechanisms, likely related to high levels of replication stress[439]. Moreover, recent preclinical studies have identified new targets that can induce a "chemical HRD" state and potentially overcome PARP inhibitor resistance[439,441–444]. In RMS, HRD are uncommon, and the phenotypic and molecular effects of PARP inhibitors in p53 WT cells have not been extensively studied.

In this thesis, cell painting[512] was employed to explore the phenotypic effects induced by olaparib, siremadlin, and their combination. To complement the cell painting results and provide a more comprehensive understanding of the effects exerted by these compounds, additional techniques were utilized, including quantification of DNA damage, apoptosis and cell death assays, and analysis of cell cycle distribution.

On the one hand, cell painting analysis revealed a notable clustering similarity between olaparib and etoposide, a TOP2 inhibitor[584,585], demonstrating the induction of analogous phenotypic changes in RH36 cells (Figure 19a). This clustering was further supported by the widespread accumulation of γH2AX, a well-established marker for DSBs[586,587], observed in all p53 WT RMS cells following treatment with these agents (Figures 21a-b). These results indicate that both olaparib and etoposide induce similar DNA damage responses in HR-intact p53 WT RMS cells. Additionally, olaparib induced significant changes in the intensity of the ER and the granularity of the nucleus, along with alterations in the size and shape of both the nucleus and cytoplasm (Figure 19c). These morphological changes are likely associated with the observed G_2/M cell cycle arrest and a mild increase in apoptosis-related cell death induced by olaparib in p53 WT RMS cells, likely due to the induced DNA damage (Figures 23a-c). These findings are consistent with previous studies demonstrating similar effects, including G_2/M cell cycle arrest and apoptosis-related cell death, in p53 MUT RMS and other tumour types[588–590]. Collectively, these results underscore the dose-dependent induction of double-strand breaks (DSBs) and their phenotypic consequences, emphasizing the G2/M cell cycle arrest induced by olaparib in HR-intact p53 WT RMS cells.

On the other hand, cell painting analysis revealed a distinct clustering profile for siremadlin, highlighting its unique phenotypic effects compared to other compounds (Figure 19a). The morphological profiles indicated a marked dose-dependent increase in features related to the granularity of multiple organelles, including the ER, Golgi apparatus, nucleoli, and mitochondria, following siremadlin treatment (Figure 19b). Additionally, alterations in the size and shape of both nucleus and cytoplasm were observed. The increased granularity likely reflects changes in the density, distribution, or organization of cellular components within these organelles, suggesting significant disruptions in organelle functions such as protein synthesis, trafficking, and metabolic activity.

Similar to olaparib, siremadlin induced mild apoptosis-related cell death in p53 WT RMS cells at 72 hours (Figure 23a-b). However, unlike olaparib, siremadlin did not cause significant alterations in the cell cycle distribution of these cells, despite notable decreases in pRb and Cyclin B1 levels at the same time point (Figures 23c-d). This finding contrasts with the otherwise consistent results suggesting cell cycle arrest, such as the accumulation of p53 and p21 following MDM2-p53 inhibition (Figures 16e-f). Indeed, previous research has consistently demonstrated that MDM2 inhibitors induce cell cycle arrest in RMS and other tumour types, primarily through p53 activation[356,591,592]. Specifically, p53-induced cell-cycle arrest is predominantly driven by the transcriptional upregulation of p21[593–595], which in turn, inhibits the CDK4/cyclin D and CDK2/cyclin E complexes, leading to G_1 phase arrest, as well as CDK2/cyclin B complexes, resulting in G_2/M phase arrest[595]. Despite this discrepancy in cell cycle distribution, the overall findings provide valuable insights into the distinct and shared mechanisms of olaparib and siremadlin. These results shed light on how these compounds modulate various aspects of cellular function in RMS, contributing to a deeper understanding of their mechanisms of action.

5.3.3. Unveiling the synergistic interaction between siremadlin and olaparib: phenotypic and molecular insights

Regarding the combination of siremadlin and olaparib, cell painting analysis revealed a distinct clustering of cells treated with both drugs, indicating unique phenotypic effects compared to individual treatments (Figure 20a). This distinct clustering strongly supports the hypothesis of a potential synergistic interaction between the compounds, significantly influencing multiple cellular processes and resulting in a novel cellular phenotype. Notably, olaparib appears to synergistically potentiate many of the subtle phenotypic changes induced by siremadlin, as observed in the hierarchical clustering analysis (Figure 20b). Radial plots further revealed alterations in morphological features associated with ER and nuclear intensity, along with increased granularity of cellular organelles compared to individual treatments (Figure 20c). These observed phenotypic changes suggested that apoptosis was induced in cells exposed to the combination of siremadlin and olaparib. To further validate this hypothesis, apoptosis and cell death assays were conducted in p53 WT RMS cell lines. Notably, the results confirmed a strong increase in both overall cell death and apoptosis with the combination treatment, surpassing the effects of each drug alone (Figures 23a-b).

Moreover, the combination treatment resulted in DNA damage and disrupted cell cycle progression, similar to the effects observed with olaparib alone (Figures 22a-b; Figure 23c). This disruption was accompanied by strong decrease in phosphorylated Rb and Cyclin B1 levels in p53 WT RMS cells treated with the combination, suggesting cell cycle arrest in both G_1 and G_2/M phases (Figure 23d). These findings underscore the potent synergistic cytotoxicity effect of siremadlin and olaparib when used in combination, resulting in a marked induction of apoptosis and demonstrating a significantly greater efficacy compared to each drug used independently. Furthermore, this enhanced effectiveness suggests that the combination treatment may induce p53-dependent apoptosis by shifting p53 dynamics from a pulsatile to a sustained activation state.

Both MDM2 and PARP inhibitors are known to induce p53 activation and p21-mediated cell cycle arrest[574,590,596]. However, the individual efficacy of these compounds partly constrained by the challenge of transitioning from pulsatile to sustained p53 activation[348,449,543]. Pulsatile p53 activation involves the induction of proteins that mediate cell cycle arrest, such as p21, and proteins that maintain negative feedback loops crucial for generating p53 activation pulses, like MDM2[449,597–599]. In contrast, sustained p53 activity can drive intrinsic apoptosis through various mechanisms in cells unable to repair DNA damage or overexposed to excessive stress signals[348,597,599,600].

To elucidate the molecular mechanisms underlying the enhanced cytotoxicity observed in p53 WT RMS cell lines treated with the combination of siremadlin and olaparib, this thesis investigated their effects on p53 dynamics and quantified the expression levels of its downstream targets. Remarkably, the combination of siremadlin and olaparib significantly increased MDM2 cleavage in all p53 WT RMS cells (Figures 24a-d). This finding is of great relevance because the ~60 kDa MDM2 species (MDM2-p60), produced by caspase-2-PIDDosome and/or caspase-3 cleavage, stabilize p53 and shifts its dynamics from pulsatile to sustained mode, thereby promoting apoptosis in extensively damaged cells[348,601,602]. Indeed, concomitant with the observed MDM2 cleavage, our results revealed a strong increase in both total and acetylated p53 (ac-p53) levels (Figures 24a-c; Figure 24e). Notably, the acetylation of p53 at lysine 382 is particularly significant, as this modification enhances the transcriptional activity of p53[603,604]. Consistent with the elevated levels of p53 expression and acetylation, a strong transcriptional upregulation of p53 target genes in response to the combination therapy, significantly exceeding the induction levels seen with the individual treatments (Figures 25a-d).

The increased induction of p21 expression compared to individual treatments is particularly significant, as p21 is a pivotal mediator of p53-induced cell cycle arrest. This result substantiates the previously observed alterations in cell cycle progression, underscoring the molecular mechanisms by which the combination therapy exerts its cytotoxic effects.

Overall, these findings suggest that combining siremadlin and olaparib significantly enhances the efficacy of PARP inhibitors by disrupting the MDM2-p53 negative feedback loop following initial p53 activation, leading to sustained p53 activation. Additionally, the transition from pulsatile to sustained p53 activation appears to be further supported by MDM2 cleavage induced by the combination treatment. The resulting increase in p53 stabilization and sustained activation likely contributes to the pronounced apoptotic response observed. These findings highlight the potential of combining siremadlin and olaparib as a potent therapeutic strategy, overcoming the limitations of each drug when used individually and offering a more effective approach to cancer treatment.

5.4. Unveiling the synergistic power of siremadlin and olaparib combination *in vivo*

The *in vivo* evaluation of combining siremadlin and olaparib in RH36 xenografts provided valuable insights into both the therapeutic potential and the underlying molecular mechanisms of this treatment. The dosing regimen for siremadlin was informed by prior research, which demonstrated that pulsed high-doses of siremadlin induce a stronger proapoptotic response in p53 WT cancer cells compared to sustained low-doses[543]. For olaparib, dosing regimen was based on established efficacy from previous studies, which identified effective oral doses of 50 or 100 mg/kg daily in xenograft models[605–607]. Interestingly, olaparib demonstrated high bioavailability and low clearance when administered orally in rats and dogs. In mice, plasma concentrations of 1 μM are achieved within 60 minutes following an oral dose of a 10 mg/kg[605].

In this study, the administration intervals for olaparib were adjusted to a biweekly schedule to align with the biweekly dosing regimen of siremadlin. Initially, a pilot study was performed to establish a dosing regimen that balanced efficacy with minimal toxicity. The treatment regimens tested included 50 mg/kg siremadlin, 100 mg/kg olaparib, and various combinations at concentrations of 1X, 0.5X, and 0.25X.

Results from the pilot study indicated that all combination regimens effectively reduced tumour growth (Figure 26a). However, the administration of 50 mg/kg siremadlin, either alone or in combination with 100 mg/kg olaparib, resulted in a significant reduction in body weight after 30 days, suggesting potential toxicity associated with this dosing regimen (Figure 26b). Consequently, a reduced dosing regimen of 25 mg/kg siremadlin and/or 50 mg/kg olaparib was evaluated in a subsequent *in vivo* study with a cohort of six mice per group. Remarkably, this combination regimen significantly reduced tumour growth and extended overall survival in mice compared to individual treatments and control groups, demonstrating synergistic therapeutic efficacy with minimal side effects (Figures 26c-e).

To elucidate the molecular mechanisms underlying the observed therapeutic effects, additional cohorts of RH36 CDOX were treated with 1, 3, and 5 doses of 25 mg/kg siremadlin and/or 50 mg/kg olaparib. Results demonstrated increased expression of both total and acetylated p53, along with elevated levels of its downstream targets, p21 and MDM2, after 3 and 5 doses of the combination treatment (Figure 27a). Further gene expression analysis revealed increased mRNA levels of *MDM2* and *CDKN1A* following 3 and 5 doses of the combination treatment (Figure 27b), providing evidence that the combination therapy significantly enhanced the transcriptional activity of p53 *in vivo* compared to individual treatments and control. However, by the study endpoint, mRNA levels of both MDM2 and CDKN1A had returned to baseline, suggesting an adaptive response by RH36 cells to prolonged combination therapy.

Overall, this thesis presents the first compelling evidence demonstrating the enhanced therapeutic efficacy of combining siremadlin and olaparib in the treatment of p53 WT RMS *in vivo*. The substantial reduction in tumour growth and extended survival, along with molecular evidence of p53 pathway activation, underscores the strong potential of this combination therapy and supports its consideration for clinical trials.

5.5. Siremadlin and olaparib can be combined with selected chemotherapies to enhance its antitumoral effects

The survival rate for relapsed/refractory RMS is notably poor, presenting a significant therapeutic challenge[608,609]. Approximately one-third of patients with localized RMS and over two-thirds of those with metastatic RMS experience disease recurrence after their initial treatment[609–611].

Despite advancements in understanding the RMS biology and the urgent need for new treatments, there have been limited successful efforts to translate these discoveries into RMS-specific clinical trials for patients. Contributing factors include insufficient preclinical data to support human trials, regulatory hurdles, and difficulties in accessing new agents for paediatric research[612]. As a result, patients experiencing their first relapse are often not enrolled in clinical trials and instead receive salvage chemotherapy[613]. patients experiencing their first relapse often receive salvage chemotherapy rather than participating in clinical trials, with therapy choices typically based on previously administered drugs, anticipated side effects, and patient and family preferences[609,614].

In light of these challenges, the present study aimed to evaluate the potential benefits of combining siremadlin and olaparib with various chemotherapy regimens to identify new therapeutic strategies for p53 WT RMS patients. By integrating these novel agents with established chemotherapy treatments, we sought to enhance their therapeutic efficacy, mitigate associated toxicities, and address the problem of treatment resistance. The outcomes of this investigation are intended to provide critical data supporting the inclusion of siremadlin and olaparib in clinical trials, whether used in conjunction with first-line or second-line therapies.

Initial experiments demonstrated that administering siremadlin and olaparib after pre-treatment with actinomycin, vincristine, or phosphoramide mustard resulted in significantly enhanced cell survival suppression compared to chemotherapy alone (Figure 28b). This finding suggests that the combination of siremadlin and olaparib maintains their antitumor efficacy even following conventional chemotherapy, supporting their potential use as effective adjuvants. In contrast, simultaneous treatment of RMS cells with siremadlin and olaparib alongside first-line chemotherapeutics for 7 days showed initial synergistic effects, which were not sustained over longer periods (Figure 28c). The reduction in efficacy at 5 and 7 days underscores the necessity of optimizing treatment schedules to sustain the therapeutic benefits of these combinations. The observed variability underscores that while initial responses may be promising, prolonged efficacy may require more nuanced dosing and scheduling strategies.

Further investigation into combining siremadlin and olaparib with second-line chemotherapies, including irinotecan, TMZ, doxorubicin, cisplatin, and etoposide, revealed that these combinations could offer alternative therapeutic options, particularly for cases resistant to first-line treatments or disease progression.

Notably, the combination of siremadlin and olaparib with irinotecan, TMZ, and doxorubicin consistently exhibited synergistic effects across all tested p53 wild-type (WT) RMS cells (Figures 20a-e). This suggests that these agents may be particularly effective when used in conjunction with second-line therapies, offering a robust strategy for managing resistant or progressive disease. However, while sustained synergistic effects were observed with these chemotherapies, the shift from synergy to additive effects over time indicates that the initial advantages of these combinations may be influenced by treatment duration.

The consistent and robust synergistic effects observed with irinotecan, TMZ, and doxorubicin provide a strong rationale for further exploration of these combinations in preclinical and clinical settings. The potential for sustained therapeutic benefits with these second-line chemotherapeutics presents an opportunity to refine treatment protocols for RMS and improve patient outcomes. Future research should focus on elucidating the underlying mechanisms that contribute to the duration and consistency of synergistic effects. Investigating the factors that influence the shift from synergistic to additive effects over time could inform strategies to overcome resistance and optimize treatment regimens.

6. Conclusions

First: p53 WT RMS cells show an increased sensitivity to MDM2 inhibitors, particularly to siremadlin (HDM201), with significant low IC_{50} values compared to p53 MUT RMS cells.

Second: Siremadlin induces a time-dependent activation of the p53 pathway in p53 WT RMS cells, evidenced by the accumulation of p53, MDM2, and p21 post-treatment.

Third: The newly synthesized MDM2/X inhibitors (ME240, ME242, ME258, ME62) demonstrated limited efficacy and specificity in RMS cell lines, as indicated by their high IC_{50} values and lack of differential response between p53 WT and p53 MUT cells.

Fourth: A comprehensive drug combination screening identifies the combination of siremadlin with olaparib as the most promising strategy tested in reducing cell viability of p53 WT RMS cells.

Fifth: The combination of siremadlin and olaparib notably disrupts cell cycle progression by significantly reducing phosphorylated Rb and Cyclin B1 levels, while strongly promoting apoptotic cell death in p53 WT RMS cells.

Sixth: The combination of siremadlin and olaparib synergistically induces profound morphological changes across key cellular structures including the ER, Golgi, cytoskeleton, and nucleus.

Seventh: The combination of siremadlin and olaparib induces MDM2 cleavage, enhances p53 accumulation, and promotes the expression of its transcriptional targets, demonstrating robust activation of p53-mediated pathways in p53 WT RMS cells compared to individual treatments.

Eighth: The combination of siremadlin and olaparib demonstrates potent anti-tumour efficacy, significantly reducing tumour growth, extending mice overall survival, and enhancing p53-mediated transcriptional activity *in vivo*.

Ninth: The combination of siremadlin and olaparib with irinotecan, TMZ, and doxorubicin, demonstrates additional sustained therapeutic efficacy in p53 WT RMS cells, highlighting potential enhanced treatment options following first-line chemotherapy.

7. Bibliography

1. Kaatsch, P. Epidemiology of childhood cancer. *Cancer Treat Rev* **36**, 277–285 (2010).
2. Bhakta, N. *et al.* Childhood cancer burden: a review of global estimates. *Lancet Oncol* **20**, e42–e53 (2019).
3. Siegel, R. L., Miller, K. D., Wagle, N. S. & Jemal, A. Cancer statistics, 2023. *Ca Cancer J Clin* **73**, 17–48 (2023).
4. Pui, C.-H., Gajjar, A. J., Kane, J. R., Qaddoumi, I. A. & Pappo, A. S. Challenging issues in pediatric oncology. *Nat Rev Clin Oncol* **8**, 540–549 (2011).
5. Fitzgerald, R. C., Antoniou, A. C., Fruk, L. & Rosenfeld, N. The future of early cancer detection. *Nat Med* **28**, 666–677 (2022).
6. Hudson, M. M. *et al.* Lessons from the past: Opportunities to improve childhood cancer survivor care through outcomes investigations of historical therapeutic approaches for pediatric hematological malignancies. *Pediatr Blood Cancer* **58**, 334–343 (2012).
7. Kopp, L. M., Gupta, P., Pelayo-Katsanis, L., Wittman, B. & Katsanis, E. Late Effects in Adult Survivors of Pediatric Cancer: A Guide for the Primary Care Physician. *Am J Med* **125**, 636–641 (2012).
8. National Cancer Institute. NCCR*Explorer: An interactive website for NCCR cancer statistics. (2023).
9. Steliarova-Foucher, E., Stiller, C., Lacour, B. & Kaatsch, P. International Classification of Childhood Cancer, third edition. *Cancer* **103**, 1457–1467 (2005).
10. Pearson, A. D. J. *et al.* Implementation of mechanism of action biology-driven early drug development for children with cancer. *Eur J Cancer* **62**, 124–131 (2016).
11. Downing, J. R. *et al.* The Pediatric Cancer Genome Project. *Nat Genet* **44**, 619–622 (2012).
12. Sweet-Cordero, E. A. & Biegel, J. A. The genomic landscape of pediatric cancers: Implications for diagnosis and treatment. *Science (1979)* **363**, 1170–1175 (2019).
13. Gröbner, S. N. *et al.* The landscape of genomic alterations across childhood cancers. *Nature* **555**, 321–327 (2018).
14. Ma, X. *et al.* Pan-cancer genome and transcriptome analyses of 1,699 paediatric leukaemias and solid tumours. *Nature* **555**, 371–376 (2018).
15. Huether, R. *et al.* The landscape of somatic mutations in epigenetic regulators across 1,000 paediatric cancer genomes. *Nat Commun* **5**, 3630 (2014).
16. Newman, S. *et al.* Genomes for Kids: The Scope of Pathogenic Mutations in Pediatric Cancer Revealed by Comprehensive DNA and RNA Sequencing. *Cancer Discov* **11**, 3008–3027 (2021).
17. Iacobucci, I. & Mullighan, C. G. Genetic Basis of Acute Lymphoblastic Leukemia. *Journal of Clinical Oncology* **35**, 975–983 (2017).
18. Thatikonda, V. *et al.* Comprehensive analysis of mutational signatures reveals distinct patterns and molecular processes across 27 pediatric cancers. *Nat Cancer* **4**, 276–289 (2023).
19. McLeod, C. *et al.* St. Jude Cloud: A Pediatric Cancer Genomic Data-Sharing Ecosystem. *Cancer Discov* **11**, 1082–1099 (2021).

20. Berlanga, P. *et al.* The European MAPPYACTS Trial: Precision Medicine Program in Pediatric and Adolescent Patients with Recurrent Malignancies. *Cancer Discov* **12**, 1266–1281 (2022).

21. Villani, A. *et al.* The clinical utility of integrative genomics in childhood cancer extends beyond targetable mutations. *Nat Cancer* **4**, 203–221 (2023).

22. Comitani, F. *et al.* Diagnostic classification of childhood cancer using multiscale transcriptomics. *Nat Med* **29**, 656–666 (2023).

23. Berlanga, P. *et al.* The European MAPPYACTS Trial: Precision Medicine Program in Pediatric and Adolescent Patients with Recurrent Malignancies. *Cancer Discov* **12**, 1266–1281 (2022).

24. Dupain, C., Harttrampf, A. C., Urbinati, G., Geoerger, B. & Massaad-Massade, L. Relevance of fusion genes in pediatric cancers: toward precision medicine. *Molecular Therapy-Nucleic Acids* **6**, 315–326 (2017).

25. Vellichirammal, N. N., Chaturvedi, N. K., Joshi, S. S., Coulter, D. W. & Guda, C. Fusion genes as biomarkers in pediatric cancers: A review of the current state and applicability in diagnostics and personalized therapy. *Cancer Lett* **499**, 24–38 (2021).

26. Liu, Y. *et al.* Etiology of oncogenic fusions in 5,190 childhood cancers and its clinical and therapeutic implication. *Nat Commun* **14**, 1739 (2023).

27. van Belzen, I. A. E. M. *et al.* Systematic discovery of gene fusions in pediatric cancer by integrating RNA-seq and WGS. *BMC Cancer* **23**, 618 (2023).

28. LaHaye, S. *et al.* Discovery of clinically relevant fusions in pediatric cancer. *BMC Genomics* **22**, 1–16 (2021).

29. Sweet-Cordero, E. A. & Biegel, J. A. The genomic landscape of pediatric cancers: Implications for diagnosis and treatment. *Science (1979)* **363**, 1170–1175 (2019).

30. Speck, N. A. & Gilliland, D. G. Core-binding factors in haematopoiesis and leukaemia. *Nat Rev Cancer* **2**, 502–513 (2002).

31. Opatz, S. *et al.* The clinical mutatome of core binding factor leukemia. *Leukemia* **34**, 1553–1562 (2020).

32. Jones, D. T. W. *et al.* Tandem duplication producing a novel oncogenic BRAF fusion gene defines the majority of pilocytic astrocytomas. *Cancer Res* **68**, 8673–8677 (2008).

33. Antonelli, M. *et al.* KIAA1549: BRAF fusion gene in pediatric brain tumors of various histogenesis. *Pediatr Blood Cancer* **62**, 724–727 (2015).

34. Pfister, S. *et al.* BRAF gene duplication constitutes a mechanism of MAPK pathway activation in low-grade astrocytomas. *J Clin Invest* **118**, 1739–1749 (2008).

35. Houghton, P. J. Advances in the treatment of BRAF-mutant low-grade glioma with MAPK inhibitors. *Transl Pediatr* **13**, 513 (2024).

36. Riggi, N. *et al.* EWS-FLI1 utilizes divergent chromatin remodeling mechanisms to directly activate or repress enhancer elements in Ewing sarcoma. *Cancer Cell* **26**, 668–681 (2014).

37. Riggi, N. *et al.* EWS-FLI-1 expression triggers a Ewing's sarcoma initiation program in primary human mesenchymal stem cells. *Cancer Res* **68**, 2176–2185 (2008).

38. Gryder, B. E. *et al.* Miswired enhancer logic drives a cancer of the muscle lineage. *iScience* **23**, (2020).

39. Gryder, B. E. *et al.* PAX3–FOXO1 establishes myogenic super enhancers and confers BET bromodomain vulnerability. *Cancer Discov* **7**, 884–899 (2017).

40. Dharia, N. V *et al.* A first-generation pediatric cancer dependency map. *Nat Genet* **53**, 529–538 (2021).

41. Henley, M. J. & Koehler, A. N. Advances in targeting 'undruggable'transcription factors with small molecules. *Nat Rev Drug Discov* **20**, 669–688 (2021).

42. Lai, A. C. & Crews, C. M. Induced protein degradation: an emerging drug discovery paradigm. *Nat Rev Drug Discov* **16**, 101–114 (2017).

43. Cromm, P. M. & Crews, C. M. Targeted protein degradation: from chemical biology to drug discovery. *Cell Chem Biol* **24**, 1181–1190 (2017).

44. Marcus, L. *et al.* FDA approval summary: entrectinib for the treatment of NTRK gene fusion solid tumors. *Clinical Cancer Research* **27**, 928–932 (2021).

45. Laetsch, T. W. *et al.* Larotrectinib for paediatric solid tumours harbouring NTRK gene fusions: phase 1 results from a multicentre, open-label, phase 1/2 study. *Lancet Oncol* **19**, 705–714 (2018).

46. Shulman, D. S. & DuBois, S. G. The evolving diagnostic and treatment landscape of NTRK-fusion-driven pediatric cancers. *Pediatric Drugs* **22**, 189–197 (2020).

47. Wachtel, M. & Schäfer, B. W. PAX3-FOXO1: Zooming in on an "undruggable" target. *Seminars in Cancer Biology* Preprint at https://doi.org/10.1016/j.semcancer.2017.11.006 (2018).

48. Singh, S. *et al.* Targeting KDM4 for treating PAX3-FOXO1–driven alveolar rhabdomyosarcoma. *Sci Transl Med* **14**, eabq2096 (2022).

49. Kim, Y. Y. *et al.* KDM3B inhibitors disrupt the oncogenic activity of PAX3-FOXO1 in fusion-positive rhabdomyosarcoma. *Nat Commun* **15**, 1703 (2024).

50. Mo, J. *et al.* Therapeutic targeting the oncogenic driver EWSR1:: FLI1 in Ewing sarcoma through inhibition of the FACT complex. *Oncogene* **42**, 11–25 (2023).

51. Chen, X., Yang, W., Roberts, C. W. M. & Zhang, J. Developmental origins shape the paediatric cancer genome. *Nat Rev Cancer* 1–17 (2024).

52. Filbin, M. & Monje, M. Developmental origins and emerging therapeutic opportunities for childhood cancer. *Nat Med* **25**, 367–376 (2019).

53. Scotting, P. J., Walker, D. A. & Perilongo, G. Childhood solid tumours: a developmental disorder. *Nat Rev Cancer* **5**, 481–488 (2005).

54. Ward, E., DeSantis, C., Robbins, A., Kohler, B. & Jemal, A. Childhood and adolescent cancer statistics, 2014. *CA Cancer J Clin* **64**, 83–103 (2014).

55. Rice, S. & Roy, A. MLL-rearranged infant leukaemia: A 'thorn in the side'of a remarkable success story. *Biochimica et Biophysica Acta (BBA)-Gene Regulatory Mechanisms* **1863**, 194564 (2020).

56. Davis, J. L. *et al.* Infantile NTRK-associated mesenchymal tumors. *Pediatric and Developmental Pathology* **21**, 68–78 (2018).

57. Ingley, K. M. *et al.* Current approaches to management of bone sarcoma in adolescent and young adult patients. *Pediatr Blood Cancer* **69**, e29442 (2022).

58. Jain, J., Sutton, K. S. & Hong, A. L. Progress update in pediatric renal tumors. *Curr Oncol Rep* **23**, 1–12 (2021).

59. Behjati, S., Gilbertson, R. J. & Pfister, S. M. Maturation Block in Childhood Cancer. *Cancer Discov* **11**, 542–544 (2021).

60. Jeong, S. U. & Kang, H. J. Recent updates on the classification of hepatoblastoma according to the International Pediatric Liver Tumors Consensus. *Journal of liver cancer* **22**, 23–29 (2022).

61. Jansky, S. *et al.* Single-cell transcriptomic analyses provide insights into the developmental origins of neuroblastoma. *Nat Genet* **53**, 683–693 (2021).

62. Young, M. D. *et al.* Single cell derived mRNA signals across human kidney tumors. *Nat Commun* **12**, 3896 (2021).

63. Hong, B. *et al.* Single-cell transcriptional profiling reveals heterogeneity and developmental trajectories of Ewing sarcoma. *J Cancer Res Clin Oncol* **148**, 3267–3280 (2022).

64. Wei, Y. *et al.* Single-cell analysis and functional characterization uncover the stem cell hierarchies and developmental origins of rhabdomyosarcoma. *Nat Cancer* **3**, 961–975 (2022).

65. Brodeur, G. M. Spontaneous regression of neuroblastoma. *Cell Tissue Res* **372**, 277–286 (2018).

66. de Thé, H. Differentiation therapy revisited. *Nat Rev Cancer* **18**, 117–127 (2018).

67. Issa, G. C., Stein, E. M. & DiNardo, C. D. How I Treat: Differentiation Therapy in Acute Myeloid Leukemia. *Blood* (2024).

68. Danielli, S. G. *et al.* Single-cell profiling of alveolar rhabdomyosarcoma reveals RAS pathway inhibitors as cell-fate hijackers with therapeutic relevance. *Sci Adv* **9**, eade9238 (2024).

69. San José-Enériz, E. *et al.* Epigenetic-based differentiation therapy for Acute Myeloid Leukemia. *Nat Commun* **15**, 5570 (2024).

70. Kratz, C. P. *et al.* Predisposition to cancer in children and adolescents. *Lancet Child Adolesc Health* **5**, 142–154 (2021).

71. Kim, J. *et al.* Frequency of pathogenic germline variants in cancer-susceptibility genes in the Childhood Cancer Survivor Study. *JNCI Cancer Spectr* **5**, pkab007 (2021).

72. Zhang, J. *et al.* Germline mutations in predisposition genes in pediatric cancer. *New England Journal of Medicine* **373**, 2336–2346 (2015).

73. Parsons, D. W. *et al.* Diagnostic yield of clinical tumor and germline whole-exome sequencing for children with solid tumors. *JAMA Oncol* **2**, 616–624 (2016).

74. Wang, Z. *et al.* Genetic risk for subsequent neoplasms among long-term survivors of childhood cancer. *Journal of Clinical Oncology* **36**, 2078–2087 (2018).

75. Chen, C. *et al.* Cancer germline predisposing variants and late mortality from subsequent malignant neoplasms among long-term childhood cancer survivors: a report from the St Jude Lifetime Cohort and the Childhood Cancer Survivor Study. *Lancet Oncol* **24**, 1147–1156 (2023).

76. McEachron, T. A. & Helman, L. J. Recent advances in pediatric cancer research. *Cancer Res* **81**, 5783–5799 (2021).

77. Khater, F. *et al.* Molecular profiling of hard-to-treat childhood and adolescent cancers. *JAMA Netw Open* **2**, e192906–e192906 (2019).

78. Wong, M. *et al.* Whole genome, transcriptome and methylome profiling enhances actionable target discovery in high-risk pediatric cancer. *Nat Med* **26**, 1742–1753 (2020).

79. Pui, C.-H., Gajjar, A. J., Kane, J. R., Qaddoumi, I. A. & Pappo, A. S. Challenging issues in pediatric oncology. *Nat Rev Clin Oncol* **8**, 540–549 (2011).

80. Boshuizen, J. & Peeper, D. S. Rational cancer treatment combinations: an urgent clinical need. *Mol Cell* **78**, 1002–1018 (2020).

81. Plana, D., Palmer, A. C. & Sorger, P. K. Independent drug action in combination therapy: implications for precision oncology. *Cancer Discov* **12**, 606–624 (2022).

82. Jin, H., Wang, L. & Bernards, R. Rational combinations of targeted cancer therapies: background, advances and challenges. *Nat Rev Drug Discov* **22**, 213–234 (2023).

83. Jaaks, P. *et al.* Effective drug combinations in breast, colon and pancreatic cancer cells. *Nature* **603**, 166–173 (2022).

84. Erdmann, F. *et al.* Childhood cancer: Survival, treatment modalities, late effects and improvements over time. *Cancer Epidemiol* **71**, 101733 (2021).

85. Geoerger, B. *et al.* Pembrolizumab in paediatric patients with advanced melanoma or a PD-L1-positive, advanced, relapsed, or refractory solid tumour or lymphoma (KEYNOTE-051): interim analysis of an open-label, single-arm, phase 1–2 trial. *Lancet Oncol* **21**, 121–133 (2020).

86. Melaiu, O., Lucarini, V., Giovannoni, R., Fruci, D. & Gemignani, F. News on immune checkpoint inhibitors as immunotherapy strategies in adult and pediatric solid tumors. *Semin Cancer Biol* **79**, 18–43 (2022).

87. Naik, S., Velasquez, M. P. & Gottschalk, S. Chimeric antigen receptor T-cell therapy in childhood acute myeloid leukemia: how far are we from a clinical application? *Haematologica* **109**, 1656–1667 (2024).

88. Majzner, R. G. *et al.* CAR T Cells Targeting B7-H3, a Pan-Cancer Antigen, Demonstrate Potent Preclinical Activity Against Pediatric Solid Tumors and Brain Tumors. *Clinical Cancer Research* **25**, 2560–2574 (2019).

89. DeRenzo, C., Krenciute, G. & Gottschalk, S. The Landscape of CAR T Cells Beyond Acute Lymphoblastic Leukemia for Pediatric Solid Tumors. *American Society of Clinical Oncology Educational Book* 830–837 (2018) doi:10.1200/EDBK_200773.

90. Gryder, B. E. *et al.* Miswired enhancer logic drives a cancer of the muscle lineage. *iScience* **23**, (2020).

91. Gryder, B. E. *et al.* PAX3–FOXO1 Establishes Myogenic Super Enhancers and Confers BET Bromodomain Vulnerability. *Cancer Discov* **7**, 884–899 (2017).

92. Zhang, S. *et al.* PAX3-FOXO1 coordinates enhancer architecture, eRNA transcription, and RNA polymerase pause release at select gene targets. *Mol Cell* **82**, 4428–4442 (2022).

93. Lawlor, E. R. & Thiele, C. J. Epigenetic changes in pediatric solid tumors: promising new targets. *Clinical cancer research* **18**, 2768–2779 (2012).

94. Jubierre, L. *et al.* Targeting of epigenetic regulators in neuroblastoma. *Exp Mol Med* **50**, 1–12 (2018).

95. Takebe, N. *et al.* Targeting Notch, Hedgehog, and Wnt pathways in cancer stem cells: clinical update. *Nat Rev Clin Oncol* **12**, 445–464 (2015).

96. Ahmed, A. A., Mohamed, A. D., Gener, M., Li, W. & Taboada, E. YAP and the Hippo pathway in pediatric cancer. *Mol Cell Oncol* **4**, e1295127 (2017).

97. Roma, J., Almazán-Moga, A., Sánchez de Toledo, J. & Gallego, S. Notch, Wnt, and Hedgehog Pathways in Rhabdomyosarcoma: From Single Pathways to an Integrated Network. *Sarcoma* **2012**, 695603 (2012).

98. Dumontet, C., Reichert, J. M., Senter, P. D., Lambert, J. M. & Beck, A. Antibody–drug conjugates come of age in oncology. *Nat Rev Drug Discov* **22**, 641–661 (2023).

99. Fu, Z., Li, S., Han, S., Shi, C. & Zhang, Y. Antibody drug conjugate: the "biological missile" for targeted cancer therapy. *Signal Transduct Target Ther* **7**, 93 (2022).

100. Hingorani, P. *et al.* Trastuzumab Deruxtecan, Antibody–Drug Conjugate Targeting HER2, Is Effective in Pediatric Malignancies: A Report by the Pediatric Preclinical Testing Consortium. *Mol Cancer Ther* **21**, 1318–1325 (2022).

101. Brivio, E., Bautista, F. & Zwaan, C. M. Naked antibodies and antibody-drug conjugates: targeted therapy for childhood acute lymphoblastic leukemia. *Haematologica* **109**, 1700–1712 (2024).

102. Hingorani, P. *et al.* ABBV-085, Antibody–Drug Conjugate Targeting LRRC15, Is Effective in Osteosarcoma: A Report by the Pediatric Preclinical Testing Consortium. *Mol Cancer Ther* **20**, 535–540 (2021).

103. Kendsersky, N. M. *et al.* The B7-H3–Targeting Antibody–Drug Conjugate m276-SL-PBD Is Potently Effective Against Pediatric Cancer Preclinical Solid Tumor Models. *Clinical Cancer Research* **27**, 2938–2946 (2021).

104. Stachowicz-Stencel, T. & Synakiewicz, A. Biomarkers for pediatric cancer detection: Latest advances and future perspectives. *Biomark Med* **14**, 391–400 (2020).

105. Henry, N. L. & Hayes, D. F. Cancer biomarkers. *Mol Oncol* **6**, 140–146 (2012).

106. Saletta, F. *et al.* Molecular profiling of childhood cancer: Biomarkers and novel therapies. *BBA Clin* **1**, 59–77 (2014).

107. Lawler, M. *et al.* Empowering effective biomarker-driven precision oncology: A call to action. *Eur J Cancer* 114225 (2024).

108. Abbou, S. D., Shulman, D. S., DuBois, S. G. & Crompton, B. D. Assessment of circulating tumor DNA in pediatric solid tumors: the promise of liquid biopsies. *Pediatr Blood Cancer* **66**, e27595 (2019).

109. Andersson, D., Fagman, H., Dalin, M. G. & Ståhlberg, A. Circulating cell-free tumor DNA analysis in pediatric cancers. *Mol Aspects Med* **72**, 100819 (2020).

110. Doculara, L., Trahair, T. N., Bayat, N. & Lock, R. B. Circulating tumor DNA in pediatric cancer. *Front Mol Biosci* **9**, 885597 (2022).

111. Campos-Carrillo, A. *et al.* Circulating tumor DNA as an early cancer detection tool. *Pharmacol Ther* **207**, 107458 (2020).

112. Sanz-Garcia, E., Zhao, E., Bratman, S. V & Siu, L. L. Monitoring and adapting cancer treatment using circulating tumor DNA kinetics: Current research, opportunities, and challenges. *Sci Adv* **8**, eabi8618 (2022).

113. Moding, E. J., Nabet, B. Y., Alizadeh, A. A. & Diehn, M. Detecting liquid remnants of solid tumors: circulating tumor DNA minimal residual disease. *Cancer Discov* **11**, 2968–2986 (2021).

114. Alix-Panabières, C. & Pantel, K. Liquid biopsy: from discovery to clinical application. *Cancer Discov* **11**, 858–873 (2021).

115. Ignatiadis, M., Sledge, G. W. & Jeffrey, S. S. Liquid biopsy enters the clinic—implementation issues and future challenges. *Nat Rev Clin Oncol* **18**, 297–312 (2021).

116. Cohen, S. A., Liu, M. C. & Aleshin, A. Practical recommendations for using ctDNA in clinical decision making. *Nature* **619**, 259–268 (2023).

117. Ruggeri, B. A., Camp, F. & Miknyoczki, S. Animal models of disease: pre-clinical animal models of cancer and their applications and utility in drug discovery. *Biochem Pharmacol* **87**, 150–161 (2014).

118. Jin, J., Yoshimura, K., Sewastjanow-Silva, M., Song, S. & Ajani, J. A. Challenges and prospects of patient-derived xenografts for cancer research. *Cancers (Basel)* **15**, 4352 (2023).

119. Yu, K. *et al.* Comprehensive transcriptomic analysis of cell lines as models of primary tumors across 22 tumor types. *Nat Commun* **10**, 3574 (2019).

120. Warren, A. *et al.* Global computational alignment of tumor and cell line transcriptional profiles. *Nat Commun* **12**, 22 (2021).

121. Liu, Y. *et al.* Patient-derived xenograft models in cancer therapy: technologies and applications. *Signal Transduct Target Ther* **8**, 160 (2023).

122. Stewart, E. *et al.* Orthotopic patient-derived xenografts of paediatric solid tumours. *Nature* **549**, 96–100 (2017).

123. Marques Da Costa, M. E. *et al.* A biobank of pediatric patient-derived-xenograft models in cancer precision medicine trial MAPPYACTS for relapsed and refractory tumors. *Commun Biol* **6**, 949 (2023).

124. He, F. *et al.* Genomic profiling of subcutaneous patient-derived xenografts reveals immune constraints on tumor evolution in childhood solid cancer. *Nat Commun* **14**, 7600 (2023).

125. Becher, O. J. & Holland, E. C. Genetically Engineered Models Have Advantages over Xenografts for Preclinical Studies. *Cancer Res* **66**, 3355–3359 (2006).

126. Langenau, D. M., Sweet-Cordero, A., Wechsler-Reya, R. J. & Dyer, M. A. Preclinical models provide scientific justification and translational relevance for moving novel therapeutics into clinical trials for pediatric cancer. *Cancer Res* **75**, 5176–5186 (2015).

127. Kersten, K., de Visser, K. E., van Miltenburg, M. H. & Jonkers, J. Genetically engineered mouse models in oncology research and cancer medicine. *EMBO Mol Med* **9**, 137-153–153 (2017).

128. Hill, W., Caswell, D. R. & Swanton, C. Capturing cancer evolution using genetically engineered mouse models (GEMMs). *Trends Cell Biol* **31**, 1007–1018 (2021).

129. Skapek, S. X. *et al.* Rhabdomyosarcoma. *Nat Rev Dis Primers* **5**, 1 (2019).

130. Chen, C., Dorado Garcia, H., Scheer, M. & Henssen, A. G. Current and future treatment strategies for rhabdomyosarcoma. *Front Oncol* **9**, 1458 (2019).

131. Hettmer, S. & Wagers, A. J. Muscling in: Uncovering the origins of rhabdomyosarcoma. *Nat Med* **16**, 171–173 (2010).

132. Searcy, M. B. *et al.* PAX3-FOXO1 dictates myogenic reprogramming and rhabdomyosarcoma identity in endothelial progenitors. *Nat Commun* **14**, 7291 (2023).

133. Ricker, C. A. *et al.* Defining an embryonal rhabdomyosarcoma endotype. *Molecular Case Studies* **6**, a005066 (2020).

134. Shern, J. F. *et al.* Comprehensive genomic analysis of rhabdomyosarcoma reveals a landscape of alterations affecting a common genetic axis in fusion-positive and fusion-negative tumors. *Cancer Discov* **4**, 216–231 (2014).

135. Agaram, N. P. Evolving classification of rhabdomyosarcoma. *Histopathology* **80**, 98–108 (2022).

136. Dehner, C. A., Rudzinski, E. R. & Davis, J. L. Rhabdomyosarcoma: Updates on classification and the necessity of molecular testing beyond immunohistochemistry. *Hum Pathol* **147**, 72–81 (2024).

137. Sciot, R. *et al.* Skeletal Muscle Tumors. in *Adipocytic, Vascular and Skeletal Muscle Tumors: A Practical Diagnostic Approach* (eds. Sciot, R., Gerosa, C. & Faa, G.) 149–178 (Springer International Publishing, Cham, 2020). doi:10.1007/978-3-030-37460-0_3.

138. Williamson, D. *et al.* Fusion gene–negative alveolar rhabdomyosarcoma is clinically and molecularly indistinguishable from embryonal rhabdomyosarcoma. *Journal of Clinical Oncology* **28**, 2151–2158 (2010).

139. Kallen, M. E. & Hornick, J. L. The 2020 WHO classification: what's new in soft tissue tumor pathology? *Am J Surg Pathol* **45**, e1–e23 (2021).

140. Furlong, M. A., Mentzel, T. & Fanburg-Smith, J. C. Pleomorphic rhabdomyosarcoma in adults: a clinicopathologic study of 38 cases with emphasis on morphologic variants and recent skeletal muscle-specific markers. *Modern Pathology* **14**, 595–603 (2001).

141. Schürch, W. *et al.* Pleomorphic soft tissue myogenic sarcomas of adulthood: a reappraisal in the mid-1990s. *Am J Surg Pathol* **20**, 131–147 (1996).

142. Deyrup, A. T. *et al.* Myoid differentiation and prognosis in adult pleomorphic sarcomas of the extremity: an analysis of 92 cases. *Cancer: Interdisciplinary International Journal of the American Cancer Society* **98**, 805–813 (2003).

143. Hornick, J. L. Subclassification of pleomorphic sarcomas: How and why should we care? *Ann Diagn Pathol* **37**, 118–124 (2018).

144. Noujaim, J. *et al.* Adult pleomorphic rhabdomyosarcoma: a multicentre retrospective study. *Anticancer Res* **35**, 6213–6217 (2015).

145. Hettmer, S. *et al.* Anaplastic rhabdomyosarcoma in TP53 germline mutation carriers. *Cancer* **120**, 1068–1075 (2014).

146. Leiner, J. & Le Loarer, F. The current landscape of rhabdomyosarcomas: an update. *Virchows Archiv* **476**, 97–108 (2020).

147. Kobayashi, H. *et al.* Prognostic factors and treatment outcomes in patients with pleomorphic rhabdomyosarcoma: a population-based cohort study. *Jpn J Clin Oncol* **54**, 471–478 (2024).

148. Saoud, C. *et al.* Genomic profiling of pleomorphic rhabdomyosarcoma reveals a genomic signature distinct from that of embryonal rhabdomyosarcoma. *Genes Chromosomes Cancer* **63**, e23238 (2024).

149. Mentzel, T. & Katenkamp, D. Sclerosing, pseudovascular rhabdomyosarcoma in adults. *Virchows Archiv* **436**, 305–311 (2000).

150. Yasui, N. *et al.* Clinicopathologic analysis of spindle cell/sclerosing rhabdomyosarcoma. *Pediatr Blood Cancer* **62**, 1011–1016 (2015).

151. Nascimento, A. F. & Fletcher, C. D. M. Spindle cell rhabdomyosarcoma in adults. *Am J Surg Pathol* **29**, 1106–1113 (2005).

152. Agaram, N. P. *et al.* MYOD1-mutant spindle cell and sclerosing rhabdomyosarcoma: an aggressive subtype irrespective of age. A reappraisal for molecular classification and risk stratification. *Modern Pathology* **32**, 27–36 (2019).

153. Whittle, S. *et al.* Congenital spindle cell rhabdomyosarcoma: An international cooperative analysis. *Eur J Cancer* **168**, 56–64 (2022).

154. Kohashi, K., Kinoshita, I. & Oda, Y. Soft tissue special issue: skeletal muscle tumors: a clinicopathological review. *Head Neck Pathol* **14**, 12–20 (2020).

155. Dashti, N. K. *et al.* Spindle cell rhabdomyosarcoma of bone with FUS–TFCP 2 fusion: confirmation of a very recently described rhabdomyosarcoma subtype. *Histopathology* **73**, 514–520 (2018).

156. Le Loarer, F. *et al.* A subset of epithelioid and spindle cell rhabdomyosarcomas is associated with TFCP2 fusions and common ALK upregulation. *Modern Pathology* **33**, 404–419 (2020).

157. Bisogno, G. *et al.* Congenital rhabdomyosarcoma: A report from the European paediatric Soft tissue sarcoma Study Group. *Pediatr Blood Cancer* **69**, e29376 (2022).

158. Alaggio, R. *et al.* A Molecular Study of Pediatric Spindle and Sclerosing Rhabdomyosarcoma: Identification of Novel and Recurrent: VGLL2-: related Fusions in Infantile Cases. *Am J Surg Pathol* **40**, 224–235 (2016).

159. Kohsaka, S. *et al.* A recurrent neomorphic mutation in MYOD1 defines a clinically aggressive subset of embryonal rhabdomyosarcoma associated with PI3K-AKT pathway mutations. *Nat Genet* **46**, 595–600 (2014).

160. Pastore, G. *et al.* Childhood soft tissue sarcomas incidence and survival in European children (1978–1997): Report from the Automated Childhood Cancer Information System project. *Eur J Cancer* **42**, 2136–2149 (2006).

161. Stiller, C. A. & Parkint, D. M. International variations in the incidence of childhood soft-tissue sarcomas. *Paediatr Perinat Epidemiol* **8**, 107–119 (1994).

162. Perez, E. A. *et al.* Rhabdomyosarcoma in children: a SEER population based study. *Journal of Surgical Research* **170**, e243–e251 (2011).

163. Amer, K. M. *et al.* Epidemiology, incidence, and survival of rhabdomyosarcoma subtypes: SEER and ICES database analysis. *Journal of Orthopaedic Research®* **37**, 2226–2230 (2019).

164. Ognjanovic, S., Linabery, A. M., Charbonneau, B. & Ross, J. A. Trends in childhood rhabdomyosarcoma incidence and survival in the United States, 1975-2005. *Cancer: Interdisciplinary International Journal of the American Cancer Society* **115**, 4218–4226 (2009).

165. (US)), S. P. (National C. I. *Cancer Incidence and Survival among Children and Adolescents: United States SEER Program, 1975-1995*. (National Cancer Institute, 1999).

166. Chow, E. J. *et al.* Childhood cancer in relation to parental race and ethnicity: a 5-state pooled analysis. *Cancer* **116**, 3045–3053 (2010).

167. Linabery, A. M. & Ross, J. A. Trends in childhood cancer incidence in the US (1992–2004). *Cancer: Interdisciplinary International Journal of the American Cancer Society* **112**, 416–432 (2008).

168. Martin-Giacalone, B. A., Weinstein, P. A., Plon, S. E. & Lupo, P. J. Pediatric rhabdomyosarcoma: epidemiology and genetic susceptibility. *J Clin Med* **10**, 2028 (2021).

169. Meyer, W. H. & Spunt, S. L. Soft tissue sarcomas of childhood. *Cancer Treat Rev* **30**, 269–280 (2004).

170. Wexler, L. H. & Helman, L. J. Pediatric soft tissue sarcomas. *CA Cancer J Clin* **44**, 211–247 (1994).

171. Dagher, R. & Helman, L. Rhabdomyosarcoma: an overview. *Oncologist* **4**, 34–44 (1999).

172. Dantonello, T. M. *et al.* Initial patient characteristics can predict pattern and risk of relapse in localized rhabdomyosarcoma. *Journal of Clinical Oncology* **26**, 406–413 (2008).

173. Ferrari, A. *et al.* Rhabdomyosarcoma in adults: a retrospective analysis of 171 patients treated at a single institution. *Cancer: Interdisciplinary International Journal of the American Cancer Society* **98**, 571–580 (2003).

174. Mazzoleni, S. *et al.* Outcomes and prognostic factors after recurrence in children and adolescents with nonmetastatic rhabdomyosarcoma. *Cancer* **104**, 183–190 (2005).

175. Agarwala, S. Pediatric rhabdomyosarcomas and nonrhabdomyosarcoma soft tissue sarcoma. *J Indian Assoc Pediatr Surg* **11**, 15–23 (2006).

176. Hettmer, S. & Wagers, A. J. Muscling in: Uncovering the origins of rhabdomyosarcoma. *Nat Med* **16**, 171–173 (2010).

177. Krsková, L., Mrhalova, M., Sumerauer, D. & Kodet, R. Rhabdomyosarcoma: molecular diagnostics of patients classified by morphology and immunohistochemistry with emphasis on bone marrow and purged peripheral blood progenitor cells involvement. *Virchows Archiv* **448**, 449–458 (2006).

178. Kumar, S., Perlman, E., Harris, C. A., Raffeld, M. & Tsokos, M. Myogenin is a specific marker for rhabdomyosarcoma: an immunohistochemical study in paraffin-embedded tissues. *Modern Pathology* **13**, 988–993 (2000).

179. Sebire, N. J. & Malone, M. Myogenin and MyoD1 expression in paediatric rhabdomyosarcomas. *J Clin Pathol* **56**, 412–416 (2003).

180. Altmannsberger, M., Weber, K., Droste, R. & Osborn, M. Desmin is a specific marker for rhabdomyosarcomas of human and rat origin. *Am J Pathol* **118**, 85 (1985).

181. Brooks, J. J. Immunohistochemistry of soft tissue tumors. Myoglobin as a tumor marker for rhabdomyosarcoma. *Cancer* **50**, 1757–1763 (1982).

182. Furlong, M. A., Mentzel, T. & Fanburg-Smith, J. C. Pleomorphic rhabdomyosarcoma in adults: a clinicopathologic study of 38 cases with emphasis on morphologic variants and recent skeletal muscle-specific markers. *Modern Pathology* **14**, 595–603 (2001).

183. Cessna, M. H. *et al.* Are Myogenin and MyoD1 Expression Specific for Rhabdomyosarcoma?: A Study of 150 Cases, With Emphasis on Spindle Cell Mimics. *Am J Surg Pathol* **25**, (2001).

184. Robin, Y.-M. *et al.* Transgelin is a novel marker of smooth muscle differentiation that improves diagnostic accuracy of leiomyosarcomas: a comparative immunohistochemical reappraisal of myogenic markers in 900 soft tissue tumors. *Modern Pathology* **26**, 502–510 (2013).

185. Downs-Kelly, E. *et al.* The utility of FOXO1 fluorescence in situ hybridization (FISH) in formalin-fixed paraffin-embedded specimens in the diagnosis of alveolar rhabdomyosarcoma. *Diagnostic Molecular Pathology* **18**, 138–143 (2009).

186. Arnold, M. A. & Barr, F. G. Molecular diagnostics in the management of rhabdomyosarcoma. *Expert Rev Mol Diagn* **17**, 189–194 (2017).

187. Fan, R., Parham, D. M. & Wang, L. L. An Integrative Morphologic and Molecular Approach for Diagnosis and Subclassification of Rhabdomyosarcoma. *Arch Pathol Lab Med* **146**, 953–959 (2022).

188. Zhang, X. *et al.* Deep learning of rhabdomyosarcoma pathology images for classification and survival outcome prediction. *Am J Pathol* **192**, 917–925 (2022).

189. Frankel, A. O. *et al.* Machine learning for rhabdomyosarcoma histopathology. *Modern Pathology* **35**, 1193–1203 (2022).

190. Milewski, D. *et al.* Predicting Molecular Subtype and Survival of Rhabdomyosarcoma Patients Using Deep Learning of H&E Images: A Report from the Children's Oncology Group. *Clinical Cancer Research* **29**, 364–378 (2023).

191. Grufferman, S., Schwartz, A. G., Ruymann, F. B. & Maurer, H. M. Parents' use of cocaine and marijuana and increased risk of rhabdomyosarcoma in their children. *Cancer Causes & Control* **4**, 217–224 (1993).

192. Grufferman, S., Ruymann, F., Ognjanovic, S., Erhardt, E. B. & Maurer, H. M. Prenatal X-ray exposure and rhabdomyosarcoma in children: a report from the children's oncology group. *Cancer Epidemiology Biomarkers & Prevention* **18**, 1271–1276 (2009).

193. Lupo, P. J. *et al.* Maternal and birth characteristics and childhood rhabdomyosarcoma: a report from the Children's Oncology Group. *Cancer Causes & Control* **25**, 905–913 (2014).

194. Lupo, P. J. *et al.* Family history of cancer and childhood rhabdomyosarcoma: a report from the Children's Oncology Group and the Utah Population Database. *Cancer Med* **4**, 781–790 (2015).

195. Kim, J. *et al.* Pathogenic Germline Variants in Cancer Susceptibility Genes in Children and Young Adults With Rhabdomyosarcoma. *JCO Precis Oncol* 75–87 (2021) doi:10.1200/PO.20.00218.

196. Li, H. *et al.* Germline cancer predisposition variants in pediatric rhabdomyosarcoma: a report from the Children's Oncology Group. *JNCI: Journal of the National Cancer Institute* **113**, 875–883 (2021).

197. Stevens, M. C. G. *et al.* Treatment of Nonmetastatic Rhabdomyosarcoma in Childhood and Adolescence: Third Study of the International Society of Paediatric Oncology—SIOP Malignant Mesenchymal Tumor 89. *Journal of Clinical Oncology* **23**, 2618–2628 (2005).

198. Arndt, C. A. S. *et al.* Vincristine, actinomycin, and cyclophosphamide compared with vincristine, actinomycin, and cyclophosphamide alternating with vincristine, topotecan, and cyclophosphamide for intermediate-risk rhabdomyosarcoma: children's oncology group study D9803. *Journal of Clinical Oncology* **27**, 5182–5188 (2009).

199. Crist, W. M. *et al.* Intergroup rhabdomyosarcoma study-IV: results for patients with nonmetastatic disease. *Journal of Clinical Oncology* **19**, 3091–3102 (2001).

200. Malempati, S. & Hawkins, D. S. Rhabdomyosarcoma: review of the Children's Oncology Group (COG) Soft-Tissue Sarcoma Committee experience and rationale for current COG studies. *Pediatr Blood Cancer* **59**, 5–10 (2012).

201. Hm, M. The intergroup rhabdomyosarcoma study-I. A final report. *Cancer* **61**, 209–220 (1988).

202. Lawrence Jr, W., Anderson, J. R., Gehan, E. A. & Maurer, H. Pretreatment TNM staging of childhood rhabdomyosarcoma: a report of the Intergroup Rhabdomyosarcoma Study Group. *Cancer: Interdisciplinary International Journal of the American Cancer Society* **80**, 1165–1170 (1997).

203. Crist, W. *et al.* The third intergroup rhabdomyosarcoma study. *Journal of Clinical Oncology* **13**, 610–630 (1995).

204. De Salvo, G. L. *et al.* Reappraisal of prognostic factors used in the European Pediatric Soft Tissue Sarcoma Study Group RMS 2005 study for localized rhabdomyosarcoma to optimize risk stratification and generate a prognostic nomogram. *Cancer* (2024).

205. Oberlin, O. *et al.* Prognostic factors in metastatic rhabdomyosarcomas: results of a pooled analysis from United States and European cooperative groups. *Journal of Clinical Oncology* **26**, 2384–2389 (2008).

206. Raney, R. B. *et al.* The Intergroup Rhabdomyosarcoma Study Group (IRSG): major lessons from the IRS-I through IRS-IV studies as background for the current IRS-V treatment protocols. *Sarcoma* **5**, 9–15 (2001).

207. Haduong, J. H. *et al.* An update on rhabdomyosarcoma risk stratification and the rationale for current and future Children's Oncology Group clinical trials. *Pediatr Blood Cancer* **69**, e29511 (2022).

208. Gallego, S. *et al.* GEIS-SEHOP clinical practice guidelines for the treatment of rhabdomyosarcoma. *Clinical and Translational Oncology* **23**, 2460–2473 (2021).

209. Chisholm, J. *et al.* Frontline and Relapsed Rhabdomyosarcoma (FAR-RMS) Clinical Trial: A Report from the European Paediatric Soft Tissue Sarcoma Study Group (EpSSG). *Cancers (Basel)* **16**, (2024).

210. Burke, M. *et al.* Assessment of response to induction therapy and its influence on 5-year failure-free survival in group III rhabdomyosarcoma: the Intergroup Rhabdomyosarcoma Study-IV experience—a report from the Soft Tissue Sarcoma Committee of the Children's Oncology Group. *Journal of clinical oncology* **25**, 4909–4913 (2007).

211. Oberlin, O. *et al.* Randomized comparison of intensified six-drug versus standard three-drug chemotherapy for high-risk nonmetastatic rhabdomyosarcoma and other chemotherapy-sensitive childhood soft tissue sarcomas: long-term results from the International Society of Pediatric Oncology MMT95 study. *Journal of clinical oncology* **30**, 2457–2465 (2012).

212. Rosenberg, A. R. *et al.* Early response as assessed by anatomic imaging does not predict failure-free survival among patients with Group III rhabdomyosarcoma: A report from the Children's Oncology Group. *Eur J Cancer* **50**, 816–823 (2014).

213. Bisogno, G. *et al.* Nonmetastatic Rhabdomyosarcoma in Children and Adolescents: Overall Results of the European Pediatric Soft Tissue Sarcoma Study Group RMS2005 Study. *Journal of Clinical Oncology* **41**, 2342–2349 (2023).

214. Ferrari, A. *et al.* Paratesticular rhabdomyosarcoma: report from the Italian and German Cooperative Group. *Journal of clinical oncology* **20**, 449–455 (2002).

215. Bisogno, G. *et al.* Addition of dose-intensified doxorubicin to standard chemotherapy for rhabdomyosarcoma (EpSSG RMS 2005): a multicentre, open-label, randomised controlled, phase 3 trial. *Lancet Oncol* **19**, 1061–1071 (2018).

216. Meza, J. L. Children's Oncology Group: Analysis of prognostic factors in patients with nonmetastatic rhabdomyosarcoma treated on intergroup

rhabdomyosarcoma studies III and IV: the children's Oncology Group. *J. Clin. Oncol.* **24**, 3844–3851 (2006).

217. Gallego, S. *et al.* Fusion status in patients with lymph node-positive (N1) alveolar rhabdomyosarcoma is a powerful predictor of prognosis: Experience of the European Paediatric Soft Tissue Sarcoma Study Group (EpSSG). *Cancer* **124**, 3201–3209 (2018).

218. Bisogno, G. *et al.* Vinorelbine and continuous low-dose cyclophosphamide as maintenance chemotherapy in patients with high-risk rhabdomyosarcoma (RMS 2005): a multicentre, open-label, randomised, phase 3 trial. *Lancet Oncol* **20**, 1566–1575 (2019).

219. Oberlin, O. *et al.* Prognostic factors in metastatic rhabdomyosarcomas: results of a pooled analysis from United States and European cooperative groups. *Journal of Clinical Oncology* **26**, 2384–2389 (2008).

220. Bergeron, C. *et al.* Revisiting the role of doxorubicin in the treatment of rhabdomyosarcoma: an up-front window study in newly diagnosed children with high-risk metastatic disease. *Eur J Cancer* **44**, 427–431 (2008).

221. Heske, C. M. & Mascarenhas, L. Relapsed rhabdomyosarcoma. *J Clin Med* **10**, 804 (2021).

222. Zarrabi, A. *et al.* Rhabdomyosarcoma: Current Therapy, Challenges, and Future Approaches to Treatment Strategies. *Cancers (Basel)* **15**, (2023).

223. Defachelles, A.-S. *et al.* Randomized phase II trial of vincristine-irinotecan with or without temozolomide, in children and adults with relapsed or refractory rhabdomyosarcoma: A European Paediatric Soft tissue Sarcoma Study Group and Innovative Therapies for Children With Cancer trial. *Journal of Clinical Oncology* **39**, 2979–2990 (2021).

224. Weigel, B. J. *et al.* Intensive Multiagent Therapy, Including Dose-Compressed Cycles of Ifosfamide/Etoposide and Vincristine/Doxorubicin/Cyclophosphamide, Irinotecan, and Radiation, in Patients With High-Risk Rhabdomyosarcoma: A Report From the Children's Oncology Group. *Journal of Clinical Oncology* **34**, 117–122 (2015).

225. Meazza, C. *et al.* Efficacy of topotecan plus vincristine and doxorubicin in children with recurrent/refractory rhabdomyosarcoma. *Medical Oncology* **26**, 67–72 (2009).

226. Heinz, A. T. *et al.* Second-line treatment of pediatric patients with relapsed rhabdomyosarcoma adapted to initial risk stratification: Data of the European Soft Tissue Sarcoma Registry (SoTiSaR). *Pediatr Blood Cancer* **70**, e30363 (2023).

227. Casanova, M. *et al.* Vinorelbine and low-dose cyclophosphamide in the treatment of pediatric sarcomas: pilot study for the upcoming European Rhabdomyosarcoma Protocol. *Cancer* **101**, 1664–1671 (2004).

228. Mascarenhas, L. *et al.* Randomized Phase II Trial of Bevacizumab or Temsirolimus in Combination With Chemotherapy for First Relapse Rhabdomyosarcoma: A Report From the Children's Oncology Group. *Journal of Clinical Oncology* **37**, 2866–2874 (2019).

229. Ruiz-Mesa, C., Goldberg, J. M., Coronado Munoz, A. J., Dumont, S. N. & Trent, J. C. Rhabdomyosarcoma in adults: new perspectives on therapy. *Curr Treat Options Oncol* **16**, 1–12 (2015).

230. Gallego, S. *et al.* Fusion status in patients with lymph node-positive (N1) alveolar rhabdomyosarcoma is a powerful predictor of prognosis: Experience of the European Paediatric Soft Tissue Sarcoma Study Group (EpSSG). *Cancer* **124**, 3201–3209 (2018).

231. Hayes-Jordan, A. *et al.* Outcome after surgical resection of recurrent rhabdomyosarcoma. *J Pediatr Surg* **41**, 633–638 (2006).

232. Cameron, A. L. *et al.* The impact of radiation therapy in children and adolescents with metastatic rhabdomyosarcoma. *Int J Radiat Oncol Biol Phys* **111**, 968–978 (2021).

233. Mohan, A. C. *et al.* Local therapy to distant metastatic sites in stage IV rhabdomyosarcoma. *Pediatr Blood Cancer* **65**, e26859 (2018).

234. Liu, A. K. *et al.* Local control of metastatic sites with radiation therapy in metastatic Ewing sarcoma and rhabdomyosarcoma. *Pediatr Blood Cancer* **57**, 169–171 (2011).

235. Dantonello, T. M. *et al.* Embryonal rhabdomyosarcoma with metastases confined to the lungs: report from the CWS Study Group. *Pediatr Blood Cancer* **56**, 725–732 (2011).

236. Rodeberg, D. *et al.* Characteristics and outcomes of rhabdomyosarcoma patients with isolated lung metastases from IRS-IV. *J Pediatr Surg* **40**, 256–262 (2005).

237. Casey, D. L., Wexler, L. H., LaQuaglia, M. P., Meyers, P. A. & Wolden, S. L. Favorable outcomes after whole abdominopelvic radiation therapy for pediatric and young adult sarcoma. *Pediatr Blood Cancer* **61**, 1565–1569 (2014).

238. Casey, D. L. *et al.* Radiation for bone metastases in Ewing sarcoma and rhabdomyosarcoma. *Pediatr Blood Cancer* **62**, 445–449 (2015).

239. Barr, F. G. *et al.* Rearrangement of the PAX3 paired box gene in the paediatric solid tumour alveolar rhabdomyosarcoma. *Nat Genet* **3**, 113–117 (1993).

240. Davis, R. J., D'Cruz, C. M., Lovell, M. A., Biegel, J. A. & Barr, F. G. Fusion of PAX7 to FKHR by the Variant t(1;13)(p36;q14) Translocation in Alveolar Rhabdomyosarcoma1. *Cancer Res* **54**, 2869–2872 (1994).

241. Galili, N. *et al.* Fusion of a fork head domain gene to PAX3 in the solid tumour alveolar rhabdomyosarcoma. *Nat Genet* **5**, 230–235 (1993).

242. Barr, F. G. Gene fusions involving PAX and FOX family members in alveolar rhabdomyosarcoma. *Oncogene* **20**, 5736–5746 (2001).

243. Bennicelli, J. L., Advani, S., Schäfer, B. W. & Barr, F. G. PAX3 and PAX7 exhibit conserved cis-acting transcription repression domains and utilize a common gain of function mechanism in alveolar rhabdomyosarcoma. *Oncogene* **18**, 4348–4356 (1999).

244. Fredericks, W. J. *et al.* The PAX3-FKHR fusion protein created by the t (2; 13) translocation in alveolar rhabdomyosarcomas is a more potent transcriptional activator than PAX3. *Mol Cell Biol* **15**, 1522–1535 (1995).

245. Davis, R. J. & Barr, F. G. Fusion genes resulting from alternative chromosomal translocations are overexpressed by gene-specific mechanisms in alveolar rhabdomyosarcoma. *Proceedings of the National Academy of Sciences* **94**, 8047–8051 (1997).

246. Thalhammer, V. *et al.* PLK1 Phosphorylates PAX3-FOXO1, the Inhibition of Which Triggers Regression of Alveolar Rhabdomyosarcoma. *Cancer Res* **75**, 98–110 (2015).

247. Bharathy, N. *et al.* P/CAF mediates PAX3–FOXO1-dependent oncogenesis in alveolar rhabdomyosarcoma. *J Pathol* **240**, 269–281 (2016).

248. Amstutz, R. *et al.* Phosphorylation Regulates Transcriptional Activity of PAX3/FKHR and Reveals Novel Therapeutic Possibilities. *Cancer Res* **68**, 3767–3776 (2008).

249. Asante, Y. *et al.* PAX3-FOXO1 uses its activation domain to recruit CBP/P300 and shape RNA Pol2 cluster distribution. *Nat Commun* **14**, 8361 (2023).

250. Cao, L. *et al.* Genome-wide identification of PAX3-FKHR binding sites in rhabdomyosarcoma reveals candidate target genes important for development and cancer. *Cancer Res* **70**, 6497–6508 (2010).

251. Milewski, D. *et al.* FOXF1 is required for the oncogenic properties of PAX3-FOXO1 in rhabdomyosarcoma. *Oncogene* **40**, 2182–2199 (2021).

252. Marques, J. G. *et al.* NuRD subunit CHD4 regulates super-enhancer accessibility in rhabdomyosarcoma and represents a general tumor dependency. *Elife* **9**, e54993 (2020).

253. Laubscher, D. *et al.* BAF complexes drive proliferation and block myogenic differentiation in fusion-positive rhabdomyosarcoma. *Nat Commun* **12**, 6924 (2021).

254. Ebauer, M., Wachtel, M., Niggli, F. K. & Schäfer, B. W. Comparative expression profiling identifies an in vivo target gene signature with TFAP2B as a mediator of the survival function of PAX3/FKHR. *Oncogene* **26**, 7267–7281 (2007).

255. Linardic, C. M. PAX3–FOXO1 fusion gene in rhabdomyosarcoma. *Cancer Lett* **270**, 10–18 (2008).

256. Vi, J. G. T. *et al.* Identification of FGFR4-activating mutations in human rhabdomyosarcomas that promote metastasis in xenotransplanted models. *J Clin Invest* **119**, 3395–3407 (2009).

257. Seki, M. *et al.* Integrated genetic and epigenetic analysis defines novel molecular subgroups in rhabdomyosarcoma. *Nat Commun* **6**, 7557 (2015).

258. Crose, L. E. S. *et al.* FGFR4 blockade exerts distinct antitumorigenic effects in human embryonal versus alveolar rhabdomyosarcoma. *Clinical Cancer Research* **18**, 3780–3790 (2012).

259. Clay, M. R. *et al.* Methylation profiling reveals novel molecular classes of rhabdomyosarcoma. *Sci Rep* **11**, 22213 (2021).

260. Kang, Z. *et al.* Downregulation of IGFBP2 is associated with resistance to IGF1R therapy in rhabdomyosarcoma. *Oncogene* **33**, 5697–5705 (2014).

261. Taulli, R. *et al.* Validation of met as a therapeutic target in alveolar and embryonal rhabdomyosarcoma. *Cancer Res* **66**, 4742–4749 (2006).

262. Szewczyk, B., Skrzypek, K. & Majka, M. Targeting MET receptor in rhabdomyosarcoma: rationale and progress. *Curr Drug Targets* **18**, 98–107 (2017).

263. Miekus, K. *et al.* The decreased metastatic potential of rhabdomyosarcoma cells obtained through MET receptor downregulation and the induction of differentiation. *Cell Death Dis* **4**, e459–e459 (2013).

264. Taniguchi, E. *et al.* PDGFR-A is a therapeutic target in alveolar rhabdomyosarcoma. *Oncogene* **27**, 6550–6560 (2008).

265. Ehnman, M. *et al.* Distinct effects of ligand-induced PDGFRα and PDGFRβ signaling in the human rhabdomyosarcoma tumor cell and stroma cell compartments. *Cancer Res* **73**, 2139–2149 (2013).

266. Stewart, E. *et al.* Identification of therapeutic targets in rhabdomyosarcoma through integrated genomic, epigenomic, and proteomic analyses. *Cancer Cell* **34**, 411–426 (2018).

267. Langdon, C. G. *et al.* Synthetic essentiality between PTEN and core dependency factor PAX7 dictates rhabdomyosarcoma identity. *Nat Commun* **12**, 5520 (2021).

268. Iolascon, A. *et al.* Analysis of cyclin-dependent kinase inhibitor genes (CDKN2A, CDKN2B, and CDKN2C) in childhood rhabdomyosarcoma. *Genes Chromosomes Cancer* **15**, 217–222 (1996).

269. Kung, C.-P. & Weber, J. D. It's getting complicated—a fresh look at p53-MDM2-ARF triangle in tumorigenesis and cancer therapy. *Front Cell Dev Biol* **10**, 818744 (2022).

270. VanArsdale, T., Boshoff, C., Arndt, K. T. & Abraham, R. T. Molecular Pathways: Targeting the Cyclin D–CDK4/6 Axis for Cancer Treatment. *Clinical Cancer Research* **21**, 2905–2910 (2015).

271. Giralt, I. *et al.* Dickkopf-1 inhibition reactivates Wnt/β-catenin signaling in rhabdomyosarcoma, induces myogenic markers in vitro and impairs tumor cell survival in vivo. *Int J Mol Sci* **22**, 12921 (2021).

272. Annavarapu, S. R. *et al.* Characterization of Wnt/β-catenin signaling in rhabdomyosarcoma. *Laboratory Investigation* **93**, 1090–1099 (2013).

273. Chen, E. Y. *et al.* Glycogen synthase kinase 3 inhibitors induce the canonical WNT/β-catenin pathway to suppress growth and self-renewal in embryonal rhabdomyosarcoma. *Proceedings of the National Academy of Sciences* **111**, 5349–5354 (2014).

274. Roma, J., Masià, A., Reventós, J., Sánchez de Toledo, J. & Gallego, S. Notch pathway inhibition significantly reduces rhabdomyosarcoma invasiveness and mobility in vitro. *Clinical Cancer Research* **17**, 505–513 (2011).

275. Belyea, B. C., Naini, S., Bentley, R. C. & Linardic, C. M. Inhibition of the Notch-Hey1 axis blocks embryonal rhabdomyosarcoma tumorigenesis. *Clinical Cancer Research* **17**, 7324–7336 (2011).

276. Slemmons, K. K. *et al.* A novel notch–YAP circuit drives stemness and tumorigenesis in embryonal rhabdomyosarcoma. *Molecular Cancer Research* **15**, 1777–1791 (2017).

277. Zarzosa, P. *et al.* Targeting the hedgehog pathway in rhabdomyosarcoma. *Cancers (Basel)* **15**, 727 (2023).

278. Drummond, C. J. *et al.* Hedgehog Pathway Drives Fusion-Negative Rhabdomyosarcoma Initiated From Non-myogenic Endothelial Progenitors. *Cancer Cell* **33**, 108-124.e5 (2018).

279. Satheesha, S. *et al.* Targeting hedgehog signaling reduces self-renewal in embryonal rhabdomyosarcoma. *Oncogene* **35**, 2020–2030 (2016).

280. Tremblay, A. M. *et al.* The Hippo transducer YAP1 transforms activated satellite cells and is a potent effector of embryonal rhabdomyosarcoma formation. *Cancer Cell* **26**, 273–287 (2014).

281. Crose, L. E. S. *et al.* Alveolar rhabdomyosarcoma–associated PAX3-FOXO1 promotes tumorigenesis via Hippo pathway suppression. *J Clin Invest* **124**, 285–296 (2014).

282. Conti, B., K Slemmons, K., Rota, R. & M Linardic, C. Recent insights into Notch signaling in embryonal rhabdomyosarcoma. *Curr Drug Targets* **17**, 1235–1244 (2016).

283. Slemmons, K. K. *et al.* Targeting Hippo-dependent and Hippo-independent YAP1 signaling for the treatment of childhood rhabdomyosarcoma. *Cancer Res* **80**, 3046–3056 (2020).

284. Kohsaka, S. *et al.* A recurrent neomorphic mutation in MYOD1 defines a clinically aggressive subset of embryonal rhabdomyosarcoma associated with PI3K-AKT pathway mutations. *Nat Genet* **46**, 595–600 (2014).

285. Szuhai, K., de Jong, D., Leung, W. Y., Fletcher, C. D. M. & Hogendoorn, P. C. W. Transactivating mutation of the gene is a frequent event in adult spindle cell rhabdomyosarcoma. *J Pathol* **232**, 300–307 (2014).

286. Gryder, B. E. *et al.* Histone hyperacetylation disrupts core gene regulatory architecture in rhabdomyosarcoma. *Nat Genet* **51**, 1714–1722 (2019).

287. Manning, B. J. & Yusufzai, T. The ATP-dependent chromatin remodeling enzymes CHD6, CHD7, and CHD8 exhibit distinct nucleosome binding and remodeling activities. *Journal of Biological Chemistry* **292**, 11927–11936 (2017).

288. Newton, A. H. & Pask, A. J. CHD9 upregulates RUNX2 and has a potential role in skeletal evolution. *BMC Mol Cell Biol* **21**, 1–9 (2020).

289. Ogawara, Y. *et al.* Akt Enhances Mdm2-mediated Ubiquitination and Degradation of p53 *. *Journal of Biological Chemistry* **277**, 21843–21850 (2002).

290. Mayo, L. D. & Donner, D. B. A phosphatidylinositol 3-kinase/Akt pathway promotes translocation of Mdm2 from the cytoplasm to the nucleus. *Proceedings of the National Academy of Sciences* **98**, 11598–11603 (2001).

291. Zhou, B. P. *et al.* HER-2/neu induces p53 ubiquitination via Akt-mediated MDM2 phosphorylation. *Nat Cell Biol* **3**, 973–982 (2001).

292. Feng, J. *et al.* Stabilization of Mdm2 via decreased ubiquitination is mediated by protein kinase B/Akt-dependent phosphorylation. *Journal of Biological Chemistry* **279**, 35510–35517 (2004).

293. Chibaya, L., Karim, B., Zhang, H. & Jones, S. N. Mdm2 phosphorylation by Akt regulates the p53 response to oxidative stress to promote cell proliferation and tumorigenesis. *Proceedings of the National Academy of Sciences* **118**, e2003193118 (2021).

294. Malmlof, M., Roudier, E., Hogberg, J. & Stenius, U. MEK-ERK-mediated phosphorylation of Mdm2 at Ser-166 in hepatocytes: Mdm2 is activated in response to inhibited Akt signaling. *Journal of Biological Chemistry* **282**, 2288–2296 (2007).

295. Zhang, S., Zhou, L. & El-Deiry, W. S. Small-Molecule NSC59984 Induces Mutant p53 Degradation through a ROS-ERK2-MDM2 Axis in Cancer Cells. *Molecular Cancer Research* **20**, 622–636 (2022).

296. Yan, H. *et al.* Regorafenib inhibits EphA2 phosphorylation and leads to liver damage via the ERK/MDM2/p53 axis. *Nat Commun* **14**, 2756 (2023).

297. Slack, A. *et al.* The p53 regulatory gene MDM2 is a direct transcriptional target of MYCN in neuroblastoma. *Proceedings of the National Academy of Sciences* **102**, 731–736 (2005).

298. Gamble, L. D., Kees, U. R., Tweddle, D. A. & Lunec, J. MYCN sensitizes neuroblastoma to the MDM2-p53 antagonists Nutlin-3 and MI-63. *Oncogene* **31**, 752–763 (2012).

299. Haupt, Y., Maya, R., Kazaz, A. & Oren, M. Mdm2 promotes the rapid degradation of p53. *Nature* **387**, 296–299 (1997).

300. Moll, U. M. & Petrenko, O. The MDM2-p53 interaction. *Molecular cancer research* **1**, 1001–1008 (2003).

301. Brooks, C. L. & Gu, W. p53 Ubiquitination: Mdm2 and Beyond. *Mol Cell* **21**, 307–315 (2006).

302. Kubbutat, M. H. G., Jones, S. N. & Vousden, K. H. Regulation of p53 stability by Mdm2. *Nature* **387**, 299–303 (1997).

303. Chène, P. Inhibiting the p53–MDM2 interaction: an important target for cancer therapy. *Nat Rev Cancer* **3**, 102–109 (2003).

304. Konopleva, M. *et al.* MDM2 inhibition: an important step forward in cancer therapy. *Leukemia* vol. 34 2858–2874 Preprint at https://doi.org/10.1038/s41375-020-0949-z (2020).

305. Cocker, H. A. *et al.* High levels of the MDM2 oncogene in paediatric rhabdomyosarcoma cell lines may confer multidrug resistance. *Br J Cancer* **85**, 1746–1752 (2001).

306. Hou, H., Sun, D. & Zhang, X. The role of MDM2 amplification and overexpression in therapeutic resistance of malignant tumors. *Cancer Cell Int* **19**, 216 (2019).

307. Fiddler, T. A., Smith, L., Tapscott, S. J. & Thayer, M. J. Amplification of MDM2 inhibits MyoD-mediated myogenesis. *Mol Cell Biol* **16**, 5048–5057 (1996).

308. Casey, D. L. *et al.* Genomic Determinants of Clinical Outcomes in Rhabdomyosarcoma. *Clinical Cancer Research* **26**, 1135–1140 (2020).

309. de Traux de Wardin, H. *et al.* Sequential genomic analysis using a multisample/multiplatform approach to better define rhabdomyosarcoma progression and relapse. *NPJ Precis Oncol* **7**, 96 (2023).

310. Engeland, K. Cell cycle regulation: p53-p21-RB signaling. *Cell Death Differ* **29**, 946–960 (2022).

311. Wang, H., Guo, M., Wei, H. & Chen, Y. Targeting p53 pathways: mechanisms, structures, and advances in therapy. *Signal Transduct Target Ther* **8**, 92 (2023).

312. Hafner, A., Bulyk, M. L., Jambhekar, A. & Lahav, G. The multiple mechanisms that regulate p53 activity and cell fate. *Nat Rev Mol Cell Biol* **20**, 199–210 (2019).

313. Abuetabh, Y. *et al.* DNA damage response revisited: the p53 family and its regulators provide endless cancer therapy opportunities. *Exp Mol Med* **54**, 1658–1669 (2022).

314. Marei, H. E. *et al.* p53 signaling in cancer progression and therapy. *Cancer Cell Int* **21**, 703 (2021).

315. Vogelstein, B. & Kinzler, K. W. p53 function and dysfunction. *Cell* **70**, 523–526 (1992).

316. Joerger, A. C. & Fersht, A. R. The p53 pathway: origins, inactivation in cancer, and emerging therapeutic approaches. *Annu Rev Biochem* **85**, 375–404 (2016).

317. Muller, P. A. J. & Vousden, K. H. p53 mutations in cancer. *Nat Cell Biol* **15**, 2–8 (2013).

318. Hassin, O. & Oren, M. Drugging p53 in cancer: one protein, many targets. *Nat Rev Drug Discov* **22**, 127–144 (2023).

319. Kocik, J. *et al.* Helping the released guardian: Drug combinations for supporting the anticancer activity of HDM2 (MDM2) antagonists. *Cancers* vol. 11 Preprint at https://doi.org/10.3390/cancers11071014 (2019).

320. Zhu, H. *et al.* Targeting p53–MDM2 interaction by small-molecule inhibitors: learning from MDM2 inhibitors in clinical trials. *J Hematol Oncol* **15**, 91 (2022).

321. Yao, Y., Zhang, Q., Li, Z. & Zhang, H. MDM2: current research status and prospects of tumor treatment. *Cancer Cell Int* **24**, 170 (2024).

322. Shangary, S. & Wang, S. Targeting the MDM2-p53 interaction for cancer therapy. *Clinical Cancer Research* **14**, 5318–5324 (2008).

323. Kussie, P. H. *et al.* Structure of the MDM2 oncoprotein bound to the p53 tumor suppressor transactivation domain. *Science (1979)* **274**, 948–953 (1996).

324. Vassilev, L. T. *et al.* In vivo activation of the p53 pathway by small-molecule antagonists of MDM2. *Science (1979)* **303**, 844–848 (2004).

325. Tovar, C. *et al.* Small-molecule MDM2 antagonists reveal aberrant p53 signaling in cancer: Implications for therapy. *Proceedings of the National Academy of Sciences* **103**, 1888–1893 (2006).

326. Vu, B. *et al.* Discovery of RG7112: a small-molecule MDM2 inhibitor in clinical development. *ACS Med Chem Lett* **4**, 466–469 (2013).

327. Ding, Q. *et al.* Discovery of RG7388, a potent and selective p53–MDM2 inhibitor in clinical development. *J Med Chem* **56**, 5979–5983 (2013).

328. Sun, D. *et al.* Discovery of AMG 232, a potent, selective, and orally bioavailable MDM2–p53 inhibitor in clinical development. *J Med Chem* **57**, 1454–1472 (2014).

329. Liao, G. *et al.* The development of piperidinones as potent MDM2-P53 protein-protein interaction inhibitors for cancer therapy. *Eur J Med Chem* **159**, 1–9 (2018).

330. Caille, S. & Lucas, B. S. Discovery of AMG 232, a Small Molecule Disrupting the p53-MDM2 Protein–Protein Interaction and Development of a Validation-Ready Process for Its Manufacture. in *Complete Accounts of Integrated Drug Discovery and Development: Recent Examples from the Pharmaceutical Industry. Volume 4* 203–247 (ACS Publications, 2022).

331. Ding, K. *et al.* Structure-based design of spiro-oxindoles as potent, specific small-molecule inhibitors of the MDM2− p53 interaction. *J Med Chem* **49**, 3432–3435 (2006).

332. Shangary, S. *et al.* Temporal activation of p53 by a specific MDM2 inhibitor is selectively toxic to tumors and leads to complete tumor growth inhibition. *Proceedings of the National Academy of Sciences* **105**, 3933–3938 (2008).

333. Canner, J. A. *et al.* MI-63: a novel small-molecule inhibitor targets MDM2 and induces apoptosis in embryonal and alveolar rhabdomyosarcoma cells with wild-type p53. *Br J Cancer* **101**, 774–781 (2009).

334. Wang, S. *et al.* SAR405838: an optimized inhibitor of MDM2–p53 interaction that induces complete and durable tumor regression. *Cancer Res* **74**, 5855–5865 (2014).

335. Wang, S. & Chen, F.-E. Small-molecule MDM2 inhibitors in clinical trials for cancer therapy. *Eur J Med Chem* **236**, 114334 (2022).

336. Aguilar, A. *et al.* Discovery of 4-((3' R, 4' S, 5' R)-6 "-Chloro-4'-(3-chloro-2-fluorophenyl)-1'-ethyl-2 "-oxodispiro [cyclohexane-1, 2'-pyrrolidine-3', 3 "-indoline]-5'-carboxamido) bicyclo [2.2. 2] octane-1-carboxylic Acid (AA-115/APG-115): A Potent and Orally Active Murine Double Minute 2 (MDM2) Inhibitor in Clinical Development. *J Med Chem* **60**, 2819–2839 (2017).

337. Arnhold, V. *et al.* Reactivating TP53 signaling by the novel MDM2 inhibitor DS-3032b as a therapeutic option for high-risk neuroblastoma. *Oncotarget* **9**, 2304 (2018).

338. Furet, P. *et al.* The central valine concept provides an entry in a new class of non peptide inhibitors of the p53–MDM2 interaction. *Bioorg Med Chem Lett* **22**, 3498–3502 (2012).

339. Holzer, P. *et al.* Discovery of a dihydroisoquinolinone derivative (NVP-CGM097): a highly potent and selective MDM2 inhibitor undergoing phase 1 clinical trials in p53wt tumors. Preprint at (2015).

340. Furet, P. *et al.* Discovery of a novel class of highly potent inhibitors of the p53–MDM2 interaction by structure-based design starting from a conformational argument. *Bioorg Med Chem Lett* **26**, 4837–4841 (2016).

341. Rinnenthal, J. *et al.* BI 907828: A highly potent MDM2 inhibitor with low human dose estimation, designed for high-dose intermittent schedules in the clinic. *Cancer Res* **78**, 4865 (2018).

342. Rinnenthal, J. *et al.* Abstract 4865: BI 907828: A highly potent MDM2 inhibitor with low human dose estimation, designed for high-dose intermittent schedules in the clinic. *Cancer Res* **78**, 4865 (2018).

343. LoRusso, P. *et al.* The MDM2–p53 antagonist brigimadlin (BI 907828) in patients with advanced or metastatic solid tumors: results of a phase Ia, first-in-human, dose-escalation study. *Cancer Discov* **13**, 1802–1813 (2023).

344. Saleh, M. N. *et al.* Phase 1 trial of ALRN-6924, a dual inhibitor of MDMX and MDM2, in patients with solid tumors and lymphomas bearing wild-type TP53. *Clinical Cancer Research* **27**, 5236–5247 (2021).

345. Meric-Bernstam, F. al *et al.* Phase I trial of a novel stapled peptide ALRN-6924 disrupting MDMX-and MDM2-mediated inhibition of WT p53 in patients with solid tumors and lymphomas. *J Clin Oncol* **35**, 2505 (2017).

346. Haronikova, L. *et al.* Resistance mechanisms to inhibitors of p53-MDM2 interactions in cancer therapy: can we overcome them? *Cellular and Molecular Biology Letters* vol. 26 Preprint at https://doi.org/10.1186/s11658-021-00293-6 (2021).

347. Purvis, J. E. *et al.* p53 dynamics control cell fate. *Science* **336**, 1440–1444 (2012).

348. Tsabar, M. *et al.* A Switch in p53 Dynamics Marks Cells That Escape from DSB-Induced Cell Cycle Arrest. *Cell Rep* **32**, (2020).

349. Burgess, A. *et al.* Clinical overview of MDM2/X-targeted therapies. *Front Oncol* **6**, 7 (2016).

350. Tisato, V., Voltan, R., Gonelli, A., Secchiero, P. & Zauli, G. MDM2/X inhibitors under clinical evaluation: perspectives for the management of hematological malignancies and pediatric cancer. *J Hematol Oncol* **10**, 133 (2017).

351. Stott, F. J. *et al.* The alternative product from the human CDKN2A locus, p14ARF, participates in a regulatory feedback loop with p53 and MDM2. *EMBO J* **17**, 5001-5014–5014 (1998).

352. Michaelis, M. *et al.* Adaptation of cancer cells from different entities to the MDM2 inhibitor nutlin-3 results in the emergence of p53-mutated multi-drug-resistant cancer cells. *Cell Death Dis* **2**, e243–e243 (2011).

353. Hu, B., Gilkes, D. M., Farooqi, B., Sebti, S. M. & Chen, J. MDMX overexpression prevents p53 activation by the MDM2 inhibitor Nutlin. *Journal of Biological Chemistry* **281**, 33030–33035 (2006).

354. Macarulla, T. *et al.* Efficacy and safety of brigimadlin (BI 907828), an MDM2–p53 antagonist, in patients (pts) with advanced biliary tract cancer: Data from two phase Ia/Ib dose-escalation/expansion trials. Preprint at (2024).

355. Stein, E. M. *et al.* Results from a First-in-Human Phase I Study of Siremadlin (HDM201) in Patients with Advanced Wild-Type TP53 Solid Tumors and Acute Leukemia. *Clinical Cancer Research* **28**, 870–881 (2022).

356. Miyachi, M. *et al.* Restoration of p53 pathway by nutlin-3 induces cell cycle arrest and apoptosis in human rhabdomyosarcoma cells. *Clinical Cancer Research* **15**, 4077–4084 (2009).

357. Phelps, D. *et al.* Inhibition of MDM2 by RG7388 confers hypersensitivity to X-radiation in xenograft models of childhood sarcoma. *Pediatr Blood Cancer* **62**, 1345–1352 (2015).

358. Huang, R. & Zhou, P.-K. DNA damage repair: historical perspectives, mechanistic pathways and clinical translation for targeted cancer therapy. *Signal Transduct Target Ther* **6**, 254 (2021).

359. Swift, L. H. & Golsteyn, R. M. Genotoxic Anti-Cancer Agents and Their Relationship to DNA Damage, Mitosis, and Checkpoint Adaptation in Proliferating Cancer Cells. *Int J Mol Sci* **15**, 3403–3431 (2014).

360. Zhang, X.-P., Liu, F. & Wang, W. Two-phase dynamics of p53 in the DNA damage response. *Proceedings of the National Academy of Sciences* **108**, 8990–8995 (2011).

361. Knights, C. D. *et al.* Distinct p53 acetylation cassettes differentially influence gene-expression patterns and cell fate. *J Cell Biol* **173**, 533 (2006).

362. Sykes, S. M. *et al.* Acetylation of the p53 DNA-binding domain regulates apoptosis induction. *Mol Cell* **24**, 841–851 (2006).

363. Luo, J. *et al.* Acetylation of p53 augments its site-specific DNA binding both in vitro and in vivo. *Proceedings of the National Academy of Sciences* **101**, 2259–2264 (2004).

364. Chung, S.-K., Zhu, S., Xu, Y. & Fu, X. Functional analysis of the acetylation of human p53 in DNA damage responses. *Protein Cell* **5**, 544–551 (2014).

365. Reed, S. M. & Quelle, D. E. p53 acetylation: regulation and consequences. *Cancers (Basel)* **7**, 30–69 (2014).

366. Puca, R. *et al.* HIPK2 modulates p53 activity towards pro-apoptotic transcription. *Mol Cancer* **8**, 85 (2009).

367. Dauth, I., Krüger, J. & Hofmann, T. G. Homeodomain-interacting protein kinase 2 is the ionizing radiation–activated p53 serine 46 kinase and is regulated by ATM. *Cancer Res* **67**, 2274–2279 (2007).

368. Saito, S. *et al.* ATM Mediates Phosphorylation at Multiple p53 Sites, Including Ser46, in Response to Ionizing Radiation∗. *Journal of Biological Chemistry* **277**, 12491–12494 (2002).

369. Kodama, M. *et al.* Requirement of ATM for rapid p53 phosphorylation at Ser46 without Ser/Thr-Gln sequences. *Mol Cell Biol* (2010).

370. Rinaldo, C. *et al.* MDM2-Regulated Degradation of HIPK2 Prevents p53Ser46 Phosphorylation and DNA Damage-Induced Apoptosis. *Mol Cell* **25**, 739–750 (2007).

371. Gu, W. & Roeder, R. G. Activation of p53 Sequence-Specific DNA Binding by Acetylation of the p53 C-Terminal Domain. *Cell* **90**, 595–606 (1997).

372. Brochier, C. *et al.* Specific Acetylation of p53 by HDAC Inhibition Prevents DNA Damage-Induced Apoptosis in Neurons. *The Journal of Neuroscience* **33**, 8621 (2013).

373. Yamaguchi, H. *et al.* p53 acetylation is crucial for its transcription-independent proapoptotic functions. *Journal of Biological Chemistry* **284**, 11171–11183 (2009).

374. Purvis, J. E. *et al.* p53 Dynamics Control Cell Fate. *Science (1979)* **336**, 1440–1444 (2012).

375. Fischer, M. & Sammons, M. A. Determinants of p53 DNA binding, gene regulation, and cell fate decisions. *Cell Death Differ* 1–8 (2024).

376. Fu, D., Calvo, J. A. & Samson, L. D. Balancing repair and tolerance of DNA damage caused by alkylating agents. *Nat Rev Cancer* **12**, 104–120 (2012).

377. Roos, W. P. & Kaina, B. DNA damage-induced cell death by apoptosis. *Trends Mol Med* **12**, 440–450 (2006).

378. Sarkaria, J. N. *et al.* Mechanisms of chemoresistance to alkylating agents in malignant glioma. *Clinical cancer research* **14**, 2900–2908 (2008).

379. Hao, X. *et al.* BI-907828, a novel potent MDM2 inhibitor, inhibits glioblastoma brain tumor stem cells in vitro and prolongs survival in orthotopic xenograft mouse models. *Neuro Oncol* **25**, 913–926 (2023).

380. Wang, H. *et al.* Combination therapy in a xenograft model of glioblastoma: enhancement of the antitumor activity of temozolomide by an MDM2 antagonist. *Journal of Neurosurgery JNS* **126**, 446–459 (2017).

381. Chen, L. *et al.* Preclinical evaluation of the first intravenous small molecule MDM2 antagonist alone and in combination with temozolomide in neuroblastoma. *Int J Cancer* **144**, 3146–3159 (2019).

382. Rottenberg, S., Disler, C. & Perego, P. The rediscovery of platinum-based cancer therapy. *Nat Rev Cancer* **21**, 37–50 (2021).

383. Kelland, L. The resurgence of platinum-based cancer chemotherapy. *Nat Rev Cancer* **7**, 573–584 (2007).

384. Jung, Y. & Lippard, S. J. Direct cellular responses to platinum-induced DNA damage. *Chem Rev* **107**, 1387–1407 (2007).

385. Todd, R. C. & Lippard, S. J. Inhibition of transcription by platinum antitumor compounds. *Metallomics* **1**, 280–291 (2009).

386. Müller, S. DNA damage-inducing compounds: unraveling their pleiotropic effects using high throughput sequencing. *Curr Med Chem* **24**, 1558–1585 (2017).

387. Zhou, J. *et al.* The drug-resistance mechanisms of five platinum-based antitumor agents. *Front Pharmacol* **11**, 343 (2020).

388. Ohnstad, H. O. *et al.* MDM2 antagonist Nutlin-3a potentiates antitumour activity of cytotoxic drugs in sarcoma cell lines. *BMC Cancer* **11**, 1–11 (2011).

389. Voon, Y.-L. *et al.* Nutlin-3 sensitizes nasopharyngeal carcinoma cells to cisplatin-induced cytotoxicity. *Oncol Rep* **34**, 1692–1700 (2015).

390. Chen, L. *et al.* Pre-clinical evaluation of the MDM2-p53 antagonist RG7388 alone and in combination with chemotherapy in neuroblastoma. *Oncotarget* **6**, 10207 (2015).

391. Zanjirband, M., Edmondson, R. J. & Lunec, J. Pre-clinical efficacy and synergistic potential of the MDM2-p53 antagonists, Nutlin-3 and RG7388, as single agents and in combined treatment with cisplatin in ovarian cancer. *Oncotarget* **7**, 40115 (2016).

392. Canon, J. *et al.* The MDM2 inhibitor AMG 232 demonstrates robust antitumor efficacy and potentiates the activity of p53-inducing cytotoxic agents. *Mol Cancer Ther* **14**, 649–658 (2015).

393. Azmi, A. S. *et al.* Network modeling of MDM2 inhibitor-oxaliplatin combination reveals biological synergy in wt-p53 solid tumors. *Oncotarget* **2**, 378 (2011).

394. Swiecicki, P. *et al.* Trial in progress: A phase I/II trial of novel MDM2 inhibitor alrizomadlin (APG-115), with or without platinum chemotherapy, in patients with p53 wild-type salivary gland carcinoma. Preprint at (2021).

395. Mathews, C. K. Deoxyribonucleotide metabolism, mutagenesis and cancer. *Nat Rev Cancer* **15**, 528–539 (2015).

396. Shelton, J. *et al.* Metabolism, biochemical actions, and chemical synthesis of anticancer nucleosides, nucleotides, and base analogs. *Chem Rev* **116**, 14379–14455 (2016).

397. Tiwari, M. Antimetabolites: established cancer therapy. *J Cancer Res Ther* **8**, (2012).

398. Kojima, K. *et al.* Mdm2 inhibitor Nutlin-3a induces p53-mediated apoptosis by transcription-dependent and transcription-independent mechanisms and may overcome Atm-mediated resistance to fludarabine in chronic lymphocytic leukemia. *Blood* **108**, 993–1000 (2006).

399. Reuther, C. *et al.* The HDM2 (MDM2) inhibitor NVP-CGM097 inhibits tumor cell proliferation and shows additive effects with 5-fluorouracil on the p53-p21-Rb-E2F1 cascade in the p53wild type neuroendocrine tumor cell line GOT1. *Neuroendocrinology* **106**, 1–19 (2017).

400. Yee, K. *et al.* Phase 1b study of the MDM2 antagonist RG7112 in combination with 2 doses/schedules of cytarabine. *Blood* **122**, 498 (2013).

401. Konopleva, M. Y. *et al.* Idasanutlin plus cytarabine in relapsed or refractory acute myeloid leukemia: results of the MIRROS trial. *Blood Adv* **6**, 4147–4156 (2022).

402. Delgado, J. L., Hsieh, C.-M., Chan, N.-L. & Hiasa, H. Topoisomerases as anticancer targets. *Biochemical Journal* **475**, 373–398 (2018).

403. Pommier, Y., Leo, E., Zhang, H. & Marchand, C. DNA topoisomerases and their poisoning by anticancer and antibacterial drugs. *Chem Biol* **17**, 421–433 (2010).

404. Koster, D. A., Palle, K., Bot, E. S. M., Bjornsti, M.-A. & Dekker, N. H. Antitumour drugs impede DNA uncoiling by topoisomerase I. *Nature* **448**, 213–217 (2007).

405. van Loenhout, M. T. J., De Grunt, M. V & Dekker, C. Dynamics of DNA supercoils. *Science (1979)* **338**, 94–97 (2012).

406. Chen, T., Sun, Y., Ji, P., Kopetz, S. & Zhang, W. Topoisomerase IIα in chromosome instability and personalized cancer therapy. *Oncogene* **34**, 4019–4031 (2015).

407. Ubhi, T. & Brown, G. W. Exploiting DNA replication stress for cancer treatment. *Cancer Res* **79**, 1730–1739 (2019).

408. da Costa, A. A. B. A., Chowdhury, D., Shapiro, G. I., D'Andrea, A. D. & Konstantinopoulos, P. A. Targeting replication stress in cancer therapy. *Nat Rev Drug Discov* **22**, 38–58 (2023).

409. Uusküla-Reimand, L. & Wilson, M. D. Untangling the roles of TOP2A and TOP2B in transcription and cancer. *Sci Adv* **8**, eadd4920 (2024).

410. Pommier, Y. Topoisomerase I inhibitors: camptothecins and beyond. *Nat Rev Cancer* **6**, 789–802 (2006).

411. Nitiss, J. L. Targeting DNA topoisomerase II in cancer chemotherapy. *Nat Rev Cancer* **9**, 338–350 (2009).

412. Wu, C.-C. *et al.* Structural basis of type II topoisomerase inhibition by the anticancer drug etoposide. *Science (1979)* **333**, 459–462 (2011).

413. Senturk, J. C., Bohlman, S. & Manfredi, J. J. Mdm2 selectively suppresses DNA damage arising from inhibition of topoisomerase II independent of p53. *Oncogene* **36**, 6085–6096 (2017).

414. Conradt, L. *et al.* Mdm2 inhibitors synergize with topoisomerase II inhibitors to induce p53-independent pancreatic cancer cell death. *Int J Cancer* **132**, 2248–2257 (2013).

415. Coll-Mulet, L. *et al.* MDM2 antagonists activate p53 and synergize with genotoxic drugs in B-cell chronic lymphocytic leukemia cells. *Blood* **107**, 4109–4114 (2006).

416. Bartelink, H., Schellens, J. H. M. & Verheij, M. The combined use of radiotherapy and chemotherapy in the treatment of solid tumours. *Eur J Cancer* **38**, 216–222 (2002).

417. Olive, P. L. The role of DNA single-and double-strand breaks in cell killing by ionizing radiation. *Radiat Res* **150**, S42–S51 (1998).

418. Riley, P. A. Free radicals in biology: oxidative stress and the effects of ionizing radiation. *Int J Radiat Biol* **65**, 27–33 (1994).

419. Cadet, J. & Davies, K. J. A. Oxidative DNA damage & repair: an introduction. *Free Radic Biol Med* **107**, 2–12 (2017).

420. Chatterjee, N. & Walker, G. C. Mechanisms of DNA damage, repair, and mutagenesis. *Environ Mol Mutagen* **58**, 235–263 (2017).

421. Perry, M. E. Mdm2 in the response to radiation. *Molecular Cancer Research* **2**, 9–19 (2004).

422. Wu, L. & Levine, A. J. Differential regulation of the p21/WAF-1 and mdm2 genes after high-dose UV irradiation: p53-dependent and p53-independent regulation of the mdm2 gene. *Molecular medicine* **3**, 441–451 (1997).

423. Arya, A. K. *et al.* Nutlin-3, the small-molecule inhibitor of MDM2, promotes senescence and radiosensitises laryngeal carcinoma cells harbouring wild-type p53. *Br J Cancer* **103**, 186–195 (2010).

424. Cao, C. *et al.* Radiosensitization of lung cancer by nutlin, an inhibitor of murine double minute 2. *Mol Cancer Ther* **5**, 411–417 (2006).

425. Villalonga-Planells, R. *et al.* Activation of p53 by nutlin-3a induces apoptosis and cellular senescence in human glioblastoma multiforme. *PLoS One* **6**, e18588 (2011).

426. Yi, H. *et al.* A novel small molecule inhibitor of MDM2-p53 (APG-115) enhances radiosensitivity of gastric adenocarcinoma. *Journal of Experimental & Clinical Cancer Research* **37**, 1–10 (2018).

427. Prabakaran, P. J. *et al.* Radiosensitization of adenoid cystic carcinoma with MDM2 inhibition. *Clinical Cancer Research* **23**, 6044–6053 (2017).

428. Welliver, M. X. *et al.* NRG-DT001 phase Ib trial of neoadjuvant navtemadlin (previously AMG232 and KRT232) concurrent with preoperative radiotherapy in wild-type p53 soft tissue sarcoma of the extremity and body wall. Preprint at (2022).

429. Ray Chaudhuri, A. & Nussenzweig, A. The multifaceted roles of PARP1 in DNA repair and chromatin remodelling. *Nat Rev Mol Cell Biol* **18**, 610–621 (2017).

430. Gibson, B. A. & Kraus, W. L. New insights into the molecular and cellular functions of poly (ADP-ribose) and PARPs. *Nat Rev Mol Cell Biol* **13**, 411–424 (2012).

431. Lord, C. J. & Ashworth, A. BRCAness revisited. *Nat Rev Cancer* **16**, 110–120 (2016).

432. Javle, M. & Curtin, N. J. The role of PARP in DNA repair and its therapeutic exploitation. *Br J Cancer* **105**, 1114–1122 (2011).

433. Zandarashvili, L. *et al.* Structural basis for allosteric PARP-1 retention on DNA breaks. *Science (1979)* **368**, eaax6367 (2020).

434. Bryant, H. E. *et al.* Specific killing of BRCA2-deficient tumours with inhibitors of poly (ADP-ribose) polymerase. *Nature* **434**, 913–917 (2005).

435. Farmer, H. *et al.* Targeting the DNA repair defect in BRCA mutant cells as a therapeutic strategy. *Nature* **434**, 917–921 (2005).

436. Helleday, T. The underlying mechanism for the PARP and BRCA synthetic lethality: clearing up the misunderstandings. *Mol Oncol* **5**, 387–393 (2011).

437. Peyraud, F. & Italiano, A. Combined PARP inhibition and immune checkpoint therapy in solid tumors. *Cancers (Basel)* **12**, 1502 (2020).

438. Cortesi, L., Rugo, H. S. & Jackisch, C. An overview of PARP inhibitors for the treatment of breast cancer. *Target Oncol* **16**, 255–282 (2021).

439. Pilié, P. G., Gay, C. M., Byers, L. A., O'Connor, M. J. & Yap, T. A. PARP inhibitors: extending benefit beyond BRCA-mutant cancers. *Clinical Cancer Research* **25**, 3759–3771 (2019).

440. Dalmasso, B. *et al.* Beyond BRCA: the emerging significance of DNA damage response and personalized treatment in pancreatic and prostate cancer patients. *Int J Mol Sci* **23**, 4709 (2022).

441. Abbotts, R. *et al.* DNA methyltransferase inhibitors induce a BRCAness phenotype that sensitizes NSCLC to PARP inhibitor and ionizing radiation. *Proceedings of the National Academy of Sciences* **116**, 22609–22618 (2019).

442. Abbotts, R., Dellomo, A. J. & Rassool, F. V. Pharmacologic induction of BRCAness in BRCA-proficient cancers: expanding PARP inhibitor use. *Cancers (Basel)* **14**, 2640 (2022).

443. Cai, C. A Novel Mechanism to Induce BRCAness in Cancer Cells. *Cancer Res* **80**, 2977–2978 (2020).

444. Li, L. *et al.* Androgen receptor inhibitor–induced "BRCAness" and PARP inhibition are synthetically lethal for castration-resistant prostate cancer. *Sci Signal* **10**, eaam7479 (2017).

445. Zanjirband, M., Curtin, N., Edmondson, R. J. & Lunec, J. Combination treatment with rucaparib (Rubraca) and MDM2 inhibitors, Nutlin-3 and RG7388, has synergistic and dose reduction potential in ovarian cancer. *Oncotarget* **8**, 69779 (2017).

446. Chipuk, J. E. *et al.* Direct Activation of Bax by p53 Mediates Mitochondrial Membrane Permeabilization and Apoptosis. *Science (1979)* **303**, 1010–1014 (2004).

447. Wei, H. *et al.* Structural insight into the molecular mechanism of p53-mediated mitochondrial apoptosis. *Nat Commun* **12**, 2280 (2021).

448. Hao, Q., Chen, J., Lu, H. & Zhou, X. The ARTS of p53-dependent mitochondrial apoptosis. *J Mol Cell Biol* **14**, mjac074 (2022).

449. Purvis, J. E. *et al.* p53 dynamics control cell fate. *Science (1979)* **336**, 1440–1444 (2012).

450. Vaseva, A. V & Moll, U. M. The mitochondrial p53 pathway. *Biochimica et Biophysica Acta (BBA) - Bioenergetics* **1787**, 414–420 (2009).

451. Cory, S., Huang, D. & Adams, J. M. The Bcl-2 family: roles in cell survival and oncogenesis. *Oncogene* **22**, 8590–8607 (2003).

452. D'Aguanno, S. & Del Bufalo, D. Inhibition of anti-apoptotic Bcl-2 proteins in preclinical and clinical studies: current overview in cancer. *Cells* **9**, 1287 (2020).

453. Qian, S. *et al.* The role of BCL-2 family proteins in regulating apoptosis and cancer therapy. *Front Oncol* **12**, 985363 (2022).

454. Wang, Y. *et al.* Abstract 257: Targeting AML through apoptosis activation using Bcl-2/Mcl-1 or Bcl-2/Hdm2 inhibitor combination therapies. *Cancer Res* **79**, 257 (2019).

455. Lehmann, C., Friess, T., Birzele, F., Kiialainen, A. & Dangl, M. Superior anti-tumor activity of the MDM2 antagonist idasanutlin and the Bcl-2 inhibitor venetoclax in p53 wild-type acute myeloid leukemia models. *J Hematol Oncol* **9**, 1–13 (2016).

456. Van Goethem, A. *et al.* Dual targeting of MDM2 and BCL2 as a therapeutic strategy in neuroblastoma. *Oncotarget* **8**, 57047 (2017).

457. De, P. *et al.* Abstract P3-03-09: Dual targeting of BCL2 and MDM2 as a novel therapeutic strategy in ER+ breast cancer model. *Cancer Res* **80**, P3-03 (2020).

458. De, P. K., Aske, J. C., Costello, J. P., Thompson, E. & Dey, N. Therapeutic value of BCL2 and MDM2-p53 axis in ovarian clear cell and endometrioid carcinomas with wild type TP53. *Cancer Res* **80**, 4872 (2020).

459. Daver, N. G. *et al.* Venetoclax and idasanutlin in relapsed/refractory AML: a nonrandomized, open-label phase 1b trial. *Blood* **141**, 1265–1276 (2023).

460. Kamdar, M. *et al.* Combination of Idasanutlin, Venetoclax and Obinutuzumab in Patients with Relapsed or Refractory (R/R) Non-Hodgkin Lymphoma (NHL): Results from a Phase I/II Study. *Blood* **136**, 30–31 (2020).

461. Wei, A. H. *et al.* Preliminary Results from a Phase Ib Study Exploring MDM2 Inhibitor Siremadlin (HDM201) in Combination with B-Cell Lymphoma-2 (BCL-2) Inhibitor Venetoclax in Patients with Acute Myeloid Leukemia (AML) or High-Risk Myelodysplastic Syndrome (HR-MDS). *Blood* **138**, 1283 (2021).

462. Daver, N. *et al.* Siremadlin in Combination with Venetoclax (VEN) Plus Azacitidine (AZA) in Adult Patients with Acute Myeloid Leukemia (AML) Who Are Ineligible for Intensive Chemotherapy: A Phase Ib/II Trial. *Blood* **140**, 11625–11627 (2022).

463. Zhang, X. *et al.* KRT-232 and navitoclax enhance trametinib's anti-Cancer activity in non-small cell lung cancer patient-derived xenografts with KRAS mutations. *Am J Cancer Res* **10**, 4464 (2020).

464. Johansson, K. B., Zimmerman, M. S., Dmytrenko, I. V, Gao, F. & Link, D. C. Idasanutlin and navitoclax induce synergistic apoptotic cell death in T-cell acute lymphoblastic leukemia. *Leukemia* **37**, 2356–2366 (2023).

465. Carter, B. Z. *et al.* Simultaneous activation of p53 and inhibition of XIAP enhance the activation of apoptosis signaling pathways in AML. *Blood, The Journal of the American Society of Hematology* **115**, 306–314 (2010).

466. Zheng, M. *et al.* Efficacy of MDM2 inhibitor MI-219 against lung cancer cells alone or in combination with MDM2 knockdown, a XIAP inhibitor or etoposide. *Anticancer Res* **30**, 3321–3331 (2010).

467. Gu, L. *et al.* Discovery of Dual Inhibitors of MDM2 and XIAP for Cancer Treatment. *Cancer Cell* **30**, 623–636 (2016).

468. Meijer, A. *et al.* Nutlin-3 preferentially sensitises wild-type p53-expressing cancer cells to DR5-selective TRAIL over rhTRAIL. *Br J Cancer* **109**, 2685–2695 (2013).

469. Urso, L. *et al.* Synergistic targeting of malignant pleural mesothelioma cells by MDM2 inhibitors and TRAIL agonists. *Oncotarget* **8**, 44232 (2017).

470. Krause, D. S. & Van Etten, R. A. Tyrosine kinases as targets for cancer therapy. *New England Journal of Medicine* **353**, 172–187 (2005).

471. Saraon, P. *et al.* Receptor tyrosine kinases and cancer: oncogenic mechanisms and therapeutic approaches. *Oncogene* **40**, 4079–4093 (2021).

472. Mascarenhas, J. *et al.* An Open-Label, Global, Multicenter, Phase 1b/2 Study of KRT-232, a First-in-Class, Oral Small-Molecule Inhibitor of Murine Double Minute 2 (MDM2), Combined with Ruxolitinib in Patients Who Have Myelofibrosis and a Suboptimal Response to Ruxolitinib. *Blood* **136**, 44–45 (2020).

473. Tucker, E. R. *et al.* Combination therapies targeting ALK-aberrant neuroblastoma in preclinical models. *Clinical Cancer Research* **29**, 1317–1331 (2023).

474. Wang, H. Q. *et al.* Combined ALK and MDM2 inhibition increases antitumor activity and overcomes resistance in human ALK mutant neuroblastoma cell lines and xenograft models. *Elife* **6**, e17137 (2017).

475. Dadone-Montaudié, B. *et al.* Novel therapeutic insights in dedifferentiated liposarcoma: a role for FGFR and MDM2 dual targeting. *Cancers (Basel)* **12**, 3058 (2020).

476. Andreeff, M. *et al.* Synergistic anti-leukemic activity with combination of FLT3 inhibitor quizartinib and MDM2 inhibitor milademetan in FLT3-ITD Mutant/p53 wild-type acute myeloid leukemia models. *Blood* **132**, 2720 (2018).

477. Voltan, R. *et al.* Ibrutinib synergizes with MDM-2 inhibitors in promoting cytotoxicity in B chronic lymphocytic leukemia. *Oncotarget* **7**, 70623 (2016).

478. Han, Y. *et al.* APG115 Enhances the Sensitivity of Ibrutinib Via Promoting p53 to Target MCL-1 in Chronic Lymphocytic Leukemia. *Blood* **140**, 5982–5983 (2022).

479. Vatsyayan, R., Singhal, J., Nagaprashantha, L. D., Awasthi, S. & Singhal, S. S. Nutlin-3 enhances sorafenib efficacy in renal cell carcinoma. *Mol Carcinog* **52**, 39–48 (2013).

480. Zauli, G. *et al.* The sorafenib plus nutlin-3 combination promotes synergistic cytotoxicity in acute myeloid leukemic cells irrespectively of FLT3 and p53 status. *Haematologica* **97**, 1722 (2012).

481. Abraham, A. G. & O'Neill, E. PI3K/Akt-mediated regulation of p53 in cancer. *Biochem Soc Trans* **42**, 798–803 (2014).

482. Aksamitiene, E., Kiyatkin, A. & Kholodenko, B. N. Cross-talk between mitogenic Ras/MAPK and survival PI3K/Akt pathways: a fine balance. *Biochem Soc Trans* **40**, 139–146 (2012).

483. Wu, G. S. The functional interactions between the MAPK and p53 signaling pathways. *Cancer Biol Ther* **3**, 156–161 (2004).

484. Santarius, T., Shipley, J., Brewer, D., Stratton, M. R. & Cooper, C. S. A census of amplified and overexpressed human cancer genes. *Nat Rev Cancer* **10**, 59–64 (2010).

485. Sondka, Z. *et al.* The COSMIC Cancer Gene Census: describing genetic dysfunction across all human cancers. *Nat Rev Cancer* **18**, 696–705 (2018).

486. Zhang, W. *et al.* Blockade of mitogen-activated protein kinase/extracellular signal-regulated kinase kinase and murine double minute synergistically induces Apoptosis in acute myeloid leukemia via BH3-only proteins Puma and Bim. *Cancer Res* **70**, 2424–2434 (2010).

487. Kojima, K., Konopleva, M., Samudio, I. J., Ruvolo, V. & Andreeff, M. Mitogen-Activated Protein Kinase Kinase Inhibition Enhances Nuclear Proapoptotic Function of p53 in Acute Myelogenous Leukemia Cells. *Cancer Res* **67**, 3210–3219 (2007).

488. Hata, A. N. *et al.* Synergistic activity and heterogeneous acquired resistance of combined MDM2 and MEK inhibition in KRAS mutant cancers. *Oncogene* **36**, 6581–6591 (2017).

489. Elkrief, A. *et al.* Combination therapy with MDM2 and MEK inhibitors is effective in patient-derived models of lung adenocarcinoma with concurrent oncogenic drivers and MDM2 amplification. *Journal of Thoracic Oncology* **18**, 1165–1183 (2023).

490. Shattuck-Brandt, R. L. *et al.* Metastatic Melanoma Patient–Derived Xenografts Respond to MDM2 Inhibition as a Single Agent or in Combination with BRAF/MEK Inhibition. *Clinical Cancer Research* **26**, 3803–3818 (2020).

491. Berberich, A. *et al.* Targeting Resistance against the MDM2 Inhibitor RG7388 in Glioblastoma Cells by the MEK Inhibitor Trametinib. *Clinical Cancer Research* **25**, 253–265 (2019).

492. Erba, H. P. *et al.* Phase 1b study of the MDM2 inhibitor AMG 232 with or without trametinib in relapsed/refractory acute myeloid leukemia. *Blood Adv* **3**, 1939–1949 (2019).

493. Moschos, S. J. *et al.* Targeting wild-type TP53 using AMG 232 in combination with MAPK inhibition in Metastatic Melanoma; a phase 1 study. *Invest New Drugs* **40**, 1051–1065 (2022).

494. Katja Seipel, Miguel A.T. Marques, Corinne Sidler, Beatrice U. Mueller & Thomas Pabst. MDM2- and FLT3-inhibitors in the treatment of FLT3-ITD acute myeloid leukemia, specificity and efficacy of NVP-HDM201 and midostaurin. *Haematologica* **103**, 1862–1872 (2018).

495. Laroche, A. *et al.* MDM2 antagonists synergize with PI3K/mTOR inhibition in well-differentiated/dedifferentiated liposarcomas. *Oncotarget* **8**, 53968 (2017).

496. Saiki, A. Y. *et al.* MDM2 antagonists synergize broadly and robustly with compounds targeting fundamental oncogenic signaling pathways. *Oncotarget* **5**, 2030 (2014).

497. Laroche-Clary, A. *et al.* Combined targeting of MDM2 and CDK4 is synergistic in dedifferentiated liposarcomas. *J Hematol Oncol* **10**, 123 (2017).

498. Abdul Razak, A. R. *et al.* Co-targeting of MDM2 and CDK4/6 with siremadlin and ribociclib for the treatment of patients with well-differentiated or dedifferentiated liposarcoma: results from a proof-of-concept, phase Ib study. *Clinical Cancer Research* **28**, 1087–1097 (2022).

499. Kato, S. *et al.* Hyperprogressors after Immunotherapy: Analysis of Genomic Alterations Associated with Accelerated Growth Rate. *Clinical Cancer Research* **23**, 4242–4250 (2017).

500. Brummer, T. & Zeiser, R. The role of the MDM2/p53 axis in antitumor immune responses. *Blood* **143**, 2701–2709 (2024).

501. Tolcher, A. W. *et al.* Phase Ib study of a novel, small-molecule MDM2 inhibitor APG-115 combined with pembrolizumab in U.S. patients with metastatic solid tumors. *Journal of Clinical Oncology* **38**, 3512 (2020).

502. Yamamoto, N. *et al.* A phase Ia/Ib, dose-escalation/expansion study of BI 907828 in combination with BI 754091 (ezabenlimab) and BI 754111 in patients (pts) with advanced solid tumors. *Journal of Clinical Oncology* **40**, 3095 (2022).

503. Macarulla, T. *et al.* Efficacy and safety of brigimadlin (BI 907828), an MDM2–p53 antagonist, in patients (pts) with advanced biliary tract cancer: Data from two phase Ia/Ib dose-escalation/expansion trials. *Journal of Clinical Oncology* **42**, 487 (2024).

504. Saha, M. N. *et al.* MDM2 antagonist nutlin plus proteasome inhibitor velcade combination displays a synergistic anti-myeloma activity. *Cancer Biol Ther* **9**, 936–944 (2010).

505. Gu, J. J., Thompson, S., Mavis, C., Torka, P. & Hernandez-Ilizaliturri, F. MDM2 inhibitor Idasanutlin potentiate therapeutic agents in Diffuse Large B-Cell Lymphoma by targeting MDM2 and XIAP. *Cancer Res* **80**, 2404 (2020).

506. Carita, G. *et al.* Dual inhibition of protein kinase C and p53-MDM2 or PKC and mTORC1 are novel efficient therapeutic approaches for uveal melanoma. *Oncotarget* **7**, 33542 (2016).

507. Wade, M., Li, Y.-C. & Wahl, G. M. MDM2, MDMX and p53 in oncogenesis and cancer therapy. *Nat Rev Cancer* **13**, 83–96 (2013).

508. Fallatah, M. M. J., Law, F. V, Chow, W. A. & Kaiser, P. Small-molecule correctors and stabilizers to target p53. *Trends Pharmacol Sci* (2023) doi:10.1016/j.tips.2023.02.007.

509. BLISS, C. I. THE TOXICITY OF POISONS APPLIED JOINTLY1. *Annals of Applied Biology* **26**, 585–615 (1939).

510. Ianevski, A., Giri, A. K. & Aittokallio, T. SynergyFinder 2.0: visual analytics of multi-drug combination synergies. *Nucleic Acids Res* **48**, W488–W493 (2020).

511. Schneider, C. A., Rasband, W. S. & Eliceiri, K. W. NIH Image to ImageJ: 25 years of image analysis. *Nat Methods* **9**, 671–675 (2012).

512. Bray, M.-A. *et al.* Cell Painting, a high-content image-based assay for morphological profiling using multiplexed fluorescent dyes. *Nat Protoc* **11**, 1757–1774 (2016).

513. Rietdijk, J. *et al.* Morphological profiling of environmental chemicals enables efficient and untargeted exploration of combination effects. *Science of The Total Environment* **832**, 155058 (2022).

514. Francisco Rodríguez, M. A., Carreras Puigvert, J. & Spjuth, O. Designing microplate layouts using artificial intelligence. *Artificial Intelligence in the Life Sciences* **3**, 100073 (2023).

515. Stirling, D. R. *et al.* CellProfiler 4: improvements in speed, utility and usability. *BMC Bioinformatics* **22**, 1–11 (2021).

516. Stringer, C., Wang, T., Michaelos, M. & Pachitariu, M. Cellpose: a generalist algorithm for cellular segmentation. *Nat Methods* **18**, 100–106 (2021).

517. Livak, K. J. & Schmittgen, T. D. Analysis of Relative Gene Expression Data Using Real-Time Quantitative PCR and the $2^{-\Delta\Delta CT}$ Method. *Methods* **25**, 402–408 (2001).

518. Gallo-Oller, G., Ordoñez, R. & Dotor, J. A new background subtraction method for Western blot densitometry band quantification through image analysis software. *J Immunol Methods* **457**, 1–5 (2018).

519. Schneider, C. A., Rasband, W. S. & Eliceiri, K. W. NIH Image to ImageJ: 25 years of image analysis. *Nat Methods* **9**, 671–675 (2012).

520. Watson, J. V, Chambers, S. H. & Smith, P. J. A pragmatic approach to the analysis of DNA histograms with a definable G1 peak. *Cytometry* **8**, 1–8 (1987).

521. Shern, J. F. *et al.* Comprehensive genomic analysis of rhabdomyosarcoma reveals a landscape of alterations affecting a common genetic axis in fusion-positive and

fusion-negative tumors. *Cancer Discov* (2014) doi:10.1158/2159-8290.CD-13-0639.

522. Shern, J. F. *et al.* Genomic Classification and Clinical Outcome in Rhabdomyosarcoma: A Report From an International Consortium. *Journal of Clinical Oncology* **39**, 2859–2871 (2021).

523. Feng, J. *et al.* Stabilization of Mdm2 via Decreased Ubiquitination Is Mediated by Protein Kinase B/Akt-dependent Phosphorylation *. *Journal of Biological Chemistry* **279**, 35510–35517 (2004).

524. Malmlöf, M., Roudier, E., Högberg, J. & Stenius, U. MEK-ERK-mediated Phosphorylation of Mdm2 at Ser-166 in Hepatocytes: Mdm2 IS ACTIVATED IN RESPONSE TO INHIBITED Akt SIGNALING *. *Journal of Biological Chemistry* **282**, 2288–2296 (2007).

525. Keleti, J., Quezado, M. M., Abaza, M. M., Raffeld, M. & Tsokos, M. The MDM2 oncoprotein is overexpressed in rhabdomyosarcoma cell lines and stabilizes wild-type p53 protein. *Am J Pathol* **149**, 143 (1996).

526. Patterson, H. *et al.* Amplification and Over-Expression of the MDM2 Gene in Human Soft Tissue Tumours. *Sarcoma* **1**, 303059 (1997).

527. Taylor, A. C. *et al.* p53 mutation and MDM2 amplification frequency in pediatric rhabdomyosarcoma tumors and cell lines. *Med Pediatr Oncol* **35**, 96–103 (2000).

528. Cocker, H. A. *et al.* High levels of the MDM2 oncogene in paediatric rhabdomyosarcoma cell lines may confer multidrug resistance. *Br J Cancer* **85**, 1746–1752 (2001).

529. Hou, H., Sun, D. & Zhang, X. The role of MDM2 amplification and overexpression in therapeutic resistance of malignant tumors. *Cancer Cell Int* **19**, 216 (2019).

530. Hawkins, D. S., Demers, G. W. & Galloway, D. A. Inactivation of p53 enhances sensitivity to multiple chemotherapeutic agents. *Cancer Res* **56**, 892–898 (1996).

531. Klimovich, B. *et al.* p53 partial loss-of-function mutations sensitize to chemotherapy. *Oncogene* **41**, 1011–1023 (2022).

532. He, C., Li, L., Guan, X., Xiong, L. & Miao, X. Mutant p53 gain of function and chemoresistance: the role of mutant p53 in response to clinical chemotherapy. *Chemotherapy* **62**, 43–53 (2016).

533. Cao, X., Hou, J., An, Q., Assaraf, Y. G. & Wang, X. Towards the overcoming of anticancer drug resistance mediated by p53 mutations. *Drug Resistance Updates* **49**, 100671 (2020).

534. Webster, M. R. *et al.* Paradoxical role for wild-type p53 in driving therapy resistance in melanoma. *Mol Cell* **77**, 633–644 (2020).

535. Martinez-Rivera, M. & Siddik, Z. H. Resistance and gain-of-resistance phenotypes in cancers harboring wild-type p53. *Biochem Pharmacol* **83**, 1049–1062 (2012).

536. Jackson, J. G. *et al.* p53-mediated senescence impairs the apoptotic response to chemotherapy and clinical outcome in breast cancer. *Cancer Cell* **21**, 793–806 (2012).

537. Shahbandi, A. *et al.* BH3 mimetics selectively eliminate chemotherapy-induced senescent cells and improve response in TP53 wild-type breast cancer. *Cell Death Differ* **27**, 3097–3116 (2020).

538. Canner, J. A. *et al.* MI-63: A novel small-molecule inhibitor targets MDM2 and induces apoptosis in embryonal and alveolar rhabdomyosarcoma cells with wild-type p53. *Br J Cancer* **101**, 774–781 (2009).

539. Carol, H. *et al.* Initial testing of the MDM2 inhibitor RG7112 by the pediatric preclinical testing program. *Pediatr Blood Cancer* **60**, 633–641 (2013).

540. Ishizawa, J. *et al.* Predictive gene signatures determine tumor sensitivity to MDM2 inhibition. *Cancer Res* **78**, 2721–2731 (2018).

541. Vuaroqueaux, V. *et al.* Pharmacogenomics characterization of the MDM2 inhibitor MI-773 reveals candidate tumours and predictive biomarkers. *NPJ Precis Oncol* **5**, 96 (2021).

542. DepMap, Broad (2024). DepMap 24Q2 Public. Figshare+. Dataset. (2024).

543. Jeay, S. *et al.* Dose and Schedule Determine Distinct Molecular Mechanisms Underlying the Efficacy of the p53–MDM2 Inhibitor HDM201. *Cancer Res* **78**, 6257 LP – 6267 (2018).

544. Shvarts, A. *et al.* MDMX: a novel p53-binding protein with some functional properties of MDM2. *EMBO J* **15**, 5349–5357 (1996).

545. Raj, N. & Attardi, L. D. The Transactivation Domains of the p53 Protein. *Cold Spring Harb Perspect Med* **7**, (2017).

546. Kobet, E., Zeng, X., Zhu, Y., Keller, D. & Lu, H. MDM2 inhibits p300-mediated p53 acetylation and activation by forming a ternary complex with the two proteins. *Proceedings of the National Academy of Sciences* **97**, 12547–12552 (2000).

547. Sabbatini, P. & McCormick, F. MDMX inhibits the p300/CBP-mediated acetylation of p53. *DNA Cell Biol* **21**, 519–525 (2002).

548. Yu, D. H. *et al.* Targeting MDMX for Cancer Therapy: Rationale, Strategies, and Challenges. *Frontiers in Oncology* vol. 10 Preprint at https://doi.org/10.3389/fonc.2020.01389 (2020).

549. Ueda, K. *et al.* MDMX acts as a pervasive preleukemic-to-acute myeloid leukemia transition mechanism. *Cancer Cell* **39**, 529–547 (2021).

550. Danovi, D. *et al.* Amplification of Mdmx (or Mdm4) directly contributes to tumor formation by inhibiting p53 tumor suppressor activity. *Mol Cell Biol* (2004).

551. Carvajal, L. A. *et al. Dual Inhibition of MDMX and MDM2 as a Therapeutic Strategy in Leukemia. Sci. Transl. Med* vol. 10 https://www.science.org (2018).

552. Graves, B. *et al.* Activation of the p53 pathway by small-molecule-induced MDM2 and MDMX dimerization. *Proc Natl Acad Sci U S A* **109**, 11788–11793 (2012).

553. Hu, B., Gilkes, D. M., Farooqi, B., Sebti, S. M. & Chen, J. MDMX overexpression prevents p53 activation by the MDM2 inhibitor nutlin. *Journal of Biological Chemistry* **281**, 33030–33035 (2006).

554. Soares, J. *et al.* DIMP53-1: A novel small-molecule dual inhibitor of p53-MDM2/X interactions with multifunctional p53-dependent anticancer properties. *Mol Oncol* **11**, 612–627 (2017).

555. Amaral, J. D., Silva, D., Rodrigues, C. M. P., Solá, S. & Santos, M. M. M. A novel small molecule p53 stabilizer for brain cell differentiation. *Front Chem* **7**, (2019).

556. Bixby, D., Kujawski, L., Wang, S. & Malek, S. N. The pre-clinical development of MDM2 inhibitors in chronic lymphocytic leukemia uncovers a central role for p53 status in sensitivity to MDM2 inhibitor-mediated apoptosis. *Cell Cycle* vol. 7 971–979 Preprint at https://doi.org/10.4161/cc.7.8.5754 (2008).

557. Gomes, A. S. *et al.* SLMP53-1 interacts with wild-type and mutant p53 DNA-binding domain and reactivates multiple hotspot mutations. *Biochimica et Biophysica Acta (BBA) - General Subjects* **1864**, 129440 (2020).

558. Gomes, S. *et al.* SLMP53-2 restores wild-type-like function to mutant p53 through Hsp70: promising activity in hepatocellular carcinoma. *Cancers (Basel)* **11**, 1151 (2019).

559. Espadinha, M. *et al.* Discovery of MDM2-p53 and MDM4-p53 protein-protein interactions small molecule dual inhibitors. *Eur J Med Chem* **241**, 114637 (2022).

560. Pan, R. *et al.* Synthetic Lethality of Combined Bcl-2 Inhibition and p53 Activation in AML: Mechanisms and Superior Antileukemic Efficacy. *Cancer Cell* **32**, 748-760.e6 (2017).

561. Lehmann, C., Friess, T., Birzele, F., Kiialainen, A. & Dangl, M. Superior anti-tumor activity of the MDM2 antagonist idasanutlin and the Bcl-2 inhibitor venetoclax in p53 wild-type acute myeloid leukemia models. *J Hematol Oncol* **9**, 50 (2016).

562. Daver, N. G. *et al.* Safety, Efficacy, Pharmacokinetic (PK) and Biomarker Analyses of BCL2 Inhibitor Venetoclax (Ven) Plus MDM2 Inhibitor Idasanutlin (idasa) in Patients (pts) with Relapsed or Refractory (R/R) AML: A Phase Ib, Non-Randomized, Open-Label Study. *Blood* **132**, 767 (2018).

563. Wei, A. H. *et al.* Preliminary Results from a Phase Ib Study Exploring MDM2 Inhibitor Siremadlin (HDM201) in Combination with B-Cell Lymphoma-2 (BCL-2) Inhibitor Venetoclax in Patients with Acute Myeloid Leukemia (AML) or High-Risk Myelodysplastic Syndrome (HR-MDS). *Blood* **138**, 1283 (2021).

564. Bing Z. Carter *et al.* Combined inhibition of MDM2 and BCR-ABL1 tyrosine kinase targets chronic myeloid leukemia stem/progenitor cells in a murine model. *Haematologica* **105**, 1274–1284 (2020).

565. Daniele, S. *et al.* Combined inhibition of AKT/mTOR and MDM2 enhances Glioblastoma Multiforme cell apoptosis and differentiation of cancer stem cells. *Sci Rep* **5**, 9956 (2015).

566. Shattuck-Brandt, R. L. *et al.* Metastatic Melanoma Patient–Derived Xenografts Respond to MDM2 Inhibition as a Single Agent or in Combination with BRAF/MEK Inhibition. *Clinical Cancer Research* **26**, 3803–3818 (2020).

567. de Weger, V. A. *et al.* A phase I study of the HDM2 antagonist SAR405838 combined with the MEK inhibitor pimasertib in patients with advanced solid tumours. *Br J Cancer* **120**, 286–293 (2019).

568. Moreno-Smith, M. *et al.* p53 Nongenotoxic Activation and mTORC1 Inhibition Lead to Effective Combination for Neuroblastoma Therapy. *Clinical Cancer Research* **23**, 6629–6639 (2017).

569. Roy, S., Garg, R., Wang, D. & Goel, A. Dual inhibition of MDM2 and p38 MAPK signaling is a potential therapeutic strategy in esophageal squamous cell carcinoma. *Cancer Res* **82**, 723 (2022).

570. Tolcher, A. W. *et al.* Preliminary results of a phase II study of alrizomadlin (APG-115), a novel, small-molecule MDM2 inhibitor, in combination with pembrolizumab in patients (pts) with unresectable or metastatic melanoma or advanced solid tumors that have failed immuno-oncologic (I-O) drugs. *Journal of Clinical Oncology* **39**, 2506 (2021).

571. Somaiah, N. *et al.* A phase 2 study of alrizomadlin, a novel MDM2/p53 inhibitor, in combination with pembrolizumab for treatment of patients with malignant peripheral nerve sheath tumor (MPNST). *Journal of Clinical Oncology* **41**, e14627–e14627 (2023).

572. Herting, F. *et al.* Antitumour activity of the glycoengineered type II anti-CD20 antibody obinutuzumab (GA101) in combination with the MDM2-selective antagonist idasanutlin (RG7388). *Eur J Haematol* **97**, 461–470 (2016).

573. Portman, N. *et al.* MDM2 inhibition in combination with endocrine therapy and CDK4/6 inhibition for the treatment of ER-positive breast cancer. *Breast Cancer Research* **22**, 87 (2020).

574. Vilgelm, A. E. *et al.* MDM2 antagonists overcome intrinsic resistance to CDK4/6 inhibition by inducing p21. *Sci Transl Med* **11**, eaav7171 (2019).

575. Palani, C. D., Beck, J. F. & Sonnemann, J. Histone deacetylase inhibitors enhance the anticancer activity of nutlin-3 and induce p53 hyperacetylation and downregulation of MDM2 and MDM4 gene expression. *Invest New Drugs* **30**, 25–36 (2012).

576. Ludwig, M. P. *et al.* Proteasome Inhibition Sensitizes Liposarcoma to MDM2 Inhibition with Nutlin-3 by Activating the ATF4/CHOP Stress Response Pathway. *Cancer Res* **83**, 2543–2556 (2023).

577. Senturk, J. C., Bohlman, S. & Manfredi, J. J. Mdm2 selectively suppresses DNA damage arising from inhibition of topoisomerase II independent of p53. *Oncogene* **36**, 6085–6096 (2017).

578. Conradt, L. *et al.* Mdm2 inhibitors synergize with topoisomerase II inhibitors to induce p53-independent pancreatic cancer cell death. *Int J Cancer* **132**, 2248–2257 (2013).

579. Kojima, K. *et al.* Concomitant inhibition of MDM2 and Bcl-2 protein function synergistically induce mitochondrial apoptosis in AML. *Cell cycle* **5**, 2778–2786 (2006).

580. Wei, A. H. *et al.* Preliminary results from a phase Ib study exploring MDM2 inhibitor siremadlin (HDM201) in combination with B-cell lymphoma-2 (BCL-2) Inhibitor venetoclax in patients with acute myeloid leukemia (AML) or high-risk myelodysplastic syndrome (HR-MDS). *Blood* **138**, 1283 (2021).

581. Lehmann, C., Friess, T., Birzele, F., Kiialainen, A. & Dangl, M. Superior anti-tumor activity of the MDM2 antagonist idasanutlin and the Bcl-2 inhibitor venetoclax in p53 wild-type acute myeloid leukemia models. *J Hematol Oncol* **9**, 50 (2016).

582. Bailly, C. Irinotecan: 25 years of cancer treatment. *Pharmacol Res* **148**, 104398 (2019).

583. Ubhi, T. & Brown, G. W. Exploiting DNA Replication Stress for Cancer Treatment. *Cancer Res* **79**, 1730–1739 (2019).

584. Hande, K. R. Etoposide: four decades of development of a topoisomerase II inhibitor. *Eur J Cancer* **34**, 1514–1521 (1998).

585. Wu, C.-C. *et al.* Structural basis of type II topoisomerase inhibition by the anticancer drug etoposide. *Science (1979)* **333**, 459–462 (2011).

586. Rogakou, E. P., Pilch, D. R., Orr, A. H., Ivanova, V. S. & Bonner, W. M. DNA double-stranded breaks induce histone H2AX phosphorylation on serine 139. *Journal of biological chemistry* **273**, 5858–5868 (1998).

587. Mah, L. J., El-Osta, A. & Karagiannis, T. C. γH2AX: a sensitive molecular marker of DNA damage and repair. *Leukemia* **24**, 679–686 (2010).

588. Lu, H.-R., Wang, X. & Wang, Y. A stronger DNA damage-induced G2 checkpoint due to over-activated CHK1 in the absence of PARP-1. *Cell Cycle* **5**, 2364–2370 (2006).

589. Vance, S. *et al.* Selective radiosensitization of p53 mutant pancreatic cancer cells by combined inhibition of Chk1 and PARP1. *Cell Cycle* **10**, 4321–4329 (2011).

590. Lombard, A. P. *et al.* Olaparib-Induced Senescence Is Bypassed through G2–M Checkpoint Override in Olaparib-Resistant Prostate Cancer. *Mol Cancer Ther* **21**, 677–685 (2022).

591. Shangary, S. *et al.* Reactivation of p53 by a specific MDM2 antagonist (MI-43) leads to p21-mediated cell cycle arrest and selective cell death in colon cancer. *Mol Cancer Ther* **7**, 1533–1542 (2008).

592. Tovar, C. *et al.* MDM2 Small-Molecule Antagonist RG7112 Activates p53 Signaling and Regresses Human Tumors in Preclinical Cancer Models. *Cancer Res* **73**, 2587–2597 (2013).

593. El-Deiry, W. S. *et al.* WAF1, a potential mediator of p53 tumor suppression. *Cell* **75**, 817–825 (1993).

594. Harper, J. W., Adami, G. R., Wei, N., Keyomarsi, K. & Elledge, S. J. The p21 Cdk-interacting protein Cip1 is a potent inhibitor of G1 cyclin-dependent kinases. *Cell* **75**, 805–816 (1993).

595. Chen, J. The Cell-Cycle Arrest and Apoptotic Functions of p53 in Tumor Initiation and Progression. *Cold Spring Harb Perspect Med* **6**, (2016).

596. Vassilev, L. T. MDM2 inhibitors for cancer therapy. *Trends Mol Med* **13**, 23–31 (2007).

597. Batchelor, E., Mock, C. S., Bhan, I., Loewer, A. & Lahav, G. Recurrent initiation: a mechanism for triggering p53 pulses in response to DNA damage. *Mol Cell* **30**, 277–289 (2008).

598. Zhang, X.-P., Liu, F., Cheng, Z. & Wang, W. Cell fate decision mediated by p53 pulses. *Proceedings of the National Academy of Sciences* **106**, 12245–12250 (2009).

599. Zhang, X.-P., Liu, F. & Wang, W. Two-phase dynamics of p53 in the DNA damage response. *Proceedings of the National Academy of Sciences* **108**, 8990–8995 (2011).

600. Stewart-Ornstein, J. *et al.* p53 dynamics vary between tissues and are linked with radiation sensitivity. *Nat Commun* **12**, 898 (2021).

601. Oliver, T. G. *et al.* Caspase-2-Mediated Cleavage of Mdm2 Creates a p53-Induced Positive Feedback Loop. *Mol Cell* **43**, 57–71 (2011).

602. Lim, Y., Dorstyn, L. & Kumar, S. The p53-caspase-2 axis in the cell cycle and DNA damage response. *Exp Mol Med* **53**, 517–527 (2021).

603. Zhao, Y. *et al.* Acetylation of p53 at lysine 373/382 by the histone deacetylase inhibitor depsipeptide induces expression of p21Waf1/Cip1. *Mol Cell Biol* (2006).

604. Tang, Y., Zhao, W., Chen, Y., Zhao, Y. & Gu, W. Acetylation is indispensable for p53 activation. *Cell* **133**, 612–626 (2008).

605. Menear, K. A. *et al.* 4-[3-(4-Cyclopropanecarbonylpiperazine-1-carbonyl)-4-fluorobenzyl]-2H-phthalazin-1-one: A Novel Bioavailable Inhibitor of Poly(ADP-ribose) Polymerase-1. *J Med Chem* **51**, 6581–6591 (2008).

606. Evers, B. *et al.* Selective Inhibition of BRCA2-Deficient Mammary Tumor Cell Growth by AZD2281 and Cisplatin. *Clinical Cancer Research* **14**, 3916–3925 (2008).

607. Weston, V. J. *et al.* The PARP inhibitor olaparib induces significant killing of ATM-deficient lymphoid tumor cells in vitro and in vivo. *Blood, The Journal of the American Society of Hematology* **116**, 4578–4587 (2010).

608. Bergamaschi, L. *et al.* Relapse after nonmetastatic rhabdomyosarcoma: Salvage rates and prognostic variables. *Pediatr Blood Cancer* **70**, e30050 (2023).

609. Heske, C. M. & Mascarenhas, L. Relapsed rhabdomyosarcoma. *J Clin Med* **10**, 804 (2021).

610. Malempati, S. & Hawkins, D. S. Rhabdomyosarcoma: review of the Children's Oncology Group (COG) Soft-Tissue Sarcoma Committee experience and rationale for current COG studies. *Pediatr Blood Cancer* **59**, 5–10 (2012).

611. Yang, L., Takimoto, T. & Fujimoto, J. Prognostic model for predicting overall survival in children and adolescents with rhabdomyosarcoma. *BMC Cancer* **14**, 1–7 (2014).

612. Yohe, M. E. *et al.* Insights into pediatric rhabdomyosarcoma research: Challenges and goals. *Pediatr Blood Cancer* **66**, e27869 (2019).

613. Winter, S., Fasola, S., Brisse, H., Mosseri, V. & Orbach, D. Relapse after localized rhabdomyosarcoma: evaluation of the efficacy of second-line chemotherapy. *Pediatr Blood Cancer* **62**, 1935–1941 (2015).

614. Borinstein, S. C. *et al.* Consensus and controversies regarding the treatment of rhabdomyosarcoma. *Pediatr Blood Cancer* **65**, e26809 (2018).